A FORCED ~~VIBRATION~~ oscillation STUDY OF THE AERODYNAMIC INSTABILITY OF A SQUARE SECTION CYLINDER

by

LUO SIAO CHUNG

Thesis submitted for the degree of Doctor of Philosophy in the Faculty of Engineering, University of London and for the Diploma of Imperial College.

ABSTRACT

The flow past a stationary and a transversely oscillating square section cylinder has been investigated over the approximate Reynolds number range of 9000 to 76000. The purpose of the research was to examine the interaction between vortex shedding and galloping. Pressure averagers were used to make measurements of mean and fluctuating face pressures and drag and lift forces at different angles of incidence and Reynolds number were recorded. Good agreement was found with results reported by other researchers using conventional measuring techniques.

In the oscillating cylinder investigation fluctuating lift, mean and fluctuating drag, Strouhal number and the phase angle between lift and cylinder displacement were measured over a wide range of reduced velocity and at different amplitudes of oscillation. For dimensionless amplitudes of oscillation of 1 and 1.5, mean drag, the root mean square of fluctuating drag and base pressure reached their minimum values and the mean base pressure reached its maximum value at approximately the same reduced velocity. At this reduced velocity the maximum instantaneous angle of incidence reached about 13.5 degrees, the angle at which flow will reattach on a side face of a stationary cylinder. Altering the amplitude of oscillation did not alter the

overall trend of the parameters measured. At high reduced velocity the parameters measured asymptotically approached the values applicable to a stationary cylinder. Spectral analysis of lift and drag forces revealed that at low reduced velocity the dominating components were at the forcing frequency and its higher harmonics. At high reduced velocity, the dominating component for the lift force was at the shedding frequency whereas the dominating components for the drag force were at twice the shedding frequency, the sum and the difference between the shedding and the forcing frequencies. An average Strouhal number of 0.126 was measured for a stationary cylinder and a cylinder at high reduced velocity.

Flow visualization revealed that flow past an oscillating square cylinder has at least four different regimes at different reduced velocities. The ways in which vorticity was shed and strength of each vortex shed were different in the four regions. It is likely that the strength of each vortex shed is one of the factors that caused the variations in the fluctuating lift coefficient.

Parkinson's quasi-steady theory for galloping was studied and it was found that at mid and high reduced velocities Parkinson's theory is capable of predicting the forcing frequency component of the lift fairly accurately. An unsteady thin aerofoil theory was also examined and it was found that this theory could be used to predict the body frequency component of the lift force and the phase angle

between it and the cylinder displacement at moderate and high reduced velocity with fairly good accuracy. The thin aerofoil theory can also predict the inertia component of the lift force qualitatively.

ACKNOWLEDGEMENT

The author is indebted to many people who have contributed their knowledge, time and effort to the fulfilment of this work. In particular, he would like to express his thanks, gratitude and appreciation to:

Dr. P.W.Bearman - for his valued guidance, encouragement, approachability and excellent supervision throughout the course of this PhD research.

Dr. S.Karanfilian and Dr. C.S.Subramanian for their advice on some machine code and main frame programming problems respectively.

Mr. P.Gasson for his advice on modifying the oscillating mechanism.

The technical staffs of the Department of Aeronautics, Imperial College of Science and Technology.

Mrs. R.Fairhurst for proof reading and typing part of the manuscript.

Finally, the author wishes to thank the National University of Singapore for granting him overseas study leave and the award of the National University of Singapore overseas postgraduate research scholarship.

CONTENT

ABSTRACT		2
ACKNOWLEDGEMENT		5
CONTENT		7
LIST OF SYMBOLS		13
CHAPTER 1	INTRODUCTION AND LITERATURE SURVEY	17
1.1	FLOW PAST A STATIONARY CYLINDER	17
1.1.1	Flow Past Rectangular Cylinder	17
1.1.1.1	Variation of C_D, C_L, C_{pA}, C_{pB}, C_{pC} and C_{pD} with α	18
1.1.1.2	$(C_{pA} - C_{pC})'$ and $(C_{pD} - C_{pB})'$ versus α	20
1.1.1.3	Strouhal Number versus α and Re	24
1.1.1.4	Spanwise and Chordwise Correlation	26
1.1.1.5	Effect of Turbulence	29
1.1.1.6	Spectra of Pressure and Velocity Signals	32
1.2	FLOW INDUCED VIBRATIONS	34
1.2.1	Galloping Oscillation	34
1.2.1.1	Elastically Suspended Cylinder	36

1.2.1.2 Forced Oscillation 42

1.2.1.3 Parkinson's Quasi-Steady Theory of Galloping Oscillation 49

1.2.2 VORTEX RESONANCE 53

1.2.2.1 Experimental Work in Vortex Resonance 54

1.2.2.2 Numerical Simulation of Vortex Resonance 59

CHAPTER 2 EXPERIMENTAL APPARATUS **64**

2.1 WIND TUNNEL 64

2.2 MANOMETERS 64

2.3 MODELS AND THEIR INSTALLATION 65

2.3.1 Model for Pressure Measurement 66

2.3.2 Model for Flow Visualization 67

2.4 PRESSURE AVERAGERS 67

2.5 PRESSURE TRANSDUCERS 68

2.6 OSCILLATING MECHANISM 69

2.7 DISPLACEMENT TRANSDUCER 70

2.8 COMPUTERISED DATA ACQUISITION SYSTEM 71

2.9 TAPE RECORDER AND SIGNAL CORRELATOR 72

2.10 SMOKE WIRE/ACCESSORIES AND PHOTOGRAPHIC EQUIPMENT 72

2.11 OTHER EQUIPMENTS 73

CHAPTER 3 EXPERIMENTAL PROCEDURE AND DATA REDUCTION/CORRECTION **74**

3.1 SET-UP FOR DATA ACQUISITION 74

3.2 SET-UP FOR ϕ VERSUS U_r MEASUREMENT 75

3.3 SET-UP FOR LIFT/DISPLACEMENT SIMULTANEOUS RECORDING 76

3.4 SET-UP FOR FLOW VISUALIZATION 77

3.5 COMPUTER PROGRAMS AND DATA REDUCTION 78

3.5.1 "TWO CH AC" 78

3.5.2 "COPHASE" 80

3.6 CORRECTIONS 82

3.6.1 Correction for Blockage Effect 82

3.6.2 "Noise" Correction 84

CHAPTER 4 FLOW PAST A STATIONARY SQUARE CYLINDER -RESULTS AND DISCUSSION **87**

4.1 C_{pA}, C_{pB}, C_{pC} AND C_{pD} VERSUS α 88

4.2 C_D AND C_L VERSUS α 88

4.3 C_{pA}', C_{pB}', C_{pC}' AND C_{pD}' VERSUS α 89

4.4 C_{Fy} AND C_x VERSUS α 92

4.5 C_x' AND C_y' VERSUS α 96

4.6 C_p AND C_p' DISTRIBUTION 99

4.7	C_D, C_D', C_{pA}, C_{pA}', C_{pC} AND C_{pC}' VERSUS REYNOLDS NUMBER	101
4.8	C_L' VERSUS REYNOLDS NUMBER	103
4.9	STROUHAL NUMBER VERSUS REYNOLDS NUMBER	104
4.10	CONCLUSION	105

CHAPTER 5 FLOW PAST A TRANSVERSELY OSCILLATING SQUARE CYLINDER -RESULTS AND DISCUSSION **106**

5.1	C_L' VERSUS U_r	107
5.2	ϕ VERSUS U_r	116
5.3	C_D, C_{pA} AND C_{pC} VERSUS U_r	122
5.4	C_D', C_{pA}' AND C_{pC}' VERSUS U_r	127
5.5	SPECTRA OF LIFT FORCE VERSUS REDUCED VELOCITY	130
5.6	SPECTRA OF DRAG FORCE VERSUS REDUCED VELCITY	133
5.7	STROUHAL NUMBER	136
5.8	CONCLUSION	137

CHAPTER 6 FLOW VISUALIZATION ANALYSIS **141**

6.1	LOCK-ON TYPE A	143
6.2	LOCK-ON TYPE B	146
6.3	TRIPLE LOCK-ON	150
6.4	QUASI-STEADY	153
6.5	INTERMEDIATE STAGES	154

6.6 STATIONARY CYLINDER 154

6.7 EFFECT OF AMPLITUDE OF OSCILLATION 155

6.8 CONCLUSION 156

CHAPTER 7 COMPARISON OF EXPERIMENTAL RESULTS WITH SEMI-THEORETICAL PREDICTIONS 159

7.1 EXPERIMENTAL AND SEMI-THEORETICAL C_{Fy}' AT FORCING FREQUENCY AND HIGHER HARMONICS 159

7.2 COMPARISON OF EXPERIMENTAL MEASUREMENT WITH SEMI-THEORETICAL PREDICTION 163

7.2.1 Drag and Inertia Components of the Lift Force --- Experimental Results 163

7.2.2 Thin Aerofoil Theory 170

7.3 CONCLUSION 181

CHAPTER 8 CONCLUSION 184

REFERENCES 190

APPENDIX A 205

TABLES

Table 5.1	211
Table 5.2	212
Table 6.1	213

FIGURES

Figures for chapter 1	214
Figures for chapter 2	233
Figures for chapter 3	237
Figures for chapter 4	240
Figures for chapter 5	253
Figures for chapter 6	289
Figures for chapter 7	303

LIST OF SYMBOLS

ALPHABETS

A — $A = \partial C_{Fy}/\partial\alpha$ at $\alpha = 0$ degree

a = Longitudinal vortex spacing

B — b = Lateral vortex spacing

C — C_D = Drag coefficient

C_D' = R.M.S. drag coefficient

C_{dl} = The part of the lift that is 90 degrees out of phase to the cylinder displacement

$C_{Fy} = -(C_{pD} - C_{pB}) = C_y$ = body axis lift coefficient or the quasi-steady theory predicted lift coefficient

C_L = Lift coefficient

C_L' = R.M.S. lift coefficient

C_{LO} = Added lift coefficient

C_{LmI} = Imaginary part of $C_L'(f_N)$

C_{mA} = Added inertia coefficient

C_{ml} = The part of the lift that is in phase with the cylinder displacement

C_{mo} = Potential flow inertia coefficient

C_{pA} = Mean face A pressure coefficient

C_{pA}' = R.M.S. face A pressure coefficient

C_{pB} = Mean face B pressure coefficient

C_{pB}' = R.M.S. face B pressure coefficient

C_{pb} = Mean base pressure coefficient = C_{pC}

C_{pb}' = R.M.S. base pressure coefficient = C_{pC}'

C_{pC} = Mean face C pressure coefficient

C_{pC}' = R.M.S. face C pressure coefficient

C_{pD} = Mean face D pressure coefficient

C_{pD}' = R.M.S. face D pressure coefficient

$C_x = (C_{pA} - C_{pC})$ = body axis drag coefficient

$C_x' = (C_{pA} - C_{pC})'$ = R.M.S. body axis drag coefficient

$C_y = (C_{pD} - C_{pB}) = C_{\bar{F}y}$ = body axis lift coefficient

$C_y' = (C_{pD} - C_{pB})'$ = R.M.S. body axis lift coefficient

D — D = Side length of a square cylinder or the length of the side of a rectangular cylinder that is normal to the free stream

F — f_N = Forcing frequency

f_n = Natural frequency

f_s = Vortex shedding frequency

H — H = The length of the side of a rectangular cylinder that is parallel to the free stream

K — $k^2 = 1 - C_{pb}$ or $k = \pi/U_r$

L — L = Lift force or length of cylinder

L_x = Turbulence length scale in the x (free stream) direction

l_f = Vortex formation length

P — p = Pressure

PSD = Power spectral density

R R(p,z) = Spanwise correlation coefficient

S S = Strouhal number

T t = Time

U U_{cr} = Critical reduced velocity in Parkinson's quasi-steady theory = $\frac{1}{S}$

U_r = Reduced velocity = $\frac{U_\infty}{f_N D}$

U_{ro} = Resonance reduced velocity

$U_{r,Dmin}$ = U_r when C_D is at its minimum

$U_{r,Dss}$ = U_r when C_D = 2.4

$U_{r,k}$ = U_r when the ϕ vs U_r curve exhibits a kink

$U_{r,min}$ = U_r when C_L' is at its minimum

$U_{r,ss}$ = U_r when C_L' = 1.4

$U_{r,0}$ = U_r when ϕ = 0 degree

$U_{r,80}$ = U_r when ϕ = 80 degrees

U_{res} = SQR($U_\infty^2 + \frac{1}{2}\dot{y}_{max}^2$)

U_∞ = free stream velocity

X x = Free stream direction

Y y = Direction that is perpendicular to x and is vertical, in this thesis this is the direction of the transverse oscillation

Z z = Direction that is perpendicular to both x and y

$Z = k_c^2/k^2$

SUBSCRIPT

c	Quantities that are corrected for wind tunnel blockage effect (chapter 4) or for inertia effect of air inside connection tubing (chapter 5)
N	Forcing frequency component
n	Natural frequency component
s	Shedding frequency component
'	R.M.S. component
^	Fluctuating component eg. $C_{pAi} = C_{pA} + \hat{C}_{pAi}$

GREEK ALPHABETS

α	Angle of incidence
α_{cr}	Critical angle of incidence, $\sim$ 13.5 degrees
α_{max}	Maximum value of α within a cycle of oscillation
$\alpha_{max,min}$	Value of α_{max} when C_L' it at its minimum
$\alpha_{max,ss}$	Value of α_{max} when $C_L' = 1.4$
$\alpha_{max,0}$	Value of α_{max} when $\phi = 0$ degree
$\alpha_{max,80}$	Value of α_{max} when $\phi = 80$ degrees
β	System damping in the absence of aerodynamic forces
Γ	Strength of a vortex
θ	Angular position measured from the mean front stagnation position of a circular cylinder
ρ_{15}	Correlation coefficient between pressure at leading and trailing edges
ϕ	Phase angle between $C_L'(f_N)$ and displacement
ω	Angular velocity = $2\pi f_N$

CHAPTER ONE

INTRODUCTION AND LITERATURE SURVEY

1.1 FLOW PAST A STATIONARY CYLINDER

Plenty of research effort in bluff body aerodynamics had been devoted to the understanding of the basic physics of the flow past bluff and semi-bluff bodies. Circle, square and rectangle are probably the three most investigated shapes due to their geometrical simplicity and hence frequent application in various discipline of engineering such as buildings, bridges, power transmission and off-shore structures, to name a few. It is hoped that the following sections will serve as a brief summary of research findings to date.

1.1.1 Flow Past Rectangular Cylinder

Flow past stationary rectangular cylinder is initially expected to be slightly less complicated than that of a circular cylinder because the separation positions are fixed at the two sharp leading edges. However, as will be shown later, aerodynamic properties such as drag coefficient are not totally independent of Reynolds number. In the following the dependence of aerodynamic properties like drag

and lift coefficients, Strouhal number and spanwise as well as chordwise correlation coefficients on Reynolds number and angle of attack of the approaching flow will be discussed. Most of the results from literature presented here apply to a special case of rectangular cylinder when the ratio of length of adjacent sides = 1, ie. a square cylinder. The square is the shape of interest in the present research.

1.1.1.1 Variation of C_D, C_L, C_{pA}, C_{pB}, C_{pC}, and C_{pD} with α

For a stationary square cylinder exposed to a free stream, the flow past the cylinder becomes asymmetrical when α increases from 0 degree. This is shown is fig. 1.1. In smooth flow, when the angle of attack α reaches a value of about 13.5 degrees (average figure obtained from those reported by other researchers like Laneville (1975), Obasaju (1977) and Pocha (1971)), the shear layer which separates from the leading edge AB reattaches on the trailing edge BC. The mean value of α when this reattachment takes place is often referred to as the critical angle of attack (α_{crit}). The behaviour of the aerodynamic properties are quite different depending on whether or not there is flow reattachment (ie. whether α is larger or less than α_{crit}).

In the following the trend of C_{pA}, C_{pB}, C_{pC} and C_{pD} versus α are examined. The variation of C_{pA}, C_{pB}, C_{pC} and C_{pD} with α as reported by Obasaju (1977) are shown in fig. 1.2. By referring to fig. 1.1, C_D and C_L are simply

calculated from the formulae:

$$C_D = (C_{pA}-C_{pC}) \cos\alpha - (C_{pD}-C_{pB}) \sin\alpha \qquad (1.1)$$

$$C_L = (C_{pA}-C_{pC}) \sin\alpha + (C_{pD}-C_{pB}) \cos\alpha \qquad (1.2)$$

C_D and C_L versus α are shown in fig. 1.3. (Note that in fig. 1.3(b) Obasaju has a slightly different definition for faces A,B,C and D. In fig. 1.3(b) $C_L = (C_{pB} - C_{pD})\cos\alpha - (C_{pA} - C_{pC})\sin\alpha$).

Referring back to fig. 1.2, in the range of α between 0 degree to α_{crit}, increasing α has relatively little effect on the average pressure C_{pA} acting on the front face A. As the angle of attack increases (see fig. 1.1), the shear layer that separates from the leading edge AB is deflected further away from the cylinder by the trailing edge BC. As a result, the vortex formation length l_f is increased, the vortices (low pressure region) are formed further away from the rear of the cylinder and this causes the average pressure on face C (C_{pC} or C_{pb}) to rise. The above can be seen in flow visualization photographs by Pocha (1971) and is also reported by Lee (1974) and Obasaju (1977). Due to the asymmetry of the flow, the shear layer that separates from AB is closer to face B than the shear layer that separates from AD is to face D. Since the shear layer is a low pressure region, shear layer B causes more entrainment from the outer region than shear layer D

and as a result C_{pB} is more negative than C_{pD}.

In the range of α between α_{crit} to 45 degrees, C_{pA} reduces slowly with increasing α because face A is now more "streamline" to the free stream. This is analogous to a reduction in pressure acting on the front face of a flat plate when it is inclined at an angle instead of normal to the free stream. Flow visualisation by Pocha (1971) showed that in this range of α the vortex formation length l_f decreases. This reduction in l_f causes C_{pC} to drop with α increasing from α_{crit}. At $\alpha \sim \alpha_{crit}$, the shear layer that separates from leading edge AB reattaches on the trailing edge BC. At this angle of attack a separation bubble is formed on face BC and has its maximum length which is equivalent to the length of side BC (ie. D). As α increases further, the reattachment position moves upstream from BC towards AB. The separation bubble (the part of the side face B from AB to the reattachment position) "shrinks". This reduction in low pressure region causes C_{pB} to rise rapidly with α increasing from α_{crit}. C_{pD} reduces slightly in this range of α but the change is much more gradual when compared with C_{pB}.

1.1.1.2 $(C_{pA} - C_{pC})'$ and $(C_{pD} - C_{pB})'$ versus α

To the best of the author's knowledge so far only Vickery (1966), Pocha (1971), Lee (1974 and 1975(a)) and Robertson et al (1977/78) have presented information on the variation of C_x' (= $(C_{pA} - C_{pC})'$) and C_y' (= $(C_{pD} - C_{pB})'$)

with angle of attack α. Vickery measured the difference between average forces on faces D and B (ie. $F_{DB} = F_D - F_B$, see fig. 1.1 for definition of faces B and D) directly on a 3 in. long section by using a uni-directional strain-gauge balance. He made measurement of F_{DB} for α = 0, 7.5, 20, 30, and 45 degrees and in both smooth and turbulent (turbulence intensity about 10%) stream. His result are shown in fig. 1.4(b), together with results from Lee (1975) and Pocha (1971). Vickery's results which were corrected for blockage and three dimensional effects show a rapid drop in $(C_{pD} - C_{pB})'$ (smooth stream) from about 1.3 at α = 0 degree to about 0.22 at α = 20 degrees. For $\alpha > 20$ degrees the reduction becomes gradual and C_y' eventually levels off at about 0.12. In a turbulent stream, the value of $(C_{pD} - C_{pB})'$ at α = 0 degree is much lower at about 0.68. The subsequent reduction when α increases is more gradual and C_y' reaches a value of about 0.22 at α = 45 degrees. Vickery, however, did not attempt to relate the observed reduction in $(C_{pD} - C_{pB})'$ to what had happened to the flow past the inclined stationary square cylinder.

Lee (1975) measured both $(C_{pA} - C_{pC})'$ and $(C_{pD} - C_{pB})'$ versus α. His results which include smooth flow and turbulent flow with four different turbulence intensities; together with Vickery's and Pocha's, are shown in fig. 1.4(a) and (b). From fig. 1.4(a) and (b) it is seen that while the results of the three researchers agree in trend, detailed quantitative agreement is poor. This poor

quantitative agreement may be attributed to differences in blockage effect, aspect ratio and detailed experimental procedure and instrumentations. Lee suggested that the reduction in $(C_{pD} - C_{pB})'$ with increasing α seen in fig. 1.4(b) is attributed to the reduction in correlation between fluctuating pressure on opposite side faces of the cylinder, which in turn is due to reattachment of one of the separated shear layers.

Robertson et at (1977/78), on the other hand, measured the distribution of C_p' via four Statham dynamic pressure gauges. Robertson et al's results are shown in fig. 1.5(a) (C_{pB}', C_{pC}' and C_{pD}' versus α) and fig. 1.5(b) (effect of 10.4% free stream turbulence on C_{pB}' and C_{pC}' versus α). If F_D, F_B and F_{DB} are the average forces on side D, B and their difference respectively, it can be shown that:

$$F_{DB}'^2 = F_D'^2 + F_B'^2 - \frac{2}{N} \sum_{i=1}^{N} \hat{F}_D(t_i)\, \hat{F}_B(t_i) \qquad (1.3)$$

where $F_D(t_i) = F_D + \hat{F}_D(t_i)$, $F_D = \dfrac{\sum_{i=1}^{N} F_D(t_i)}{N}$

$$F_B(t_i) = F_B + \hat{F}_B(t_i), \quad F_B = \frac{\sum_{i=1}^{N} F_B(t_i)}{N}$$

$$F_D'^2 = \frac{\sum_{i=1}^{N} \left[\hat{F}_D(t_i)\right]^2}{N}$$

$$F_B'^2 = \frac{\sum_{i=1}^{N} \left[\hat{F}_B(t_i)\right]^2}{N}$$

and $C_y' = C_{DB}' = \frac{F_{DB}'}{\frac{1}{2}\rho D U_\infty^2}$

From the above it can be appreciated that due to the lack of knowledge of the term $\sum_{i=1}^{N} \hat{F}_D(t_i)\, \hat{F}_B(t_i)$, Robertson et al's results cannot be compared directly with those obtained by others. However, despite the inability to directly compare Vickery and Robertson et al's results, it is seen from fig. 1.4 and 1.5 that the general trend of their results agree.

It must be pointed out that in fig. 1.5, Robertson et al made a mistake by joining the three "wake" data points they measured in the -ve α region by a simple smooth curve. The curve for C_{pC}' (the dotted one) should be symmetrical about the α = 0 degree axis. Robertson et at also did not provide any detail analysis of the trend of C_{pB}' and C_{pC}' versus α. They attributed the rapid changes in r.m.s pressure in the region $10 < \alpha < 20$ degrees to the reattachment of flow which occurs at $\alpha \sim \alpha_{crit}$. Robertson et al reported that their α_{crit} is about 14 degrees.

1.1.1.3 Strouhal Number versus α and Re

The dependence of Strouhal number S on α is shown in fig. 1.6(a). In fig. 1.6(a), in the range $0 \leq \alpha \leq 10$ degrees, some researchers' results show that S increases slightly with increasing α whereas the results of others show otherwise. Obasaju (1977) pointed out that those researchers like Pocha (1971), Lee (1974) and himself, whose results show S increases with increasing α in the above mentioned α range, measured their f_s by "peak counting" on a storage oscilloscope. This method can be rather inaccurate because:

(1) The shedding frequency actually varies slightly (not necessarily symmetrically) about a mean value.

(2) At any time only about 20 cycles of shedding can be displayed on a normal size storage oscilloscope.

The rest of the researchers like Rockwell (1976) and Obasaju (1977) (Obasaju estimated S by using both methods) estimated f_s from the spectra of lift force. Their results show that S reduces slightly with α increasing from 0 to 10 degrees and that is believed to be the more accurate trend. Between α = 10 to about 13.5 degrees S rises very rapidly to a maximum at $\alpha \sim$ 13.5 degrees. For $\alpha >$ 13.5 degrees S reduces at first rather quickly and later more gradually with increasing α. Lee suggested that the increase in S with increasing α in the range $10 \leq \alpha \leq 13.5$ degrees was associated with reduction in wake width and hence reduction in longitudinal vortex spacing if a constant

ratio of vortex spacing to wake width is to be maintained (see Lee (1974) pg.17 and Obasaju (1977) pg.24). It therefore leads to an increase in vortex shedding frequency and hence Strouhal number S. The reverse of the above occurs when α increased beyond α_{crit}.ie. The two shear layers diverge, causing an increase in longitudinal vortex spacing and hence reduction in shedding frequency and Strouhal number. Obasaju (1983) pointed out that the trend of the Strouhal number in the range $0 \leq \alpha \leq \alpha_{crit}$ is similar to the changes in S when the H/D ratio (H and D are dimensions of sides of a rectangular cylinder that are parallel and perpendicular to the stream direction respectively) increases from very low value. In both cases S initially reduces slightly and then increases abruptly when flow reattachment on the side face(s) takes place at either $\alpha \sim$ 13.5 degrees or at H/D $\sim$ 2.5. Bearman and Trueman (1972) suggested that for a rectangular cylinder with H/D = 0.6, increasing either H/D or α will increase the interference between the trailing edge corner and a shear layer; this forces vortices to form further downstream. Besides causing a drop in $-C_{pb}$ and hence C_D, the longer distance between separation and vortex formation point means that the shear layers will be more diffused and thicker by the time the first vortex is formed. According to Gerrard's (1966) model of vortex formation, the more diffused shear layer will take a longer time to feed a fully grown vortex. This implies a reduction in f_s and hence a reduction in S.

The dependence of S on Re is shown in fig. 1.6(b) and (c). The results in fig. 1.6(b) were obtained by Obasaju (1977) by either peak counting or from digital spectral analysis on vortex shedding signal. Despite some scatter, Obasaju's results show a slight reduction in S from 0.128 at Re = 5×10^3 to 0.123 at Re = 1.2×10^5. Fig. 1.8(c) (from Okajima (1982)) includes results obtained from experiments conducted in both air and water. Okajima's results cover a Reynolds number range from about 80 to 2×10^4. His results therefore complement those reported by Obasaju rather than overlapping with the latter. At Re $\sim 10^4$, Obasaju (1977) reported S $\sim$ 0.125 while Okajima reported S $\sim$ 0.13. The agreement is thus fairly acceptable. The author also wishes to point out that as in the case of C_D and S versus α, C_D and S again show opposite trend when they are plotted against Re. ie. One increases while the other decreases and vice versa. The opposite going tendency of C_D and S is also observed in circular cylinder and is thought to be related to the vortex formation length l_f (see Goldstein (1938) and fig. 2.12 of Luo (1982)).

1.1.1.4 Spanwise and Chordwise Correlation

Spanwise correlation measurement along a side face by Lee (1974), Pocha (1971), Obasaju (1977), Vickery (1966) and Wilkinson (1974) are shown in fig. 1.7(a). Lee carried out his measurement along a line 5D/12 from and parallel to the front leading edge AB (see fig. 1.1). The rest of the

researchers all carried out their measurement along the centre line of a side face. With the exception of those correlation results reported by Wilkinson, the results of other researchers agree fairly well with the solid line in fig. 1.7(a) representing the mean. From fig. 1.7(a) it is seen that the spanwise correlation coefficient R(p,z) remains at 1 with z/D increasing up to about 0.7. Above z/D = 0.7 R(p,z) begins to drop and reaches a value of about 0.5 at z/D = 4. Beyond this spanwise separation R(p,z) continues to drop gradually to zero at z/D $\sim$12. Wilkinson's results, on the other hand, show that R(p,z) drops quickly to 0.5 at z/D = 2.1 and to 0 at z/D = 7. As a result of the much quicker reduction in R(p,z), Wilkinson (1981(b)) reported a shorter spanwise correlation length of 2.7D while other researchers all reported a spanwise correlation length of about 5.6D. The latter value is larger than that of a circular cylinder which is only about 3.5D (Prendergast (1958) and Baroudi (1960)). This is not unexpected because the separation line on a circular cylinder may actually be a curve whereas the sharp edge separation of a square cylinder will mean that the separation line is a straight line.

Since Wilkinson's results do not agree with the results reported by other researchers, it is possible that his results are in error. His experiment parameters (aspect ratio = 14, $3 \times 10^4 < Re < 1.1 \times 10^5$) are not very different from those of other researchers and it is not immediately

obvious what may be wrong with his experiment.

Lee (1975) measured R(p,z) on front, side and rear faces of the cylinder. His results, which include those for smooth flow (0.5% turbulence intensity) as well as turbulent (turbulence intensities = 4.4%, 6.5%, 8% and 12.5%) flow, are shown in fig. 1.7(b), (c) and (d). For the side face, the smooth flow data of Lee agrees fairly well with those of Obasaju, Pocha and Vickery. Lee reported that turbulence in the free stream has the effect of reducing spanwise correlation and hence causing a reduction in the spanwise correlation length.

More recently, Kareem & Cermak (1984) carried out measurement on a square cylinder in two types of boundary layer flow which simulate open country and urban flow conditions. Throughout their experiment the angle of attack was kept at 0 degree. Kareem & Cermak found that on the side face the spanwise correlation is higher within the separation bubble. Near the downstream edge where intermittent flow reattachment occurs, the spanwise correlation is poor. The average values of spanwise correlation length scale are 1.88D and 1.43D for open country and urban flow conditions respectively. It is not unexpected that their correlation lengths are much shorter than those found by other researchers as the flow in Kareem & Cermak's experiment is highly three dimensional.They also reported that the addition of free stream turbulence reduces the spanwise correlation.

Chordwise correlation for two dimensional smooth flow is high. Obasaju (1977) reported that at mid span, the correlation is higher than 0.92 over the mid 75% of a chord. Vickery (1966) also presented some chordwise correlation results but he did not quote the correlation length. Vickery's results show that chordwise correlation is very much reduced in the presence of free stream turbulence. Kareem & Cermak reported that in highly three dimensional flow, the chordwise correlation is much higher at mid span than at the two ends of the cylinder. They quoted average chordwise correlation lengths of 0.74D and 0.5D for open area and urban flow conditions respectively.

1.1.1.5 Effect of Turbulence

Effect of turbulence is not really within the scope of the present research. However, having said that, the author wishes to quickly point out that the effect of turbulence is actually a very important aspect of problems concerning flow past bluff body as most of the flow that are involved in real life engineering problems are highly turbulent.

In the following, effects of high free stream turbulence found by various researchers are summarized in point form:

(1) Reduction in C_L'. Vickery (1966) calculated C_L' from C_p' distribution and chordwise pressure correlation. He found that C_L' reduces from 1.27 in smooth flow to 0.63 in a

turbulent flow of about 10% intensity. Directly measured C_L' reduces from 1.32 (smooth flow) to 0.68 (turbulent flow).

(2) Reduction in $-C_{pb}$ and hence C_D. Vickery (1966) reported that at α = 0 degree, the addition of turbulence (10% intensity) in the free stream causes $-C_{pb}$ to reduce from 1.3 (smooth flow) to 0.7 (turbulent flow). This 46% reduction in $-C_{pb}$ causes a 25 to 30% reduction in drag. For angle of attack $\alpha > 25$ degrees, the effect of free stream turbulence is very much reduced. Lee (1975(a)) also reported the same finding. He suggested that the addition of turbulence "thickens" the separated shear layers, causes them to be deflected away by the downstream corners, increases the vortex formation length l_f and hence causes a reduction in $-C_{pb}$ and C_D.

(3) High free stream turbulence (sometimes abbreviated as FST) causes early flow reattachment on side faces of an inclined square cylinder. ie. Reduces the value of α_{crit}. This is the basis of Lee's (1975(a)) explanation regarding the reduction in $-C_{pb}$ and C_D mentioned in (2) above (see Lee (1975(a) and (b)), Kwok (1983) and Nakamura & Ohya (1983)). Kareem & Cermak (1984) also reported that in 3-D flow (angle of incidence = 0 degree) increasing the free stream turbulence can induce early reattachment and associated pressure recovery on the side faces, resulting in reduction of the lift coefficient.

(4) When studying rectangular cylinders of various H/D ratio, Laneville, Gartshore & Parkinson (1975) reported that

for H/D < 0.5, extra turbulence causes $-C_{pb}$ and C_D to increase. For H/D > 0.5, the reverse (ie. reduction in $-C_{pb}$ and C_D) were observed. That is in agreement with Vickery's (1966) and Lee's (1975(a)) finding mentioned in (2) above because square cylinder belongs to the H/D > 0.5 category. Nakamura & Ohya (1983) also reported similar findings to that of Laneville et al.

(5) High free stream turbulence causes rectangular cylinders (including square) to become more stable to galloping oscillation. In some cases (eg. Turbulence intensity = 12%, H/D = 2), the cylinder becomes completely stable to galloping oscillation (Laneville et al (1975)).

(6) Reduction in spanwise correlation. Vickery (1966) reported a reduction in spanwise correlation length from 5.6D to 3.3D. (See also Lee (1975(a))).

(7) Effect of varying turbulence intensity is stronger than effect of varying turbulence length scale. (Courchesne & Lanveille (1982) and Petty (1979)). Lee (1975(b)) plotted C_D against L_x/D where L_x is the turbulence length scale in the free stream direction, Lee observed a maximum in C_D at L_x/D between 1.5 to 2.

(8) Effect on Strouhal number is small (Vickery (1966)).

(9) Effect on spectra of side face surface pressure signal is small (Lee (1975(a)).

1.1.1.6 Spectra of Pressure and Velocity Signals

Obasaju (1977) carried out some spectral analysis on surface pressure and velocity signals. His findings are summarized as follows:

(1) By connecting a pressure transducer to a pressure tapping on the reattachment side and at a distance of D/12 from the leading edge and by positioning a hot wire 3.5D downstream and 3D off the wake centre-line (reattachment side), the pressure and velocity spectra of a square cylinder inclined to the free stream were measured. Both pressure and velocity spectra reveal peaks at the shedding frequency f_s. The peaks are rather broad band indicating a slight variation in the value of f_s. At α = 0 degree, small peaks can also be seen at $2f_s$ and $3f_s$. For α = 5 and 10 degrees, broad band peaks centered at $f_s/2$ are also observed in both pressure and velocity spectra. Obasaju suggested that these low frequency peaks could be due to oscillation of the vortex formation position. At α = 40 and 45 degrees, broad band peaks can only be seen in the pressure but not in the velocity spectra.

(2) Obasaju also obtained the spectra of pressure signal round the mid-section of the cylinder. α was kept to zero throughout that investigation. At the front face, besides peaks at the 50 Hz main's frequency and its higher harmonics, only a weak broad band peak is observed at a frequency approximately equal to $2f_s$. On the side faces, most of the pressure energy is centered at f_s but there is

also a small amount of energy at $2f_s$. Obasaju was surprised to observe fairly prominent spectral peaks at $3f_s$ on the side and back faces close to the trailing edges. At the centre of the rear face, a dominant peak is seen at $2f_s$ but not at f_s. This is to be expected as the pressure at the centre of the rear face is affected by both shear layers, each of them alternatively shedding vortices at a frequency of f_s. As mentioned in section 1.1.1.5(9), Lee (1975(a)) reported that extra turbulence in the free stream has very little effect on the spectra of the side face surface pressure.

1.2 FLOW INDUCED VIBRATIONS

Parkinson (1971) classified flow induced oscillation into three main categories. They are flutter, galloping and vortex resonance.

Flutter is probably the most complex one among the three types of flow induced oscillation mentioned, it is not within the scope of the present research. The main interest of the present research is to study galloping and vortex resonance individually as well as in the range of wind speed where they co-exist and interact with each other in a complex (non-linear) manner. The last case is relatively unexplored and very limited information is available in the literature. In the following galloping and vortex resonance are described individually.

1.2.1 Galloping Oscillation

The galloping instability has been known since as early 1907 when Lanchester described an "aerial tourbillion" which consisted of a pivoted D-section cylinder with flat face normal to the wind and which developed a steady rotation in the wind. Den Hartog (1956) associated the instability with the aerodynamics coefficients of a cross section.

Characterised by single degree of freedom low frequency and high amplitude oscillation, galloping oscillation arises from an instability of the elastic system to small displacements (either linear or angular) of the

elastic structure. For example, if a small translational velocity is given to an unstable elastically restrained section in the presence of a steady wind normal to the span, the flow asymmetry caused by the small translational velocity will creat a force which is in the same direction as the original disturbance. This causes an oscillation to build up and a final amplitude is reached when the energy extracted from the wind by the structure is balanced by the energy dissipated through system damping.

Parkinson (1971) classified galloping oscillation into four different types:

(1) Translational galloping such as those that occurred to ice-laden transmission lines.

(2) Torsional galloping which is responsible for the final catastrophic oscillation of the original Tacoma Narrows suspension bridge in 1940.

(3) The type which occurs for stranded conductors in a wind directed a few degrees from the normal to the span. It is essentially translational.

(4) Stall "flutter". It occurs to airfoils oscillating about their stalling angle and hence "flutter". Its excitation involves a hysteresis in the separation and reattachment of the air flow as the body oscillates about the stalling angle.

Although all four types of galloping oscillation have engineering importance, only translational galloping is investigated in the present research.

Most of the previous experimental research in translational galloping oscillation fall into either one of the following categories: Elastically suspended cylinder or forced oscillation. They are discussed separately in the following.

1.2.1.1 Elastically Suspended Cylinder

Parkinson & Brooks (1961) was one of the first of a series of theoretical and experimental investigation in galloping oscillations carried out by Parkinson and his students. In that paper Parkinson & Brooks investigated the flow past and stability of various bluff body shapes. They found that while some shapes such as the D-cylinder (flat face upstream) and the short rectangular cylinder (longer sides normal to flow) are stable to galloping oscillation and vibrate (when elastically suspended) only near the vortex resonance region, others such as the square and the long rectangular cylinders (longer sides H parallel to flow $1 < H/D < 3.5$) are unstable to both vortex resonance and galloping-induced oscillations. Parkinson & Brooks also proposed a quasi-steady theory which represented the dimensionless aerodynamic force C_{Fy} by a fifth order odd power polynomial in $\dot{y}/U_\infty$. They showed that values of amplitude of vibration and build up time estimated by the theory are in fairly good agreement with corresponding experimental results over a certain range of reduced velocity U_r. However, despite their success with their

mathematical model, Parkinson & Brooks are wrong in concluding that the flow characteristics are not affected by Reynolds number. Later investigation carried out by Wawzonek (1979) and Bearman & Obasaju (1982) all found that Reynolds number has an effect on drag coefficient of the square prism.

Parkinson & Smith (1964) extended the mathematical model used by Parkinson & Brooks by representing C_{Fy} by a seventh order odd power polynomial in $\dot{y}/U_\infty$. They considered a seventh order polynomial to be necessary because there are five important changes of curvature in the range $-16 \leq \alpha \leq 16$ degrees; α being the angle of attack of the square cylinder relative to the free stream. By equating the structural dissipating force to the aerodynamic force, they obtained a non-linear ordinary differential equation which can be solved by the first approximation method of Krylov & Bogoliubov. By substituting appropriate coefficients which were determined from steady flow experiment, Parkinson & Smith showed that their model was capable of predicting results which agreed with experimental measurements in a fairly convincing manner when the reduced velocity was (see fig. 1.8) high. The high reduced velocity constraint is due to the inherent assumption of their theory as Parkinson & Smith assumed that the flow field around a cylinder moving with velocity dy/dt in a direction transverse to the free stream U_∞ is identical to that of a stationary cylinder inclined at an angle of attack α (= $\tan^{-1}$

($\dot{y}/U_\infty$)) to the free stream U_{res} (= ($U_\infty^2 + \dot{y}^2$)$^{0.5}$). Their assumption ignores the effect of the cylinder's acceleration and as a result is only valid when the free stream velocity is considerably higher than the maximum transverse velocity of the cylinder. It is also due to this assumption that Parkinson & Smith theory is often referred to as the "quasi-steady theory".

Parkinson & Sullivan (1979) investigated the characteristics of three dimensional turbulent flow past a finite height square prism which simulated a tower exposed to natural wind. They found, as expected, strong dependence of local force on the dimensionless height. By substituting local (ie. function of height) force instead of an average (over full height) force as Novak (1972) did into the quasi-steady theory, they found that the prediction by the theory was fairly close to experimental measurements especially at high reduced wind velocity.

Through the research work carried out up to the mid seventies, it is now clear that while the quasi-steady theory of galloping oscillation can fairly accurately predict the flow characteristics at reasonably high reduced wind velocity ($U_r >> U_{ro}$) it is unreliable when the critical wind velocity U_{cr} is near the resonance wind velocity U_{ro}. Different researchers have reported different values of the lower bound of the ratio U_{cr}/U_{ro} above which quasi-theory will apply. Nakamura & Mizota (1975) suggested a value of U_{cr}/U_{ro} between 2 to 3, Parkinson (1981) suggested a higher

value of 4 while Wawzonek (1981) suggested a value of about 2.5. Furthermore, preliminary experimental evidence had shown that the interaction between the two flow-induced vibration mechanisms, namely, vortex resonance and galloping is non-linear and flow/structure characteristics like the response amplitude of vibration cannot be predicted by either theory or a simple amalagmation of the two. Wawzonek (1979) and Parkinson & Wawzonek (1981) reported on the finding of experiments carried out over a range of reduced velocity where both vortex resonance and galloping are important. Their experiments were conducted at three different values of U_{cr}/U_{ro}, namely, 1.06, 1.49 and 2.15. For the first two cases oscillations starts at U_{ro} and the amplitude increases linearly as wind velocity increases (see fig. 1.9(a) and (b)). There is a range of reduced velocity where two stable amplitudes of vibration (separated by another unstable amplitude) co-exist. For the highest ratio case, flow-induced vibrations due to vortex resonance and galloping seem to have separated from each other as there is a range of reduced velocity between U_{ro} and U_{cr} ($1.5 < U_r < 2.1$) where no flow-induced vibration was detected (fig. 1.9(c)). However, the findings of the two lower ratio cases were sufficient to cause concern as the results show that engineering design basing on the quasi-steady theory could over-estimate the wind velocity where flow-induced vibration begins. In otherwords, there exists a wind velocity range where flow-induced vibration is possible but

is not predicted by the theory. More investigation is obviously required in the range of reduced velocity where vortex resonance and galloping oscillations are both important. Parkinson & Wawzonek also carried out their experiments with different amount of turbulence in the free stream and their findings indicate that extra free stream turbulence has the same effect of reducing the value of the ratio U_{cr}/U_{ro} .

More recently Bearman et al (1984(a)) conducted some experiments on a vertical elastically suspended square-section cylinder. Their basic experimental set-up is essentially similar to that used by Wawzonek (1979) except that they used a newly constructed free-standing (ie. independent of the structure of the wind tunnel) frame to hold the cylinder and accessories like linear air bearing etc. They used a pressure averager similar to that used in the present investigation (see chapter 2 for more details) to directly obtain the average pressure on a side face. They conducted altogether nine different sets of experiments at three different damping and three different turbulence levels in the Reynolds number range of 10^4 to 3×10^4 ($18.85 \leq U_r \leq 56.55$). As will be shown in equation (1.16), the critical velocity in Parkinson's quasi-steady theory is given by $U_{cr} = 2\beta/nA$ where $A = [\partial C_{Fy}/\partial\alpha]_{\alpha=0}$, the slope of the C_{Fy} versus α curve at $\alpha = 0$ degree. In Bearman et al's experiment, for the highest damping cases, the critical velocity U_{cr} is much higher than the resonance wind speed

U_{ro} whereas in the lowest damping case U_{cr} is lower than U_{ro}. They found that for the three highest damping cases experimental results agree well with the quasi-steady prediction at least qualitatively. This include the magnitude of the critical velocity U_{cr}, A (= $[\partial C_{Fy}/\partial\alpha]_{\alpha=0}$) measured either dynamically or statically have about the same value, $\phi \sim 90$ degrees where ϕ is the angle that the body frequency component of the lift force leads the cylinder displacement and the way in which the amplitude of oscillation varies with U_r. For medium damping only the results for the lowest turbulence agree qualitatively with theoretical prediction. For lowest damping although $U_{cr} < U_{ro}$, Bearman et al found that for all turbulence level oscillation does not take place until $U_r \sim U_{ro}$. This is contrary to the prediction of the quasi-steady theory but is in agreement with the earlier findings of Wawzonek (1979). Through spectral analysis and considering only the components of the lift at the body frequency and its higher harmonics (ie. excluding $C_L'(f_s)$), Bearman et al found that the dominating component of the r.m.s. lift force C_L' in the range $12.57 \leq U_r \leq 31.42$ is at the body frequency. Near $U_r \sim 3U_{ro}$, they observed a kink in their amplitude of oscillation versus U_r plot which cannot be explained by the quasi-steady theory (see fig. 1.10(a)). They also found that $C_L'(3f_N)$ rises rapidly to its peak value at $U_r \sim 3U_{ro}$. At even higher U_r, Bearman et al observed that $C_L'(5f_N)$ begins to increase in magnitude but they were unable to collect even higher U_r

results as their set-up's maximum allowable amplitude of oscillation was reached. The even number harmonics were found to be low throughout the experiment (see fig. 1.10(b)). As for vortex shedding frequency, Bearman et al were surprised to find that despite the amplitude of oscillation reaching values as large as 1.27 times the characteristic dimension D, the mean Strouhal number for oscillating was found to be 0.132 which was practically the same as the stationary cylinder value of 0.133. Finally, Bearman et al suggested that two Karman wake vortex streets co-exist in their experiment. One is due to the vortex shedding from a stationary square cylinder while the other one is due to the transverse oscillation of the cylinder which sheds vortices at the body frequency. The two vortex street wakes interact in a complex manner and this may be related to the high $C_L'(3f_N)$ and kink in amplitude versus U_r plot near $U_r \sim 3U_{ro}$ mentioned earlier. Further investigation is obviously necessary in this area of flow-induced vibration.

1.2.1.2 Forced Oscillation

While Parkinson, his students and other researchers carried out their experiments on an elastically suspended cylinder, other researchers including Otsuki et al (1974), Nakamura & Mizota (1975), Obasaju (1977), Washizu et al (1978) and Bearman & Obasaju (1982) preferred the better controlled forced oscillation experiment. They believe that

if parameters which include free stream velocity, amplitude and frequency of oscillation remain unchanged, the flow field around the cylinder is the same regardless of whether the cylinder is forced to oscillate by some external means or is simply set into oscillation due to flow instability.

Otsuki et al (1974) performed experiment by oscillating a square cylinder transverse to the free stream inside a wind tunnel. They found that for square cylinder C_{LmI} (the imaginative part of $C_L(f_N)$, the dimensionless lift force at the forcing frequency) is positive only in the upper half of the lock-in range. Phase angle between C_{Lm} and cylinder displacement ϕ can be shown to be equal to $\tan^{-1}$ (C_{LmI}/C_{LmR}). For C_{LmI} to be positive therefore requires ϕ to have a value between 0 to 180 degrees, a criteria for galloping oscillation to take place (see fig. 1.11). Otsuki et al also illustrated the effect of the mass-damping parameter ($2M\ \delta_s/(\rho\ d^2L)$) by classifying the flow into three categories: At low damping oscillation starts at the resonance wind velocity and slowly approachs the quasi-steady prediction. At intermediate damping the effect of vortex resonance and galloping are separated. At high damping only galloping oscillation is observed. They also compared their experimental results with Parkinson's quasi-steady prediction, they found that the agreement was good for reduced wind velocity ($U_r = U_\infty /(f_N D)$ greater than 12 and dimensionless amplitude of oscillation less than 0.1. Otsuki et al eliminated the inertia loading that was acting

on their cylinder by oscillating an identical dummy cylinder together with the actual one but with the dummy outside the wind tunnel. They then subtracted the load on the dummy cylinder from the actual cylinder. Unfortunately, Otsuki et al failed to appreciate that the dummy cylinder was subjected to aerodynamic loading as well as inertia loading. A more accurate method would be to employ a lump mass which has the same inertia effect as the actual cylinder.

Nakamura & Mizota (1975) carried out free and forced oscillation experiments on rectangular cylinders having three different side ratio (H/D) of 1, 2 and 4. Oscillation was always transverse to the flow. They found agreement between the results obtained from free and forced oscillation. In their experiment Nakamura & Mizota found that both the 1:1 and 1:2 cylinders begin to oscillate at a wind velocity near the resonant wind velocity and amplitude of vibration increases approximately linearly with wind velocity (see fig. 1.12(a) and (b)). Another unstable region near half of the resonant wind velocity can also be detected for the 1:2 cylinder. For the 1:4 cylinder, although unstable regions were also detected near $0.5U_{ro}$ and U_{ro}, in both cases the amplitude of oscillation decay back to zero as free stream wind velocity increases; indicating that the 1:4 cylinder is stable to galloping oscillation (fig. 1.12(c)). They also found abrupt changes in the phase angle ϕ within the lock-in range. The phase angle crosses from the negative into the positive region at approximately

the same wind velocity when flow-induced vibration begins to take place. Phase angle versus reduced wind velocity results reported by Nakamure & Mizota are shown in fig. 1.13(a), (b) and (c). Nakamura & Mizota also pointed out that the agreement between tneir experimental results and prediction by the quasi-steady theory was good for a reduced velocity range which starts from value as low as 2 to 3 x U_{ro}. However, Nakamura & Mizota committed the same error as Otsuki et al by subtracting the load acting on a dummy cylinder from the actual cylinder which incurred some slight inaccuracy into their results.

Washizu et al (1978) carried out both free and forced oscillation experiments on rectangular cylinders with H/D ratio of 2 and 4. It was meant to be a "part 2" of experiment reported by Otsuki et al (1974). Washizu et al investigated the effect of damping on the oscillation of both cylinders and found that galloping oscillation only occurred in the case of the 1:2 cylinder and the effect of damping was to suppress vortex resonance. For the 1:2 cylinder, aeroelastic coupling between vortex resonance and galloping was possible when U_{cr} was not much greater than U_{ro}. May be expectedly, Washizu et al found that the agreement of the experimental findings with theoretical prediction was good at high reduced velocity. For 1:2 cylinder, they found that the agreement is good for reduced velocity greater than 20 and dimensionless amplitude of vibration less than about 0.2. For 1:4 cylinder,

approximately the same restriction on reduced velocity was found but the dimensionless amplitude of vibration must be less than about 0.15.

Obasaju (1977) and Bearman & Obasaju (1982) also investigated the flow field and surface pressure distribution around stationary and oscillating square cylinder. From knowledge on the spanwise correlation of pressure and the fluctuating pressure at the centre of the side faces, they estimated the fluctuating lift force and found that it varies with dimensionless amplitude of vibration in the same manner (ie. qualitatively) as that measured in Nakamura & Mizota's (1975) experiment. However, quantitative agreement was poor as the value of the dimensionless fluctuating lift estimated by Bearman & Obasaju was about 20% higher than Nakamura & Mizota's results (see fig. 1.14(a)). They suggested that differences in experimental arrangement and aspect ratio of the cylinders used in the two experiments may be the causes of the discrepency. May be due to the same reason, comparison of phase angle (between pressure at centre of a side face and cylinder's displacement) versus reduced velocity measured in Bearman & Obasaju's experiment with those reported by Nakamura & Mizota again revealed similarity in trend but poor quantitative agreement. They also found that during lock-in there were some fundamental differences between square and circular cylinders. For example, amplification of the fluctuating lift coefficient is much

larger for circular cylinder than for square cylinder. As for the variation of the angle between surface suction at the forcing frequency and cylinder displacement through the lock-in range, it was found that while the phase angle for circular cylinder's case is positive (hence flow-induced vibration possible) throughout the lock-in range, for square cylinder the phase angle is positive only in the upper half of the lock-in range (see fig. 1.14(b)). They pointed out that these fundamental differences must be taken into consideration when one tries to formulate a mathematical model like the one presented by Hartlen and Currie (1970) for vortex resonance of circular cylinder to predict the response of a square cylinder during vortex resonance. Bearman & Obasaju classified the flow past an oscillating cylinder into three categories:

(1) Below lock-in where the flow is completely dominated by the effects of imposed oscillation. Concentrated vorticity is generated and shed at the body frequency. Natural vortex-shedding can be completely suppressed.

(2) Lock-in where vortex shedding frequency f_s is transferred to the body frequency f_N.

(3) Above lock-in where the two frequencies are far apart and the flow is quasi-steady.

Flow visualization also shows that the wake structure of oscillating square cylinder are completely different below and during lock-in.

Wilkinson (1974) also looked into the problem of flow past stationary and oscillating square cylinder. Wilkinson (1981(a)) investigated the effect of transverse oscillation on the chordwise pressure distribution. He found that when the correlation coefficient of pressure at leading and trailing edges (ρ_{15}) was plotted against dimensionless forcing frequency (f_N/f_s), there was no change in the value of the correlation coefficient up to f_N/f_s = 1.1. Above this value of dimensionless forcing frequency the correlation coefficient begins to drop. The drop was more rapid for bigger amplitude of vibration (see fig. 1.15). Wilkinson also observed that the fluctuating pressure was amplified in the lock-in range. He suggested that it was due to more vigorous vortex shedding. By assuming perfect chordwise pressure correlation and also assuming that the pressure fluctuation on opposite side faces were completely out of phase, Wilkinson estimated a two dimensional fluctuating lift coefficient of about 1.35. This is in fairly reasonable agreement with results reported by other researchers like Vickery (1.29, smooth flow), Lee (1.23, smooth flow) and Chaplin (1.2); especially if one takes the fairly big differences in experimental conditions into consideration.

Wilkinson (1981(b)) measured the spanwise pressure and velocity (by placing a hot-wire in the wake) correlation of a stationary square-section cylinder and found average correlation length of 2.6D and 1.2D for pressure and velocity respectively. Wilkinson suggested that the increase

in spanwise correlation when the cylinder is oscillated is a result of non-linear interaction between vortex shedding and structural movement. He further suggested that the improvement in spanwise correlation when the cylinder is oscillated is due to the addition of an inertial pressure component and that the eddies shed become more parallel to the cylinder axis (ie. more straight). The increase in spanwise correlation, together with the more vigorous vortex shedding (and hence pressure amplification) are believed to be the causes of amplification of loading on square cylinder during resonance.

1.2.1.3 Parkinson's Quasi-Steady Theory of Galloping Oscillation

The fundamental assumption of Parkinson's theory states that the normal force that acts on a square cylinder oscillating transversely with velocity $\dot{y}$ in a free stream U_∞ is the same as the force that acts on a stationary cylinder inclined to the free stream U_{res} at an angle α. α and U_{res} can be expressed in terms of $\dot{y}$ and U_∞ as follows:

$$\alpha = \tan^{-1} (\dot{y}/U_\infty) \qquad (1.4)$$

and

$$U_{res} = (U_\infty{}^2 + \dot{y}^2)^{0.5} \qquad (1.5)$$

See, for example, Parkinson & Smith (1964)

Assuming a linear elastic system, the differential

equation that governs the oscillation is:

$$\ddot{my} + r\dot{y} + ky = 0.5C_{Fy}\,\rho U_\infty^2 DL \qquad (1.6)$$

The aerodynamic force coefficient C_{Fy}, measured on stationary cylinder in the wind tunnel is a function of α and therefore a function of $\dot{y}/U_\infty$ (= $\tan\alpha$) (see fig. 1.16). To represent five important changes of curvature in the range $0 \leq \alpha \leq 16$ degrees, the polynomial that approximates C_{Fy} has to be of order 7 but the even powered terms can easily be shown to be zero from symmetry consideration. Thus:

$$C_{Fy} = A\left(\frac{\dot{y}}{U_\infty}\right) - B\left(\frac{\dot{y}}{U_\infty}\right)^3 + C\left(\frac{\dot{y}}{U_\infty}\right)^5 - D\left(\frac{\dot{y}}{U_\infty}\right)^7 \qquad (1.7)$$

where A, B, C and D are real positive numbers. Substituting the expression for C_{Fy} into equation (1.6), and the resulting equation made dimensionless by dividing through by kD, it becomes:

$$\ddot{Y} + Y = nA\left\{\left(\bar{U}_r - \frac{2\beta}{nA}\right)\dot{Y} - \left(\frac{B}{A\bar{U}_r}\right)\dot{Y}^3 + \left(\frac{C}{A\bar{U}_r^3}\right)\dot{Y}^5 - \left(\frac{D}{A\bar{U}_r^5}\right)\dot{Y}^7\right\}^* \qquad (1.8)$$

*where $Y = y/D$, $\dot{Y} = dY/d\tau$, $\tau = \omega t$ and $\bar{U}_r = U_\infty/(2\pi f_N D)$

where n is equal to half the ratio of displaced air (or fluid) mass to the mass of the cylinder and β is the system damping in the absence of aerodynamic forces.

Equation (1.8) is of the well-known form of an autonomous differential equation with small non-linear damping

$$\ddot{Y} + Y = \mu f(\dot{Y}) \ , \ \mu = nA << 1 \tag{1.9}$$

If $\mu \neq 0$ but small, the approximate solution of equation (1.9) is (see Parkinson & Smith (1964)):

$$Y = \bar{Y} \cos (\tau+\phi), \ \dot{Y} = -\bar{Y} \sin (\tau+\phi) \tag{1.10}$$

where $\bar{Y}$ and ϕ are slowly varying function of τ.
Multiplying both sides of equation (1.9) by $\dot{Y}$ and substituting (1.10) into (1.9), one obtains:

$$\frac{1}{2} \frac{d\bar{Y}^2}{d\tau} = -\mu f\left[-\bar{Y} \sin (\tau+\phi)\right] \bar{Y} \sin (\tau+\phi) \tag{1.11}$$

Since $\bar{Y}$ varies only slowly with τ, (ie. cycle period is much smaller than the time interval during which appreciable changes of amplitude occur), it is therefore justifiable to average the behaviour over a single cycle, (1.11) can thus be written as:

$$\frac{1}{2} \frac{d\bar{Y}^2}{d\tau} = - \frac{\mu}{2\pi} \int_0^{2\pi} f(-\bar{Y}\sin\nu) \ \bar{Y}\sin\nu \ d\nu \tag{1.12}$$

where $\nu = \tau + \phi$

Inserting the function f from (1.8) and integrating, (1.12)

becomes:

$$\frac{d\bar{Y}^2}{d\tau} = nA\left\{\left(\bar{U}_r - \frac{2\beta}{nA}\right)\bar{Y}^2 - \frac{3}{4}\left(\frac{B}{A\bar{U}_r}\right)\bar{Y}^4 + \frac{5}{8}\left(\frac{C}{A\bar{U}_r^3}\right)\bar{Y}^6 - \frac{35}{64}\left(\frac{D}{A\bar{U}_r^5}\right)\bar{Y}^8\right\} \quad (1.13)$$

Equation (1.13) can be integrated directly to give the relation between amplitude of vibration and time. Alternatively, the amplitudes of stationary oscillation can be calculated by equating the LHS of equation (1.13) to zero. ie. The amplitudes are given by roots of the equation:

$$F(\hat{Y}) = a\hat{Y} - b\hat{Y}^2 + c\hat{Y}^3\ d\hat{Y}^4 \quad (1.14)$$

where $\hat{Y} = \bar{Y}^2$ and a, b, c, d are the coefficients of $\bar{Y}^2$, $\bar{Y}^4$, $\bar{Y}^6$ and $\bar{Y}^8$ respectively on the RHS of equation (1.13). On-set of galloping oscillation occur when $dF/d\hat{Y}$ ($\hat{Y} = 0$) changes from negative to positive, since:

$$\left.\frac{dF}{d\hat{Y}}\right|_{\hat{Y}=0} = a = nA\left(\bar{U}_r - \frac{2\beta}{nA}\right) \quad (1.15)$$

Critical reduced velocity U_{cr}, velocity above which galloping oscillation will take place is therefore given by the expression:

$$\bar{U}_{cr} = \frac{2\beta}{nA} \quad (1.16)$$

Parkinson's theory is quite successful in predicting galloping oscillation phenomena provided the

quasi-steady assumption is satisfied (ie. $U_r >> U_{ro}$). Fig. 1.8 demonstrated this quite clearly. See also fig. 1.9(a) to (c).

1.2.2 VORTEX RESONANCE

When a bluff body is exposed to a free stream, except in very low Reynolds number (O(1)), two shear layers will separate from opposite sides of the body. The shear layers thus separated are unstable and they have a tendency to roll up and form discrete vortices alternating from the two layers. Each shear layer sheds vortices at a frequency f_s and the results of this alternate vortex shedding is that the generating body (primarily the afterbody) is subjected to a oscillatory pressure loading of frequency f_s.

Unlike galloping, vortex resonance occurs only through a narrow range of wind speed centred approximately at the resonant wind speed U_{ro}, the wind speed at which the vortex shedding frequency f_s is equal to the system's natural frequency f_n. The amplitude of oscillation is normally much smaller than that in galloping oscillation. Also unlike galloping, the classic shape for experimental research in vortex resonance is the circle, probably due primarily to the fact that circular cylinder is not subjected to galloping oscillation and hence effects due to vortex resonance can be singled out.

Many experimental as well as numerical research

investigations have been carried out into vortex resonance in the past. They are discussed in the following.

1.2.2.1 Experimental Work in Vortex Resonance

Research in circular cylinder excited into vibration by the flow can be dated back to as early as the late nineteenth century. Names such as Strouhal and Rayleigh will be familiar to most present researchers in flow-induced vibration. Main findings from Strouhal and Rayleigh's research include that the dimensionless frequency $f_s D/U_\infty$ (now commonly known as the Strouhal number) is a function of the Reynolds number and that when the vortex shedding frequency from one shear layer f_s coincides with the natural frequency of the system f_n, flow-induced vibration occurs in a plane perpendicular to the flow direction. In 1936, Thoma reported an observation which is in apparent violation of the Strouhal relation. Thoma reported that over a range of free stream wind speed centred approximately at the wind speed where the vortex shedding frequency is identical to the system natural frequency, the shedding frequency actually locks on to the system's natural frequency. There is therefore a drop in the Strouhal number over the above mentioned speed range. The lift coefficient of an oscillating circular cylinder is also different from that of a stationary circular cylinder. More recently, Bishop & Hassan (1964(a) and (b)) are among the pioneering researchers to carry out experiments on a cylinder

oscillating transversely to the free stream. Bishop & Hassan (1964(a)) first conducted a series of stationary cylinder experiments which serves as a check of their instrumentation and also as a basis for comparison with results for oscillating cylinder. They found that their stationary cylinder results were in good agreement with existing data at the time of their research. In Bishop & Hassan (1964(b)), they conducted experiment by oscillating a circular cylinder in a direction that is transverse to the free stream (flowing water in their case). They found that when the driving frequency f_N was sufficiently different from the shedding frequency f_s, the lift and drag forces fluctuated at f_s and $2f_s$ respectively. However, when f_s was sufficiently close to f_N, vortex shedding locked on to the forcing frequency and that was observed to persist over a range of free stream velocity commonly known as the synchronization or lock on (or lock in) range. Within the range of synchronization, lift and drag forces change in both amplitude and phase (relative to displacement) when the forcing frequency is varied (see fig. 1.17(a) and (b)). Bishop & Hassan observed that the way that the amplitude changes is similar to that of a simple oscillator under the influence of an applied harmonic force. They also observed corresponding abrupt changes in phase angle between lift force and cylinder displacement. Hysteresis is another observation of Bishop & Hassan. They observed that the critical forcing frequency at which the amplitude of lift

and drag forces went through a step change was different depending on whether the forcing frequency was increasing or decreasing (see fig. 1.17(c)). Finally, they also observed what they termed "frequency demultiplication"; ie. sychronization taking place when the forcing frequency was near an integer multiple of the shedding frequency. They concluded their investigation by suggesting that the wake/cylinder combination behaved like a non-linear oscillator which initiated a productive line of theoretical studies. See, for example, Hartlen & Currie (1970), Griffin, Skop & Koopmann (1973), Skop & Griffin (1973) and Landl(1975).

Ferguson & Parkinson (1967) carried out experimental investigation on a circular cylinder which was either stationary or undergoing vortex excited oscillation at subcritical Reynolds number. They found fairly good spanwise pressure correlation for the stationary cylinder. Within the synchronization range, Ferguson & Parkinson reported that there were much less modulation in both displacement and pressure amplitude, indicating a much more organised wake vortex system. Their observation is in agreement with the findings of Bishop & Hassan (1964(b)). Also, they measured the variation of the phase angle between the lift force and the cylinder displacement with the cylinder's reduced frequency and once again found reasonable agreement with the findings of Bishop & Hassan (1964(b)) (see fig. 1.18).

Bearman and Currie (1979) oscillated a circular cylinder transversely to the water flowing inside a water channel. They examined experimentally the fluctuating pressure at 90 degrees from the mean front stagnation position for a range of amplitude ratio and reduced velocity. They found that the r.m.s. pressure C_p' at $\theta = 90$ degrees increases as the reduced wind velocity is reduced and C_p' reaches a local maximum within the lock-in range (see fig. 1.19(a)). They also predicted that the maximum amplitude that an elastically suspended undamped cylinder would ever reach was limited to twice the cylinder diameter. Hysteresis effect in the response of an elastically suspended cylinder, similar to that reported by Feng in his MSc thesis (University of British Columbia 1968) was also thought to be possible. Bearman and Currie also found that the phase angle between the lift and the cylinder displacement measured in their forced oscillation experiment is in fairly good agreement with the results of Feng which were obtained from a elastically suspended cylinder experiment (see fig. 1.19(b)). Bearman & Currie reported that free stream turbulence did not seem to have any effect on their results. Finally, when away from lock-in, they found that potential-flow modelling could give surprisingly good prediction of the pressure fluctuation at the body frequency.

Komatsu & Kobayashi (1980) conducted experiments on both elastically suspended and force oscillated cylinders. Four different cross sectional shapes were investigated (see

fig. 1.20). They found that there are two different types of vortex-induced oscillations. The first and more conventional type is due to Karman vortex shedding. It is often observed in tne case of bluff body having trailing edge separation such as the "T" cylinder in their experiment. The frequency of vortex-induced oscillation is very close to the vortex shedding frequency in the range $4.5 \leq U_\infty / f_n D \leq 8$ where f_n is the natural frequency of the system. That type of oscillation has comparatively small amplitude at U_{ro}. The second type which can also be thought of as an afterbody effect occurs over a limited speed range centred aproximately at U_{ro}. It occurs to bluff body with leading edge flow separation and therefore includes all the other three shapes investigated by Komatsu & Kobayashi. In the case of the second type of vortex-induced oscillation motion of the cylinder causes vortices to be formed on the sides of the cylinder and hence those vortices are named "motion induced". Those motion induced vortices are synchronised with tne motion of the cylinder and hence produce a lift force which oscillates at the natural frequency of the system and is IN-PHASE with the motion of the cylinder. That causes the motion of the cylinder to become self-sustained. The amplitude of oscillation due to the second type of vortex-induced oscillation can be as much as ten times larger than that of the first type. The proposed mechanism of motion induced vortices also helps to explain the following experimental observations by Komatsu & Kobayashi:

(1) Oscillation occurs at wind speed other than the resonant wind speed.

(2) The maximum amplitude of flow-induced oscillation often occurs at a wind speed different from the resonant wind speed.

(3) For some cylinders (hard oscillator), self-sustained galloping oscillation takes place only after some initial displacement is given to the cylinder. In some occasion the initial displacement is provided by the Karman type vortex shedding.

1.2.2.2 Numerical Simulation of Vortex Resonance

Hartlen & Currie (1970) proposed a simple mathematical model based on the concept that the fluctuating lift associated with vortex shedding may be considered to arise from the action of something akin to an oscillator in the separated flow (and hence the name lift-oscillator model). The three primary characteristics include:

(1) The oscillator must be self-excited and self-limiting.

(2) The natural frequency of the oscillator must be proportional to free stream velocity in order to satisfy Strouhal relation.

(3) The cylinder motion should interact with the oscillator through some kind of forcing term.

Taking into consideration the three characteristics just mentioned Hartlen & Currie proposed a two equations

model in which one equation governs the cylinder motion and the other the instantaneous lift force. In dimensionless form the two equations can be expressed as:

$$y_r'' + 2\zeta y_r' + y_r = a\omega_o^2 C_L \tag{1.17}$$

and

$$C_L'' - \alpha\omega_o C_L' + \frac{\gamma}{\omega_o}\left(C_L'\right)^3 + \omega_o^2 C_L = bx_r' \tag{1.18}$$

where $y_r = y/D$

$\zeta = R/(2M\omega_n)$

$a = \dfrac{eD^2L}{8\pi^2S^2M}$

$\omega_0 = f_s/f_n$

α, γ, b = parameters for the mathematical model

$' = d/d\tau$

$\tau = t\sqrt{\dfrac{K}{M}} = t\omega_n$

$\omega_n \sqrt{\dfrac{K}{M}} = 2\pi f_n$

M = system mass

R = system daming

K = system stiffness

Other variables like C_L, y, f_s, f_n, t and D etc have their usual meaning and are explained in LIST OF SYMBOLS.

Hartlen & Currie used their model to predict the motion of an elastically mounted cylinder and the lift force on an externally driven cylinder. They concluded that the proposed model could simulate most of the physical phenomena observed.

Skop & Griffin (1973) employed a modified Van der Pol equation similar to that used by Hartlen & Currie (1970) and claimed that their model was an improvement over Hartlen & Currie's because it could get good quantitative agreement with experimental results whereas Hartlen & Currie's model only gave qualitative agreement. Furthermore, Skop & Griffin postulated relations between some theoretical parameters used in the two equations model and physical parameters like mass and damping parameters so that their model could be applied to many practical engineering problems. They showed that their model could predict results observed in experiments which were not used for development of the mathematical model (see fig. 1.21). They further reported comparison of magnitude of peak resonant amplitude between their model prediction and experimental measurement and

again quantitative agreement was obtained (see fig. 1.22(a) and (b)).

Landl (1975) attempted to modify Hartlen & Currie's lift-oscillator model by introducing a fifth order term into the lift equation. He showed that with the addition of the fifth order term some important characteristics including hysteresis effect and the existence of hard and soft oscillators which could not be explained by Hartlen & Currie's original model could then be explained. However, the prediction of his model agreed only with experimental measurement in a qualitative manner.

Obasaju (1977) investigated the usefulness of the Hartlen & Currie's lift oscillator in predicting the behaviour of a square cylinder oscillating transversely to the free stream. He found that while for circular cylinder good qualitative agreement between experimental measurement and theoretical prediction can be obtained by assuming the forcing function to be in-phase with the cylinder's velocity, for square cylinder better agreement is achieved by assuming the forcing function to be in-phase with the cylinder's displacement (fig. 1.23). He also found that the Van der Pol oscillator used in Hartlen & Currie model could not predict the characteristics of the lift force as $U_r \rightarrow 0$. Obasaju concluded by emphasising that while it is always possible (by choosing correct values for the three parameters α, γ and b in the Van der Pol equation, see eqn (1.18)) to use the lift oscillator model to fit well

onto a certain set of experimental data, the usefulness of a particular mathematical model also depends on whether its parameters (eg. α , γ and b) can be related to some characteristics of the actual flow. It is this quality that the lift oscillator model is lacking and more thought should be given in this aspect for the future development of the model.

CHAPTER TWO

EXPERIMENTAL APPARATUS

This chapter briefly describes all the experimental apparatus used in the present research.

2.1 WIND TUNNEL

The experiments were conducted in a general purpose low speed wind tunnel in the Department of Aeronautics Imperial College of Science and Technology. The tunnel has a square working section of 3ft x 3ft x 18ft (0.91m x 0.91m x 5.49m). It is of closed-return design. With a 50 h.p. motor driving an axial fan and a 9 to 1 contraction ratio immediately before the working section, the empty tunnel is capable of producing a maximum wind speed of about 150 ft/s at a turbulence level of no more than 0.05%. More information about the wind tunnel can be found in Clements & Urwin (1973).

2.2 MANOMETERS

Two types of manometer were used to measure tunnel wind speed throughout the present research. A Betz manometer, which is easier to use and is capable of measuring higher wind speed, was used when the tunnel wind

speed was greater than about 4 m/s. On the other hand, when wind speed was low (U_∞ < 4m/s) and accuracy of the manometer became more critical, the more accurate Combist micromanometer was employed.

2.3 MODELS AND THEIR INSTALLATION

Two models were employed in the present research. Both models have a 2in x 2in square cross section. They were always held horizontally at mid-height of the wind tunnel. For stationary cylinder (either normal or inclined to free stream) measurement and flow visualization, the cylinder and end plate assembly was fitted tightly onto two circular discs which in turn were connected to, and formed part of, the two vertical side walls of the wind tunnel. The angle of attack α of the cylinder in the range $0 \leq \alpha \leq 45$ degrees was determined by a Hilger & Watts inclinometer. Once the desired position had been obtained, the two circular end discs were clamped tightly to the wind tunnel side walls and all further movement/rotation of the cylinder was inhibited. For oscillating cylinder experiment, two vertical slots were cut in the wind tunnel side walls to accommodate the cylinder's movement. The two ends of the cylinder protruded out of the side walls and were connected to the vertical push rods of an oscillating mechanism. The height of the mechanism and length of the push rods had been adjusted such that the mean position of the cylinder corresponded to the mid-height of the wind tunnel.

2.3.1 Model for Pressure Measurement

This model was made of aluminium plates 3 mm in thickness. Care had been taken to ensure all corners were sharp. Six pressure tappings made of brass tubing about 1/16" in internal diameter were positioned along a chord at mid-span of the cylinder. They were at D/12, 3D/12, 5D/12, 7D/12, 9D/12 and 11D/12 from the front leading edge respectively where D (= 2 inches) is the length of each side of the square cylinder. Another six identical pressure tappings were located at identical position but on an opposite face of the cylinder. The length of each tube is about 30mm. By positioning the cylinder such that the pressure tappings were at faces A and C (see fig. 1.1), front and rear face pressure distributions as well as drag forces could be measured. Similarly, pressure distributions on faces B and D (see fig. 1.1) and hence lift force could be measured by rotating the cylinder through 90 degrees.

End plates (see fig. 2.1) which were identical to the No. 2 end plates employed by Obasaju (1977) were firmly attached to the cylinder with a distance of 17D (34 inches) between them. The clearance between each end plate and the corresponding tunnel side wall was about 1 inch. This particular pair of end plates is quite effective in suppressing axial flow. Further details about the end plates can be found in Obasaju (1977) and Obasaju (1979).

2.3.2 Model for Flow Visualization

This model was made of solid light-weight wood. It had no pressure tappings and was painted matt black to provide optimum contrast with the white smoke. A 1 cm width silver colour reflective tape was glued around the circumference of the cylinder at mid-span to reflect the vertical sheet of light shone from a strobe light located at the top of the wind tunnel, through a slot cut in the wind tunnel ceiling.

The end plates for this cylinder were made of perspex. They were also at 17D (34 inches) apart. Dimensions of the two pairs of end plates are shown in fig. 2.1.

2.4 PRESSURE AVERAGERS

Two identical pressure averagers were used in the present research. Their design was based on the paper by Surry (1977/78). Basically each pressure averager consists of six inputs and one output and they are all interconnected. The construction and dimensions are shown in fig. 2.2. In the present design of the pressure averager the output pressure was found to be equivalent to the arithmetic mean of the six different inputs. By connecting two identical pressure transducers (one directly and the other via a pressure averager) to a fluctuating pressure source (essentially an audio speaker driving the air inside a sealed enclosure), the gain and phase shift caused by the

pressure averager can be measured over a certain frequency range. The calibration set-up is shown in fig. 2.3. It was found that the pressure averager has a gain of unity and zero phase shift over the frequency range of 0.5 to 150 Hz. This unity gain and zero phase shift frequency range is quite sufficient for the present research because even at the highest free stream velocity ($\sim$ 23.3 ms^{-1}) employed in the present research, the vortex shedding frequency (assuming Strouhal number is about 0.133) is still less than 62 Hz. When measurement of average face pressure was carried out, the six inputs were connected to six pressure tappings on one particular face of the cylinder (see section 2.3.1); the output of the pressure averager then represents the mean pressure acting on that face and was fed to the Setra pressure transducer for measurement.

2.5 PRESSURE TRANSDUCERS

Two Setra $\pm$0.1 p.s.i. differential pressure transducers were used for all pressure measurement in the present research. They were calibrated before every series of experiment and their response were found to be linear and practically unchanged throughout the duration of the research. The two pressure transducers were held tightly within the cylinder during both stationary and oscillating cylinder experiments. That was necessary as it prevented the pressure signal from being affected by the vibration and also enabled a minimum length of tubing to be used. Use of

excessive length of tubing was undesirable as the damping and resonance effects of air inside the tubing could affect the accuracy of the measurement of fluctuating and instantaneous pressure. When measuring a point pressure, the pressure transducer was connected directly to a particular pressure tapping. On the other hand, when average face pressure was needed, the pressure transducer was connected to the output of the corresponding pressure averager (see section 2.4).

2.6 OSCILLATING MECHANISM

The original oscillating mechanism was designed by Mr.P.Gasson of the Department of Aeronautics, Imperial College of Science and Technology. It is essentially a twin Scotch-Yoke mechanism device. The two Scotch-Yoke were driven by a Normand 2 h.p. three phase motor via a Carter infinitely variable hydraulic reduction gearbox (see fig. 2.4). The output motion was found to be indistinguishable from a pure sinusoid and the maximum peak to peak amplitude of oscillation was about 1 inch. In this form the oscillating mechanism was used by Davies (1975) and Obasaju (1977). For use in the present research, the author (with the help of the original designer Mr. Gasson) quite extensively modified the design of the Scotch-Yoke mechanism so that the maximum peak to peak amplitude of oscillation became 8 inches. This much bigger amplitude of oscillation was achieved by compromising on a much lower maximum

frequency of oscillation. It was reduced from the original 40Hz at A/D = 0.25 (approximately) to about 10Hz at A/D = 2. The whole oscillating mechanism rested on some spring/damper device which helped to reduce feedback problem (ie. pressure transducers picking up vibration signal from the oscillating rig).

2.7 DISPLACEMENT TRANSDUCER

A Schlumberger displacement transducer was used to generate an electrical signal which represented the motion of the cylinder. To do this the displacement transducer was attached to one of the arms of the oscillating mechanism. The moving core of the displacement transducer, on the other hand, was firmly attached to the cylinder so that it moved together with the cylinder. The displacement transducer was capable of accommodating a peak to peak amplitude of 14 inches and its response was found to be practically linear. The output of the displacement transducer was sent to an Enertec Schlumberger storage CRO and a Muirhead wave analyser so that the frequency of oscillation could be determined. In addition to frequency determination, the displacement signal and either the lift or drag force signals were also simultaneously recorded on a EMI SElab 3000 fourteen channels tape recorder for further analysis (see section 3.5.2)

2.8 COMPUTERISED DATA ACQUISITION SYSTEM

The "heart" of the on-line computerised data acquisition system used in the present research is a Commodore PET 4032. Its CPU is a Rockwell 6502 microprocessor and it has a core memory of 32 K bytes and can be programmed in either BASIC version 4.0 or machine language. The computer acted as a central controller and was interfaced to and controlled (either directly or indirectly) the following devices:

(1) Logic signal generating card. It could output multiple logic signals which were either 0 or 5 volts.

(2) Sample and hold card: It accepted an analogue signal as an input. When it was triggered "on" by a 0 volt signal, it held on to the value of the input analogue signal at the instant at which the triggering signal was received. It could be triggered "off" later by a 5 volts signal.

(3) Analogue to digital conversion card: It could digitised a continuous analogue signal in the range of $\pm$10 volts to a series of 10 bits words.

(4) Commodore 4022P printer.

(5) Commodore 4040 dual disk drive unit.

Connection of all the above equipment for data acquisition will be explained in chapter 3.

2.9 TAPE RECORDER AND SIGNAL CORRELATOR

An EMI SELabs 3000 open reel analogue tape recorder was used for simultaneous recording of lift or drag force and displacement signals. This tape recorder is capable of simultaneously recording 14 different signals. The recording/playback speed varies from 15/32 to 60 i.p.s.. As the odd and even numbered channels are on two different recording and two playback heads, care was taken to ensure that the two channels used for lift or drag/displacement simultaneous recording were either both odd or both even numbered.

The HP 3721A correlator has its own CPU and is capable of accepting up to two signals simultaneously. It can therefore compute the auto-correlation of a single signal or the cross correlation of two different signals.

2.10 SMOKE WIRE/ACCESSORIES AND PHOTOGRAPHIC EQUIPMENT

Smoke wire accessories consist of high resistance Ni/Cr/Fe alloy wire 0.125 inch in diameter, Y shape glass tube, AC power supply, retort stands, silicone oil and various light sources.

Still photographic equipment used included Canon A1 SLR camera fitted with Canon 50mm f1.2 lens, 5 f.p.s. motor drive MA and data back A. Cine photographic equipment included a Bolex H16 movie camera (maximum speed 64 f.p.s.), Bolex H16RX 16-100mm zoom lens and Kern 10mm f1.6 wide angle

lens. Film used for both still and cine photography was Ilford ASA 400 black and white film (pushed processed to ASA 1000).

2.11 OTHER EQUIPMENT

Other equipment used do not really require any introduction and are simply listed below:

Enertec Schlumberger storage CRO

Aron BS-635 CRO

Kemo VBF8 filter/amplifier

Coutant LQT 100 power suply

Solartron LM 1420.2 voltmeter

CHAPTER THREE

EXPERIMENTAL PROCEDURE AND DATA REDUCTION/CORRECTION

This chapter briefly describes the various techniques used to collect experimental data, data reduction procedure and various corrections used to improve the accuracy of experimental data.

3.1 SET-UP FOR DATA ACQUISITION

For two channels simultaneous data acquisition the interfacing of the computer to various peripheral devices is shown in fig. 3.1. The computer controlled a logic signal generating card which was capable of simultaneously generating multiple logic signals (either 0 or 5 volts). Only two such signals were required in the present set-up. They were used to trigger the "on" and "off" of two sample and hold (S/H) cards to which the output of the two pressure transducers (see section 2.5) were fed. The output of those two S/H cards were fed to channel 0 and 1 of an analogue to digital (A/D) conversion card which was in turn interfaced to the computer. The reason for making such a rather complex connection was to ensure that each pair of digitized data samples acquired from the two pressure transducers were read at the same instant in real time.

The program used for data acquisition is called "TWO CH AC". It will be described in more details later in this chapter. The set-up and program introduced here were used for the following data acquisition:

(1) C_D, C_D' and C_L' versus Re (stationary cylinder).

(2) C_{pA}, C_{pA}', C_{pC} and C_{pC}' versus Re (stationary cylinder).

(3) C_D, C_D', C_L and C_L' versus α (stationary cylinder).

(4) C_{pX} and C_{pX}' (X = A, B, C or D) versus α (stationary cylinder).

(5) C_D, C_D' and C_L' versus U_r (oscillating cylinder).

(6) C_{pA}, C_{pA}', C_{pC} and C_{pC}' versus U_r (oscillating cylinder).

Another program called "ONE CH AC" which is basically the same as "TWO CH AC" but handles only one channel of signal (and hence does not require the use of sample and hold cards) was used for C_p and C_p' distribution measurement. When conducting C_p and C_p' distribution measurement, the pressure averager was of course not required and the pressure transducer was connected directly to each individual pressure tappings in turn.

3.2 SET-UP FOR ϕ VERSUS U_r MEASUREMENT

The phase angle ϕ by which the body frequency component of the lift force leads the displacement of the cylinder (defined to be positive if lift leads displacement)

was measured by feeding both the lift force and displacement signals to the two input channels of the Hewlett Packard 3721A signal correlator. The cross correlation function had the form $f(t)\cos(2\pi f_N t + \phi)$ where $f(t)$ and f_N are some function of t and the forcing frequency respectively. By storing the cross correlation function on the display screen of the HP3721A, the value of ϕ can be estimated fairly accurately.

To obtain the signal that represents the lift force the output from the pressure transducer that measured the average pressure on face B (see fig. 1.1) was subtracted from the output of the pressure transducer that measured the average pressure on face D. The "subtraction" was acheived by making use of an operational amplifier. Since the output of the displacement transducer happened to be inverted (ie. maximum negative signal when cylinder was at top dead centre and vice versa), another identical operational amplifier was used to invert the output signal from the displacement transducer. For ϕ measurement, care had been taken to ensure that both lift and displacement signals passed through identical circuits in order to avoid any undesired phase shifts. The connection is summarized in fig. 3.2.

3.3 SET-UP FOR LIFT/DISPLACEMENT SIMULTANEOUS RECORDING

The author used two different methods to estimate the phase angle between the lift at the forcing frequency and displacement signals. The first one was the direct

measurement method explained in the previous section. The second method was by running an essentially dual FFT program called COPHASE (more details will be given in section 3.5.2) and using the digitised lift and displacement signals as input data. It was therefore necessary to first of all record the lift and displacement signals simultaneously on a multi-track tape recorder. The set-up used for this simultaneous recording was identical to that explained in section 3.2 and shown in fig. 3.2 except that the HP3721A signal correlator was replaced by the analogue tape recorder EMI SELabs 3000.

3.4 SET-UP FOR FLOW VISUALIZATION

A high resistance smoke wire was held vertically by a retort stand located on top of the wind tunnel. The wire passed through a hole in the tunnel ceiling and spanned almost the full height of the wind tunnel. The upper end of the smoke wire went through the "vertical limb" of a Y shape glass tube and was connected to one terminal of the AC power supply. The wire was set into tension by hanging a small weight at its lower end which was also connected to the other terminal of the AC power supply. When silicone oil was fed through the "inclined limb" of the Y snape glass tube, gravity effect caused it to drip continuously along the high resistance smoke wire. If AC power was then supplied to the wire, the wire heated up and burnt the silicone oil. White smoke was generated and it was carried down stream, past the

cylinder in the form of fine filaments by the free stream. The cameras were placed on tripods and focused through the perspex side wall of the wind tunnel.

The wind tunnel laboratory was kept under total darkness during flow visualization experiments. Two lamps located on top of the wind tunnel produced a vertical sheet of light parallel to the free stream. As the amount of light produced by the two lamps was not sufficient for exposing the Ilford ASA 400 film properly, a third light source (a projector lamp) was placed downstream of the model and shone upstream onto the area of interest. The set-up explained above is summarised in fig. 3.3.

3.5 COMPUTER PROGRAMS AND DATA REDUCTION

Like most research work, quite a number of computer programs (more than 20) were written during various different stages of the present research. Most of them are short and rather straightforward programs written in BASIC 4.0 (a special version of BASIC used by the 4 series Commodore micro-computer) for some specific purpose. Only two programs are thought to deserve some explanation and they are introduced in the following sections.

3.5.1 "TWO CH AC"

This program was co-written for the present research by Dr. S. Karanfilian (a former research assistant in the department) and the author. It was designed to work

in conjunction with the set-up introduced in section 3.1. The main part of the program was written in BASIC 4.0 but the data acquisition routine was written in machine language in order to achieve a higher sampling frequency (about 93 samples per second in the present case, although the maximum possible sampling frequency is about 6600 samples per second). The data acquisition routine performed the following:

(1) Triggered both sample and hold cards to "hold".

(2) Read a data sample from S/H card No.1 and store the data in some unused register in the microprocessor.

(3) Read a second data from S/H card No.2 and store the data in some unused register in the microprocessor.

(4) Sent another signal to "let go" the two S/H cards and go back to step(1) until a pre-determined number of data had been read.

After the desired amount of data had been read, the program transferred control back to BASIC and the following calculations were carried out:

(1) Read all the data from the registers and convert them into pressure in pascal by using individual calibration equation for the two pressure transducers.

(2) Calculated mean and r.m.s. pressure of each channel according to:

$$p_j = \frac{\sum_{i=1}^{N} p_{ji}}{N} \qquad (3.1)$$

$$p_j' = \sqrt{\frac{\sum_{i=1}^{N} (p_{ji}-p_j)^2}{N}} \qquad (3.2)$$

where $p_{ji} = p_j + \hat{p}_{ji}$ and j = 1 or 2.

(3) Calculated the difference between corresponding (ie. sampled at the same instant in real time) pair of data and calculate the mean and r.m.s. values of the difference in pressure:

$$p_{21i} = p_{2i} - p_{1i} \qquad (3.3)$$

$$p_{21} = \frac{\sum_{i=1}^{N} p_{21i}}{N} \qquad (3.4)$$

$$p_{21}' = \sqrt{\frac{\sum_{i=1}^{N} (p_{21i}-p_{21})^2}{N}} \qquad (3.5)$$

(4) Non-dimensionalised all pressure data by dividing them through by $0.5\ \rho U_\infty^2$.

The output of the program gave C_{p1}, C_{p2}, C_{p1}', C_{p2}', C_{p21} and C_{p21}'. If channel 1 and 2 applied to faces C and A respectively (see fig. 1.1), then C_{p21} and C_{p21}' became C_D and C_D'. Alternatively, if channel 1 and 2 applied to faces B and D, the values of C_L and C_L' were obtained.

3.5.2 "COPHASE"

This program was written in FORTRAN by Dr. M.E. Davies during his PhD research. The program read in two series of data (lift force and displacement in the present case), performed an FFT on each of the sets of data and also

a cross correlation calculation between them. The output of this program gave the individual spectra of the two input signals and coherence and phase angle between the two sets of data.

The digitising system was changed from a PDP-8 controlled, 7 track digital tape recorder system to the present BBC micro controlled, 9 track tape recorder system during the course of the present research. Two subroutines ("BUFFIN" and "UNPACK") which were responsible for sorting out the digitised data, had to be modified in order to suit the format of the new digitising system. That was achieved with the help of Dr. C. S. Subramanian, a research assistant in the department. The rest of the Cophase program remained unchanged. More detailed information about Cophase can be found in Davies (1974) and (1975).

Provided that C_L' is known, quantities such as $C_L'(f_N)$ and $C_L'(2f_N)$ etc can be estimated from Cophase printout using the following equation. For example:

$$C_L'(f_N)=\left[\frac{\sum_{i=-1}^{1} PSD(f_N+i\Delta f)x\Delta f}{\text{TOTAL AREA UNDER SPECTRUM}}\right]^{0.5} x\ C_L' \qquad (3.6)$$

where $PSD(f_N)$ represents the power spectral density of the lift force at the body frequency and $\Delta f = 1/SF$, where SF is the sampling frequency during digitizing.

3.6 CORRECTIONS

This section describes various correction methods used to improve the accuracy of data acquired.

3.6.1 Correction for Blockage Effect

The method adopted to compensate the inaccuracy incurred by wind tunnel blockage effect was originally proposed by Maskell. Theoretical consideration about the formulation of his theory was given in Maskell (1963) and (1965). Maskell showed that:

$$\frac{k^2}{k_c^2} = 1 + \frac{C_D}{k_c^2 - 1}\left(\frac{S}{C}\right) \tag{3.7}$$

and

$$\frac{1-C_p}{1-C_{pc}} = \frac{C_D}{C_{Dc}} = \frac{U_{\infty c}^2}{U_\infty^2} = \frac{k^2}{k_c^2} \tag{3.8}$$

where S = "representive" area of the model

C = wind tunnel cross-sectional area

$k^2 = 1 - C_{pb}$

subscript "c" indicates corrected quantities.

At any Reynolds number, by experimentally measuring C_D and C_{pb}, k_c can be calculated from:

$$k_c^2 = \frac{1+k^2 - C_D\frac{S}{C} \pm \sqrt{\left[C_D\frac{S}{C} - (1+k^2)\right]^2 - 4k^2}}{2} \tag{3.9}$$

Once the value of k_c is known, eqn. (3.8) can then be used to calculate C_{pc}, C_{Dc} and $U_{\infty c}$ etc. From (3.8) it can also be

shown that the corrected C_p', C_{pX}, C_{pX}' (X = A, B, C or D), C_L', C_D' and Strouhal number S are given by:

$$C_{pc}' = ZC_p' \tag{3.10}$$

$$C_{pXc} = 1 - Z + ZC_{pX} \tag{3.11}$$

$$C_{pXc}' = ZC_{pX}' \tag{3.12}$$

$$C_{Dc}' = ZC_D' \tag{3.13}$$

$$C_{Lc}' = ZC_L' \tag{3.14}$$

$$S_c = \sqrt{Z}S \tag{3.15}$$

where $Z = k_c^2/k^2$.

Equations (3.8) and (3.10) through (3.15) were used to correct various parameters measured in the "stationary cylinder" part (chapter four) of the present research. For the oscillating cylinder, at high amplitude and/or high frequency of oscillation (ie. at low U_r), flow reattachment could take place on the side of the cylinder which greatly increased C_{pb}. As a result κ_c in eqn (3.9) could become imaginary! Maskell's correction method is obviously not suitable. As no totally satisfactory correction method applicable to unsteady flow (oscillating cylinder) is available, the author had decided to present the oscillating

cylinder's results as measured. The only correction carried out to oscillating cylinder's data was that to eliminate the "noise" due to the inertia effect of air inside the tubings that connect the pressure tappings to the sensing area of the pressure transducers. This correction will be discussed in the next section.

3.6.2 "Noise" Correction

To measure the surface pressure accurately it is desirable to mount the pressure transducer with its diaphragm flush with the surface of the model. However, the large diaphragm area often prevents "point" pressure to be measured and the sheer size of the pressure transducer frequently make it impossible for the user to mount it in the way mentioned above. In the present experiment, flush mounting is further prevented by the use of a pressure averager to measure average surface pressure. Use of connection tubings allows the author to overcome the problems mentioned above but unfortunately another problem emerges; if the connection tubing(s) (or part of it) is parallel to the acceleration of the cylinder, a pressure difference will be developed between the two ends of that part of the tubing. A "noise" pressure signal is generated which is not a genuine aerodynamic signal. Bearman & Currie (1979) had proposed some means of correcting the fluctuating pressure coefficient and the phase angle between the surface pressure and the cylinder displacement. Their method is used

in the present research to calculate the "noise corrected" fluctuating lift, the component of the fluctuating lift at the body frequency and the phase angle between the lift at the body frequency and the cylinder displacement. Corrected quantities are calculated as follows:

$$C_{Lc}' = \left[C_{Lm}'^2 + C_{Ln}'(f_N)^2 - 2C_{Lm}'(f_N)C_{Ln}'(f_N)\cos\phi_m\right]^{\frac{1}{2}} \quad (3.16)$$

$$C_{Lc}'(f_N) = C_{Lm}'(f_N)\sin\phi_m/\sin\phi_c \quad (3.17)$$

$$\phi_c = \tan^{-1}\left[\frac{C_{Lm}'(f_N)\sin\phi_m}{C_{Lm}'(f_N)\cos\phi_m - C_{Ln}'(f_N)}\right] \quad (3.18)$$

wnere C_L' = r.m.s. lift coefficient

$C_L'(f_N)$ = forcing frequency component of r.m.s. lift coefficient

f_N = forcing frequency (sometimes referred to as body frequency)

ϕ = phase angle between $C_L'(f_N)$ and cylinder displacement, +ve. if $C_L'(f_N)$ leads displacement

suffix m = measured quantities

c = corrected values

n = noise only (the non-aerodynamic signal mentioned above)

C_L' and ϕ data that will be presented in chapter five are all corrected by eqns. (3.16) and (3.18). In the

drag measurement configuration, the connection tubings are always perpendicular to the acceleration of the cylinder and hence no noise correction is carried out.

CHAPTER FOUR

FLOW PAST A STATIONARY SQUARE CYLINDER -RESULTS AND DISCUSSION

The problem of flow past a stationary square cylinder is a relatively (compared with oscillating cylinder) well investigated one. The main objective of the present chapter is therefore not to investigate any new aspect of the problem but to measured quantities such as C_D, C_D' and C_L' etc directly using two Setra pressure transducers, two pressure averagers and a Commodore PET 4032 based on-line data acquisition system mentioned in chapter 2. The results of the present investigation will then be compared with those measured by Obasaju (1977) using similar set-up and the same wind tunnel but without the pressure averagers and the on-line data acquisition system. Agreement of the results in these two investigations will then provide some justification for using the pressure averagers in subsequent oscillating cylinder measurements. Results presented in the present chapter of course will also serve as reference for comparison with results measured with an oscillating cylinder which will be presented in the next chapter. Unless otherwise stated, all the experimental data presented in the present chapter can be assumed to be corrected for tunnel blokage effect by using Maskell's

method as explained in section 3.6.1.

4.1 C_{pA}, C_{pB}, C_{pC} AND C_{pD} VERSUS α

Average pressure were measured on all four sides of the square cylinder (see pp. 240 for convention) at Re $\sim 4.6 \times 10^4$. The non-dimensionalised average face pressure are plotted against α in fig. 4.1(a) and (b). From these plots it can be seen that, after blockage correction by using Maskell's method, the average face pressure coefficients measured via the pressure averagers by the pressure transducers agree very well with Obasaju's (1977) results which were also corrected for blockage effect and were deduced from surface pressure distribution measurement at Re = 4.74×10^4. The good agreement between the present and Obasaju's results justifies the use of the pressure averagers in steady flow pressure measurement. The trend of C_{pA}, C_{pB}, C_{pC} and C_{pD} versus α had been explained earlier in section 1.1.1.1.

4.2 C_D AND C_L VERSUS α

C_D and C_L are calculated at each α by equations (1.1) and (1.2)*. Again they are compared with C_D and C_L which Obasaju (1977) deduced from his pressure distribution measurement. Both sets of data are shown in fig. 4.2(a) and (b).

After blockage correction by Maskell's method, both C_D and C_L measured in the present investigation are seen to

---

* As the $+C_L$ in chapter 1 and in chapter 4 to 8 are defined in opposite direction, for chapter 4 to 8 "C_L" in eqn. (1.2) should be replaced by "$-C_L$".

agree well with that reported by Obasaju (fig. 4.2(a) and (b)). This is not unexpected because C_D and C_L are computed from C_{pA} etc which are themselves in good agreement with Obasaju's results.

4.3 C_{pA}', C_{pB}', C_{pC}' AND C_{pD}' VERSUS α

The dimensionless r.m.s. surface pressure for the four faces are defined as:

$$C_{pA}' = \sqrt{\frac{\sum_{i=1}^{N} \left(C_{pAi} - C_{pA}\right)^2}{N}} \qquad (4.1)$$

where $C_{pAi} = C_{pA} + \hat{C}_{pAi}$

and similarly for faces B, C and D.

The corrected (for blockage) C_p' for all four faces and results of Robertson et al (1977/78) (not corrected for blockage) are plotted against α in fig. 4.3(a). From fig. 4.3(a) it can be seen that the agreement between the two sets of results is only qualitative and detail quantitative agreement is poor. The poor agreement between the two sets of results can partly be attributed to:

(1) Difference in Reynolds number. The Reynolds number where the present data were obtained is 4.6×10^4. This is less than one third of 1.4×10^5, the Reynolds number employed in Robertson et al 's experiment.

(2) Robertson et al employed rather long tubing ($\sim$ 30 cm) in their fluctuating pressure measurement which quite certainly will affect the accuracy of their results. They

also did not carry out any correction to eliminate the damping effect due to the air inside the tubing. In contrast the distance between each pressure tapping and the pressure transducer's sensing surface is less than 10 cm in the present experiment.

(3) The blockage is higher in Robertson et al 's experiment (8.47%) than in the present experiment (5.56%).

(4) The aspect ratio of Robertson et al 's model (11.81) is shorter than that of the model used in the present experiment (L/D = 17 between end plates). No end plates were used in Robertson et al 's experiment although their cylinder did span the full 1.8m height of the wind tunnel.

(5) Difference in wind tunnel turbulence intensity. The turbulence intensity of the wind tunnel used for the present research is 0.05% whereas Robertson et al's tunnel has a turbulence intensity of 0.33%.

(6) The present results are corrected for tunnel blockage effect. This is carried out despite of the fact that at $\alpha > 13.5$ degrees (approximate figure), a separation bubble is formed on one of the side faces which causes the "size" of the model to be altered and as a result the amount of correction estimated by Maskell's method becomes insufficient. Robertson et al, on the other hand, did not correct their results for blockage because of the uncertainty mentioned above.

At the present moment it is not fully understood

why C_{pFACE}' vary with α in the way shown in fig. 4.3(a). Robertson et al only suggested that the rapid changes in C_{pFACE}' in the range $10 \leq \alpha \leq 20$ degrees is due to the flow reattachment on side B which first occurs at $\alpha \sim 13.5$ degrees. Although Robertson et al 's suggestion is thought to be true, it does not really explain what is happening to the flow around the cylinder when the angle of attack increases from zero.

Close examination of the present results in fig. 4.3(a) reveals the following interesting points:

(1) There is hardly any change in C_{pA}'. It only increases slightly with increasing α. This is perhaps not unexpected because the flow on face A remains attached throughout.

(2) C_{pB}' reduces sharply in the range $5 \leq \alpha \leq 12.5$ degrees. This is most likely related to the flow reattachment that takes place at $\alpha \sim 13.5$ degrees. For $\alpha > 13.5$ degrees, C_{pB}' continues to reduce (although rather slowly), probably because more and more of surface B has attached flow.

(3) C_{pC}' at first increases with α and reach a maximum value of about 0.286 at $\alpha \sim 5$ degrees. Beyond this α C_{pC}' reduces and reaches a minimum of about 0.104 at $\alpha \sim 12.5$ degrees. From $\alpha > 12.5$ degrees C_{pC}' increases again with increasing α and approaches a value of about 0.33 asymptotically. The variation in C_{pC}' may be explained in terms of vortex formation length l_f. Between $\alpha = 5$ to 12.5

degrees, the shear layer that separates from AB is "deflected" by trailing corner BC, causing vortices to be formed further downstream. This increases l_f and also causes a reduction in the fluctuating pressure acting on face C. For $\alpha > 12.5$ degrees, flow reattaches on side B and the reverse occurs. ie. l_f decreases and C_{pC}' increases.

(4) C_{pD}' resembles C_{pB}' very closely up to $\alpha = 12.5$ degrees. Above this angle of attack, C_{pD}' rises above C_{pB}' and becomes almost identical to C_{pC}'. For $\alpha < 12.5$ degrees, C_{pD}' resembles C_{pB}' because the asymmetry is not too large and the two shear layers separate from AB and AD (see fig. 4.3(b)). For $\alpha > 12.5$ degrees, flow reattaches on side B near BC and the flow subsequently re-separates at the corner BC. Faces C and D become the two faces that are facing the wake and the fluctuation in pressure acting on them become very similar (see fig.4.3(c)).

(5) $C_{pA}' \sim C_{pB}'$ and $C_{pC}' \sim C_{pD}'$ when $\alpha = 45$ degrees. This is expected from symmetry consideration.

4.4 C_{Fy} AND C_x VERSUS α

C_{Fy} in Parkinson' quasi-steady theory is identical to $-(C_{pD} - C_{pB})$ (body axis lift, also denoted by C_y) in the present experiment. Experiment results of $-C_{Fy}$ (not corrected for blockage) versus α are shown in fig. 4.4(a). Results from Bearman et al (1984(a)), Parkinson & Smith (1964) and Wawzonek (1979) are also included for comparison.

In spite of the fact that the results shown are not

corrected for tunnel blockage, direct comparison is still fairly justifiable as the blockage ratio in all the experiments reported here are similar. The blockage ratio are approximately 3.63%, 4.19% and 5.56% for Wawzonek, Bearman et al and the present experiment respectively.

From fig. 4.4(a) it is seen that the three present sets of results (all at low turbulence with Re x 10^{-4} = 2.26, 4.54 and 6.69) fit into the "band" of low turbulence results reported by other researchers. The lowest Reynolds number results obtained in the present experiment agree very well with the results from Parkinson & Smith (1964) which were collected at a very similar Reynolds number of 2.1 x 10^4. On the other hand, the author is a little surprised to find that the present medium Reynolds number results agree quite well (except in the range $9 \leq \alpha \leq 13$ degrees) with the results of Wawzonek (1979) which were actually collected at a lower Reynolds number of about 1.2 x 10^4. In the range $9 \leq \alpha \leq 13$ degrees, Wawzonek reported slightly higher values of $-C_{F_y}$. The small difference among those results shown in fig. 4.4(a) are most likely due to the following factors:

(1) Differences in detailed wind tunnel characteristics. Many experimentalists are fully aware that supposedly identical experiments carried out in different wind tunnels do not give rise to identical results. This is thought to be due to the present lack of knowledge in identifying ALL the characteristics of a wind tunnel which

can affect results measured in them.

(2) Details of models used (size and hence blockage ratio, aspect ratio etc) are different.

(3) Instrumentation and methods of force measurement: Wawzonek, for example, measured forces by strain guages whereas Bearman et al and the author estimate forces by measuring average pressure by using pressure transducer and micromanometer respectively.

The medium and high turbulence results from Bearman et al (1984(a)), together with their low turbulence results, are shown in fig.4.4(b). From fig.4.4(b) the medium and high turbulence results are seen to be quite different from those low turbulence results. $-C_{Fy}$ reaches a maximum which approximately corresponds to the situation at which flow reattachment on one side face commences at a much lower angle of attack than in low turbulence free stream. As mentioned in section 1.1.1.5, Lee (1975(a)) suggested that high free stream turbulence causes the separated shear layer to "thicken" and hence reattaches onto the trailing edge corner at a lower angle of attack.

The trend of $-C_{Fy}$ versus α is a direct consequence of the trend of C_{pB} and C_{pD} versus α which had been explained in section 1.1.1.1. The maximum value of $-C_{Fy}$ corresponds to a value of α at which flow reattachment onto the trailing edge BC commences. $-C_{Fy}$ versus α is a required input to the quasi-steady theory. The sign of $\partial C_{Fy}/\partial\alpha$ ($\alpha = 0$) also determines whether a particular cross

sectional shape is susceptible to galloping oscillation. A particular cross sectional shape is stable to galloping oscillation if $\partial C_{Fy}/\partial\alpha \ (\alpha = 0) \geq 0$ and is unstable if $\partial C_{Fy}/\partial\alpha(\alpha=0) < 0$. Blevins (1977) quoted a figure of -2.7 (Re = 6.6×10^4) for a square. Bearman et al (1984(a)) reported that $\partial C_{Fy}/\partial\alpha \ (\alpha = 0)$ equals to -5.4, -3.9 and -3.4 for low, medium and high free stream turbulence respectively. Parkinson & Smith (1964) and Wawzonek (1979), on the other hand, reported values of -2.69 and -4.01 respectively. In the present experiment, by least square fitting a straight line onto the seven data points within the range $-1.5 \leq \alpha \leq 1.5$ degrees, $\partial C_{Fy}/\partial\alpha \ (\alpha = 0)$ was found to be -3.55, -4.17 and -3.87 for Re x 10^{-4} = 2.26, 4.51 and 6.69 respectively. Values of $\partial C_{Fy}/\partial\alpha \ (\alpha = 0)$ obtained in the present experiment therefore come in between the lower (more negative) values reported by Bearman et al and the higher (less negative) values reported by Parkinson & Smith and Blevins. The scatter in $\partial C_{Fy}/\partial\alpha \ (\alpha=0)$ is, as pointed out by Bearman et al, due to the scarcity and limits on the accuracy of the data points. The quasi-steady theory had been discussed in section 1.2.1.3 and some of its prediction will be compared with experimental results in chapter seven.

As the body axis lift versus angle of incidence data measured in the present research and presented in fig. 4.4(a) are not corrected for blockage (to facilitate direct comparison with other researchers' results), the same data are corrected for blockage and re-presented in

fig. 4.4(c).

Body axis drag (C_x) measured in the present experiment are corrected for blockage and plotted against α in fig. 4.4(d). C_x equals to ($C_{pA} - C_{pC}$) and the shape of the C_x curve can therefore be explained in terms of a superposition of C_{pA} and $-C_{pC}$, shape of which had been discussed in section 4.1.

4.5 C_x' AND C_y' VERSUS α

C_x' and C_y' are the r.m.s. body axis drag and lift coefficients respectively. They are defined as:

$$C_x' = (C_{pA} - C_{pC})' \tag{4.2}$$

$$C_y' = (C_{pD} - C_{pB})' \tag{4.3}$$

C_x' measured in the present experiment are corrected for blockage effect and are plotted against α in fig. 4.5(a). Also shown are results obtained by Pocha (1971) and Lee (1974). All the results shown in fig. 4.5(a) show similar trend in that as α increases from 0 degree, C_x' increases at first to a maximum at $\alpha \sim 5$ degrees before decreasing to a minimum at $\alpha \sim \alpha_{crit} \sim 12.5$ degrees. For $\alpha > \alpha_{crit}$, C_x' increases rather rapidly at first and then slowly later with increasing α. However, although the trends are similar, detail quantitative agreement of results presented in fig. 4.5(a) is not very good. Pocha's results

are consistantly lower in magnitude than the present results and do not really show a peak in C_x' at $\alpha \sim 5$ degrees. Since blockage correction will further reduce the value of C_x', the disagreement between Pocha's and the present results is therefore not attributed to blockage effect. Although not consistent throughout, the present results show that higher Reynolds number generally tend to yield higher values of C_x'. This again cannot be used to explain the discrepancy between Pocha's results and results measured in the present investigation because the present results were obtained at Reynolds numbers ($2.26, 4.51$ and 6.69×10^4) which are lower than the Reynolds number (1.38×10^5) employed by Pocha. The author can therefore only suggest that the quantitative disagreement may be due to the totally different methods used to measured C_x'. In the present experiment average pressure on opposite faces were measured and subsequently C_x' was calculated digitally. The present method therefore gives the magnitude of C_x' at mid-span. On the other hand, Pocha measured his C_x' by feeding the output of strain gauges to r.m.s. meter. Pocha's results are therefore averaged over the length of the cylinder. Due to the lack of perfect spanwise pressure correlation, Pocha's C_x' is likely to be lower than the C_x' measured in the present experiment.

Lee's (1974) results, on the other hand, are so sparse that comparison can only be made at $\alpha = 0$ and 15 degrees. At $\alpha = 0$ degree, Lee's results (uniform flow, Re =

1.76 x 10^5) agree fairly well with the highest Reynolds number (6.69 x 10^4) results of the present investigation. At α = 15 degrees however, the agreement is less satisfactory as Lee's results are lower than those measured in the present investigation. Other factors which may contribute to the poor quantitative agreement are differences in blockage ratio (5.56% for present investigation and 3.6% for Lee's experiment) and aspect ratio (17 for the present investigation and 9.27 for Lee).

The variation of the r.m.s. body axis lift C_y' with angle of attack α measured in the present investigation, together with results of Pocha (1971), Lee (1974) and Vickery (1966) are shown in fig. 4.5(b). Again, all the results show similar trend. C_y' is seen to reduce rapidly with α increasing from 0 degree to about α_{crit}, beyond α_{crit} there is very little changes in C_y'.

The present results are again corrected for blockage effect but surpringly this time they agree fairly well quantitatively with Pocha's results throughout the range $0 \leq \alpha \leq 20$ degrees. The present results also agree well ($0 \leq \alpha \leq 15$ degrees) with Vickery's smooth flow results which were corrected for blockage effect by the method of Allen & Vincenti. For $\alpha > 15$ degrees, Vickery's results continue to reduce which, according to Lee, may be due to the type of blockage correction Vickery used. Lee's own results (not corrected for blockage), agree less well with others and this may be caused by the difference in

blockage and aspect ratio as mentioned earlier in this section. Lee suggested that the rapid reduction in C_y' with increasing α in the range $0 \leq \alpha \leq \alpha_{crit}$ may be attributed to the reduction in correlation between surface pressure of two opposite faces. As will be discussed in section 1 of the next chapter, the shape of C_y' can be used to explain the behaviour of C_L' versus U_r at medium to high reduced velocity.

4.6 C_p AND C_p' DISTRIBUTION

The distribution of C_p and C_p' are of course obtained by connecting the pressure transducer to the pressure tappings directly without using the pressure averagers. This is carried out in order to see if the present experiment is capable of reproducing Obasaju's (1977) results. The results of the two experiments should agree well if both are conducted correctly and accurately.

The comparison of C_p distribution is shown in fig. 4.6(a). Obasaju's results were measured at Re $\sim 4.74 \times 10^4$ and using No. 1 end plates (see fig. 2.1 for end plates details). The present results, on the other hand, were measured at a Reynolds number of about 4.6×10^4 with No. 2 end plates. Despite the use of different end plates, the two sets of results agree extremely well.

The comparison of C_p' is shown in fig. 4.6(b). The present results were again measured at Re $\sim 4.6 \times 10^4$ with No. 2 end plates installed. Obasaju's results, on the other

hand, were collected at Re $\sim$ 6.06 x 10^4 and without any end plates. A comparison between the two sets of results is made in fig. 4.6(b). It is immediately obvious that quantitative agreement between the two sets of results is very poor on side B, C and D although the general trend are similar. The probable causes of the discrepency are:

(1) Obasaju's C_p' were collected without end plates attached to the cylinder and hence three dimensional effect may be more severe than in the present experiment.

(2) The Reynolds number in Obasaju's enperiment was almost 30% higher than in the present experiment.

(3) A 1/4" B & K microphone (model 4136) was employed in Obasaju's experiment whereas a $\pm$ 0.1 p.s.i. Setra pressure transducer was used in the present experiment. As pointed out by Obasaju himself (pg. 124 of Obasaju (1977)), due to changes in dynamic sensitivity factor at low frequency, C_p' measured by the 1/4" B & K microphone was about 3% lower than actual value.

From comparison in fig. 4.6(b) it therefore seems that the effect of three dimensionality in flow past stationary square cylinder with its front face normal to the free stream is to cause a reduction in C_p' on the side and rear faces.

4.7 C_D, C_D', C_{pA}, C_{pA}', C_{pC} AND C_{pC}' VERSUS REYNOLDS NUMBER*

Experimental results of C_D versus Re is shown in fig. 4.7(a). Comparison of the present C_D results (after blockage correction) with those reported by Obasaju (1977) reveals some interesting features: Obasaju presented results of C_D measured with cylinder fitted with either No.1, 2 or 3 end plates (see fig. 2.1). No.1 is the smallest while No.3 is the largest among the three pairs of end plates. However, his results do not show a consistent trend of magnitude of C_D with respect to size of end plates and C_D measured with No.2 (medium size) end plates are consistently lower than those measured with either No.1 or 3 end plates. Another unexplainable finding is that the present results, although measured with No.2 end plates installed, agree better with Obasaju's No.1 and 3 end plates results. Despite the minor discrepancy pointed out above, the author feels that the overall agreement between the present and Obasaju's drag results is fair and therefore justifies the use of pressure averagers to give average face pressure. Obasaju suggested that the slight increase in C_D with increasing Re (as observed in fig. 4.7(a)) is attributed to the upstream movement of the laminar to turbulent transition in the separated shear layer. He suggested that earlier transition causes an increase in shear layer entrainment which decreases C_{pb} ($C_{pb} = C_{pC}$) and hence increases C_D with

---

* The two pressure transducers were referenced to the same pressure which is different from the wind-tunnel static pressure. This should be taken into consideration when interpreting C_{pAc} and C_{pCc} vs Re shown in fig. 4.8(a).

increasing Re. At even higher Reynolds number the transition takes place just behind the separation, further increase in Reynolds number therefore has little effect on $-C_{pb}$ and C_D. This explains why C_D levels off at high Reynolds number.

C_D' versus Re is shown in fig. 4.7(b). At Reynolds number below about 3.3×10^4, C_D' is found to reduce with increasing Reynolds number and reaches a minimum of about 0.2 at Re 3.3×10^4. Beyond this Reynolds number C_D' increases with increasing Re and asymptotically approaches a value of about 0.27 at high Reynolds number.

C_{pA} and C_{pC} are corrected for blockage and plotted against Re in fig. 4.8(a). C_{pA} is seen to remain practically constant at about 0.935 for Re $> 2 \times 10^4$. This is not unexpected as face A is always ahead of flow separation. $-C_{pC}$, on the other hand, increases slightly with increasing Re and asymptotically approaches a value of about 1.3 at high Reynolds number. The trend of $-C_{pC}$ found in the present experiment supports Obasaju's (1977) idea that the upstream movement of the laminar to turbulent transition in the separated shear layer increases shear layer entrainment which in turn increases $-C_{pC}$ and C_D. As C_{pA} remains more or less independent of Reynolds number, it is expected that C_D versus Re and $-C_{pC}$ versus Re show the same trend.

C_{pA}' and C_{pC}' versus Re are shown in fig. 4.8(b). At lower Reynolds number, C_{pA}' is found to reduce with increasing Re. At higher Re ($> 4 \times 10^4$), C_{pA}' levels off and remains more or less constant at about 0.069. C_{pC}', on the

other hand, show more scatter when plotted against Re. This is expected as face C is facing the wake. Within the range of Reynolds number investigated in the present research, C_{pC}' is found to increase with increasing Re. The trend of C_D' versus Re reported earlier can therefore be explained in terms of some kind of "superposition" of C_{pA}' and C_{pC}' versus Re. More rigorous mathematics shows that:

$$C_D'^2 = C_{pA}'^2 + C_{pC}'^2 - 2 \frac{\sum_{i=1}^{N} \hat{C}_{pAi} \hat{C}_{pCi}}{N} \qquad (4.4)$$

where $C_{pAi} = C_{pA} + \hat{C}_{pAi}$

and $C_{pCi} = C_{pC} + \hat{C}_{pCi}$.

4.8 C_L' VERSUS REYNOLDS NUMBER

Experimentally measured C_L' are corrected for blockage and plotted against Reynolds number in fig. 4.9. At a low Reynolds number of about 1.37×10^4, C_L' is found to be at about 1.05. At this low Reynolds number end, free stream wind speed is very low and hence the pressure signals are very weak; outputs from the pressure transducers have poor signal/noise ratio and hence the accuracy of measurement is less satisfactory. As Reynolds number increases, C_L' also increases gradually and levels off at a value of about 1.33 at high Reynolds number.

The trend of C_L' versus Re can again be explained by referring to the upstream movement of the laminar to

turbulent transition of the separated shear layer. At low Reynolds number, the separated shear layers adjacent to the side faces B and D are laminar, the fluctuating pressure (and hence C_L') is relatively low. As Reynolds number increases, the laminar to turbulent transition location moves upstream, part of the shear layers adjacent to the side faces become turbulent, this increases the entrainment of fluid from the outer region which causes the pressure fluctuation on the side faces and hence C_L' to increase. At even higher Reynolds number, the transition occurs immediately after flow separation at the two leading edges AB and AD, the shear layers adjacent to the cylinder side faces become fully turbulent and hence C_L' reaches its maximum value. Further increase in Reynolds number therefore has no effect on C_L'.

4.9 STROUHAL NUMBER VERSUS REYNOLDS NUMBER

Strouhal number estimated from the frequency of the autocorrelation function of the lift signal is plotted against Reynolds number in fig. 4.10(a). Also shown in fig. 4.10(a) are Obasaju's (1977) results. The agreement between the two sets of results is very good. A possible explanation for the slight reduction of Strouhal number with increasing Reynolds number as seen in fig. 4.10(a) is that the vortex formation length l_f increases slightly as free stream wind speed (and hence Re) increases. This causes the shear layer to be more diffused at the location where vortices are

formed. According to Gerrard's (1966) model of vortex formation, the more diffused shear layers require longer time to feed fully grown vortices which in turn causes a reduction in shedding frequency and hence Strouhal number. This had been mentioned in section 1.1.1.3. After blockage correction, the present results are shown in fig. 4.10(b).

4.10 CONCLUSION

None of the results/findings presented in this chapter are new as they have all been reported by several researchers in the literature. The square cylinder and wind tunnel used in the present research are identical to that used by Obasaju (1977). However, despite the employment of the same cylinder and wind tunnel, the technique used are different. In the present research computerised data acquisition is adopted. Two pressure averagers are also used to generate average pressure over two faces of the cylinder which therefore enable direct calculation of C_D and C_L. The results reported in the present chapter are generally found to be in good agreement with those reported by Obasaju (1977). It therefore gives the author confidence in the quality of results obtained and also justifies the use of pressure averagers in drag and lift forces measurement.

CHAPTER FIVE

FLOW PAST A TRANSVERSELY OSCILLATING SQUARE CYLINDER -RESULTS AND DISCUSSION

Unlike its stationary cylinder counterpart, the problem of flow past a transversely oscillating cylinder is less well investigated and understood. Results presented in the present chapter will be compared with the findings of other researchers whenever the latter are available. All the results reported in the present chapter are obtained by making use of two pressure averagers each receiving inputs from six pressure tappings and with their outputs connected to two Setra pressure transducers. The ability of the pressure averager to give accurate results has been demonstrated in the previous chapter. All the results presented in this chapter are not corrected for blockage, because to the author's best of knowledge, there does not exist a totally satisfactory method for compensating blockage effect in unsteady flow situation. The effect of the inertia of air inside the connection tubing on fluctuating lift and the phase angle between the component of lift at the forcing frequency and the cylinder displacement has been corrected as explained in section 3.6.2.

5.1 C_L' VERSUS U_r

The fluctuating lift force C_L' for various dimensionless amplitude in the range $0.1 \leq A/D \leq 2$ are plotted against reduced velocity U_r in fig. 5.1. It is immediately obvious that all the C_L' versus U_r curves are similar in shape. At low reduced velocity, C_L' as high as 2.76 (see fig. 5.1(d)) has been measured in the present investigation. As reduced velocity increases, C_L' reduces fairly rapidly to a minimum of about 0.75. Further increases in reduced velocity causes C_L' to increase again and asymptotically approaches the steady state C_L' ($\sim$ 1.45) at high reduced velocity. The magnitude of the reduced velocity which corresponds to the minimum in C_L' and the value when steady state C_L' (arbitrarily assumed to be 1.4) is reached are denoted by $U_{r,min}$ and $U_{r,ss}$ respectively (see fig. 5.2); they are A/D dependent. For $A/D > 0.5$ and $U_r < U_{r,min}$, some "local peaks" are seen to superimpose onto the overall reducing trend of C_L'.

According to Bearman et al (1984(a)), they suggested that the flow can be divided into three regions (see also fig. 5.2). They are:

(1) Multiple harmonic region (MH) : This is the region where $U_r < U_{r,min}$.

(2) Intermediate transition region (IT) : This is the region where $U_{r,min} < U_r < U_{r,ss}$.

(3) Quasi-steady region (QS) : This is the region where $U_r > U_{r,ss}$.

At any arbitrary reduced velocity U_r, within a cycle of oscillation, the maximum instantaneous angle that the "resultant flow" will be inclined to the cylinder is denoted by α_{max}. α_{max} can be calculated from :

$$\alpha_{max} = \tan^{-1}(\dot{y}/U_\infty) = \tan^{-1}(2 \pi \times A/D \times 1/U_r) \qquad (5.1)$$

The values of $U_{r,min}$, $U_{r,ss}$ and their corresponding α_{max} for various A/D are tabulated in table 5.1. $U_{r,min}$, $U_{r,ss}$, $\alpha_{max,min}$ and $\alpha_{max,ss}$ (values of α_{max} at $U_r = U_{r,min}$ and $U_{r,ss}$ respectively) are plotted against A/D in fig. 5.3(a) and (b). From fig. 5.3(a) it is seen that $U_{r,min}/(A/D)$ and $U_{r,ss}/(A/D)$ are almost constant. The relation between the two U_r's and A/D can be approximated by the the following straight lines:

$$U_{r,min} = 8.30 + 21.12(A/D) \qquad (5.2)$$

$$U_{r,ss} = 25.04 + 39.71(A/D) \qquad (5.3)$$

The relation between $\alpha_{max,min}$, $\alpha_{max,ss}$ and A/D are non-linear. The magnitude of $\alpha_{max,min}$ varies from about 3.43 degrees at A/D = 0.1 to about 14.14 at A/D = 2. This suggests that the minimum in C_L' may not be simply explained as due to the consequence of flow reattachment (for a stationary inclined cylinder flow reattachment takes place when the angle of incidence is about 13.5 degrees). From

table 5.1 and fig. 5.3(b) it also appears that the flow approaches the quasi-steady state at different values of α_{max}.

It was mentioned earlier that at low reduced velocity C_L' was found to be much higher than its value for a stationary cylinder at similar Reynolds number. This finding is probably not unexpected as "lift amplification" during lock-in had been reported by some researchers in the literature (Bishop & Hassan (1964(b)) for circular cylinder and Nakamura & Mizota (1975) for square cylinder). In fact, the ability to accurately predict the lift amplification phenomena is often used as one of the criterion for assessing how successful a certain mathematical model for vortex resonance is (Griffin, Skop & Koopmann (1973)). In fig. 5.1(a) and (b), peaks in C_L'($\sim$ 1.69 and 2.13 respectively) were measured at $U_r \sim 8$ and 8.5 respectively. For the other higher A/D ($\geq$ 0.5) cases, maximum forcing frequency was restricted to 5 Hz (for A/D = 0.1 forcing frequency as high as 10 Hz was employed) and the velocity in the lock-in range was too low to make accurate pressure measurements. As a result it is not clear whether C_L' exhibits peaks at $U_r \sim U_{ro}$ for other A/D's. Obasaju (1977) had carried out some fluctuating pressure measurement at the centre of a side face and his results also indicates that for A/D = 0.25 and at $U_r \sim 7.6$ (see fig. 7.21 of Obasaju (1977)), C_p' (after inertia effect of air inside pressure tubing had been corrected) exhibits a maximum value

of about 1.12.

In fig. 4.5(b) it was observed that when the blockage corrected fluctuating body axis lift $(C_{pD} - C_{pB})'$ of a stationary square cylinder was plotted against α, it reduces from about 1.3 (about 1.42 before blockage correction) at α = 0 degree to as low as 0.42 (about 0.46 before blockage correction) at α = 20 degrees. It therefore appears that the behaviour of C_L' in the quasi-steady region and at least in the upper part of the intermediate transition region can be explained by referring to the variation in $(C_{pD} - C_{pB})'$ with α of a stationary inclined cylinder. From the knowledge of stationary cylinder's C_y and C_y' versus α (uncorrected for blockage effect as the data presented in chapter 5 are also not corrected for blockage effect due to reason mentioned at the beginning of the present chapter), a time-averaged quasi-steady fluctuating lift coefficient C_{Lqs}' is estimated from:

$$C_{Lqs}' = \left[C_{Lqs}'(f_s)^2 + C_{Fy}'(f_N)^2\right]^{\frac{1}{2}} \qquad (5.4(a))$$

where $C_{Lqs}'(f_s) = \frac{1}{T} \int_0^T C_y'(\alpha)dt$ * $\qquad (5.4(b))$

and $\alpha = \alpha(t)$

The method of estimating the magnitude of $C_{Fy}'(f_N)$ will be explained in detail in section 7.1 and fig. 7.1.

The quasi-steady estimated C_{Lqs}' for A/D = 0.5, 1.0 and 2.0 are then superimposed onto the experimental data

---

* $C_y'(\alpha)$ being the r.m.s. body axis lift and C_y' vs α is shown in fig. 4.5(b).

(from fig. 5.1(c), (e) and (g)) in fig. 5.4 (a), (b) and (c). From fig.5.4(a), (b) and (c) it can be seen that C_{Lqs}' predicts the trend of the experimentally measured C_L' in the upper intermediate transition and in the quasi-steady region well. For A/D = 1 and 2, C_{Lqs}' even agree quantitatively well with C_L' for $U_r \geq 70$. Fig. 5.4 therefore provides a clear indication of the range of reduced velocity where the quasi-steady theory is applicable.

Bearman et at (1984(a)) suggested that for the case of a square cylinder oscillating transversely to the free stream, two vortex wakes co-exist. They are the conventional Karman vortex wake and a second one which is generated by the transverse motion of the cylinder. The second wake is such that its flow field exerts a pressure loading on the cylinder that is synchronized with but out of phase to the body motion. The relative strength of the two vortex wakes vary in the three different regions of flow. In the multiple harmonic region, the body frequency signal has a much stronger effect than the Strouhal signal. Some of the experimental phenomena observed in this region which excludes the locking of the shedding frequency onto an integer multiple of the forcing frequency (eg. f_s locks on to $3f_N$) can be predicted (qualitatively at least) by the wake oscillator model (see Hartlen & Currie (1970), Griffin, Skop & Koopmann (1973), Skop & Griffin (1973), Landl (1974) and Obasaju(1977)). On the other hand, the Strouhal signal has a much more dominating effect than the body frequency

signal in the quasi-steady region. In the QS region, Parkinson's quasi-steady theory is extremely useful as it can predict the body frequency component of the experimentally measured results well. In the upper part of the multiple harmonic and in the intermediate transition region, both shedding and body frequency signals are of approximately equal importance and it is thought that they interact in a complex (non-linear) manner. This presumably causes the minimum in C_L' observed which has a magnitude of only about half the value of C_L' for a stationary cylinder at similar Reynolds number. Some flow visualization has been conducted at different reduced velocities. Preliminary results suggest that different flow structures exist at different reduced velocities and the magnitude of the fluctuating lift coefficient is related to the strength of the vortex shed. This will be discussed in more detail in the next chapter.

By displaying both the lift force and displacement signals simultaneously on a CRO, it is observed that at $U_r \sim 1/S$, where S is the stationary cylinder's Strouhal number (values between 0.12 to 0.14 had been reported in the literature), the vortex shedding frequency f_s locks on to the body frequency (also called forcing frequency) f_N. As the reduced velocity increases, the lift signal exhibits a frequency which is three times the body frequency and for A/D = 1.5, $f_s = 5f_N$ is also detected at even higher reduced velocity. Some traces of even harmonics (eg. $f_s = 2f_N$) are

detected during the transition between two consecutive odd harmonics but they are never as distinct as the odd order harmonics. This observation is in good agreement with the experimental findings of Bearman et al (1984(a)) reported in section 1.2.1.1. By carrying out spectral analysis, they found that:

(1) Near $U_r \sim 1/S$ the vortex shedding frequency locks on to the forcing frequency. Within the lock-on range $C_L'(f_S)$ and $C_L'(f_N)$ become the same quantity. At high reduced velocity $C_L'(f_S)$ is the dominating component of C_L'.

(2) The even order harmonics remain unimportant throughout the speed range investigated.

(3) $C_L'(3f_N)$ peaks at $U_r \sim 3U_{ro}$ and $C_L'(5f_N)$ was also rising as U_r was increasing towards $5U_{ro}$.

The frequencies indicated in some of the C_L' versus U_r plot in fig. 5.1 refer to the frequency of the lift force signal observed on a CRO at the corresponding reduced velocity. At very high U_r (QS region) "beating" of the lift force signal is observed. Beating of circular cylinder lift force signal at high U_r has also been reported by Bishop and Hassan (1964(b)). Photographs of simultaneous lift/displacement traces taken from a storage CRO at A/D = 0.675 and at different U_r's are shown in fig. 5.5 and are discussed as follows:

(1) At a reduced velocity of about 7.75 (fig. 5.5(a) and (b)), the shedding frequency locks on to the forcing frequency. Comparing the top traces of fig. 5.5(a) and (b)

reveals that the lift signal is being amplified and hence C_L' at this reduced velocity should be greater than the stationary cylinder's approximate C_L' of 1.45 (see fig. 5.1(d)). Comparing the top and bottom traces of fig. 5.5(a) also reveals that at this reduced velocity the lift lags the displacement (ie. ϕ is negative), this can also be seen in fig. 5.7(d) which will be discussed in the next section.

(2) At a reduced velocity of about 14.37 (fig. 5.5(c) and (d)), the shedding frequency still locks on to the forcing frequency but a trace of $2f_N$ component is beginning to become detectable in the lift signal (fig. 5.5(c)). At this reduced velocity because f_N still locks on to f_s, the Strouhal number in the oscillating cylinder case is lower than the stationary cylinder's approximate value of 0.13. Comparison of the lift traces in fig. 5.5(c) and (d) shows that at $U_r \sim 14.37$ the value of C_L' in both cases should be about the same. This is supported by fig. 5.1(d). Fig. 5.5(c) also shows that the phase angle between the lift at the body frequency and the displacement is very small. This can also be seen in fig. 5.7(d).

(3) At a reduced velocity of about 21.6 (fig. 5.5(e) and (f)), the shedding frequency is about three times the forcing frequency. Near this reduced velocity it was found that f_s locks on to $3f_N$ over a small range of U_r, although the range of U_r that this lock-on takes place is smaller than that of the f_s/f_N lock-on. Comparing the lift traces of

fig. 5.5(e) and (f) shows that the value of C_L' for oscillating cylinder at this U_r should be smaller than the corresponding value (about 1.45) for stationary cylinder. This can also be seen in fig. 5.1(d).

(4) At a reduced velocity of about 27.04 (fig. 5.5(g) and (h)), the shedding frequency is approximately three times the forcing frequency although no locking on of frequency is evident. Comparing the lift force traces of fig. 5.5(g) and (h), it is seen that the shedding frequency is hardly affected by the oscillation although at this reduced velocity the oscillation still slightly reduces the value of C_L' (see fig. 5.1(d)).

(5) At a reduced velocity of about 35.79 (fig. 5.5(i) and (j)), both C_L' and the shedding frequency are little affected by the oscillation of the cylinder. At this reduced velocity f_s is approximately five times f_N.

(6) At an even higher reduced velocity of about 72.76 (fig. 5.5(k) and (l)), the flow becomes quasi-steady and the lift force is not affected by the oscillation of the cylinder (see also fig. 5.1(d)).

The fact that the maximum angle that the flow would appear to be inclined to an oscillating cylinder α_{max} is dependent on $U_r/(A/D)$ (see eqn.(5.1)) prompts one to think that $U_r/(A/D)$ might be used as an universal parameter. C_L' for different A/D's are plotted against $U_r/(A/D)$ in fig. 5.6. From the figure it can be seen that some scatter exists (mainly in the range $40 \leq U_r \leq 100$). The author is

not sure at this stage whether the scatter is attributed to $U_r/(A/D)$ not being a good choice as an universal parameter or to experimental error.

5.2 ϕ VERSUS U_r

Plots of the phase angle that the lift force leads the displacement versus reduced velocity for different A/D values are shown in fig. 5.7. At very low reduced velocity, ϕ is negative and this means that flow-induced oscillation of a freely suspended cylinder will not take place. This part of the ϕ curve shows a rapid variation in ϕ with relatively small changes in reduced velocity. In fig. 5.7(d) (e) and (f) ϕ reaches a "local maximum" before it finally increases with increasing U_r to cross the ϕ = 0 degree line. The magnitude of U_r at which this takes place is denoted by $U_{r,0}$. After crossing the ϕ = 0 degree line ϕ initially increases rapidly with increasing U_r. At higher U_r, the rate of increase of ϕ with U_r ($\partial\phi / \partial U_r$) reduces and ϕ approaches the quasi-steady theory predicted value of 90 degrees. The magnitude of U_r at which $\phi \rightarrow 90$ degrees is very ill-defined. The author have therefore decided to use $U_{r,80}$, the magnitude of U_r when ϕ = 80 degrees (an arbitrary choice) as a rough indication of when the quasi-steady state is reached. For the smaller A/D investigated (A/D = 0.1, 0.25, 0.5 and 0.675), in the positive ϕ range, ϕ actually reduces with increasing U_r over a small range of U_r. This causes a "local maximim" in

ϕ (see fig.5.7(a), (b), (c) and (d)).

The values of $U_{r,0}$, $U_{r,80}$, $\alpha_{max,0}$ (α_{max} when ϕ = 0 degree) and $\alpha_{max,80}$ (α_{max} when ϕ = 80 degrees) are plotted against A/D in fig. 5.8(a) and (b). In fig. 5.8(a) it is seen that the relation between $U_{r,0}$ and A/D, $U_{r,80}$ and A/D are approximately linear. The latter shows more scattter but this is quite expected because $\partial\phi / \partial U_r$ at ϕ = 0 degree is much larger than $\partial\phi / \partial U_r$ at ϕ = 80 degrees and as a result the $U_{r,0}$ can be read off the ϕ versus U_r plots with much higher accuracy. The $U_{r,0}$ versus A/D line has a physical importance because it can be used to determine, for a freely suspended square cylinder and at a particular A/D, what reduced velocity is required (for zero or small dampings) to sustain that amplitude of oscillation.

Before the present experiment, it was known from the finding of researchers like Nakamura & Mizota (1975), Obasaju (1977) and Parkinson & Wawzonek (1981), that at low reduced velocity ϕ is negative and flow-induced oscillations will not take place. As reduced velocity increases, ϕ increases and crosses the ϕ = 0 line at U_r = U_{cr}, the critical reduced wind velocity. On the other hand, at very high reduced velocity, the flow is quasi-steady; Parkinson's theory, which had been shown to be valid at high reduced velocity by various researchers including Wawzonek (1979) and Bearman et al (1984(a)) etc, predicts that the phase angle will approach 90 degrees. However, having established the approximate values of ϕ at two extremes of

the reduced velocity range, one still has very little idea about how ϕ will behave at intermediate reduced velocities except that the ϕ versus U_r curve should vary reasonably smoothly without any discontinuity. The common feature shared by all the ϕ versus U_r plots in fig. 5.7 is that between low reduced velocity where $\phi < 0$ degree and high reduced velocity (when $\phi \to 90$ degrees), the ϕ curve has a high $\partial\phi/\partial U_r$ region at the lower part of the intermediate reduced velocity range followed by a low $\partial\phi/\partial U_r$ region at the upper part of the same reduced velocity range. At the reduced velocity where the two regions meet, the ϕ curve exhibits a "kink". The reduced velocity at which the ϕ curve exhibits this "kink" is denoted by $U_{r,k}$. By comparing fig. 5.7 with the corresponding (ie. same A/D value) plot in fig. 5.1, one very interesting finding is that $U_{r,min}$ is always approximately equal to $U_{r,k}$. It is therefore tentatively suggested at this stage that the same "mechanism" causes $\partial C_L'/\partial U_r$ to change from negative to positive (and hence a minimum in C_L') and $\partial\phi/\partial U_r$ to change (for the same A/D and at the same reduced velocity because $U_{r,min} \sim U_{r,k}$) from high to low values (and hence a kink in the ϕ versus U_r curve). This "mechanism" is thought to be the changes in the way in which vortices are shed and convected downstream which affects the magnitudes of C_L' and ϕ. Some further discussion on this issue will be given in the next chapter.

In the literature there are only a small group of

researchers who have reported on the variation of ϕ with reduced velocity. To the author's best of knowledge, this small group of researchers includes Bearman et al (1984(a)), Bearman & Obasaju (1982) (based mainly on the results reported in Obasaju (1977)), Nakamura & Mizota (1975), Obasaju (1977), Otsuki et al (1974) and Wilkinson (1974). However, due to one reason or another, some of the results reported by the researchers mentioned above are not suitable for direct quantitative comparison with the experimental results reported here. For example, Obasaju (1977) and Bearman & Obasaju (1982) reported only on the phase angle between the fluctuating pressure at the centre of the side face (instead of the lift) and the displacement. This is said despite of the fact that Obasaju's (1977) results have shown good chordwise pressure correlation at mid-span and hence the phase angle between the pressure at the centre of a side face and the cylinder displacement should not be too different from the phase angle between lift and displacement. Over the small overlapping reduced velocity range where both Obasaju's results and the present results are available, the two sets of results show the same trend of variation with U_r. For Wilkinson, his results are not very accurate (see discussion by Obasaju (1977) pp 164) and therefore no comparison with his results were made. Nakamura & Mizota (see fig. 5.13) and Otsuki et al have also presented some experimentally measured ϕ versus U_r. Their results for A/D = 0.1 are included in fig. 5.7(a) for

comparison. From fig. 5.7(a) it is immediately obvious that there is no quantitative agreement between Nakamura & Mizota and Otsuki et al's data and the data obtained in the present experiment. However, qualitatively all three sets of data show similar trend of variation. This includes the "local maximum" in ϕ in the negative ϕ region and the "kink" and "local maximum" in ϕ in the positive ϕ region mentioned at the beginning of the present section. The causes of the discrepancies among the three sets of data just mentioned are thought to include the following:

(1) Differences in cylinder aspect ratio: The aspect ratio (between end plates) are 4.67, 4.4 and 17 for Nakamura & Mizota, Otsuki et al and the present experiment respectively.

(2) Differences in blockage ratio: The blockage ratio are 5%, 8.33% and 5.56% for Nakamura & Mizota, Otsuki et al and the present experiment respectively. Otsuki et al's blockage ratio is therefore considerably higher than the other two experiments.

(3) Differences in lift force measuring technique: Nakamura & Mizota and Otsuki et al used strain gauges to measure the load (lift force in the present case) acting on their cylinder whereas the author deduced the magnitude of the lift force from pressure measurement at mid-span. The present results are therefore sectional values, whereas Nakamura & Mizota and Otsuki et al's results are averaged over the length of the cylinder. The two sets of results

will only agree with each other if the pressure variation is perfectly correlated over the whole length of the cylinder. This is normally impossible even if end plates are employed.

The only complete set of results which is suitable for comparison with the present results is the recent measurement carried out by Bearman et al (1984(a)) on a freely suspended square cylinder. Their results are shown in fig. 5.7. There are only three points of Bearman et al's measurement on each A/D plot because they only conducted three sets of low turbulence experiment. However, despite the differences in the nature of the two experiments and insufficient number of experimental data available for comparison, the agreement between the two sets of totally independent experimental data is good. This has undoubtedly increased one's confidence in the accuracy of both experiments.

It has already been mentioned at the beginning of this section that all ϕ versus U_r curves have a similar shape. The effect of different amplitude of oscillation (A/D) is therefore to "shift" the ϕ curve parallel to the U_r axis. ie. For higher A/D, higher reduced velocity has to be reached before the flow will become quasi-steady. Also mentioned earlier (see section 5.1) was that for a cylinder oscillating sinusoidally in a free stream, the maximum angle of attack that the flow is in relation to the cylinder is dependent on the ratio $U_r/(A/D)$ (see eqn. (5.1)). It

therefore seems logical for one to plot ϕ versus $U_r/(A/D)$ for different A/D onto a same plot. This is shown in fig. 5.9. As in the case for C_L' (fig. 5.6), a fair amount of scatter is apparent.

Finally, from an engineering point of view, it is noted that in all the different A/D cases investigated in the present research; in the region where $\phi \geq 0$ (ie. $U_r \geq U_{r,0}$) the maximum value of C_L' is the quasi-steady value of approximately 1.45. It therefore appears that it is reasonably safe for the engineers to design a structure by assuming $C_L' \sim 1.45$, the fluctuating lift for a stationary cylinder.

5.3 C_D, C_{pA} AND C_{pC} VERSUS U_r*

Variation of C_D, C_{pA} and C_{pC} with reduced velocity at different amplitude of oscillation are shown in fig. 5.10 and fig. 5.11 respectively. Within the range of reduced velocity investigated in the present research, C_D is found to initially decrease with increasing reduced velocity and reaches a minimum value of approximately 2.1 (this part of the C_D curve is actually seen only in the three largest amplitude of oscillation (A/D = 1, 1.5 and 2) cases). As reduced velocity increases further, C_D begins to increase with increasing reduced velocity and asymptotically approaches the stationary cylinder's C_D (at high Re, before blockage correction) of about 2.48. The reduced velocity at which the drag coefficient is at a minimum is designated as

---

* The two pressure transducers were referenced to the same pressure which is different from the wind-tunnel static pressure. This should be taken into consideration when interpreting C_{pA} and C_{pC} vs U_r shown in fig. 5.11.

$U_{r,Dmin}$, to distinguish from $U_{r,min}$, the reduced velocity at which C_L' is at a minimum. Also, the reduced velocity at which C_D reaches a value of 2.4 (C_D = 2.4 is arbitarily chosen as a criterion that the flow has become quasi-steady) is designated as $U_{r,Dss}$. This should be distinguished from $U_{r,ss}$, the value of U_r when $C_L' = 1.4$ (C_L' = 1.4 is also an arbitrary steady state criterion).

As for C_{pA}, fig. 5.11 shows that at the low reduced velocity end, C_{pA} decreases from somewhere between 1.2 to 1.25 with increasing reduced velocity and eventually levels off at about 0.93 at higher reduced velocity.

Curves for C_{pC} versus reduced velocity show that C_{pC} is higher (less negative) at low reduced velocity. Values as high as -0.75 had been measured at A/D = 1.5, f_N = 5Hz. As reduced velocity increases, C_{pC} decreases asymptotically to about -1.55 which is the same as the value reported for stationary cylinder at high Reynolds number. (See fig. 4.8(a), note that the results presented in fig. 4.8(a) are corrected for blockage whereas the results in fig. 5.11 are not. Before blockage correction, $-C_{pC}$ in fig. 4.8(a) reaches about 1.55 at Re $\sim$ 8.5 x 10^4).

By comparing C_{pA} versus U_r at different amplitude of oscillation (A/D) with C_{pA} versus Re for stationary square cylinder (see fig.4.8(a)), it is obvious that for intermediate and high wind velocity, the oscillation does not cause much changes to the average pressure on face A. Both curves are similar in shape and all the oscillating

cylinder cases show that $C_{pA} \rightarrow 0.93$ at high reduced velocity, which is the same as the before blockage correction value of C_{pA} for a stationary cylinder at high Reynolds number. This observation is not surprising as face A is upstream of the flow separation position whereas most of the consequences of oscillating the cylinder (eg. changes in vortex shedding frequency, strength of vortices shed, longitudinal and lateral vortex spacing etc (see chapter 6)) occurs downstream to flow separation. The high values of C_{pA} at low reduced velocity is likely to be attributed to the fact that at low reduced velocity, the maximum transverse velocity ($= 2\pi f_N A$) becomes comparable in magnitude to the free stream velocity U_∞. The quantity $0.5\rho U_\infty^2$ used to non-dimensionalise the mean pressure on face A becomes appreciably smaller than $0.5\rho U_{res}^2$ where $U_{res}^2 = U_\infty^2 + 2(\pi f_N A)^2$. For example, in fig. 5.11(e) for A/D = 1.5, f_N = 5Hz and at $U_r \sim 15$, $C_{pA} \sim 1.26$. However, if the mean pressure on face A is non-dimensionalised by $0.5\rho U_{res}^2$ instead of $0.5\rho U_\infty^2$, then C_{pA} would have a value of 1.047 which is much closer to the high reduced velocity C_{pA} of about 0.93. The rise in C_{pA} at low reduced velocity is therefore not necessarily a genuine aerodynamic effect.

For C_{pC}, at high U_r the value of C_{pC} is again similar to the value of C_{pC} of a stationary cylinder at high Reynolds number. In fact, it is believed that the trend of decreasing C_{pC} with increasing reduced velocity (at least in the higher reduced velocity part) can be considered as a

Reynolds number effect rather than a reduced velocity effect as it can be explained in terms of "upstream movement of laminar to turbulent transition causes increase in flow entrainment and hence a reduction in base pressure". The same reason was used to explain the experimental observation that the base pressure of a stationary square cylinder decreases when the Reynolds number increases (see section 4.7). At low reduced velocity, however, C_{pC} reaches values that are higher (less negative) than that measured in a stationary square cylinder. This is the region where the wake due to the cylinder's transverse motion is more dominating than the Karman vortex wake. The "resultant" wake structure is therefore quite different from that at high reduced velocity (where the Karman vortex wake dominates) and as a result C_{pC} is expected to have a value that is different from the high reduced velocity quasi-steady value.

If the drag and the pressure on faces A and C are separable into mean and fluctuating components, then:

$$C_{Di} = C_D + \hat{C}_{Di}$$

$$C_{pAi} = C_{pA} + \hat{C}_{pAi}$$

and $$C_{pCi} = C_{pC} + \hat{C}_{pCi}$$

The relation between the instantaneous drag and pressure on faces A and C can be expressed as:

$$C_{Di} = C_{pAi} - C_{pCi}$$

Time averaging the above equation one gets:

$$C_D = C_{pA} - C_{pC} \tag{5.5}$$

Since C_{pA} remains fairly constant throughout most part of the reduced velocity range investigated, the trend of C_D resembles that of $-C_{pC}$ fairly closely. A "trough" can be seen in the C_D versus U_r plot in fig. 5.10(d), (e) and (f) at $U_r \sim$ 25.9, 32.9 and 44.2 respectively. From eqn. (5.1), the maximum angle of attack during a cycle of oscillation in the two above cases can be shown to be 13.65, 15.99 and 15.89 degrees respectively. It therefore appears that the minimum value in C_D approximately corresponds to the reduced velocity at which the maximum angle of incidence of the "resultant flow" is equal to the angle at which flow reattachment will commence on one side of a stationary inclined cylinder. A similar situation occurs in steady flow, when the body axis drag (C_x) of the cylinder is plotted against the angle of incidence (see fig. 4.4(d)), C_x reaches a minimum value at $\alpha \sim$ 13.5 degrees. In both cases it is thought that when α (or α_{max} in the case of oscillating cylinder) is around 13.5 degrees, there is appreciable interaction between the separated shear layer(s) and the trailing corner(s) of the cylinder and as a result

the first vortex is formed further downstream than when no interaction occurs. The increase in distance between the first vortex in the wake and the rear of the cylinder causes the pressure on face C to rise and hence C_D to drop. The above explanation seems logical because it also explains why there are no "troughs" in the lower amplitude of oscillation cases as for those cases, even at the lowest reduced velocity investigated, α_{max} is less than 13 degrees.

5.4 C_D', C_{pA}' AND C_{pC}' VERSUS U_r

Variation of C_D', C_{pA}' and C_{pC}' with reduced velocity are shown in fig. 5.12 and fig. 5.13 respectively.

From fig. 5.12, it is seen that C_D' has rather high value (eg. about 2.61 at U_r = 12.8, f_N = 4Hz, A/D = 2 in fig. 5.12(f)) at low reduced velocity. As reduced velocity increases, C_D' reduces very rapidly to a minimum value. Beyond the reduced velocity at which C_D' is a minimum, C_D' increases very slightly (in some A/D cases this very slight increase in C_D' is not detectable) with increasing reduced velocity and then levels off at a value of approximately 0.29 at high reduced velocity. This general trend is not affected by the amplitude of oscillation A/D.

For C_{pA}', it also starts off from a relatively high value (eg. 0.405 at U_r = 15, f_N = 5Hz, A/D = 1.5 in fig. 5.13(e)) and reduces rapidly with increasing reduced velocity. The rate of reduction of C_{pA}' with U_r decreases as reduced velocity increases and C_{pA}' levels off at a constant

value of approximately 0.07 at high reduced velocity.

C_{pC}' again starts off at high value (eg. 0.85 at U_r = 15, f_N = 5Hz, A/D = 1.5 in fig. 5.13(e)) at low reduced velocity. Like C_D', it reduces rapidly and reaches a minimum as reduced velocity increases. As reduced velocity continue to increase, C_{pC}' recovers slightly and eventually approaches an asymptotic value of about 0.28. For the same amplitude of oscillation, C_D' and C_{pC}' attain their respective minimum values at approximately the same reduced velocity which in turn is approximately the same as the reduced velocity at which C_D (for A/D = 1 and 1.5, see previous section) reaches its minimum.

At low reduced velocity and especially at high A/D, the transverse oscillation velocity of the cylinder becomes comparable in magnitude to the free stream velocity. For example, at U_r = 15, f_N = 5Hz and A/D = 1.5, the ratio of maximum transverse velocity to free stream velocity is 0.63, the maximum angle that the flow is inclined to the cylinder is 32.14 degrees (eqn. (5.1)). ie. Within a cycle of oscillation the angle at which the "resultant flow" approaches the cylinder varies continuously within a cone of $\pm$32.14 degrees. Since C_{pA}' has a higher value when the "resultant" flow approaches face A at an acute angle rather than approaching it at an angle of 90 degrees, the continuous variation in the angle in which the flow is approaching the cylinder causes greater pressure fluctuation on face A and hence higher C_{pA}'. The above argument is

supported by the fact that for a stationary inclined cylinder (see fig. 4.3(a)), C_{pA}' has a value of about 0.02 at α = 0 degree but it increases to about 0.05 at α = 32 degrees. Quantitative agreement between C_{pA}' for stationary inclined cylinder and for oscillating cylinder is of course not expected as the quasi-steady theory is known to be invalid at low reduced velocity. At higher reduced velocity, the maximum value of α during a cycle of oscillation (α_{max}) is much smaller, the flow becomes quasi-steady and C_{pA}' approaches the stationary cylinder's before blockage correction value of 0.075 (see fig. 4.8(b)).

The arguments used to explain the large value of C_{pA}' at low reduced velocity can also be used to explain the large value of C_{pC}' at low reduced velocity. Again from fig. 4.3(a), C_{pC}' reaches about 0.325 at $\alpha \sim$ 32 degrees whereas at α = 0 degree C_{pC}' is only about 0.23. From fig. 4.3(a), it is also seen that C_{pC}' drops to a minimum at $\alpha \sim$ 13 degrees. The minimum in C_{pC}' at $\alpha \sim$ 13 degrees is related to flow reattachment on one of the side faces which have been covered in section 4.3. If one subsitutes α = 13 degrees, A/D = 1.5 and f_N = 5Hz into eqn. (5.1), U_r can be shown to have a value of 42.51. It is by no coincidence that in fig. 5.13(e), C_{pC}' also reaches its minimum value at $U_r \sim 42$. It therefore appears that this is again the consequence of substantial interaction between the separated shear layers and the trailing corners at $\alpha_{max} \sim 13.5$ degrees which had already been pointed out in the previous

section. This argument once again helps to explain why a minimum in C_{pC}' is not observed in the lower A/D cases because for these cases, even at the lowest reduced velocity investigated, the value of α_{max} is way below the flow reattachment value of approximately 13.5 degrees (α_{crit}). As an example, for A/D = 0.25, the lowest reduced velocity investigated is about 18 (see fig. 5.13(a)). From eqn. (5.1), α_{max} has a value of only 5 degrees.

The relation between C_D', C_{pA}' and C_{pC}' has been expressed in eqn. (4.4) as:

$$C_D'^2 = C_{pA}'^2 + C_{pC}'^2 - 2 \frac{\sum_{i=1}^{N} \hat{C}_{pAi} \hat{C}_{pCi}}{N} \qquad (4.4)$$

From eqn. (4.4) one therefore expects the trend of C_D' to be approximately equivalent to a "superposition" of C_{pA}' and C_{pC}'. This can be shown to be the case by comparing the corresponding (ie. same A/D) plots in fig. 5.12 and fig. 5.13.

5.5 SPECTRA OF LIFT FORCE VERSUS REDUCED VELOCITY

Fig. 5.14 displays a series of lift spectra at different reduced velocities at an oscillation amplitude of 0.675 (for fig. 5.14(d), A/D = 1). Unless otherwise stated, the forcing frequency f_N in all the spectra shown can be assumed to be about 5Hz.

In fig. 5.14(a), at $U_r \sim 8.05$, the lowest reduced

velocity investigated, $C_L'(f_N)$ is seen to be the dominating component of C_L'. The ratio $C_L'(f_N)/C_L'$ has a value of about 0.995. Some contribution to C_L' is also seen to come from $C_L'(2f_N)$, $C_L'(3f_N)$ and $C_L'(5f_N)$ but the power spectral density (from now on abbreviated as PSD) at $f = 2f_N$, $3f_N$ and higher harmonics are at least two order of magnitude smaller than $PSD(f_N)$. The vortex shedding frequency locks on to the forcing frequency up to a reduced velocity of about 10.24.

In fig. 5.14(b), $U_r = 11.25$, f_s has a value of 8.01 Hz which is between f_N and $2f_N$. At this reduced velocity $C_L'(f_N)$ is still the dominating component of C_L' and $C_L'(f_N)/C_L' = 0.975$.

At $U_r = 12.98$, the peak at $2f_N$ seems to have "merged" with the peak at f_s and instead of two, one now sees one broader peak at $f \sim 2f_N$ (see fig. 5.14(c)). At this reduced velocity $C_L'(f_N)$ is still the dominating component of C_L' and $C_L'(f_N)/C_L' = 0.978$. Peaks at $3f_N$ and $5f_N$ are also fairly distinct although they are still two order of magnitude smaller when compared with $PSD(f_N)$.

At $U_r = 14.87$ the peak at f_s begins to "break away" from the peak at $2f_N$.

In fig. 5.14(d), $U_r = 16.89$, a relatively broad peak which is thought to represent f_s is seen situated between peaks at $2f_N$ and $3f_N$. $C_L'(f_N)$ continues to be the dominating component of C_L'.

In fig. 5.14(e), $U_r = 19.54$. At this reduced velocity the shedding frequency seems to have locked on to

the third harmonic ($3f_N$) of the body frequency. The PSD's at f_N and $3f_N$ are comparable in magnitude. Both $C_L'(f_N)$ and $C_L'(3f_N)$ are now dominating components of C_L'. For this case $C_L'(f_N)/C_L' = 0.697$ and $C_L'(3f_N)/C_L' = 0.613$.

f_s locks on to $3f_N$ up to a reduced velocity of about 22.5. At $U_r = 23.57$, the spectrum shown in fig. 5.14(f) shows that f_s has separated from $3f_N$.

At $U_r = 25.45$, fig. 5.14(g), the peak at f_s can now be easily distinguished from the peak at $3f_N$ which is weaker. The two dominating components of C_L' are $C_L'(f_N)$ and $C_L'(f_s)$. In fact, $C_L'(f_N)/C_L' = 0.447$, $C_L'(3f_N)/C_L' = 0.286$ and $C_L'(f_s)/C_L' = 0.645$. As free stream velocity (and hence reduced velocity because forcing frequency is kept constant at 5Hz) continue to increase, f_s increases accordingly and the ratio $C_L'(f_s)/C_L'(f_N)$ also increases (ie. $C_L'(f_s)$ has slowly taken over $C_L'(f_N)$'s role to become the dominating component of C_L').

At $U_r = 35.42$ in fig. 5.14(h), $C_L'(f_N)$ is almost one order of magnitude smaller than $C_L'(f_s)$. At this reduced velocity $C_L'(f_N)/C_L' = 0.193$ whereas $C_L'(f_s)/C_L' = 0.899$. From this stage onwards further increase in reduced velocity has little effect on the characteristics of the lift spectrum except that the peak at f_s moves further and further away from the peak at f_N.

At $U_r = 72.68$ and 110.68 ($f_N = 4$Hz for the latter case), the spectra in fig. 5.14(i) and (j) represent the typical lift force spectrum for quasi-steady flow. Peaks at

f_N and f_s are well separated, most dominating component of C_L' is the one at the shedding frequency (ie. $C_L'(f_s)$). $C_L'(f_N)$ is the only other important component but $PSD(f_N)/PSD(f_s) = O(0.1)$ or smaller.

Comparing the observation made above with Bearman et al's (1984(a)) results reveals good agreement in the following area:

(1) Excluding $C_L'(f_s)$, $C_L'(f_N)$ is the dominating component of C_L' throughout the range of reduced velocity investigated.

(2) $C_L'(2f_N)$, $C_L'(4f_N)$ and higher even order harmonics are negligible throughout the range of reduced velocity investigated.

(3) Magnitude of $C_L'(3f_N)$ becomes appreciable when $U_r \sim 21$, ie. when $f_s \sim 3f_N$.

(4) At low reduced velocity f_s locks on to f_N. At high reduced velocity (quasi-steady region) $C_L'(f_s) >> C_L'(f_N)$.

5.6 SPECTRA OF DRAG FORCE VERSUS REDUCED VELOCITY

Spectra of fluctuating drag force versus reduced velocity are shown in fig. 5.15. Unless otherwise stated, the amplitude of oscillation (A/D) can be assumed to be 1.5. Forcing frequency for fig. 5.15(a), (b) and (c) is about 4.88Hz while for fig. 5.15(d), (e) and (f) the forcing frequency is about 3Hz.

In fig. 5.15(a), at a low reduced velocity of about 20.56 (f_N = 4.88Hz), vortex shedding frequency (assuming

Strouhal number = 0.13) is estimated to be about 13.03Hz. However, no peak is observed in the drag spectrum at f_s or $2f_s$. Instead, all the peaks are at the forcing frequency and its higher harmonics (both odd and even). The drag spectrum therefore shows that at low reduced velocity, the dominating components of the drag force are at the forcing frequency and its higher harmonics and not at the shedding frequency or twice the shedding frequency.

In fig. 5.15(b), U_r = 26.11, f_s (assuming S $\sim$ 0.13) $\sim$ 16.58. In addition to peaks at the forcing frequency and its harmonics, three other more "broad band" like peaks are also observed. Interestingly, these three peaks are at frequencies approximately equal to f_s-f_N, f_s+f_N and $2f_s$ respectively.

As free stream velocity (and hence reduced velocity) increases, spectra similar to fig. 5.15(b) are observed. However, at higher reduced velocity, the magnitude of the PSD at f_s-f_N, f_s+f_N and $2f_s$ increase and become comparable with the PSD's at the forcing frequency and its higher harmonics.

At a reduced velocity of about 30.9, (fig. 5.15(c)), ratio of $C_D'(f_N)$, $C_D'(2f_N)$, $C_D'(3f_N)$, $C_D'(f_s-f_N)$, $C_D'(f_s+f_N)$ and $C_D'(2f_s)$ to C_D' are estimated to be 0.499, 0.487, 0.243, 0.18, 0.235 and 0.091 respectively.

Fig. 5.15(d) ($U_r \sim 55.54$, $f_N \sim 2.84$Hz) is still similar to fig. 5.15(b) and (c) but now the values of the six ratio mentioned above are 0.186, 0.277, 0.164, 0.253,

0.25 and 0.211 respectively.

A "typical" spectrum at even higher reduced velocity is similar to those shown in fig. 5.15(e) ($U_r \sim 72.26$, $f_N \sim 3$Hz) and fig. 5.15(f) ($U_r \sim 159.07$, $f_N \sim 3$Hz). The peaks at the forcing frequency and its higher harmonics seem to have totally disappeared. The only peaks remaining are at $f_s - f_N$, $f_s + f_N$ and $2f_s$ respectively.

By analysing all the spectra in fig. 5.15, it is noted that some observations can be explained while others cannot. For example, the peak at $2f_s$ is explainable because each shear layer sheds vortices at a frequency of f_s. The pressure at the base (face C) is affected by the pressure fluctuation induced by both the top and bottom shear layers and hence its spectrum is expected to have a dominating component at $2f_s$. The above argument is supported by Obasaju's (1977) findings. He observed (see section 1.1.1.6) a peak at $2f_s$ in the spectrum of the pressure acting on the centre of the rear face (face C) of a stationary square cylinder. Bishop & Hassan (1964(b)) also observed that the drag force acting on a transversely oscillating circular cylinder has dominating components at two times the forcing frequency and two times the shedding frequency. The peaks at $f_s - f_N$ and $f_s + f_N$ are obviously due to some sort of interaction between the shedding frequency and the forcing frequency. However, the detail of this interaction in unknown.

A common feature of the lift and drag spectra is

that f_N and its higher harmonics are the dominating components at low reduced velocity whereas the shedding frequency plays the dominating role at high reduced velocity. On the other hand, the even order harmonics of f_N were never important in the lift spectra whereas they are of appreciable importance in the drag spectra at low reduced velocity.

5.7 STROUHAL NUMBER

The shedding frequency for a particular A/D, f_N and U_r combination can be estimated from the spectrum of the lift signal, one of the four outputs of Cophase. Experimentally measured values of f_s/f_N are plotted against U_r in fig. 5.16(a) and (b) (fig. 5.16(b) is identical to fig. 5.16(a) but with U_r limited to $\leq$ 50). From fig. 5.16(a) and (b) it is seen that most of the experimental data points fall fairly well onto a straight line and lock on of the shedding frequency to the body frequency and to three times the body frequency at U_r ranges of 7-10 and 19-22 respectively can also be seen. By least square fitting a straight line through the experimental data in fig. 5.16(a), the average Strouhal number, which is equal to the gradient of the least square fit line, is found to be about 0.126. This is in good agreement with the stationary cylinder's Strouhal number (before blockage correction) at $Re \sim 4.5 \times 10^4$ (see section 4.9 and fig. 4.10). Bearman et al (1984(a)) also have similar findings although their

average Strouhal number for transversely oscillating and stationary square cylinder are slightly higher at 0.132 and 0.133 respectively.

5.8 CONCLUSIONS

Fluctuating lift (C_L') measured at different amplitude of oscillation (A/D) show similar variation with reduced velocity (U_r). Following the suggestion of Bearman et al (1984(a)) the flow is divided into three region. In the multiple harmonic (low U_r) region it was found that C_L' can have values that are much larger than the C_L' acting on a stationary cylinder at similar Reynolds number. This is related to lift amplification in the vortex lock-in region. In the quasi-steady (high U_r) region C_L' is similar to its stationary cylinder C_L'. In the intermediate transition (medium U_r) region a minimum in C_L' exists. This minimum value of C_L' was found to be only about half that of a stationary cylinder's C_L' at a similar Reynolds number. The cause(s) of this minimum in C_L' is not clear at the present moment. The trend of the C_L' curve at the higher reduced velocities was found to be predictable by the quasi-steady theory.

The trend of ϕ versus U_r (negative ϕ at low reduced velocity, positive ϕ at higher reduced velocity with ϕ approaching 90 degrees at very high reduced velocities) reported in the present research, agrees fairly well with the findings of other researchers that are

reported in the literature. In the intermediate ϕ range ($35 \leq \phi \leq 75$ degrees approximately), there exists a discontinuity in $\partial\phi / \partial U_r$ in that $\partial\phi / \partial U_r$ suddenly changes from a higher to a lower value at a certain reduced velocity designated as $U_{r,k}$. At lower A/D a local maximum is also observed in the ϕ curve at $U_r \sim U_{r,k}$. The value of $U_{r,k}$ is found to be very similar to $U_{r,min}$, the value of U_r at which C_L' is a minimum. It is therefore suggested that the changes in C_L' and ϕ are both due to the interaction of the two vortex wakes (see page 111) which changes the way in which vortices are shed and convected downstream (ie. changes in flow structure). This idea will be examined in greater detail in the next chapter. Due to the differences in aspect ratio, blockage ratio and methods used to measure lift, the present ϕ results at A/D = 0.1 does not agree well with those reported by Nakamura & Mizota (1975) and Otsuki et al (1974). However, the ϕ versus U_r results reported in the present investigation agree well with those reported by Bearman et al (1984(a)). Although at low reduced velocity C_L' can have values that are much higher than their corresponding values in steady flow, this takes place in the U_r range where $\phi < 0$ where flow-induced vibration will not take place. In the $\phi > 0$ range where flow-induced vibration becomes possible, the maximum C_L' encountered is about the same as the steady flow C_L'. This finding therefore suggests that for an engineer who is concerned with structural integrity (assumming 2-D

flow), it is quite safe for him to base his design on a maximum C_L' of about 1.45.

Variation of C_{pA} with reduced velocity show that C_{pA} is little affected by the oscillation as face A remains upstream of flow separation. C_{pC} decreases to an asymptotic value as reduced velocity increases. This, as in steady flow, is believed to be a Reynolds number effect and is related to the upstream movement of the laminar to turbulent transition in the separated shear layer which increases entrainment of fluid from the outer region and causes a reduction in base pressure.

For dimensionless amplitude of oscillation (A/D) of 1 and 1.5, C_D, C_D' and C_{pC}' reach their minima and C_{pC} reaches its maximum value at approximately the same reduced velocity. This reduced velocity corresponds to $\alpha_{max} \sim 13.5$ degrees where stationary inclined cylinder experiments show there is substantial interaction (including the possibility of flow reattachment) between the separated shear layers and the trailing corners. It appears that the minima in C_D, C_D' and C_{pC}' and the maximum in C_{pC} are all consequences of the above mentioned interaction which causes the first vortex to form further downstream from the cylinder (ie. increase in vortex formation length l_f). At high reduced velocity the values of C_{pA}, C_{pC}, C_D, C_{pA}', C_{pC}' and C_D' are very similar to the stationary cylinder's (before blockage correction) values.

Spectral analysis on the lift force shows that near

the resonance reduced velocity ($U_r \sim U_{ro}$) the shedding frequency locks on to the forcing frequency. At intermediate reduced velocity $C_L'(3f_N)$ can be of appreciable importance. At high reduced velocity the lift force is dominated by its component at the shedding frequency ($C_L'(f_s)$) and throughout the reduced velocity range investigated the even harmonics ($C_L'(2f_N)$ and $C_L'(4f_N)$ etc) are of negligible importance.

For drag force spectra, at low reduced velocity the dominating components are at the forcing frequency and its higher harmonics (both odd and even). At high reduced velocity, the dominating components are at twice the shedding and at the sum and the difference between the shedding and forcing frequencies. At intermediate reduced velocity, all the above mentioned components are of appreciable importance.

By least square fitting a straight line through experimentally measured ratios of shedding to forcing frequencies versus reduced velocity, the average Strouhal number was found to be 0.126.

CHAPTER SIX

FLOW VISUALIZATION ANALYSIS

The main reason for carrying out the flow visualization is to acquire more information on the variation in the flow structure at different reduced velocities. It is hoped that through visualizing the flow, certain experimental findings like the variation of fluctuating lift (C_L') with reduced velocity can be explained.

Choosing the correct tunnel wind speed to carry out the flow visualization needs some "trial and error". If the wind speed is too low, buoyancy effect on the white smoke generated will become too severe. On the other hand, if the wind speed is too high, it will over-cool the smoke wire and as a result insufficient smoke will be generated. A possible solution to the "wire over-cooled by high wind speed" problem is of course to apply higher voltage across the smoke wire. The possibility of doing so had been considered but later rejected because higher voltage has two associated drawback. Firstly, higher voltage across the smoke wire causes the part of the wire that is outside the wind tunnel to become red hot, much weaker in strength and breaks frequently. Secondly, as the smoke wire is in tension, the extra heat generated by the higher voltage causes the wire

to elongate and its diameter reduces, thus increasing the size of the gap between the smoke wire and the Y-shape glass tube. This results in an increase in the oil flow rate and the net result is a smoke pattern which is not as good as that obtained by using a lower voltage. The wind speed finally used in all the flow visualization work reported in this chapter was about 2.72m/s. It is thought to be a reasonable compromise between the conflicting criteria of no buoyancy effect (higher wind speed is desired) and thick smoke (lower wind speed is preferred). At this wind speed the cylinder vortex shedding frequency is estimated to be about 7Hz (assuming S = 0.13). A fastest possible film speed of 64 f.p.s. was used throughout the flow visualization. This film speed enabled each shedding cycle to be captured on about 9 frames of the film. Large number of frames per shedding cycle is desirable for detailed analysis of the shedding process and vortex movement.

In addition to cine-film, some still photographs were also taken. While most of the flow analysis were carried out by watching the cine-film in slow motion (2f.p.s. and sometimes frame by frame), the still photographs complement the former and are also more suitable for presentation in this thesis.

Most of the flow visualizations reported here were conducted at an oscillation amplitude of A/D = 0.675 because a large number of experimental measurements were made at this amplitude. However, some flow visualization were also

conducted at A/D = 0.25 and 1 in order to study the effect of amplitude. As only one free stream wind velocity was used, different reduced velocities were obtained by oscillating the cylinder at different frequencies. In the present research f_N varied between 7 to 0.6 Hz, the corresponding range of reduced velocity is therefore between 7 to 90.

Flow visualization revealed that at an amplitude of A/D = 0.675, there are at least four different types of flow structure. They are discussed separately as follows:

6.1 LOCK-ON TYPE A

At a forcing frequency of f_N = 7Hz, the reduced velocity is 7.65. At this reduced velocity vortex shedding locks on to the body frequency and hence one vortex per cycle is shed from each shear layer. The vortex shedding process is shown in fig. 6.1(b). Starting from the top dead centre (from now on abbreviated as TDC), the cylinder begins to move downwards. A vortex is formed and continues to grow near the top face B (see fig. 6.1(a) for definition of faces A, B, C and D). The vortex grows to its maximum size when the cylinder reaches approximately the bottom dead centre (from now on abbreviated as BDC). When the cylinder reverses its direction and moves upwards again, the cylinder's upward motion, together with the free stream; causes the aforementioned vortex to go past the cylinder. When the cylinder reaches approximately the TDC again, flow

reattachment occurs on face B for a short duration of time and the vortex is cut off from the feeding shear layer while the latter was lying very close to the top face. As the cylinder begins the second cycle and moves down again, a second vortex begins to grow on the top face B and the process repeats itself. Identical shedding occurs on the bottom face D but it is about 180 degrees out of phase with the shedding that takes place near face B.

A "typical" wake in the present case therefore looks like the one shown in fig. 6.1(c). The vortices remain on the same side of the cylinder as their feeding shear layer. Two separate rows of vortices are therefore seen. Vortices in the same row are relatively closely packed and appears to be fairly weak. Vortices in one row initially do not interact with vortices with opposite vorticity fed by the opposite shear layer until approximately three longitudinal spacing downstream from face C. Here the vortex that originated from shear layer B merges with its counterpart that originated from the opposite shear layer D. As a result no distinct vortex can be seen at three longitudinal spacing or more downstream from the rear face (face C) of the cylinder. By projecting (and hence enlarging) reasonably "representative" frames of the flow visualization film on a screen, the distances between two consecutive vortices in the same row (longitudinal spacing) and between the two rows of vortices (lateral spacing) are estimated to be about 2.74D and 2.39D respectively. This is

equivalent to a spacing ratio (ratio of lateral to longitudinal vortex spacing) of about 0.87. On the other hand, Von Karman suggested that the spacing ratio should be 0.281 for a stationary bluff body if the vortex streets are stable to first order disturbances (see Bearman (1967)). The Strouhal number was found to be about 0.12 at the present reduced veloctiy of 7.65. Assuming an infinite street of point vortices it can be shown that the dimensionless strength of a vortex in the wake $\Gamma/U_\infty D$ can be expressed as a function of longitudinal spacing (a/D), spacing ratio (b/a) and Strouhal number (S).

$$\frac{\Gamma}{U_\infty D} = \frac{2a}{D}\left(1 - S\cdot\frac{a}{D}\right) \Big/ \tanh\left(\frac{\pi b}{a}\right) \qquad (6.1)$$

By substituting the above mentioned value of Strouhal number and the estimated values of a/D, b/a into eqn. (6.1), the dimensionless vortex strength $\Gamma/U_\infty D$ is estimated to be about 3.71.

The present method of estimating the aforementioned distances and vortex strength are of course by no means quantitatively accurate. However, by comparing their respective magnitudes applicable to different flow structures, it is hoped that one will at least gain some qualitative information about the distances among vortices and strength of vortices shed in different types of flow structure discussed in this chapter.

In the present case vortices shed from both shear

layers are seen to be relatively far away from the rear face C of the oscillating cylinder. It therefore appears that the base pressure in the present case is likely to be relatively high and consequently the average drag coefficient low.

During one cycle of oscillation, the distance between the separated shear layer and the corresponding side face varies considerably. The shear layer remains fairly close to the side face when the cylinder is moving towards it and becomes relatively far away from the side face when the cylinder is moving away from it. This observed movement of the shear layer in relation to the cylinder side face, together with the observation that the shedding process on the two shear layers are about 180 degrees out of phase are believed to be some of the contributing factors to the high C_L' (= 2.76, see fig. 5.1(d)) measured at the present reduced velocity. Simultaneous lift/displacement photograph taken from a storage CRO is shown in fig. 5.5(a). Some flow visualization photographs are shown in fig. 6.5.

6.2 LOCK-ON TYPE B

At a forcing frequency of f_N = 4Hz, the reduced velocity is 13.39. At this reduced velocity the vortex shedding still locks on to the body frequency. The vortex shedding process is shown in fig. 6.2(a). The vortex growing process is similar to lock-on type A reported in section 6.1 in that a vortex grows on the side which the cylinder is moving away from. For example, during the first half of an

oscillating cycle the cylinder moves downwards from the TDC and a vortex is growing on the top face (face B). However, because of the lower (compare with type A) forcing frequency (and hence shedding frequency, because it locks on to the forcing frequency), each vortex has a longer time to grow. This results in:

(1) Each vortex contains more vorticity and is hence stronger than the vortices in type A.

(2) At the end of first half of a cycle, instead of sitting on the side face, the fully grown vortex is sited near the trailing corner of the cylinder (eg. corner BC for the vortex that is fed by shear layer B).

During the second half of the cycle, the cylinder reverses its direction. Recalling that the fully grown vortex is located near the trailing corner BC at the end of the first half cycle, the reverse upwards motion of the cylinder, and possibly together with the opposite vorticity from the opposite shear layer D, "draw" the aforementioned vortex across the wake and finally cause it to end up on the opposite side of the cylinder. When this takes place, the vortex formed on side B also seems to cut the grown vortex (previous cycle) fed by shear layer D off from its feeding shear layer. Flow reattachment on side B is also observed to take place momentarily near corner BC when the cylinder is near the TDC. The vortex shedding process therefore appears to be in agreement with the vortex shedding mechanism proposed by Gerrard (1966). Using his exact words, in his

1966 paper Gerrard suggested that "The growing vortex continues to be fed by circulation from the shear layer until the vortex becomes strong enough to draw the other shear layer across the wake. The approach of oppositely-signed vorticity in sufficient concentration cuts off further supply of circulation to the vortex, which then ceases to increase in strength. We may speak of the vortex as being shed from the body at this stage". Gerrard's vortex shedding mechanism does not seem to be applicable to the shedding process reported in lock-on type A. On the other hand, as in the type A flow, the vortex shedding from the two shear layers in the present case appears to be nearly 180 degrees out of phase to each other.

As a result of the longer (compared with type A) time available for each vortex to grow before being shed, the vortex shed from the previous cycle has a longer time to travel downstream, this causes the longitudinal spacing to be larger than in type A. In the present case the longitudinal spacing is estimated to be 6.84D. Each vortex is also stronger and as a result substantial entrainment of the outer initially irrotational fluid into the wake can clearly be seen in the flow visualization. Each vortex persists for a much longer distance downstream from the cylinder before diffusion and annihilation of vorticity really affect them. The lateral vortex spacing is estimated to be about 1.16D and hence the spacing ratio is about 0.17. Strouhal number at the present reduced velocity was found to

be about 0.0715. Dimensionless strength of vortex (eqn. (6.1)) is estimated to be about 14.36. This high value of $\Gamma/U_\infty D$ supports the deduction of flow visualization observation (see point (1) at the beginning of the present section). It is also much higher than the corresponding quantity of the two flow structures which will be reported in the next two sections (triple lock-on and quasi-steady). A "typical" wake pattern is shown in fig. 6.2(b), it resembles the classic Von Karman vortex street.

As mentioned earlier, in the present case the strong vortices (low pressure region) are drawn across the wake, swept past rear face C of the cylinder and finally ends up on the side opposite to its feeding shear layer. One would expect this motion of the vortex to cause a low average pressure on face C and hence a high average drag. However, this is not supported by experimental measurement. At $U_r \sim 14$ C_{pC} is found to be fairly high (estimated by extrapolation to be around -0.7, at high reduced velocity $C_{pC} \sim -1.55$, see fig. 5.11(c)) and C_D fairly low (estimated by extrapolation to be around 1.95, at high reduced velocity $C_D \sim 2.48$, see fig. 5.10(c)). The cause of this discrepency is presently unknown. On the other hand, the variation in distance between a shear layer and the corresponding cylinder side face within one cycle of oscillation is similar to that reported in section 6.1. As a result the C_L' measured at this reduced velocity (= 1.36 see fig. 5.1(d)) is still fairly high. Storage CRO photographs of

simultaneous lift force and displacement signals at the present reduced velocity of 13.39 is shown in fig. 5.5(c). Some flow visualization photographs are shown in fig. 6.6.

6.3 TRIPLE LOCK-ON

For f_N = 2.5Hz, U_r = 21.42. At this reduced velocity C_L' has the value of 0.83. ie. It corresponds to the trough of the C_L' versus U_r curve shown in fig. 5.1(e). At this reduced velocity flow visualization revealed that three vortices are shed per cycle by each shear layer. The vortex shedding process is shown in fig. 6.3(a). In the first half of an oscillating cycle, the cylinder moves from the TDC to the BDC. Two consecutive vortices are shed by the top shear layer B. In the second half of the oscillating cycle, the cylinder reverses its direction and moves upwards. A third and much weaker looking vortex is shed by the top shear layer. At the same time the first of the two vortices shed by the top shear layer during the first half of the cycle mixes with a vortex fed by the bottom shear layer D (the third vortex shed by shear layer D during the previous cycle). Near the TDC shear layer B lies very close to face B and momentarily flow reattachment may occur near trailing corner BC. The above process then repeats itself. Vortex shedding process of the two shear layers are about 180 degrees out of phase to each other.

After close examination of the flow visualization film the following points are noted:

(1) The observation that three vortices are shed per cycle per shear layer means that the feeding shear layer has relatively little time (when compared with lock-on type B) to feed each vortex. As a result each vortex shed appears to be much weaker than vortices shed in lock-on type B or vortices shed by a stationary square cylinder at a similar free stream wind speed. Diffusion and cancellaion of vorticity therefore take place a short distance downstream from the cylinder. For example, at a short distance of 1 to 1.5 longitudinal spacing downstream from face C, the vortices become so diffused that sometimes they can hardly be recognised.

(2) Due to the same reasoning as in (1), the longitudinal spacing is relatively short (around 3.49D).

(3) The vortices shed no longer get drawn across the wake as in lock-on type B. They stayed at the same side of the cylinder as in lock-on type A. The lateral spacing is estimated to be about 1.73D. The dimensionless vortex shedding frequency (Strouhal number) was measured to be about 0.139 in the present case. Substituting this value of Strouhal number and the values of a/D and b/a into eqn. (6.1), the dimensionless strength of vortex shed is estimated to be about 3.93.

A "typical" wake is shown in fig. 6.3(b) with an estimated spacing ratio of about 0.50. It must be emphasized that the present wake pattern is less "repeatable" in the sense that the wake pattern at any instance may not be

identical to the wake pattern exactly one (or any integer number N) cycle(s) of vortex shedding before or after it. Sometimes the weak third vortex shed in the shedding cycle cannot be identified in the flow visualization at all. The wavy lines emphasize that the wake is very diffused. Since the core of a vortex represents a low pressure region, the alternating presence and absence (when the vortex formed is shed and get carried downstream by the free stream) of vortices near the side faces of the oscillating square cylinder causes the pressure to fluctuate. Vortex shedding is thought to be the cause of fluctuation of pressure acting on the side faces of the cylinder. In the present case since the strength of each vortex shed is much weaker than in lock-on type B or in the case of a stationary cylinder, the resulting pressure fluctuation is also much lower in amplitude. This is thought to be one of the causes of the low C_L' (about 0.83) measured in the present case. Storage CRO photograph of simultaneous lift force and cylinder displacement signals is shown in fig. 5.5(e). The photograph confirms that there are three vortices shed per cycle of cylinder movement. Some flow visualization photographs of the present case are shown in fig. 6.7.

6.4 QUASI-STEADY

The present category includes flow visualization conducted at forcing frequencies of 1Hz and 0.55Hz. The corresponding reduced velocities are therefore 53.56 and 97.38 respectively.

In this quasi-steady category the vortex shedding frequency is no longer related to the forcing frequency but is such that the dimensionless shedding frequency (Strouhal number) is approximately a constant. The oscillation of the cylinder is so slow that the wake of the cylinder looks like that of a stationary cylinder. It is therefore not surprising to find that the C_L' measured are approximately 1.4 and 1.46 at U_r = 53.56 and 97.38 respectively. These values of C_L' are about the same as the stationary cylinder's r.m.s. lift.

A "typical" wake is shown in fig. 6.4. For the case of $U_r \sim 97.38$, longitudinal and lateral vortex spacing are estimated to be 6.36D and 0.87D respectively. The approximate spacing ratio is 0.14. Strouhal number is estimated to be about 0.13 and hence the dimensionless strength of vortex shed is estimated (eqn. (6.1)) to be about 5.47. This value is smaller than the corresponding quantity in lock-on type B (14.36) but is larger than that in triple lock-on (3.93). This probably explains the differences in C_L' measured in lock-on type B (1.36), triple lock-on (0.83) and in the present case (1.4 and 1.46). Vortex shedding from the two shear layers alternate and are

nearly 180 degrees out of phase to each other. The vortex wake, as expected, now resembles the classic Von Karman vortex street. Storage CRO photograph of simultaneous lift force and displacement signals is shown in fig. 5.5(k). Flow visualization photograph for $U_r \sim 85$ is shown in fig. 6.8.

6.5 INTERMEDIATE STAGES

The two remaining flow visualizations were conducted at forcing frequencies of 2Hz and 1.5Hz. The corresponding reduced velocities are 26.78 and 35.71 respectively. The flow fields at these two reduced velocities appear to be a combination of "triple lock-on" and "quasi-steady". In the former ($U_r = 26.78$) the flow structure resembles "triple lock-on" more, while in the latter ($U_r = 35.71$) the flow structure looks more like "quasi-steady". Flow visualization photographs of these two cases are shown in fig. 6.9. Photographs of simultaneous lift/displacement signals taken from a storage CRO are shown in fig. 5.5(g) and (i) for $U_r \sim 27.64$ and 35.79 respectively.

6.6 STATIONARY CYLINDER

Some flow visualization was also carried out with the cylinder stationary. When the cylinder is not oscillating the following points are noted:

(1) The way vortices are shed seems to be in agreement with the shedding mechanism proposed by Gerrard (1966).

(2) The wake resembles Von Karman vortex wake.

The longitudinal spacing, lateral spacing and spacing ratio are estimated to have values of 6.38D, 0.86D and 0.13 respectively. From fig. 4.10 the Strouhal number (before blockage correction) at the present Reynolds number of about 9.16×10^3 has a value of about 0.128. By substituting the above quantities into eqn. (6.1) the dimensionless strength of vortex shed has a value of about 6.13. A "typical" wake looks like the one shown in fig. 6.4 (for quasi steady) and a flow visualization photograph for stationary cyclinder is shown in fig. 6.10 Storage CRO photograph of lift signal is shown in fig. 5.5(1).

6.7 EFFECT OF AMPLITUDE OF OSCILLATION

From fig. 5.1 it can be seen that the effect of changing the amplitude of oscillation (A/D) is approximately equivalent to displacing the C_L' curve along the U_r axis without any significant alteration to its shape. A similar conclusion is arrived at in the flow visualization work. Film shot at A/D = 1 reveals essentially the same four structures introduced in sections 6.1 to 6.4 but they take place at different reduced velocities.

6.8 CONCLUSION

Within the range of reduced velocity investigated, there appears to be at least four different flow structures. In terms of the way that vortices are shed, "lock-on type B" and "quasi-steady" seem to agree with the vortex shedding mechanism proposed by Gerrard (1966). In "lock-on type A" flow reattachment on the side face appears to be responsible for "cutting" a grown vortex off from the feeding shear layer. How vortices are shed in "triple lock-on" is uncertain, from flow visualization there seems to be instances where two consecutive vortices are shed by the same shear layer.

Although the method of estimating longitudinal and lateral vortex spacing (and hence spacing ratio) used in the present research is very primitive, it is sufficient to show that the spacing ratio in unsteady flow can vary considerably and are different from the value of 0.281 proposed by Von Karman.

Throughout the whole reduced velocity range investigated, the shedding of vortices by the two shear layers always appears to be about 180 degrees out of phase. Thus it seems that the phase relation between the two shedding processes is not responsible for altering the magnitude of C_L'. On the other hand, the amount of time available for each vortex to be shed appears to affect the vortex's strength which in turn affects the magnitude of the r.m.s. lift. This argument can be used to explain the

differences in magnitude of C_L' measured in lock-on type B, triple lock-on and quasi-steady and is supported by the magnitude of the strength of vortex shed ($\Gamma/U_\infty D$) estimated from eqn. (6.1). However, if this argument is valid and is the only factor that decides the magnitude of r.m.s. lift, then one would expect the value of r.m.s. lift in "lock-on type B" to be higher than that in "lock-on type A" because f_s locks on to f_N in both cases but f_N is lower in type B, which means that the shedding period $T(= 1/f_s)$ is longer and hence strength of vortex shed larger in type B. The above deduction is also supported by the magnitude of $\Gamma/U_\infty D$ estimated by eqn. (6.1). ($\Gamma/U_\infty D$ has estimated values of 3.71 and 14.36 in lock-on type A and B respectively). Furthermore, flow visualization also reveals that the vortices shed in lock-on type B are much stronger than those shed in lock-on type A and is seen to cause more entrainment of fluid from the outer region. Experimental measurements, on the other hand, revealed the contrary. C_L' was found to be about 2.76 for lock-on type A and only about 1.36 for lock-on type B. It is therefore believed that the magnitude of r.m.s. lift is affected by many factors. Strength of vortices shed is only one of them. Other factors are not readily identified at this stage. The magnitudes of a/D, b/D, b/a and $\Gamma/U_\infty D$ estimated in all the flow visualization cases are summarised in table 6.1. As pointed out earlier, with the exception of lock-on type A, the estimated strength of shed vortices show the same trend (versus reduced

velocity) as the fluctuating lift.

Different amplitudes of oscillation do not alter the four flow structures reported but merely cause them to take place at different reduced velocity.

CHAPTER SEVEN

COMPARISON OF EXPERIMENTAL RESULTS WITH SEMI-THEORETICAL PREDICTIONS

In this chapter various relevant theories like Parkinson's quasi-steady galloping theory and the "oscillating thin aerofoil theory" are examined. Their usefulness in engineering is assessed by comparing their prediction with experimental measurements. However, the prediction by both the above mentioned theories can only be regarded as semi-theoretical as the experimentally measured C_{Fy} $(=-(C_{pD} - C_{pB}))$ versus α (see section 4.4) and $\partial C_L/\partial\alpha$ (α = 0 degree) are used as empirical data in the quasi-steady theory and the thin aerofoil theory respectively.

7.1 EXPERIMENTAL AND SEMI-THEORETICAL C_{Fy}' AT FORCING FREQUENCY AND HIGHER HARMONICS

When a square cylinder oscillates sinusoidally in a direction transverse to the free stream, the effective "angle of attack" that the free stream is in relation to the cylinder varies between $\pm\ \alpha_{max}$ where α_{max} is equal to $\tan^{-1}(\dot{y}/U_\infty)$ (eqn 5.1). The normal force that acts on the cylinder, assuming the validity of the quasi-steady theory;

therefore varies continuously between $\pm C_{Fy}(\alpha = \alpha_{max})$. From a knowledge of stationary cylinder's C_{Fy} versus α (see fig. 4.4(a) and 4.4(c)) it is therefore possible to calculate C_{Fy} versus t/T in one cycle of oscillation where t/T varies from 0 to 1. With C_{Fy} versus t/T known, C_{Fy}' can then be calculated and by using Fourier analysis, the sine and cosine coefficients of C_{Fy} at body frequency and higher harmonics (ie. $C_{Fy}(f_N)$, $C_{Fy}(2f_N)$, $C_{Fy}(3f_N)$ etc) and their r.m.s. values can also be calculated. A computer programme called "QUASI PREDICT" was written in Commodore PET BASIC in order to perform the above mentioned calculation. The flow chart of "QUASI PREDICT" is shown in fig. 7.1. Results of calculation of "QUASI PREDICT", together with relevant experimental measurements (where available), are plotted in fig. 7.2 to fig. 7.5. For the rest of the present chapter the quasi-steady theory predicted r.m.s. lift and its components will be referred to as C_{Fy}' and $C_{Fy}'(f_N)$ etc whereas the experimentally measured r.m.s. lift and its components that the theory is predicting will be denoted by C_L' and $C_L'(f_N)$ etc.

In fig. 7.2, C_{Fy}', $C_{Fy}'(f_N)$ and the odd harmonics (up to $C_{Fy}'(7f_N)$) are plotted against Af_N/U_∞ ($Af_N/U_\infty = (A/D)/U_r = \tan \alpha_{max}/(2\pi)$, where α_{max} is the maximum value of the "resultant angle of incidence" between the free stream and the oscillating cylinder). From fig. 7.2 it is immediately obvious that $C_{Fy}'(f_N)$ is the dominant component of C_{Fy}' throughout a major part of the range of Af_N/U_∞

investigated. At the upper end of Af_N/U_∞ in fig. 7.2, $C_{Fy}'(3f_N)$ begins to rise and exceed the value of $C_{Fy}'(f_N)$. $C_{Fy}'(5f_N)$ and $C_{Fy}'(7f_N)$ remain small throughout the range of Af_N/U_∞ shown in fig. 7.2. The even harmonics ($C_{Fy}'(2f_N)$ and $C_{Fy}'(4f_N)$ etc) are not shown in fig. 7.2 as they are negligible throughout. It must be pointed out, however, that since $Af_N/U_\infty = (A/D)/U_r$, large Af_N/U_∞ means that either the value of U_r is small or A/D is large; in either case the inherent assumption of the quasi-steady theory is not satisfied and hence the theory is not applicable. The high Af_N/U_∞ quasi-steady theory prediction is therefore not expected to be accurate. By qualitatively comparing the quasi-steady theory prediction shown in fig. 7.2 and the experimental findings of the present research (see chapter 5) and Bearman et al (1984(a)), it is interesting to find that they agree in certain aspect. For example, all three find that among $C_{Fy}'(f_N)$ (or $C_L'(f_N)$) and its higher harmonics (ie. excluding $C_L'(f_s)$):

(1) $C_{Fy}'(f_N)$ (or $C_L'(f_N)$) is the dominant component.

(2) Even harmonics like $C_{Fy}'(2f_N)$ and $C_{Fy}(4f_N)$ (or $C_L'(2f_N)$ and $C_L'(4f_N)$) etc are negligible throughout.

The comparison of quasi-steady theory predicted $C_{Fy}'(f_N)$, $C_{Fy}'(3f_N)$ and $C_{Fy}'(5f_N)$ with experimentally measured $C_L'(f_N)$, $C_L'(3f_N)$ and $C_L'(5f_N)$ are plotted against $U_r/(A/D)$ for various A/D in fig. 7.3, 7.4 and 7.5 respectively. $U_r/(A/D) = (1/(Af_N/U_\infty))$ is used as a parameter here, it is not a new parameter but its use

facilitates the comparison of experimental and theoretical results as most of the experimental measurements reported in chapter five are plotted against either U_r or $U_r/(A/D)$. The experimental results are obtained by calculating the area under the lift force spectrum at the frequency of interest (ie. at f_N, $3f_N$ or $5f_N$ etc, see eqn. (3.6)). They are corrected for "noise" (inertia effect of air inside the connecting tubing) as explained in section 3.6.2.

From fig. 7.3 it is seen that the agreement between quasi-steady theory prediction and experimental measurement is generally good for $U_r/(A/D)$ from as low as about 45. For A/D = 1.5 and 2 agreement between measurement and prediction is also fairly good in the range $25 \leq U_r/(A/D) \leq 45$. For amplitude of oscillation other than 1.5 and 2 and for $U_r/(A/D)$ less than 45 the theory under-predicts the value of $C_L'(f_N)$. The theory also predicts that $C_{Fy}'(f_N)$ reaches its maximum value of about 0.381 at $U_r/(A/D) \sim 25$ and thereafter decreases with decreasing $U_r/(A/D)$. Experimental measurement, on the other hand, shows that $C_L'(f_N)$ continues to rise for $U_r/(A/D)$ decreasing below 25. Since it had already been pointed out that the quasi-steady theory prediction is not expected to work at low reduced velocity, the present findings are considered as satisfactory.

From fig. 7.4, it is seen that the quasi-steady theory can only roughly predict the trend of $C_L'(3f_N)$. Throughout the range of $U_r/(A/D)$ investigated, the theory under-predicts the value of $C_L'(3f_N)$. There is virtually no

agreement between the quasi-steady theory predicted $C_{Fy}'(5f_N)$ and experimentally measured $C_L'(5f_N)$. This is shown in fig. 7.5.

7.2 COMPARISON OF EXPERIMENTAL MEASUREMENT WITH SEMI-THEORETICAL PREDICTION

When a cylinder oscillates in either still or steadily flowing fluid or when an unsteady stream flows past a stationary cylinder, the force that acts on the cylinder can be separated into drag and inertia components. In this section, the experimental inertia coefficient which is estimated by using Sarpkaya's (1978) approach will be compared with the inertia coefficient estimated from "thin aerofoil theory" (see Bisplinghoff, Ashley & Halfman (1957)). The results obtained will also provide some idea about the relative importance of the inertia and drag components of the lift force. The thin aerofoil theory just mentioned can also be used to predict the magnitude of $C_L'(f_N)$ and ϕ, these predictions will be compared with experimental data in the latter part of the present section.

7.2.1 Drag and Inertia Components of the Lift Force --- Experimental Results

The method of estimating C_{ml} presented in the present section is essentially the same as that used by Sarpkaya (1978) and is based on Morison's equation (see Morison et al (1950)). Considering unit length of the

cylinder, the lift force that acts on a transversely oscillating square cylinder can be expressed in terms of Morison equation as:

$$L = -C_{dl}\frac{1}{2}\rho DV|V| - C_{ml}\frac{\pi D^2}{4}\rho\frac{dV}{dt} \qquad (7.1)$$

The transverse oscillation of the cylinder can be described by:

$$y = A\sin\omega_N t \quad \text{where} \quad \omega_N = 2\pi f_N \qquad (7.2(a))$$

$$V = dy/dt = A\,\omega_N\cos\omega_N t \qquad (7.2(b))$$

$$dV/dt = -A\,\omega_N^2\sin\omega_N t \qquad (7.2(c))$$

Substitute eqn. (7.2) into (7.1) and divide through by $0.5\rho\,DU_\infty^2$

$$C_L = \frac{L}{\frac{1}{2}\rho DU_\infty^2}$$

$$= \frac{-C_{dl}\frac{1}{2}\rho D|2\pi\frac{A}{T}\cos\omega_N t|\ 2\pi\frac{A}{T}\cos\omega_N t}{\frac{1}{2}\rho DU_\infty^2}$$

$$+ \frac{C_{ml}\frac{\pi D^2}{4}\rho A\frac{4\pi^2}{T^2}\sin\omega_N t}{\frac{1}{2}\rho\,DU_\infty^2}$$

$$C_L = -C_{dl}\left(\frac{U_m T}{D}\right)^2\left(\frac{D}{U_\infty T}\right)^2 |\cos\omega_N t|\cos\omega_N t$$

$$+ C_{ml}\pi^2\frac{U_m T}{D}\left(\frac{D}{U_\infty T}\right)^2 \sin\omega_N t \qquad (7.3)$$

where $U_m = A \times 2\pi f_N$

Expand $|\cos\omega_N t|\cos\omega_N t$ and as an approximation retain only the first term:

$$C_L = C_{ml}\pi^2\frac{U_m T}{D}\left(\frac{D}{U_\infty T}\right)^2 \sin\omega_N t$$

$$- \frac{8}{3\pi} C_{dl}\left(\frac{U_m T}{D}\right)^2\left(\frac{D}{U_\infty T}\right)^2 \cos\omega_N t \qquad (7.4)$$

On the other hand, the body frequency component of the lift force $C_L(f_N,t)$ can also be expressed as:

$$C_L(f_N,t) = C_L(f_N)\sin(\omega_N t+\phi)$$

$$= C_L(f_N)\cos\phi\sin\omega_N t + C_L(f_N)\sin\phi\cos\omega_N t \qquad (7.5)$$

Equating coefficients of $\sin\omega_N t$ and $\cos\omega_N t$ in (7.4) and (7.5) gives:

$$C_L(f_N)\cos\phi = C_{ml}\frac{\frac{2\pi^3 A}{D}}{U_r^2}$$

$$C_{ml} = \frac{C_L(f_N)\cos\phi\, U_r^2}{2\pi^3\left(\frac{A}{D}\right)} \qquad (7.6)$$

and $$C_L(f_N)\sin\phi = -C_{dl}\frac{32\pi\left(\frac{A}{D}\right)^2}{3U_r^2}$$

$$C_{dl} = -\frac{3C_L(f_N)\sin\phi U_r^2}{32\pi\left(\frac{A}{D}\right)^2} \tag{7.7}$$

Since $C_L(f_N,t)$ is sinusoidal, one can further replace $C_L(f_N)$ by $\sqrt{2}C_L'(f_N)$. Eqn. (7.6) and (7.7) therefore become:

$$C_{ml} = \frac{\sqrt{2}C_L'(f_N)\cos\phi U_r^2}{2\pi^3\left(\frac{A}{D}\right)} \tag{7.8}$$

$$C_{dl} = \frac{-3\sqrt{2}C_L'(f_N)\sin\phi U_r^2}{32\pi\left(\frac{A}{D}\right)^2} \tag{7.9}$$

The only two unknown quantities on the R.H.S of eqns (7.8) and (7.9) are $C_L'(f_N)$ and ϕ. The former can be obtained from the corresponding (ie. same U_r, f_N and A/D) COPHASE printout by using eqn (3.6). The latter can be obtained from the experimentally measured ϕ versus U_r (see section 5.2). $C_L'(f_N)$ and ϕ can be corrected for inertia effect of air inside connection tubing by using eqn. (3.17) and (3.18) respectively. C_{dl} and C_{ml} calculated this way are plotted against $U_r/(A/D)$ in fig. 7.6 and fig. 7.7 respectively.

From fig. 7.6 the value of C_{dl} is positive at low $U_r/(A/D)$ and becomes progressively negative as $U_r/(A/D)$ increases. The relation between C_{dl} and $U_r/(A/D)$ is practically linear. It must be emphasized at this stage that C_{dl} must not be confused with C_D. The latter is in the same

direction as the free stream and is defined to be positive if the drag force acting on the object is in the same direction as the free stream. C_{dl}, on the other hand, is the part of $C_L(f_N)$ that is 90 degrees out of phase to the cylinder displacement, it is in the direction transverse to the free stream. Since there is a negative sign preceding the term involving C_{dl} in eqn. (7.4), negative C_{dl} means that the second term in eqn (7.4) is positive, this term therefore becomes in phase with the cylinder's velocity; under this flow condition a freely suspended cylinder will gallop transversely to the free stream. On the other hand, if C_{dl} is positive, the second term becomes 180 degrees out of phase to the cylinder's velocity and flow-induced vibration is not possible. Negative value of C_{dl} for $U_r/(A/D) > 22$ therefore means that for $U_r/(A/D) > 22$, the surrounding flow is actually "exicting" the cylinder instead of opposing its motion. This is the familiar self-sustaining oscillation situation of galloping oscillation. The present result therefore suggests that galloping oscillation is possible for $U_r/(A/D)$ greater than about 22. This deduction is in fairly good agreement with the experimentally measured ϕ results reported in chapter 5. Fig. 5.9 shows that ϕ changes from negative to positive (flow-induced oscillation is possible only when $\phi > 0$ degree) at $U_r/(A/D) \sim 20$. The agreement is expected because fig. 7.6 and fig. 5.9 are derived from the same data. However, it must also be pointed out at this stage that for galloping oscillation to take

place, another criterion must also be satisfied. This criterion is $U_r > U_{ro}$ (~ 7.69). Wawzonek & Parkinson (1979) and Bearman et al (1984(a)) had demonstrated from their experimental findings that for system with very low damping (ie. β is small), $U_{cr} < U_{ro}$ (~ 7.69); galloping oscillation will not commence until U_r is slightly less than U_{ro}. A more correct set of criteria for galloping oscillation to take place is therefore $U_r/(A/D) > 22$ (approximately) AND $U_r > 7.69$ (approximately).

By using eqn. (5.1), $U_r/(A/D) \sim 22$ corresponds to $\alpha_{max} \sim 15.94$ degrees. The present finding is also in fairly good agreement with stationary cylinder's measurement reported in fig. 4.4(a). In fig. 4.4(a) $\partial C_{Fy}/\partial\alpha$ is negative (and hence the cylinder is aerodynamically unstable to galloping oscillation) for $\alpha < 13.5$ degrees approximately and $\alpha < 13.5$ degrees corresponds to $U_r/(A/D) > 26.17$. This therefore implies that for $U_r/(A/D) > 26.17$ and $U_r > U_{ro}$, $\alpha(t)$ within a cycle of oscillation is always less than 13.5 degrees, $\partial C_{Fy}/\partial\alpha$ is always negative and hence flow induced oscillation is possible. ie. A freely suspended cylinder will oscillate transversely to the flow under the present flow condition. When $U_r/(A/D) = 26.17$, $\alpha_{max} = 13.5$ degrees. When $U_r/(A/D)$ decreases below 26.17, $\alpha_{max} > 13.5$ degrees and this means that during part of the oscillation cycle, $\alpha(t) > 13.5$ degrees, $\partial C_{Fy}/\partial\alpha > 0$ and hence flow induced oscillation is not possible. The lower the value of $U_r/(A/D)$, the part of the oscillation

cycle when flow induced oscillation is not possible ($\alpha(t) >$ 13.5 degrees) will become longer. This is the situation where a freely suspended cylinder will not oscillate transversely to the free stream. For a cylinder that is forced to oscillate under the present flow condition, during part of the cycle the force that the surrounding fluid acts on the cylinder is such that it opposes the cylinder's motion.

As for C_{ml}, it generally exhibits more scatter than C_{dl}. At low $U_r/(A/D)$, C_{ml} shows a peak value of about 9.86 at $U_r/(A/D) \sim 22$. To the author's best of knowledge, no other researchers have reported on the inertia component of the lift force that acts on a square cylinder oscillating transversely to the free stream. Comparison with other people's results is therefore not possible at this stage. Potential flow value of C_{ml} (denoted by C_{mo}) for oscillating flow past a stationary square cylinder is about 2.8 (see Bearman et al (1984b)). For cylinder oscillating in a stationary fluid or a steady stream (the present case), a value of $\rho D^2 \frac{dV}{dt} / \left(\rho \frac{\pi D^2}{4} \frac{dV}{dt}\right) = 4/\pi \sim 1.27$ should be subtracted from 2.8. C_{mo} in the present case therefore has an approximate value of 1.53.

Finally, it can be shown that the ratio of the magnitude of the inertia component of the lift force to the magnitude of the drag component of the lift force in eqn. (7.4) is equal to $(3\pi^2/16) \times (C_{ml}/C_{dl}) \times (1/A/D)$. Within the present range of $U_r/(A/D)$ (C_{ml} and C_{dl} are

$U_r/(A/D)$ dependent, see figs.7.6 and 7.7) and A/D (0.1 to 2), it is seen that although 90 degrees out of phase, the drag and the inertial components of the lift force are of comparable magnitude (ie. the ratio of (drag component)/(inertia component) is of O(1)).

7.2.2 Thin Aerofoil Theory

For a thin aerofoil (flat plate) oscillating transversely in incompressible flow, Bisplinghoff, Ashley & Halfman (1957) have shown that the lift force induced by the translational oscillating motion is given by:

$$L = -C_{mo}\frac{\rho\pi D^2}{4}\left[\ddot{y}+U_\infty\dot{\beta}-\frac{D}{2}a\ddot{\beta}\right]-\frac{\partial C_L}{\partial\alpha}\rho U_\infty\frac{D}{2}\cdot C(k)$$

$$x\left[\dot{y}+U_\infty\beta+\frac{D}{2}\left(\frac{1}{2}-a\right)\dot{\beta}\right] \qquad (7.10)$$

where C_{mo} = Potential flow inertia coefficient and = 1.53 for a square cylinder oscillating in a steady stream

$C(k)$ = Theodorsen's functional, a complex function expressible in Hankel functions

$k = \pi/U_r$

$\partial C_L/\partial\alpha$ = slope of C_L (or C_{Fy}) versus α at $\alpha = 0$ degree

$a = x/(D/2)$, where x is the distance between the axis of rotation (pitching of the aerofoil) and

the mid-point of the thin aerofoil

β = angle rotated about axis that passes through the C.G. of the flat plate

If the flat plate does not rotate (pitch) about its own axis as in the present case, then $\beta = \dot{\beta} = \ddot{\beta} = 0$. Equation (7.10) can therefore be simplified to:

$$L = -C_{mo} \frac{\rho\pi D^2}{4} \ddot{y} - \frac{\partial C_L}{\partial \alpha} \rho U_\infty \frac{D}{2} C(k)\dot{y} \qquad (7.11)$$

In eqn. (7.11), the first term represents the conventional inertia force term while the second term may require a little extra physical explanation. From Kutta-Joukowski's law (see Duncan et al (1974)), it is known that for a steady stream past a two dimentional aerofoil, the lift ($L = \rho U_\infty \Gamma$) is associated with a circulation of strength Γ and a starting vortex also of strength Γ but opposite in sign is left behind. For an aerofoil oscillating transversely in a steady stream, the resultant angle of incidence and hence the lift force varies periodically, from Kelvin's circulation theorem (Tritton (1977) pp.94) which says that since the total initial circulation within a close loop surrounding the wing is zero, the total circulation must remains zero thereafter, ie. $D\Gamma/Dt = 0$; the varying lift acting on the aerofoil (and hence the varying circulation around it) must therefore be associated by many vortices which are shed and carried downstream by the free stream continuously. The vortices shed can affect the flow

around the aerofoil and hence the lift acting on it in both magnitude and phase (with respect to displacement). This effect is accounted for by the second term in eqn. (7.11). The fact that the phase of the lift force acting on the aerofoil can be affected by the vortices shed is taken care of by the complex C(k) (= F(k) + iG(k)) term. It will be shown later that at high reduced velocity $F(k) \to 1$, $G(k) \to 0$ and hence $C(k) \to 1$.

From eqn (7.2), let

$$y = \text{Im}\left[Ae^{i\omega_N t}\right] \tag{7.12(a)}$$

$$\dot{y} = \text{Im}\left[iA\omega_N e^{i\omega_N t}\right] \tag{7.12(b)}$$

$$\ddot{y} = \text{Im}\left[-A\omega_N^2 e^{i\omega_N t}\right] \tag{7.12(c)}$$

substitute eqn (7.12) into eqn (7.11)

$$L = \text{Im}\left[\left(C_{mo}\frac{\rho\pi D^2}{4}\omega_N - i\frac{\partial C_L}{\partial\alpha}\rho U_\infty \frac{D}{2} C(k)\right)A\omega_N e^{i\omega_N t}\right]$$

Now let $C(k) = F(k) + iG(k)$ where $F(k)$ and $G(k)$ are real

$$L = \text{Im}\left[\left(C_{mo}\frac{\rho\pi D^2}{4}\omega_N + \frac{\partial C_L}{\partial\alpha}\rho U_\infty \frac{D}{2} G(k) - i\frac{\partial C_L}{\partial\alpha}\rho U_\infty \frac{D}{2} F(k)\right)A\omega_N e^{i\omega_N t}\right]$$

$$= \left(C_{mo}\frac{\rho\pi D^2}{4}\omega_N + \frac{\partial C_L}{\partial\alpha}\rho U_\infty\frac{D}{2}G(k)\right)(A\omega_N\sin\omega_N t)$$

$$- \left(\frac{\partial C_L}{\partial\alpha}\rho U_\infty\frac{D}{2}F(k)\right)(A\omega_N\cos\omega_N t)$$

$$= L_{IN} + L_{OUT} \qquad (7.13)$$

where $L_{IN} = \left[C_{mo}\frac{\rho\pi D^2}{4}\omega_N + \frac{\partial C_L}{\partial\alpha}\rho U_\infty\frac{D}{2}G(k)\right](A\omega_N\sin\omega_N t)$

= the part that is in-phase with the cylinder's acceleration

$$L_{OUT} = -\left[\frac{\partial C_L}{\partial\alpha}\rho U_\infty\frac{D}{2}F(k)\right](A\omega_N\cos\omega_N t)$$

= the part that is 90 degrees out of phase with the cylinder's displacement

$$C_{ml} = \frac{L_{IN}}{-\frac{\rho\pi D^2}{4}\ddot{y}}$$

$$= \frac{L_{IN}}{\frac{\rho\pi D^2}{4}A\omega_N{}^2\sin\omega_N t}$$

$$= \frac{\frac{\rho\pi D^2}{4}\omega_N A\omega_N\sin\omega_N t}{\frac{\rho\pi D^2}{4}A\omega_N{}^2\sin\omega_N t}C_{mo} + \frac{\frac{\partial C_L}{\partial\alpha}\rho U_\infty\frac{D}{2}G(k)A\omega_N\sin\omega_N t}{\frac{\rho\pi D^2}{4}A\omega_N{}^2\sin\omega_N t}$$

$$= C_{mo} + \frac{\frac{\partial C_L}{\partial\alpha}U_\infty G(k)}{\pi^2 D f_N}$$

$$= C_{mo} + \frac{1}{\pi k}\frac{\partial C_L}{\partial\alpha}G(k) \qquad (7.14)$$

The term "$\frac{1}{\pi k}\frac{\partial C_L}{\partial\alpha}G(k)$" "modifies" the potential flow inertia coefficient and is therefore called the "added

inertia" coefficient (C_{mA}) in this thesis.

The other part of the lift that is induced by the translational oscillation of the cylinder, L_{OUT}, is 90 degrees out of phase to the cylinder displacement. The part of the lift that is 90 degrees out of phase to the cylinder's displacement can be non-dimensionalised by $0.5\rho DU_\infty^2$. In dimensionless form:

$$C_{LO} = \frac{L_{OUT}}{\frac{1}{2}\rho DU_\infty^2}$$

$$= \frac{\frac{-\partial C_L}{\partial \alpha}\rho U_\infty \frac{D}{2} F(k) A 2\pi f_N}{\frac{1}{2}\rho DU_\infty^2} \cos\omega_N t$$

$$= -\frac{\partial C_L}{\partial \alpha} F(k)\ 2\pi \frac{A}{D} \frac{f_N D}{U_\infty} \cos\omega_N t$$

$$= -\bar{C}_{LO} \cos\omega_N t \qquad (7.15(a))$$

where $\bar{C}_{LO}$ is the amplitude of C_{LO} and is given by:

$$\bar{C}_{LO} = \frac{\partial C_L}{\partial \alpha} F(k) \left[2\pi . \frac{A}{D} . \frac{1}{U_r}\right]$$

$$= \frac{\partial C_L}{\partial \alpha} F(k) \tan\alpha_{max} \qquad (7.15(b))$$

where α_{max} is defined in eqn. (5.1).

From Bisplinghoff, Ashley & Halfman (1957), Theodorsen's function C(k) can be expressed as:

$$C(k) = \frac{H_1^{(2)}(k)}{H_1^{(2)}(k) + iH_0^{(2)}(k)} \qquad (7.16)$$

where $H_0^{(2)}$ = Hankel function of the second kind of order 0

$H_1^{(2)}$ = Hankel function of the second kind of order 1

Through some mathematical manipulation and assuming k is small (O(0.1) or less as k^3 and higher powers of k are neglected in the series approximation to Bessel function), it can be shown (see Appendix A) that:

$$C(k) = F(k) + iG(k)$$

$$= \frac{D_1(k)}{D(k)} + i\,\frac{D_2(k)}{D(k)} \tag{7.17}$$

where $D_1(k)$ $= \frac{k^2}{\pi^2}\left(\ell n\,\frac{k}{2}\right)^2 + \ell n\,\frac{k}{2}\left(\frac{2\nu k^2}{\pi} - \frac{k^2}{\pi^2} - \frac{4}{\pi^2}\right)$

$$+ k^2\left[\frac{1}{\pi^2}\left(\nu - \frac{1}{2}\right)^2 + \frac{1}{4}\right] + \frac{k}{2\pi} + \frac{2-4\nu}{\pi^2}$$

$$+ \frac{2}{\pi k} + \frac{4}{\pi^2 k^2} \tag{7.18}$$

$$D_2(k) = \frac{2k}{\pi^2}\left(\ell n\,\frac{k}{2}\right)^2 + \frac{2}{\pi^2}\,\ell n\,\frac{k}{2}\left(2\nu k - \frac{k}{2} - \frac{2}{k}\right)$$

$$+ \frac{2k}{\pi^2}\left(\frac{\pi^2}{4} + \nu^2 - \frac{\nu}{2} - \frac{1}{2}\right) - \frac{4\nu}{\pi^2 k} \tag{7.19}$$

$$D(k) = \frac{1}{\pi^2}(4+k^2)(\ell n\frac{k}{2})^2+\ell n\frac{k}{2}.\ \frac{1}{\pi^2}(k^2+8\nu+2\nu k^2-4+2\pi k)$$

$$+\ \frac{k^2}{\pi^2}\left[\left(\nu+\frac{1}{2}\right)^2+\frac{\pi^2}{4}\right]+\frac{k}{\pi}$$

$$+\ \frac{2}{\pi^2}(2\nu^2-2\nu+1)+(1+\frac{2}{\pi k})^2 \qquad (7.20)$$

and ν = Euler's constant ~ 0.5772.

By making use of eqns (7.17) to (7.20), a computer programme was written and values of C_{m1} and C_{LO} can therefore be calculated from eqns (7.14) and (7.15) directly.

In eqn. (7.14), since both $\frac{\partial C_L}{\partial \alpha}$ and G(k) are negative quantities, the added inertia coefficinet is therefore positive and is added to C_{mo}, the potential flow inertia coefficient.

The theoretically calculated C_{m1} are superimposed onto the experimental results in fig. 7.7. It is seen from fig. 7.7 that when $U_r/(A/D)$ increases, the theoretically estimated C_{m1} also increases but the rate of increase of C_{m1} w.r.t. $U_r/(A/D)$ decreases. The agreement between the two is fairly reasonable in the range $50 \leq U_r/(A/D) \leq 170$. The scatter in the experimentally measured C_{m1} is thought to be attributed to the difficulties in accurately measuring $C_L'(f_N)$ which is required for calculating C_{m1}. This is especially so at high reduced velocity because at high

reduced velocity, the main contributor to C_L is $C_L(f_s)$ and $C_L(f_N)/C_L(f_s) = O(0.1)$ or smaller. The theory fails to predict C_{ml} (even qualitatively) for $U_r/(A/D) < 40$. This is not unexpected as the assumption "k^3 and higher order k terms ($k = \pi/U_r$) are negligible" that was adopted to obtain an approximate series expansion of C(k) becomes less valid. Also, at low value of $U_r/(A/D)$, α_{max} is quite different from zero and the justification of the use of $\partial C_L/\partial\alpha$ (α = 0 degree) in the equation that is used to calculate C_{ml} (eqn. (7.14) is questionable.

As for the part of the lift that is 90 degrees out of phase to the cylinder's displacement, the thin aerofoil theory predicts that whether a certain cross sectional shape is stable to flow-induced oscillation is dependent on the sign of $\partial C_L/\partial\alpha$ (= $\partial C_{Fy}/\partial\alpha$ at α = 0 degree). If $\partial C_L/\partial\alpha$ is negative, C_{LO} becomes in phase with the velocity of the cylinder and flow-induced oscillation becomes possible. On the other hand, if $\partial C_L/\partial\alpha$ is positive, C_{LO} becomes 180 degrees out of phase to the cylinder's velocity and flow-induced oscillation will not take place. The above prediction from the theory agrees very well with the already well known relationship between stability of a certain cross sectional shape to flow-induced oscillation and the sign of $\partial C_{Fy}/\partial\alpha$ at α = 0 degree.

The magnitude of C_{LO} (ie. $\overline{C}_{LO}$) is plotted against $U_r/(A/D)$ in fig. 7.8. F(k) and G(k) are plotted against U_r in fig. 7.9.

Now by substituting eqn. (7.14) and (7.15) back into eqn (7.13), the body frequency component of the lift force can be written as:

$$L(f_N) = C_{ml}\left(\frac{\rho\pi D^2}{4} A\omega_N{}^2\right)\sin\omega_N t - \overline{C}_{LO}\left(\frac{1}{2}\rho DU_\infty{}^2\right)\cos\omega_N t \qquad (7.21)$$

However, the body frequency component of the lift force can also be written as:

$$L(f_N) = L(f_N)\sin(\omega_N t + \phi)$$

$$= L(f_N)\cos\phi\sin\omega_N t + L(f_N)\sin\phi\cos\omega_N t \qquad (7.22)$$

By separately equating the coefficients of $\sin\omega_N t$ and $\cos\omega_N t$ in eqn. (7.21) and (7.22), one gets:

$$L(f_N)\cos\phi = C_{ml}\left(\frac{\rho\pi D^2}{4} A\omega_N{}^2\right) \qquad (7.23)$$

and

$$L(f_N)\sin\phi = -\overline{C}_{LO}\left(\frac{1}{2}\rho DU_\infty{}^2\right) \qquad (7.24)$$

Non-dimensionalising eqn. (7.23) and (7.24) by dividing them through by $0.5\,\rho DU_\infty{}^2$ and simplifying:

$$C_L(f_N)\cos\phi = C_{ml}\,\pi^2\frac{1}{U_r}\tan\alpha_{max} \qquad (7.25)$$

$$C_L(f_N)\ \sin\phi = -\frac{\partial C_L}{\partial \alpha} F(k)\ \tan\alpha_{max} \tag{7.26}$$

From eqn. (7.25) and (7.26) it can be shown that:

$$C_L(f_N) = \sqrt{\left[\frac{C_{m1}\pi^2 \tan\alpha_{max}}{U_r}\right]^2 + \left[\frac{\partial C_L}{\partial \alpha} F(k)\ \tan\alpha_{max}\right]^2}$$

$$\text{or} \quad C_L'(f_N) = \sqrt{\frac{1}{2}\left[\left[\frac{C_{m1}\pi^2 \tan\alpha_{max}}{U_r}\right]^2 + \left[\frac{\partial C_L}{\partial \alpha} F(k) \tan\alpha_{max}\right]^2\right]} \tag{7.27}$$

$$\text{and} \quad \phi = \tan^{-1}\left[\frac{-\frac{\partial C_L}{\partial \alpha} F(k) U_r}{C_{m1}\pi^2}\right] \tag{7.28}$$

The theoretically predicted $C_L'(f_N)$ is superimposed onto the experimentally measured $C_L'(f_N)$ and the quasi-steady theory predicted $C_{Fy}'(f_N)$ in fig. 7.3. From fig. 7.3 it is seen that the agreement between the experimental data and the prediction by the thin aerofoil theory is good for $U_r/(A/D) \geq 20$ approximately. For $U_r/(A/D) \geq 100$ the prediction by the thin aerofoil theory and by the quasi-steady theory are practically identical to each other. However, overall the prediction by the thin aerofoil theory is more accurate.

The theoretically predicted ϕ are superimposed onto the experimental data (see fig. 5.9) in fig. 7.10. From fig. 7.10 it is seen that the agreement between experimental

data and theoretical prediction is good for $U_r/(A/D) \geq 25$.

By now, apart from the fact that neither the quasi-steady theory nor the thin aerofoil theory can predict phenomena like the locking on of f_s onto f_N and $3f_N$ at $U_r \sim U_{ro}$ and $3U_{ro}$ (where U_{ro} is the resonance reduced velocity) respectively; the reason for the inability of the thin aerofoil theory to predict experimental data ($C_L'(f_N)$ and ϕ) for $U_r/(A/D) \leq 25$ approximately is clear. $U_r/(A/D) = 25$ corresponds to $\alpha_{max} = 14.11$ degrees. At about this value of α_{max} flow reattachment on the side faces of a transversely oscillating square cylinder begins to take place. From our knowledge in stationary cylinder's C_{Fy} versus α , we know that $\partial C_{Fy}/\partial\alpha$ changes its sign from negative ($\alpha < 13.5$ degrees) to positive ($\alpha > 13.5$ degrees) at $\alpha \sim 13.5$ degrees. If for $\alpha > 13.5$ degrees ($U_r/(A/D) < 26.17$) one substitutes $\partial C_L/\partial\alpha$ in eqn. (7.28) by a positive quantity, the numerator of the R.H.S. of eqn. (7.28) will become negative and ϕ will then have a value somewhere between 0 to -180 degrees. This is indeed what the experimental data have shown. For $C_L'(f_N)$ the disgreement between experimental measurement and theoretical prediction for $U_r/(A/D) < 26.17$ is less obvious because the squaring process used to calculate $C_L'(f_N)$ has made the sign of $\partial C_L/\partial\alpha$ in eqn. (7.27) unimportant. The author therefore concludes that the thin aerofoil theory is capable of predicting experimentally measured $C_L'(f_N)$ and ϕ with fairly remarkable accuracy for $U_r/(A/D) > 26$. However, for $U_r/(A/D)$

that is only slighty bigger than and for $U_r/(A/D)$ that is less than 26, to acheive better accuracy of prediction $\partial C_L/\partial\alpha$ (α = 0) which appears in eqn. (7.11), (7.14), (7.15), (7.27) and (7.28) must be replaced by $\partial C_L/\partial\alpha$ ($\alpha = \tan^{-1}(\dot{y}(t)/U_\infty)$). However, the author wishes to reiterate that even by using a more accurate $\partial C_L/\partial\alpha$, the thin aerofoil theory is still not very useful for $U_r/(A/D) < 26$ because it still cannot predict the vortex lock-on phenomena mentioned in the previous page. Finally, when U_r is fairly small, the assumption used to derive the series expansion of $F(k)$ and $G(k)$, namely, that k^3 and higher powered k terms ($k = \pi/U_r$) are negligible also becomes less justified. For more accurate $F(k)$ and $G(k)$ one may have to start including k^4 and k^5 etc terms in eqn. (7.17) to (7.20).

7.3 CONCLUSION

The present chapter again demonstrates the usefulness of Parkinson's quasi-steady theory in predicting the body frequency component of the fluctuating lift acting on a square cylinder oscillating transversely to a free stream of reasonably high reduced velocity. The absolute lower bound for the range of $U_r/(A/D)$ where the quasi-steady theory is applicable is about 25. For $U_r/(A/D) < 25$ (or $\alpha_{max} > 14.11$ degrees) the quasi-steady theory predicts that $C_L'(f_N)$ decreases with decreasing $U_r/(A/D)$ whereas experimentally measured $C_L'(f_N)$ increases with decreasing

$U_r/(A/D)$. The finding that the quasi-steady theory cannot predict experimental measurement for $U_r/(A/D) < 25$ can be explained by referring to the C_{Fy} versus α measurement of a stationary inclined cylinder. For a stationary inclined cylinder, $\partial C_{Fy}/\partial\alpha$ changes from negative to positive at $\alpha \sim 13.5$ to 14 degrees. For $\alpha > 14$ degrees $\partial C_{Fy}/\partial\alpha$ becomes positive and the cylinder becomes stable to galloping oscillation. It is therefore not unreasonble for the quasi-steady theory to predict that $C_L'(f_N)$ reduces quickly to zero when $U_r/(A/D)$ reduces below 25 which is shown in fig. 7.3. The quasi-steady theory, however, is not very useful in predicting the magnitude of $C_L'(3f_N)$ and $C_L'(5f_N)$.

By using Sarpkaya's (1978) approach, the dimensionless drag and inertia components (C_{dl} and C_{ml}) of the lift force were estimated from experimental data. Within the range of $U_r/(A/D)$ and A/D investigated in the present research, it is found that the drag and inertia components of the lift force are of comparable magnitude. C_{ml} calculated were compared with the C_{ml} estimated by the thin aerofoil theory and the agreement between the two is quite reasonable.

The thin aerofoil theory can also be used to estimate the magnitude of $C_L'(f_N)$ and ϕ. These estimation were compared with experimental measurement and it was found that agreement between theory and measured data is fairly good for $U_r/(A/D) > 26$ approximately. The poor agreement

between experimental and theoretical results for $U_r/(A/D) < 26$ is partly attributed to the unjustifiable use of $\partial C_L/\partial\alpha$ (α = 0 degree) in the derivation of $C_L'(f_N)$ and ϕ at such low reduced velocity. When $U_r/(A/D)$ is low, the magnitude of $\alpha(t)$ is far from 0 degree for most part of the oscillation cycle except at the two extreme end. At low reduced velocity, for more accurate prediction, more accurate expression for F(k) and G(k) than eqn. (7.17) to (7.20) will also be required.

Despite their sucess in predicting the magnitude of $C_L'(f_N)$ and ϕ in a certain reduced velcocity range, both the quasi-steady theory and the thin aerofoil theory cannot predict phenomena like the locking on of f_s on to f_N and $3f_N$ at $U_r \sim U_{ro}$ and $3U_{ro}$ (where U_{ro} is the resonance reduced velocity and $\sim$ 7.69) respectively.

CHAPTER EIGHT

CONCLUSIONS

Detailed conclusions can be found at the end of chapter four to seven. The present chapter provides an overall summary of the results of the research.

Most of the results reported in the stationary cylinder chapter (chapter four) are already available in the literature. The main reason for presenting those results is to demonstrate that the experimental set-up (especially the pressure averager since it is a relatively new technique) and software used in the present research are capable of generating accurate results. The author believes that this objective had been acheived as most of the results reported in chapter four are in fairly good agreement with earlier results reported by other researchers especially Obasaju (1977). Some of the results reported in chapter four like the mean and fluctuating body axis drag and lift (C_x, C_x', C_y(= C_{Fy}) and C_y' respectively) versus angle of incidence (α) are less widely reported because without the use of the pressure averagers, the deduction of C_x and C_y from surface pressure distribution measurement becomes more tedious and the direct measurement of C_x' and C_y' is difficult. It is of course possible to measure C_x' and C_y' from total load (using strain guages etc) measurement but

then the results obtained may be less applicable to the idealised two dimensional flow situation. While C_y(= C_{Fy}) versus α was used by Parkinson to form the basis of his quasi-steady theory, C_x, C_x' and C_y' versus α also show some interesting features. They (C_x, C_x' and C_y') reach their minimum values at $\alpha \sim 13.5$ degrees, the cause of these minima is believed to be the interaction between one of the separated shear layers and one of the trailing corners which forces the vortices to form further downstream from the cylinder. These minima, as will be mentioned later, shows up in the results for a transversely oscillating square cylinder.

Transversely oscillating cylinder results are reported in chapter five. The author has attempted to explain some of the interesting features in the experimental results presented. For example, at the same amplitude of oscillation, the minimum in the fluctuating lift and the "kink" in the phase angle between lift at the forcing frequency and the cylinder displacement (and hence discontinuity in $\partial\phi / \partial U_r$) always take place at approximately the same reduced velocity. It had been suggested that this observation is due to the non-linear interaction between two vortex wakes, the conventional Karman vortex wake and a second one that is generated by the transverse oscillation of the cylinder (Bearman et al (1984(a)) which alters the resultant flow structure. Also at the same amplitude of oscillation, the mean and

fluctuating drag and the fluctuating base pressure reach their respective minima and the mean base pressure reaches its maximum at approximately the same reduced velocity. By substituting the values of U_r, A/D and f_N into eqn (5.1), it was found that these minima (or maximum for the case of C_{pb}) always take place when the maximum value of the instantaneous angle of incidence (α_{max}) during a cycle was about 13.5 degrees ($\sim \alpha_{crit}$ for a stationary inclined cylinder). It therefore appears that the cause of these minima or maximum is the same as that of the minima in stationary inclined cylinder's C_x, C_x' and C_y' mentioned earlier. ie. Interaction between shear layers and cylinder trailing corners. The author found this quasi-steady observation to be quite unexpected because it took place at fairly low reduced velocity. At high enough reduced velocity, all the aerodynamic parameters measured always approach their stationary cylinder's values. Increasing the amplitude of oscillation causes the quasi-steady state to be reached at higher reduced velocity but the general trends of the parameters measured are otherwise unaltered.

Spectral analysis of the lift and drag forces confirm that the forces are dominated by their body frequency and higher harmonics components at low reduced velocity and by the shedding frequency component (f_s for lift and $2f_s$ for drag) at high reduced velocity.

Smoke wire flow visualization clearly demonstrates that different flow structures exist at different reduced

velocities. In the present research four different structures have been identified. Wake parameters like longitudinal and lateral vortex spacing (and hence spacing ratio) are all quite different in these four structures and it was found that the spacing ratio can be quite different from the value of 0.281 suggested by Von Karman. The key factor that causes the formation of different flow structures seems to be the ratio of the cylinder transverse velocity to the free stream velocity (this is equivalent to the instantaneous angle of incidence between the "resultant flow" and the cylinder as $\alpha(t) = \tan^{-1}(\dot{y}(t)/U_\infty)$, see also eqn (5.1)). This above mentioned ratio affects the duration of time that each growing vortex receives its vorticity from the feeding shear layer and hence the amount of vorticity that goes into each vortex shed and also affects the position of a vortex when it is cut off from the feeding shear layer. The strength of each vortex shed was found to be one of the factors that affects the magnitude of the fluctuating lift. For example, for a particular A/D, at the reduced velocity that C_L' reaches its minimum value of about 0.7, the combination of U_∞ and y_{max} ($= A \times 2\pi f_N$) was such that the vortices shed were seen (by visualizing the flow) to be very weak. Also, it was found, as might be expected, that the position of the cylinder within an oscillation cycle when a vortex is shed, affects the phase angle between the forcing frequency component of the lift force and the cylinder displacement. It should be pointed here that if

$\dot{y}_{max}/U_\infty$ is an important parameter, then, when away from lock-on, the useful aerodynamic parameter for flow past a transversely oscillating cylinder should be $U_r/(A/D)$ as it is equal to $2\pi/(\dot{y}_{max}/U_\infty)$. This is in a sense in agreement with one of the findings in chapter five; ie. the increase in A/D merely causes the quasi-steady state to be reached at higher reduced velocity. The scatter seen in figures 5.6 and 5.9 (C_L' and ϕ versus $U_r/(A/D)$ respectively) may be due to experimental error.

By using the stationary cylinder body axis lift versus angle of incidence measured experimentally in the present research as empirical data, Parkinson's quasi-steady theory was used to predict various components of the lift force ($C_L'(f_N)$, $C_L'(2f_N)$ and $C_L'(3f_N)$ etc) and later comparison with experimental measurements was made. It was found that Parkinson's theory could quite accurately predict the body frequency component of the fluctuating lift at moderate and high reduced velocity but failed to predict the magnitude of the higher frequency components of the fluctuating lift. A simplified thin aerofoil theory was also briefly examined and it was found that the thin aerofoil theory is capable of predicting (qualitatively at least) the inertia component of the lift force acting on a transversely oscillating square cylinder. $C_L'(f_N)$ and ϕ predicted by the thin aerofoil theory were compared with experimental measurements and it was found that agreement between the two is good for $U_r/(A/D) > 26$ approximately. For $U_r/(A/D) \leq 26$,

the transverse velocity of the cylinder becomes comparable with the free stream wind velocity and $\alpha(t)$ (= $\tan^{-1}(\dot{y}(t)/U_\infty)$) can be considerably different from zero except at the two extremes of a cycle of oscillation. The use of $\partial C_L/\partial\alpha$ (α = 0 degree) in the equations used to predict $C_L'(f_N)$ and ϕ is no longer justified and that partly explains why the thin aerofoil theory fails to predict $C_L'(f_N)$ and ϕ for $U_r/(A/D) \leq 26$. Despite their success in predicting the mangitude of $C_L'(f_N)$ and ϕ at moderate and high reduced velocity, both the quasi-steady theory and the thin aerofoil theory cannot predict the locking on of f_s on to f_N and $3f_N$ at $U_r \sim U_{ro}$ and $3U_{ro}$ respectively.

REFERENCES

BARNES, F.H. & GRANT, I. Vortex shedding in unsteady flow. Journal of Wind Engineering and Industrial Aerodynamics, Vol.11, pp 335-344, 1983.

BAROUDI, M.Y. Measurement of two-point correlations of velocity near a circular cylinder shedding a Karman vortex street. UTIA Technical Note, NO.31, 1960.

BATILL, S.M. & MUELLER, T.J. Visualization of transition in the flow over an airfoil using the smoke-wire technique. AIAA Journal, Vol.19, No.3, pp 340-345, 1981.

BEARMAN, P.W. Investigation of the flow behind a two-dimensional model with a blunt trailing edge and fitted with splitter plates. Journal of Fluid Mechanics, Vol.2, Part 2, pp 241-255, 1965.

BEARMAN, P.W. On vortex street wakes. Journal of Fluid Mechanics, Vol.28, Part 4, pp 625-641, 1967.

BEARMAN, P.W. Turbulence-induced vibrations of bluff bodies. IUTAM-IAHR Symposium Karlsruhe, (Ed. NAUDASCHER), Springer, 1972.

BEARMAN, P.W. Pressure-fluctuation measurements on an oscillating circular cylinder. Journal of Fluid Mechanics, Vol.91, Part 4, pp 661-677, 1979.

BEARMAN, P.W. Vortex shedding from oscillating bluff bodies. Annual Review in Fluid Mechanics, Vol.16, pp 195-222, 1984.

BEARMAN, P.W. & CURRIE, I.G. Pressure-fluctuation measurements on an oscillating circular cylinder. Journal of Fluid Mechanics, Vol.91, Part 4, pp 661-677, 1979.

BEARMAN, P.W., GARTSHORE, I.S., MAULL, D.J. & PARKINSON, G.V. Experiments on flow-induced vibration of a square-section cylinder. A.S.M.E. Winter Annual Meeting, Symposium on Flow Induced Vibrations, 1984(a).

BEARMAN, P.W. & GRAHAM, J.M.R. Vortex shedding from bluff bodies in oscillating flow: A Report on Euromech 119. Journal of Fluid Mechanics, Vol.99, Part 2, pp 225-246, 1980.

BEARMAN, P.W., GRAHAM, J.M.R., OBASAJU, E.D. & DROSSOPOULOS, G.M. The influence of corner radius on the forces experienced by cylindrical bluff bodies in oscillatory flow. Applied Ocean Research, Vol.6, No.2, 1984(b).

BEARMAN, P.W., GRAHAM, J.M.R. & SINGH, S. Forces on cylinders in harmonically oscillating flow. Mechanics of Wave-Induced Forces on Cylinders (Ed. SHAW, T.L.), pp 437-449, Pitman, 1979.

BEARMAN, P.W. & OBASAJU, E.D. An experimental study of pressure fluctuations on fixed and oscillating square-section cylinders. Journal of Fluid Mechanics, Vol.119, pp 297-321, 1982.

BEARMAN, P.W. & TRUEMAN, D.M. An investigation of the flow around rectangular cylinders. Imperial College Aero Report 71-15, London, 1971.

BEARMAN, P.W. & TRUEMAN, D.M. An investigation of the flow around rectangular cylinders. The Aeronautical Quarterly, Vol.23, 1972.

BISHOP, R.E.D. & HASSAN, A.Y. The lift and drag forces on a circular cylinder in a flowing fluid. Proceedings of the Royal Society of London, Vol.277A, pp 32-50, 1964(a).

BISHOP, R.E.D. & HASSAN, A.Y. The lift and drag forces on a circular cylinder oscillating in a flowing fluid. Proceedings of the Royal Society of London, Vol.277A, pp 51-75, 1964(b).

BISPLINGHOFF, R.L., ASHLEY, H. & HALFMAN, R.L. Aeroelasticity. Addison-Wesley, 1957.

BLEVINS, R.D. Flow-induced vibration. Van Nostrand Reinhold Company, 1977.

BUBLITZ, P. Unsteady pressures and forces acting on an oscillating circular cylinder in transverse flow. IUTAM-IAHR Symposium Karlsruhe, (Ed. NAUDASCHER), 1972.

CLEMENTS, M.P.M. & UNWIN, G.P. Calibration of the 3ft x3ft low speed wind tunnel of Imperial College. Third Year Project Report, Department of Aeronautics, Imperial College, London, 1973.

COURCHESNE, J. & LANEVILLE, A. An experimental evaluation of drag coefficient for rectangular cylinders exposed to grid turbulence. Journal of Fluids Engineering, Trans A.S.M.E, Vol.4, pp 523-527, 1982.

DAVIES, M.E. Spectral analysis programmes Powspec and Cophase. Technical Note 74-103, Department of Aeronautics, Imperial College, London, 1974.

DAVIES, M.E. Wakes of oscillating bluff bodies. PhD Thesis, Department of Aeronautics, Imperial College, London, 1975.

DAVIES, M.E. A comparison of the wake structure of a stationary and oscillating bluff body, using a conditional averaging technique. Journal of Fluid Mechanics, Vol.75, Part 2, pp 209-231, 1976.

DEN HARTOG. Mechanical vibrations. McGraw Hill, 1956.

DUNCAN, W.J., THOM, A.S. & YOUNG, A.D. Mechanics of fluids, 2nd edition. Arnold 1974.

ENGINEERING SCIENCE DATA UNIT. Fluid forces on non-streamline bodies - Background notes and description of the flow phenomena. Item No. 71012, 1971.

ENGINEERING SCIENCE DATA UNIT. Fluid forces, pressures and moments on rectangular blocks.Item No. 71016, 1971

ENGINEERING SCIENCE DATA UNIT. Blockage for bluff bodies in confined flows. Item No. 80024, 1980.

FACKRELL, J.E. Blockage effects on two-dimensional bluff body flow. The Aeronautical Quarterly, 1975.

FERGUSON, N & PARKINSON, G.V. Surface and wake flow phenomena of the vortex-excited oscillation of a circular cylinder. Trans A.S.M.E Journal of Engineering for Industry, pp 831-838, 1967.

FREYMUTH, P., BANK, W. & PALMER, M. Flow visualization and hot-wire annemometry. TSI Quarterly, Vol.IX, Issue 4, 1983.

GERRARD, J.H. An experimental investigation of the oscillating lift and drag of a circular cylinder shedding turbulent vortices. Journal of Fluid Mechanics, Vol.11, 1961.

GERRARD, J.H. The mechanics of the formation region of vortices behind bluff bodies. Journal of Fluid Mechanics, Vol.25, Part 2, pp 401-413, 1966.

GOLDSTEIN, S. Modern developments in fluid dynamics. Volume 2, Oxford University Press, 1938.

GRIFFIN, O.M., SKOP, R.A. & KOOPMANN, G.H. The vortex-excited resonant vibrations of circular cylinder. Journal of Sound and Vibration, Vol.31(2), pp 235-249, 1973.

HARTLEN, R.T. & CURRIE, I.G. Lift-oscillator model of vortex-induced vibration. Proc. A.S.C.E. Journal of Engineering Mechanics Division, pp 577-591, 1970.

IRWIN, H.P.A.H, COOPER, K.R. & GIRARD, R. Correction of distortion effects caused by tubing systems in measurements of fluctuating pressures. Journal of Industrial Aerodynamics, Vol.5, pp 93-107, 1979.

KAREEM, A. & CERMAK, J.E. Pressure fluctuations on a square building model in boundary-layer flows. Journal of Wind Engineering and Industrial Aerodynamics, Vol.16, pp 17-41, 1984.

KOMATSU, S. & KOBAYASHI, H. Vortex-induced oscillation of bluff cylinders. Journal of Wind Engineering and Industrial Aerodynamics, Vol.6, pp 335-362, 1980.

KREYSZIG, E. Advanced engineering mathamatics. John Wiley & sons, 1979.

KWOK, K.C.S. Effects of turbulence on the pressure distribution around a square cylinder and possibility of reduction. Trans A.S.M.E. Journal of Fluids Engineering, Vol.105, pp 140-145, 1983.

LANDL, R. A Mathematical model for vortex-excited vibrations of bluff bodies. Journal of Sound and Vibration, Vol.42(2), pp 219-234, 1975.

LANEVILLE, A. GARTSHORE, I.S. & PARKINSON, G.V. An explanation of some effects of turbulence on bluff bodies. Proc. of the Fourth International Conference on "Wind Effects on Building and Structure", (Ed. Eaton, K.J.), 1975.

LANEVILLE, A. & LU ZHI YONG Mean flow patterns around two-dimensional rectangular cylinders and their interpretation. Journal of Wind Engineering and Industrial Aerodynamics, Vol.14, pp 387-398, 1983.

LANEVILLE, A. & PARKINSON, G.V. Effect of turbulence on galloping of bluff bodies. Proc. 3rd Int. Conf. Wind Effects, pp 787-798, Tokyo, 1971.

LEE, B.E. The surface pressure field experienced by a two-dimensional square prism. Central. Electricity Generating Board RD/L/N 17/74, 1974.

LEE, B.E. The effect of turbulence on the surface pressure field of a square prism. Journal of Fluid Mechanics, Vol.69, Part 2, pp 263-282, 1975(a).

LEE, B.E. Some effects of turbulence scale on the mean forces on a bluff body. Journal of Industrial Aerodynamics, Vol.1, pp 361-370, 1975(b).

LUO. S.C. Steady and unsteady flow past a circular cylinder. M.Eng. thesis, National University of Singapore, 1982.

MAIR, W.A. & MAULL, D.J. Bluff bodies and vortex shedding: A Report on Euromech 17. Journal of Fluid Mechanics, Vol.45, Part 2, pp 209-224, 1971.

MASKELL, E.C. A theory of the blockage effects on bluff bodies and stalled wings in a closed wind tunnel. RAE Aero Report 2685, 1963.

MASKELL, E.C. Theory of the blockage effects on bluff bodies and stalled wings in a closed wind tunnel. ARC R and M No.3400, 1965.

MORISON, J.R., O'BRIEN, M.P., JOHNSON, J.W. & SCHAAF, S.A. The force exerted by surface waves on piles. AIME Petroleum Transactions, Volume 189, 1950.

NAKAMURA, Y. & MIZOTA, T. Unsteady lifts and wakes of oscillating rectangular prisms. Proc. A.S.C.E. Vol.101, pp 855-871, 1975.

NAKAMURA, Y. & OHYA, Y. The effects of turbulence intensity and scale on the mean flow past square rods. Journal of Wind Engineering and Industrial Aerodynamics, Vol.11, pp 421-430, 1983.

NOVAK, M. Aeroelastic galloping of prismatic bodies. Proc. A.S.C.E., pp 115-142, 1969.

NOVAK, M. & DAVENPORT, A.G. Aeroelastic instability of prisms in turbulent flow. Proc. A.S.C.E. Journal of the Engineering Mechanics Division, pp 17-39, 1970.

OBASAJU, E.D. Pressure fluctuations on stationary and oscillating square section cylinders. PhD Thesis, Department of Aeronautics, Imperial College, London, 1977.

OBASAJU, E.D. On the effects of end plates on the mean forces on square section cylinders. Journal of Industrial Aerodynamics, Vol.5, pp 179-186, 1979.

OBASAJU, E.D. Forced-vibration study of the aeroelastic instability of a square-section cylinder near vortex resonance. Journal of Wing Engineering and Industrial Aerodynamics, Vol.12, pp 313-327, 1983(a).

OBASAJU, E.D. An investigation of the effects of incidence on the flow around a square section cylinder. The Aeronautical Quarterly, Vol.XXXIV, Part 4, pp 243-259, 1983(b).

OKAJIMA, A. Strouhal numbers of rectangular cylinders. Journal of Fluid Mechanics, Vol.123, pp 379-398, 1982.

OLIVARI, D. An investigation of vortex shedding and galloping induced oscillation on prismatic bodies. Journal of Wind Engineering and Industrial Aerodynamics, Vol.11, pp 307-319, 1983.

OTSUKI, Y., WASHIZU, K., TOMIZAWA,H. & OHYA, A. A note on the aeroelastic instability of a prismatic bar with square section. Journal of Sound and Vibration, Vol.34(2), pp 233-248, 1974.

PARKINSON, G.V. Wind induced instability of structures. Phil. Trans. Roy. Soc. Lond. A, Vol.269, pp 395-409, 1971.

PARKINSON, G.V. Mathematical models of flow-induced vibrations of bluff bodies. IUTAM-IAHR Symposium Karlsruhe, (Ed. NAUDASCHER), 1972.

PARKINSON, G.V. Nonlinear oscillator modelling of flow-induced vibrations. IUTAM-IAHR Symposium Karlsruhe, pp 786-791, (Ed. NAUDASCHER), 1979.

PARKINSON, G.V. Some considerations of combined effects of galloping and vortex resonance. Journal of Wind Engineering and Industrial Aerodynamics, Vol.8, pp 135-143, 1981.

PARKINSON, G.V. & BROOKS, N.P.H. On the aeroelastic instability of bluff cylinders. Trans. A.S.M.E. Journal of Applied Mechanics, pp 252-258, 1961.

PARKINSON, G.V. & SMITH, J.D. The square prism as an aeroelactic non-linear oscillator. Quarterly Journal of Mechanics and Applied Mathematics, Vol.17, 1964.

PARKINSON, G.V. & SULLIVAN, P.D. Galloping response of towers. Journal of Industrial Aerodynamics, Vol.4, pp 253-260, 1979.

PARKINSON, G.V. & WAWZONEK, M.A. Some considerations of combined effects of galloping and vortex resonance. Journal of Wing Engineering and Industrial Aerodynamics, Vol.8, pp 135-143, 1981.

PETTY, D.G. The effects of turbulence intensity and scale on the flow past square prisms. Journal of Industrial Aerodynamics, Vol.4, pp 247-252, 1979.

PIPES, L.A. & HARVILL, L.R. Applied mathematics for engineers and physicists. McGraw Hill, 1970.

POCHA, J.J. On unsteady flow past cylinders of square-section. PhD Thesis, Department of Aeronautics, Queen Mary College, London, 1971.

PRENDERGAST, V. Measurement of two-points correlation of the surface pressure on a circular cylinder, UTIA Technical Note No.23, 1958.

ROBERTSON, J.M., WEDDING, J.B., PETERKA, J.A. & CERMAK, J.E. Wall pressure of separation-reattachment flow on a square prism in uniform flow. Journal of Industrial Aerodynamics, Vol.2, pp 345-359, 1977/78.

ROCKWELL, D.O. Organized fluctuations due to flow past a square cross section cylinder. Unpublished report, Institute of Hydromechanics, University of Karlsruhe, West Germany, 1976.

SAKAMOTO, H. & ARIE, M. Vortex shedding from a rectangular prism and a circular cylinder placed vertically in a turbulent boundary layer. Journal of Fluid Mechanics, Vol.126, pp 147-165, 1983.

SARPKAYA, T. Fluid forces on oscillating cylinders. A.S.C.E. Journal of the Waterway Port Coastal and Ocean Division, 1978.

SARPKAYA, T. Vortex-induced oscillations - A selective review. Trans. A.S.M.E. Journal of Applied Mechanics, Vol.106, pp 241-258, 1979.

SARPKAYA, T. & ISAACSON, M. Mechanics of wave forces on offshore structures. Van Nostrand Reinhold Co., 1981.

SKOP, R.A. & GRIFFIN, O.M. A model for the vortex-excited resonant response of bluff cylinders. Journal of Sound and Vibration, Vol.27, pp225-233, 1973.

SURRY, D. & STATHOPOULOS, T. An experimental approach to the economical measurement of spatially-averaged wind loads. Journal of Industrial Aerodynamics, Vol.2, pp 385-397, 1977/78.

TRITTON, D.J. Physical fluid dynamics. Van Nostrand Reinhold Company, 1977.

VAN DER POL, B. Forced oscillations in a circuit with non-linear resistance. Philosophical Magazine, Vol.3, Series 7, 1927.

VICKERY, B.J. Fluctuating lift and drag on a long cylinder of square cross-section in a smooth and in a turbulent stream. Journal of Fluid Mechanics, Vol.25, Part 3, pp 481-494, 1966.

WASHIZU, K., OHYA, A., OTSUKI, Y. & FUJII, K. Aeroelastic instability of rectangular cylinders in a heaving mode. Journal of Sound and Vibration, Vol.59, pp 195-210, 1978.

WAWZONEK, M.A. Aeroelastic behaviour of square prisms in uniform flow. M.A.Sc Thesis, Department of Mechanical Engineering, University of British Columbia, 1979.

WAWZONEK, M.A. & PARKINSON, G.V. Combined effects of galloping instability and vortex resonance. Fifth International Conference on Wind Effects on Building and Structures, pp VI-2-1 to VI-2-12, 1979.

WILKINSON, R.H. On the vortex induced loading on long bluff cylinders. PhD Thesis, Department of Civil Engineering, University of Bristol, 1974.

WILKINSON, R.H. Fluctuating pressures on an oscillating square prism. Part 1: Chordwise distribution of fluctuating pressure. Aeronautical Quarterly, Vol.32, pp 97-110, 1981(a).

WILKINSON, R.H. Fluctuating pressure on an oscillating square prism. Part II: Spanwise correlation and loading. Aeronautical Quarterly, Vol.32, pp 111-125, 1981(b).

ZAKS, R. Programming the 6502. 3rd edition, Sybex, 1980.

ZDRAVKOVICH, M.M. Modification of vortex shedding in the synchronization range. Trans. A.S.M.E. Journal of Fluids Engineering, Vol.104, pp 513-517, 1982.

APPENDIX A

TO EXPAND C(k) AS A SERIES OF k

An expression from Bisplinghoff, Ashley & Halfman (1957) for lift force acting on an aerofoil oscillating in incompressible flow was adopted in section 7.2.2 for derivation of the in phase and 90 degrees out of phase (with respect to cylinder displacement) part of the lift coefficient. The function C(k) where $k = \pi/U_r$ appeared in the expression for the lift force eqn (7.11). C(k) is expressed as:

$$C(k) = \frac{H_1^{(2)}(k)}{H_1^{(2)}(k) + iH_0^{(2)}(k)} \qquad (A.1)$$

where $H_0^{(2)}$ = Hankel function of the second kind of order 0

$H_1^{(2)}$ = Hankel function of the second kind of order 1

and $i = \sqrt{-1}$.

Hankel function (sometimes known as Bessel function of the third kind) is expressible in Bessel function of the first and second kind ($J_n(k)$ and $Y_n(k)$ respectively) as follows:

$$H_0^{(2)} = J_0(k) - iY_0(k) \tag{A.2}$$

$$H_1^{(2)} = J_1(k) - iY_1(k) \tag{A.3}$$

Substitute eqns (A.2) and (A.3) into (A.1) and in order to save space represent $J_0(k)$ by J_0 etc.

$$C(k) = \frac{J_1 - iY_1}{J_1 - iY_1 + iJ_0 - i^2Y_0}$$

$$= \frac{(J_1 - iY_1)(A - iB)}{A^2 + B^2} \quad \text{where} \quad \begin{aligned} A &= J_1 + Y_0 \\ B &= J_0 - Y_1 \end{aligned}$$

$$= \frac{(J_1A - Y_1B) - i(J_1B + Y_1A)}{A^2 + B^2}$$

$$= \frac{J_1(J_1+Y_0) - Y_1(J_0 - Y_1) - i\left[J_1(J_0 - Y_1) + Y_1(J_1 + Y_0)\right]}{J_0^2 + J_1^2 + Y_0^2 + Y_1^2 + 2J_1Y_0 - 2J_0Y_1}$$

$$= \frac{J_1^2 + Y_1^2 + J_1Y_0 - J_0Y_1 - i(J_0J_1 + Y_0Y_1)}{J_0^2 + J_1^2 + Y_0^2 + Y_1^2 + 2J_1Y_0 - 2J_0Y_1}$$

or $$C(k) = \frac{D_1(k) - iD_2(k)}{D(k)}$$

$$= F(k) + iG(k) \tag{A.4}$$

where:

$$D_1(k) = J_1^2 + Y_1^2 + J_1Y_0 - J_0Y_1 \tag{A.5}$$

$$D_2(k) = J_0J_1 + Y_0Y_1 \tag{A.6}$$

$$D(k) = J_0^2 + J_1^2 + Y_0^2 + Y_1^2$$

$$+ 2J_1Y_0 - 2J_0Y_1 \qquad (A.7)$$

$J_n(k)$, Bessel function of the first kind of order "n" can be expressed as:

$$J_n(k) = \sum_{s=0}^{\infty} \frac{(-1)^s}{\Pi(s)\,\Pi(n+s)} \left(\frac{k}{2}\right)^{n+2s} \qquad (A.8)$$

It can be shown (see appendix B of Pipes & Harvill) that:

$$\lim_{k\to o} J_n(k) \sim \frac{k^n}{2^n \Pi(n)}$$

if n is an positive integer, then

$$\lim_{k\to o} J_n(k) = \frac{k^n}{2^n n!} \qquad (A.9)$$

Therefore

$$\lim_{k\to o} J_o(k) = 1 \qquad (A.10)$$

$$\lim_{k\to o} J_1(k) = \frac{k}{2} \qquad (A.11)$$

From appendix B of Pipes & Harvill, $Y_0(k)$ and $Y_1(k)$, Bessel function of the second kind and order zero and one respectively, can be expressed as:

$$Y_0(k) = \frac{2}{\pi}\left[J_0(k)\left(\ln\frac{k}{2}+\nu\right)+\left(\frac{k}{2}\right)^2 - \frac{\left(1+\frac{1}{2}\right)\left(\frac{k}{2}\right)^4}{(2!)^2}+\left(1+\frac{1}{2}+\frac{1}{3}\right)\frac{\left(\frac{k}{2}\right)^6}{(3!)^2}-\ldots\right] \qquad (A.12)$$

where $\ln = \log_e$ and ν = Euler constant.

$$\nu = \lim_{n\to\infty}\left[1+\frac{1}{2}+\frac{1}{3}+\ldots\ldots\ldots+\frac{1}{n}-\ln(n)\right]$$

$$\sim 0.5772157$$

For small k (O(0.01)), k^3 and higher order terms are negligible

$$Y_0(k) \sim \frac{2}{\pi}\left[\ln\frac{k}{2}+\frac{k^2}{4}+\nu\right] \qquad (A.13)$$

and

$$Y_1(k) = \frac{1}{\pi}\left[2J_1(k)\left(\ln\frac{k}{2}+\nu\right)-\sum_{r=0}^{\infty}(-1)^r\frac{\left(\frac{k}{2}\right)^{1+2r}}{r!(r+1)!}\cdot\left(\sum_{m=1}^{1+r}m^{-1}+\sum_{m=1}^{r}m^{-1}\right)-\sum_{r=0}^{0}\left(\frac{k}{2}\right)^{2r-1}\frac{(-r)!}{r!}\right] \qquad (A.14)$$

Substituting $J_1(k)$ by k/2 and expand all the summation terms to k^2, it can be shown that:

$$Y_1(k) \sim \frac{1}{\pi}\left[k\ln\frac{k}{2}+k\nu-\frac{k}{2}-\frac{2}{k}\right] \qquad (A.15)$$

Squaring eqns (A.10), (A.11), (A.13) and (A.15), it can be shown that:

$$J_0^2(k) \sim 1 \tag{A.16}$$

$$J_1^2(k) \sim k^2/4 \tag{A.17}$$

$$Y_0^2(k) \sim \frac{4}{\pi^2}\left[\ln^2\frac{k}{2} + \nu^2 + \frac{k^2}{2}\ln\frac{k}{2} + \frac{\nu k^2}{2} + 2\nu\ln\frac{k}{2}\right] \tag{A.18}$$

$$Y^2(k) \sim \frac{1}{\pi^2}\left[k^2\ln^2\frac{k}{2} + \ln\frac{k}{2}(2\nu k^2 - k^2 - 4) + k^2\left(\nu^2 + \frac{1}{4} - \nu\right) + (2-4\nu) + \frac{4}{k^2}\right] \tag{A.19}$$

Substituting eqns (A.10), (A.11), (A.13), (A.15), (A.16), (A.17), (A.18) and (A.19) into (A.5), (A.6) and (A.7), it can be shown that:

$$D_1(k) = \frac{k^2}{\pi^2}\ln^2\frac{k}{2} + \ln\frac{k}{2}\left(\frac{2\nu k^2}{\pi} - \frac{k^2}{\pi^2} - \frac{4}{\pi^2}\right) + k^2\left[\frac{1}{\pi^2}\left(\nu - \frac{1}{2}\right)^2 + \frac{1}{4}\right] + \frac{k}{2\pi} + \frac{2-4\nu}{\pi^2} + \frac{2}{\pi k} + \frac{4}{\pi^2 k^2} \tag{A.20}$$

$$D_2(k) = \frac{2k}{\pi^2} \ln^2 \frac{k}{2} + \frac{2}{\pi^2} \cdot \ln \frac{k}{2}\left(2\nu k - \frac{k}{2} - \frac{2}{k}\right)$$

$$+ \frac{2k}{\pi^2}\left(\frac{\pi^2}{4} + \nu^2 - \frac{\nu}{2} - \frac{1}{2}\right)$$

$$- \frac{4\nu}{\pi^2 k} \qquad \text{(A.21)}$$

$$D(k) = \frac{1}{\pi^2}\left(4+k^2\right)\ln^2\frac{k}{2} + \ln\frac{k}{2} \cdot \frac{1}{\pi^2}\left(k^2+8\nu+2\nu k^2-4+2\pi k\right)$$

$$+ \frac{k^2}{\pi^2}\left[\left(\nu+\frac{1}{2}\right)^2 + \frac{\pi^2}{4}\right] + \frac{k}{\pi} + \frac{2}{\pi^2}\left(2\nu^2-2\nu+1\right)$$

$$+ \left(1 + \frac{2}{\pi k}\right)^2 \qquad \text{(A.22)}$$

Substituting (A.20), (A.21) and (A.22) into (A.4) therefore provide a series expansion of C(k) for small k (O(0.01)).

A/D	$U_{r,min}$	$U_{r,ss}$	$\alpha_{max,min}$	$\alpha_{max,ss}$
.1	10.47	20.29	3.43	1.77
.25	13.06	38.17	6.86	2.36
.5	18.04	47.27	9.88	3.80
.675	23.77	57.19	10.12	4.24
1.0	29.56	66.15	12.0	5.43
1.5	40.59	82.53	13.07	6.51
2.0	49.87	102.98	14.14	6.96

TABLE 5.1

A/D	$U_{r,0}$	$U_{r,80}$	$\alpha_{max,0}$	$\alpha_{max,80}$
.1	7.54	57.54	4.76	0.63
.25	8.82	63.97	10.10	1.41
.5	16.18	64.71	10.99	2.78
.675	15.96	64.95	14.88	3.74
1.0	20.35	88.18	17.16	4.08
1.5	25.85	84.06	20.03	6.40
2.0	37.53	96.71	18.51	7.40

TABLE 5.2

U_r	a/D	b/D	b/a	S	$\Gamma/U_\infty D$	Remarks
7.65	2.74	2.39	0.87	0.12	3.71	Type A
13.39	6.84	1.16	0.17	0.072	14.36	Type B
21.42	3.49	1.73	0.5	0.139	3.93	Triple
26.78	5.57	2.01	0.36	0.129	3.82	Intermediate
35.71	5.43	1.58	0.29	0.13	4.31	Intermediate
53.56	6.18	1.29	0.21	0.13	4.22	QS
97.38	6.36	0.87	0.14	0.13	5.47	QS
∞	6.38	0.86	0.13	0.128	6.13	Stationary

TABLE 6.1

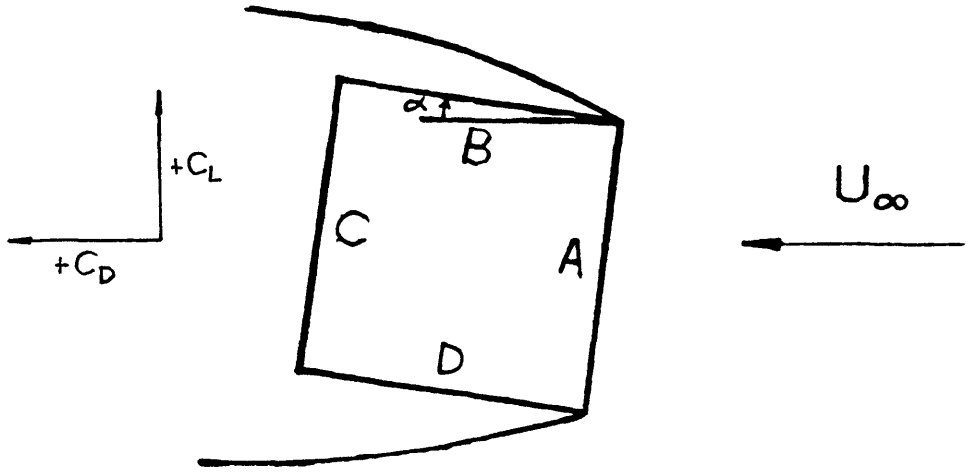


Fig. 1.1 Square Cylinder inclined to free stream
Nomenclature of faces.

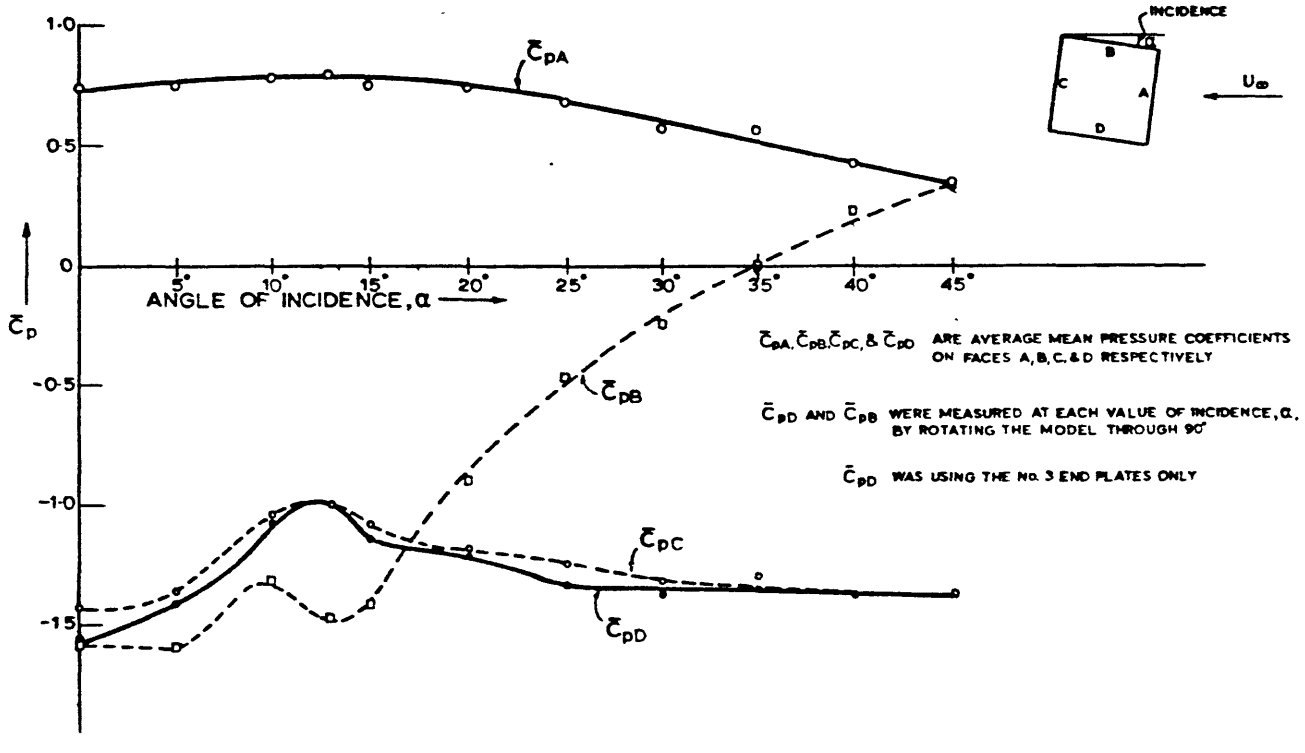
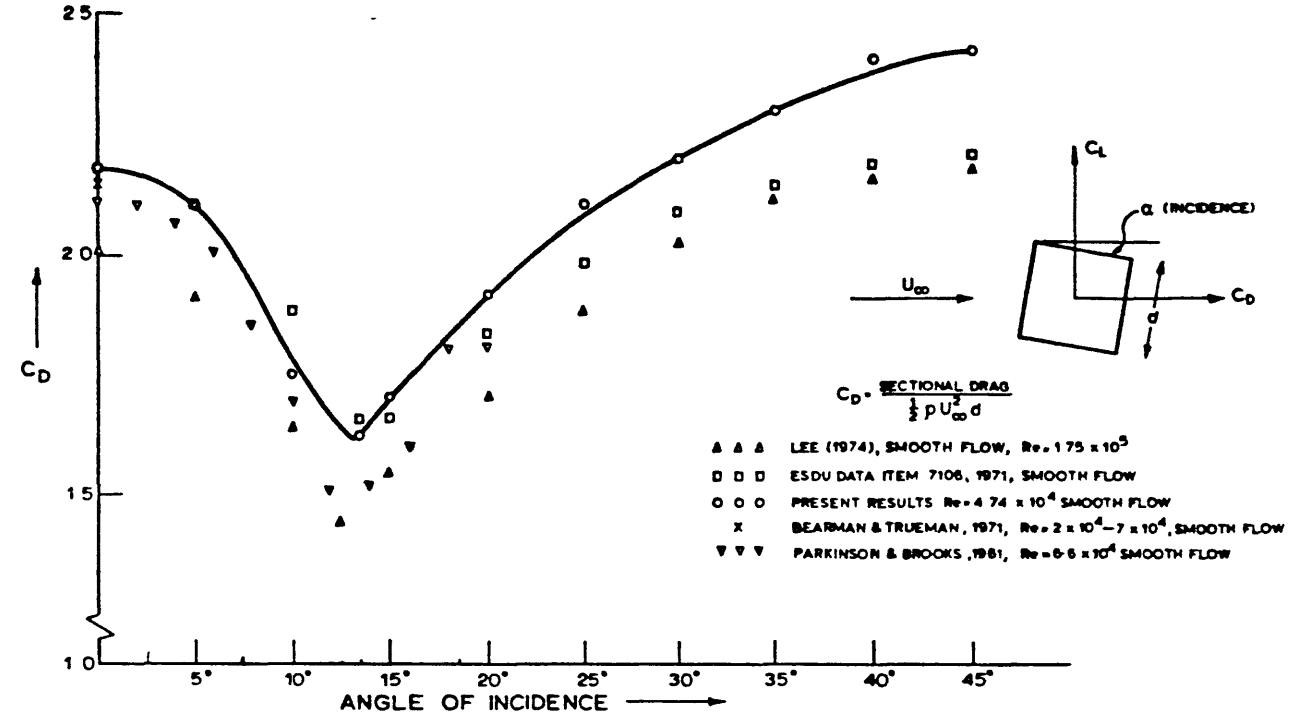


Fig. 1.2 Average face pressure coefficients vs angle of incidence.
From Obasaju (1977).



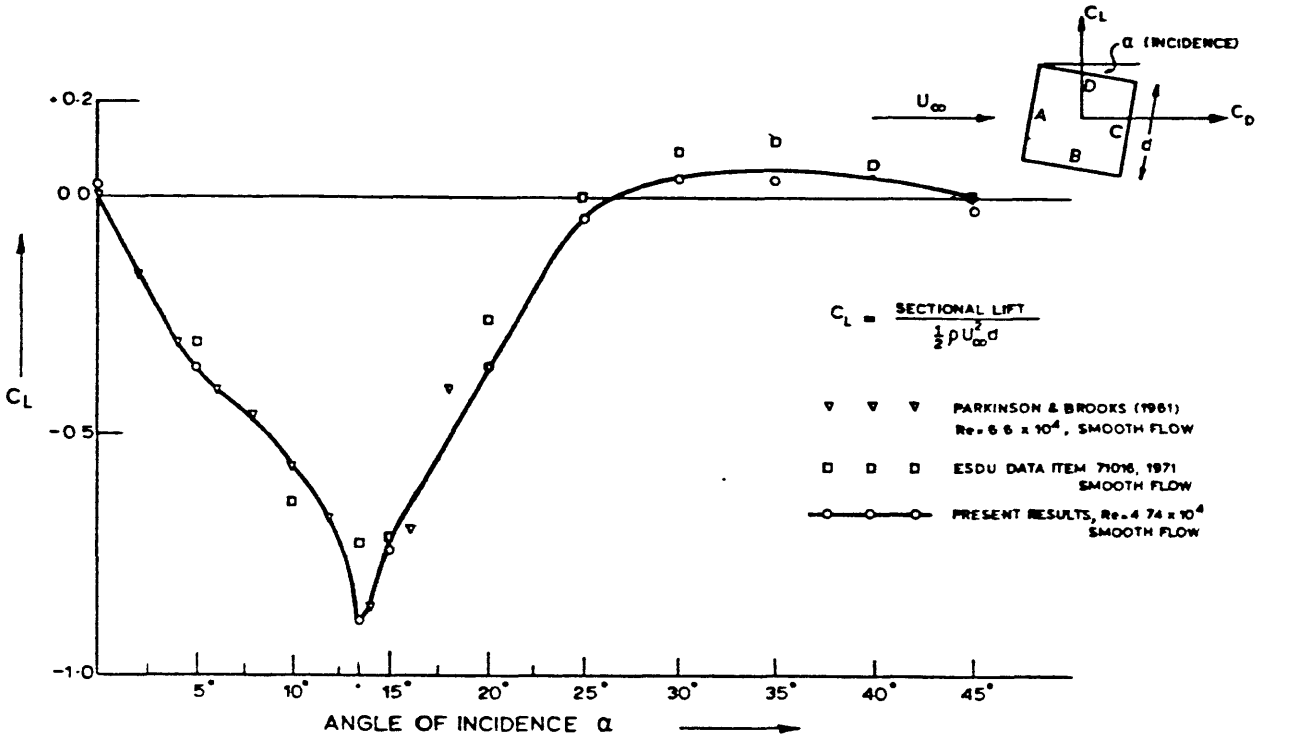
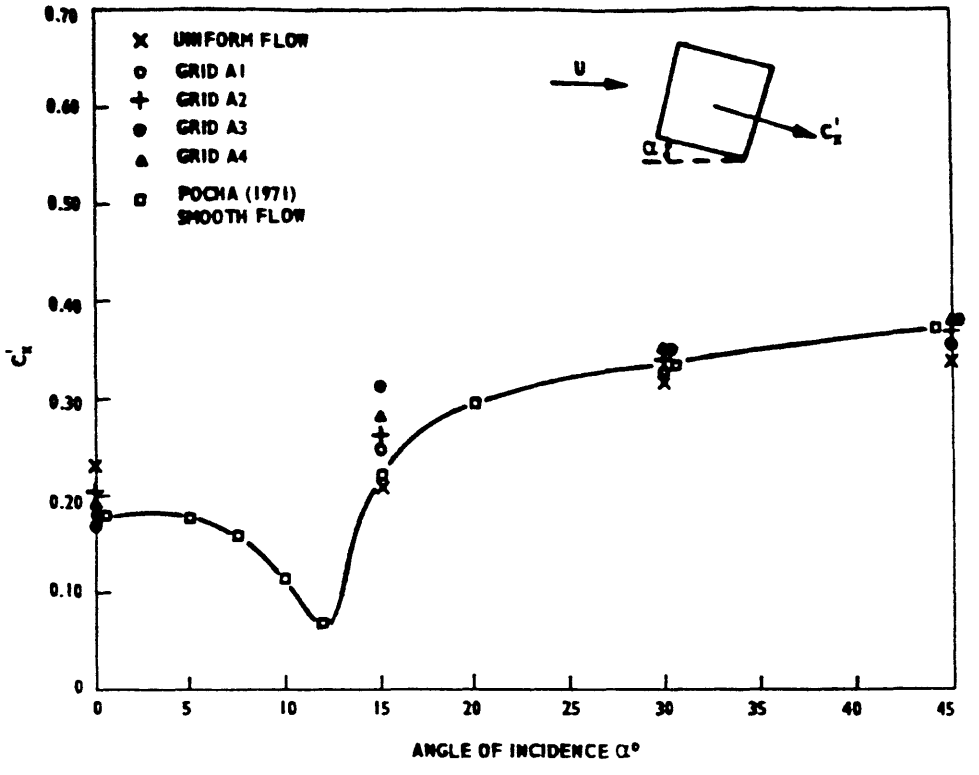


Fig. 1.3(a) Drag coefficient vs angle of incidence. From Obasaju (1977).

Fig. 1.3(b) Lift coefficient vs angle of incidence. From Obasaju (1977).



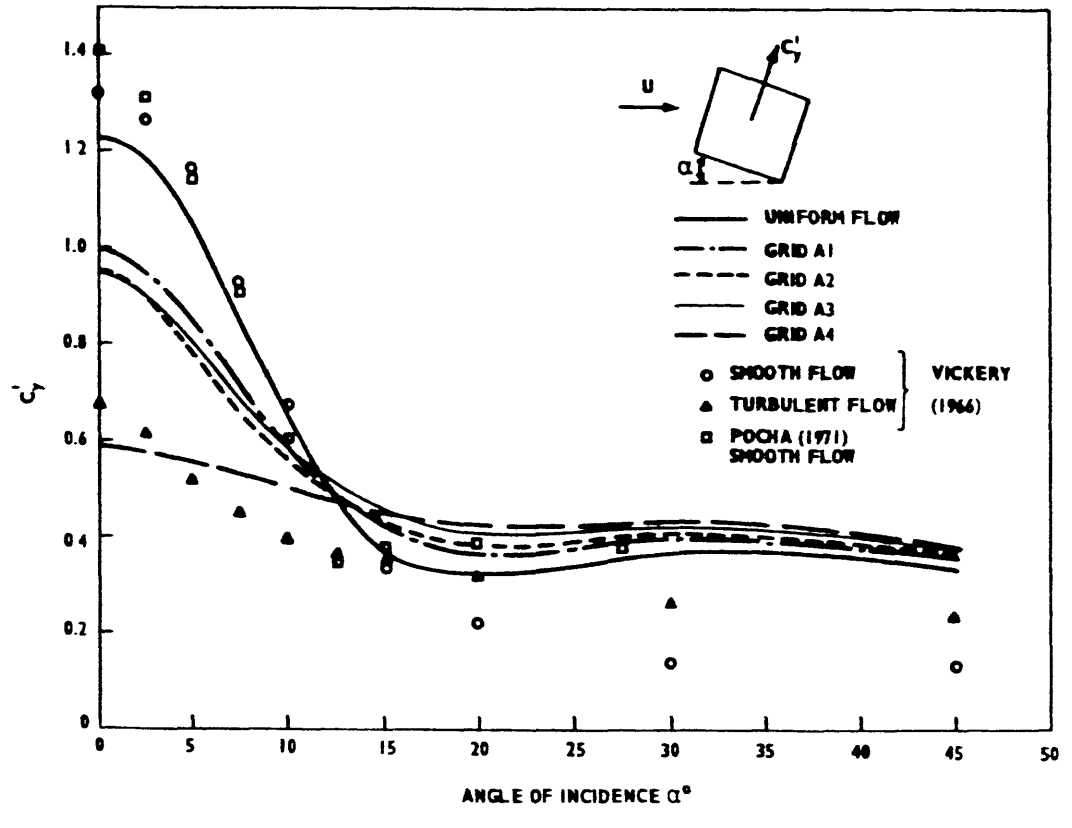


Fig. 1.4(a) R.M.S. body-axis drag vs angle of incidence
From Lee (1974)

Fig. 1.4(b) R.M.S. body-axis lift vs angle of incidence
From Lee (1974)

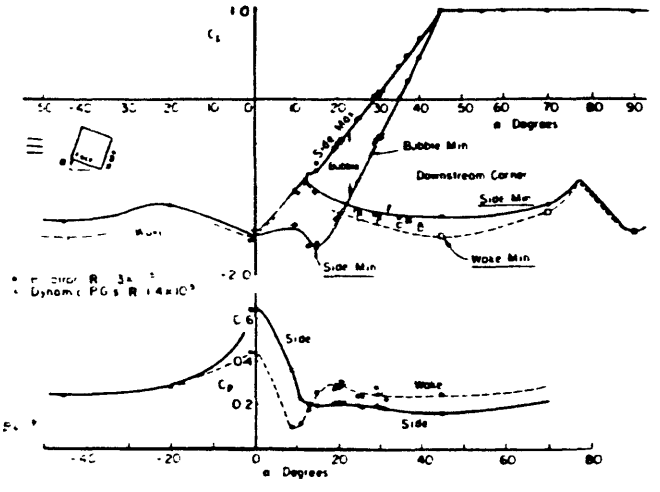


Fig. 1.5(a) Maximum mean and r.m.s. pressure coefficients vs angle of incidence. From Robertson et al (1977/78).

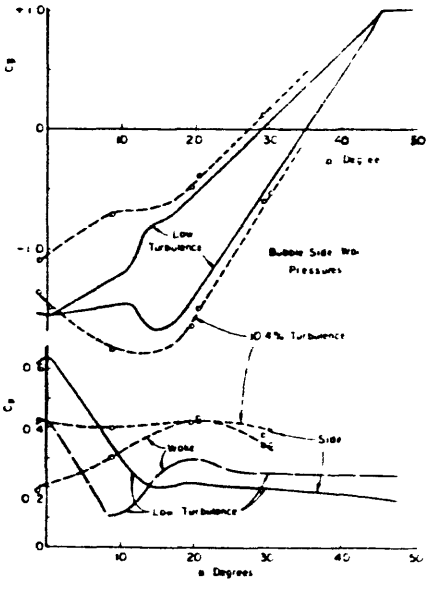
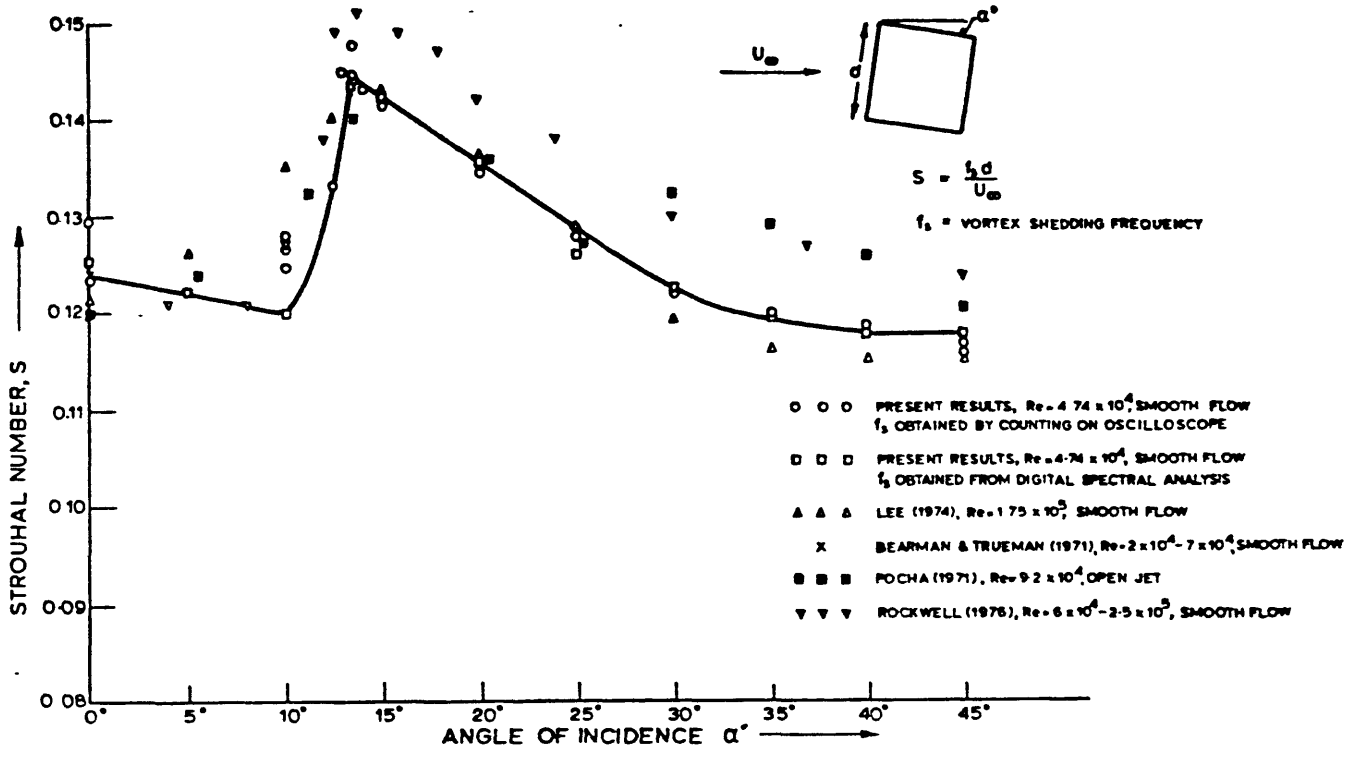


Fig. 1.5(b) Effect of turbulence on mean and r.m.s. pressure coefficients vs angle of incidence. From Robertson et al. (1977/78).



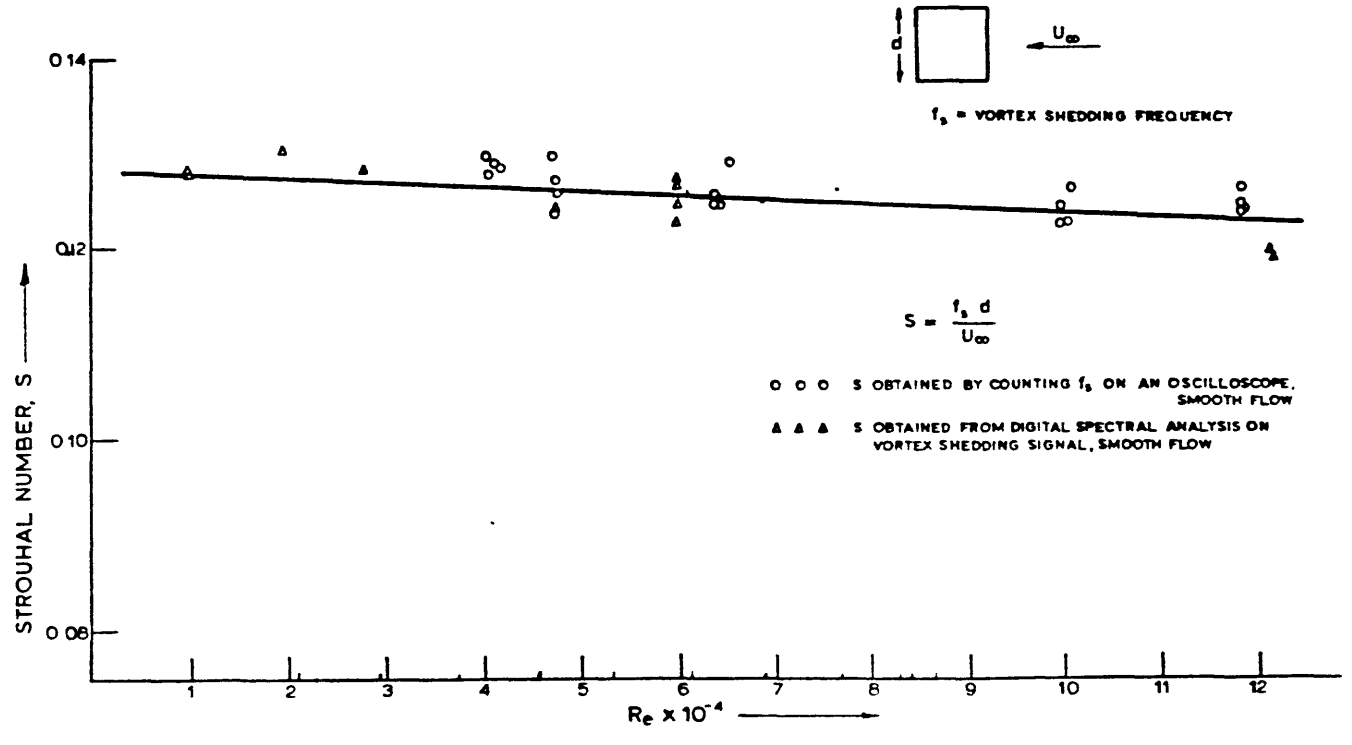


Fig. 1.6(a) Strouhal number vs angle of incidence. From Obasaju (1977).

Fig. 1.6(b) Strouhal number vs Reynolds number. From Obasaju (1977).

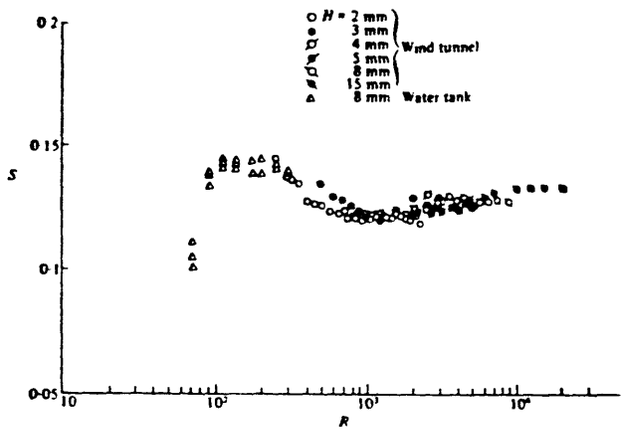


Fig. 1.6(c) Strouhal number vs Reynolds number for a square cylinder. From Okajima (1982).

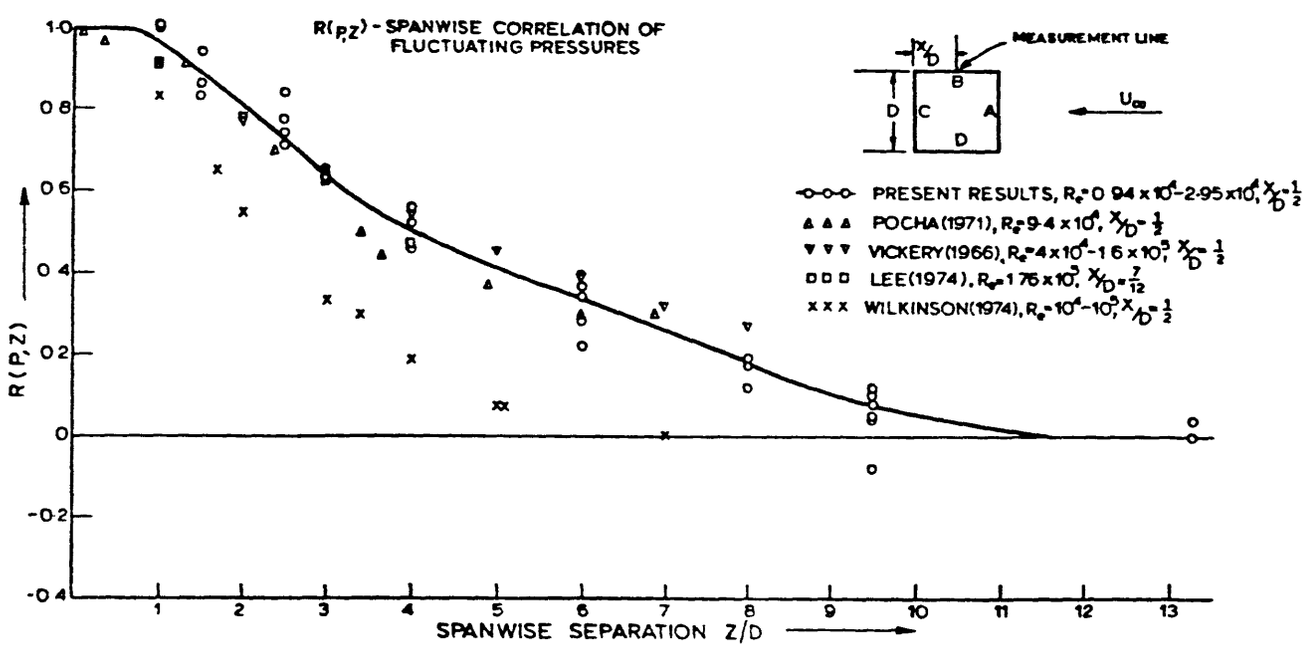


Fig. 1.7(a) Spanwise correlation of fluctuating pressures vs spanwise separation. From Obasaju (1977).

Axial correlation coefficient vs spanwise separation

. Fig. 1.7(b) Face (a)

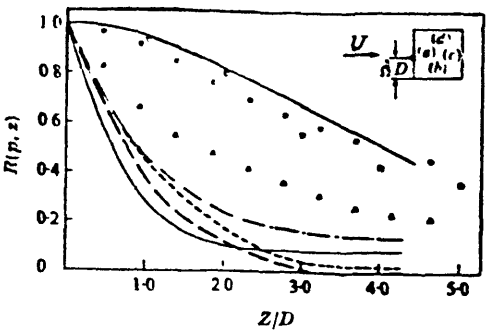


Fig. 1.7(c) Face (b)

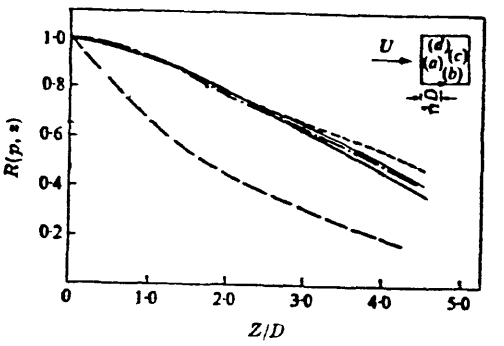
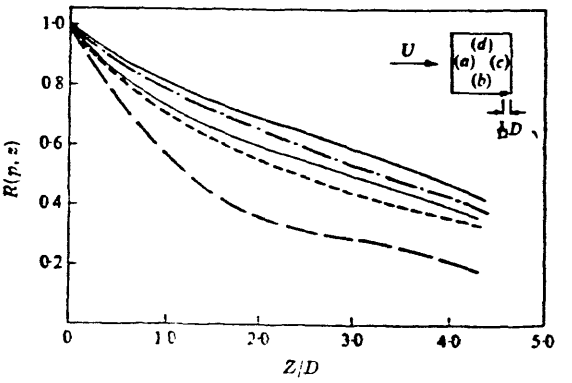


Fig. 1.7(d) Face (c)



Vickery: O, smooth flow; Δ, turbulent. Pocha: ◘,
Lee: Smooth flow ——— ; turbulent flow, grid A1 —·—;
grid A2 ---- ; grid A3 ——— ; grid A4 — — —.
From Lee (1975(a)).

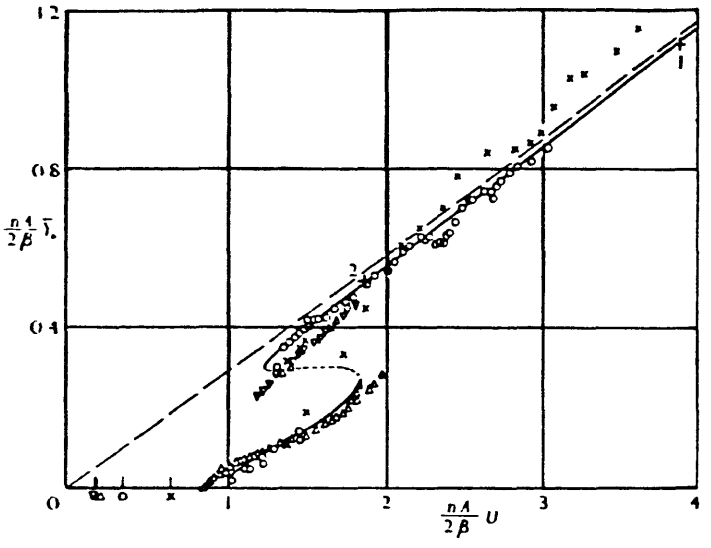


Fig. 1.8 Collapsed amplitude-velocity characteristics. Theory: ——— stable limit cycle, ---- unstable limit cycle. Experiment: x, $\beta = 0.00107$; 0, $\beta = 0.00364$; ∇, $\beta = 0.00372$; +1, $\beta = 0.0012$; +2, $\beta = 0.0032$. Reynolds number 4000 to 20000. From Parkinson and Smith (1964).

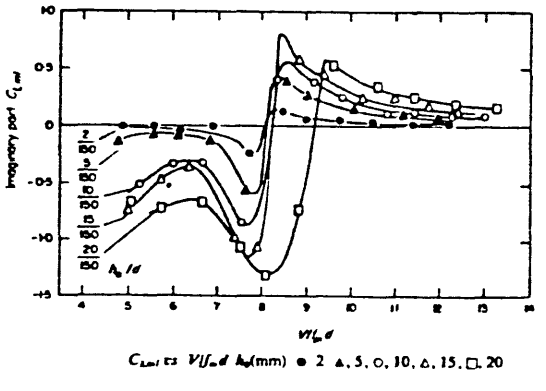


Fig. 1.11 C_{LmI} vs $V/(f_m d)$. From Otsuki et al. (1974).

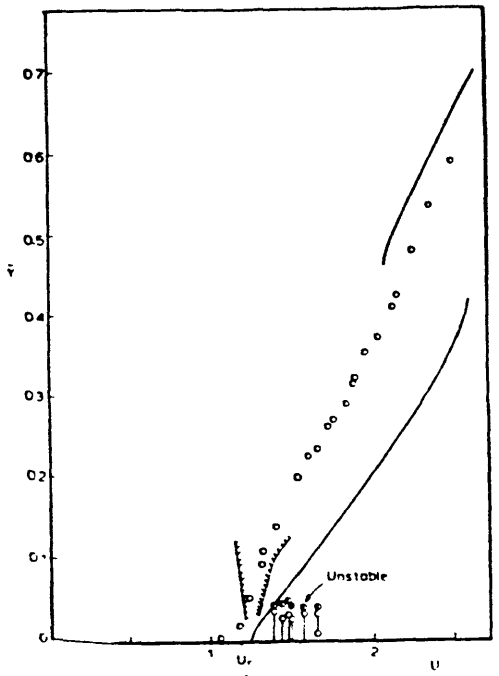


Fig. 1.9(a)

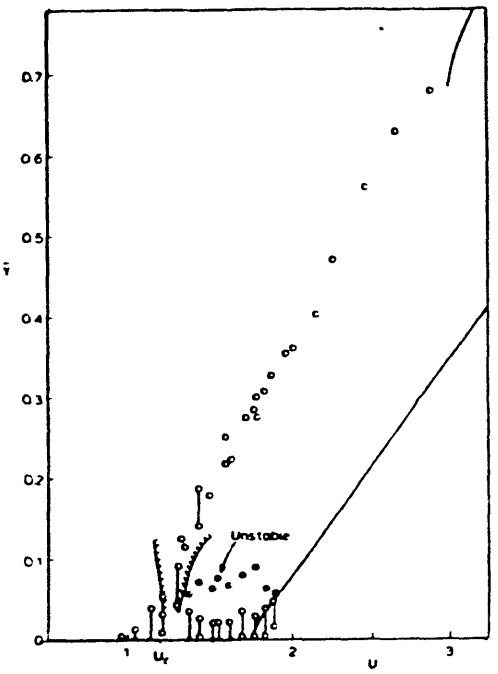


Fig. 1.9(b)

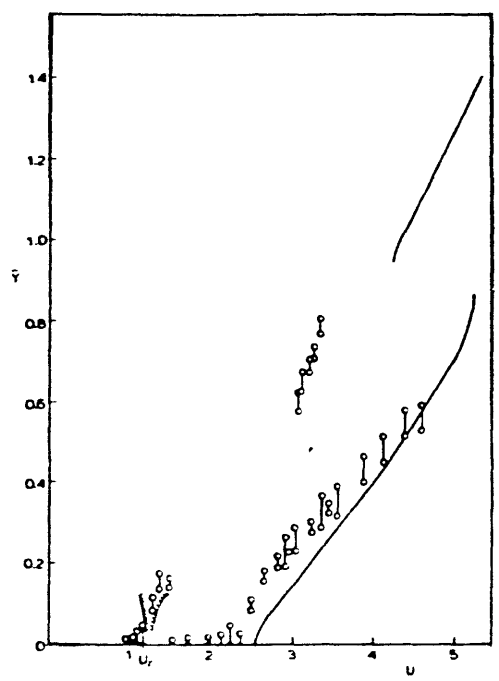


Fig. 1.9(c)

Fig. 1.9(a) Galloping tests, $U_{cr}/U_{ro} = 1.06$, $U_{cr} = 1.25$.

Fig. 1.9(b) Galloping tests, $U_{cr}/U_{ro} = 1.49$, $U_{cr} = 1.76$.

Fig. 1.9(c) Galloping tests, $U_{cr}/U_{ro} = 2.15$, $U_{cr} = 2.54$.
From Parkinson & Wawzonek (1981).

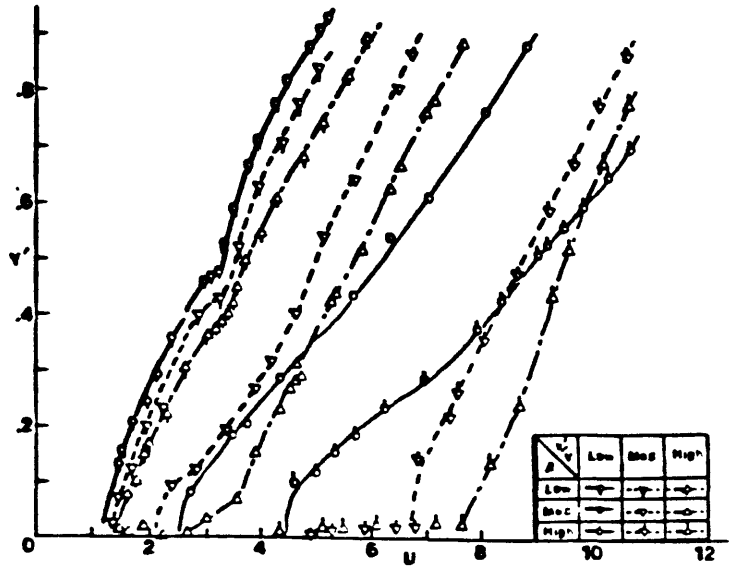


Fig. 1.10(a) R.M.S. displacement vs wind speed.
From Bearman et al. (1984(a)).

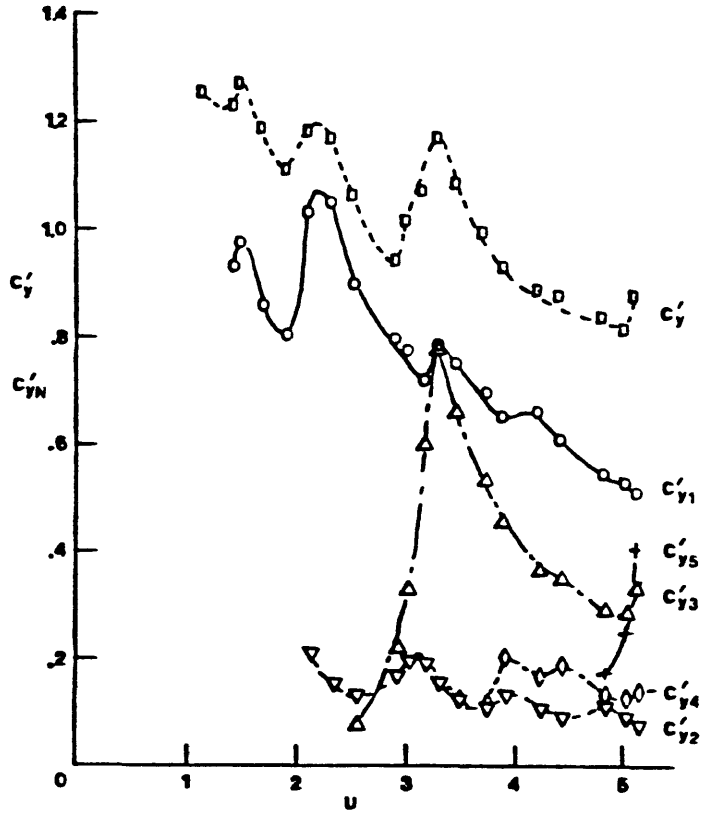


Fig. 1.10(b) C_y' and C_{yN}' vs wind speed.
From Bearman et al. (1984(a)).

Fig. 1.12(a)

Fig. 1.12(b)

Fig. 1.12(c)

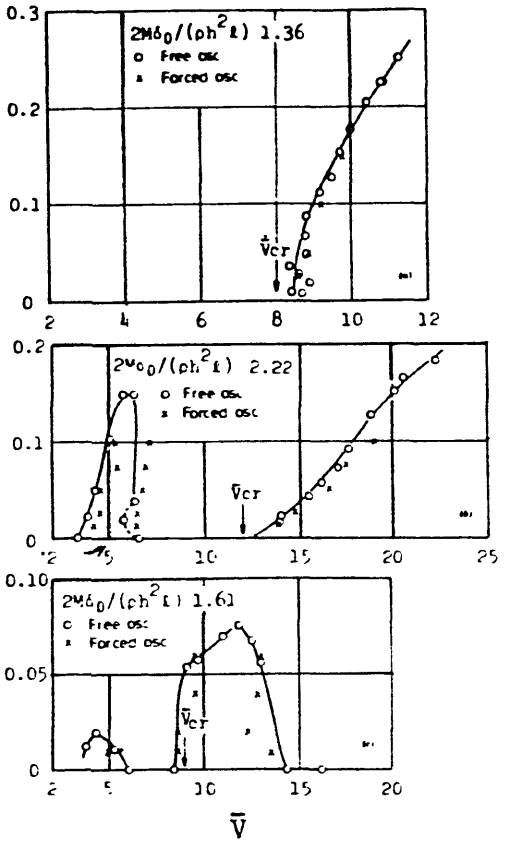


Fig. 1.12 Steady state amplitude vs reduced wind velocity in free oscillation. (a) Model 1:1, (b) model 1:2, (c) model 1:4. From Nakamura & Mizota (1975).

Fig. 1.13(a)

Fig. 1.13(b)

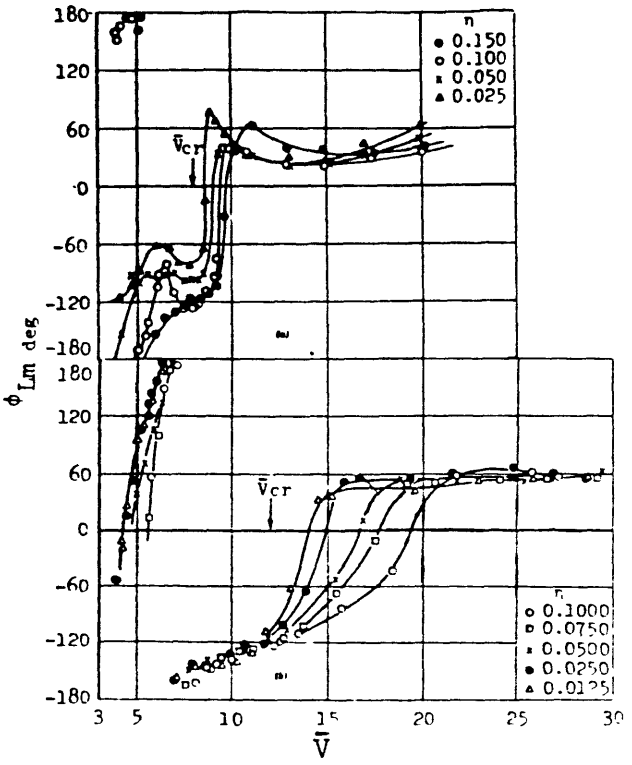


Fig. 1.13(c)

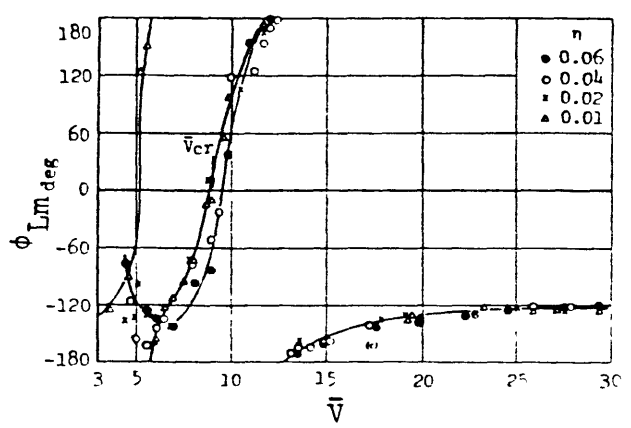


Fig. 1.13 Phase angle of frequency response component of unsteady force coefficient vs reduced wind velocity. (a) Model 1:1, (b) model 1:2, (c) model 1:4. From Nakamura & Mizota (1975).

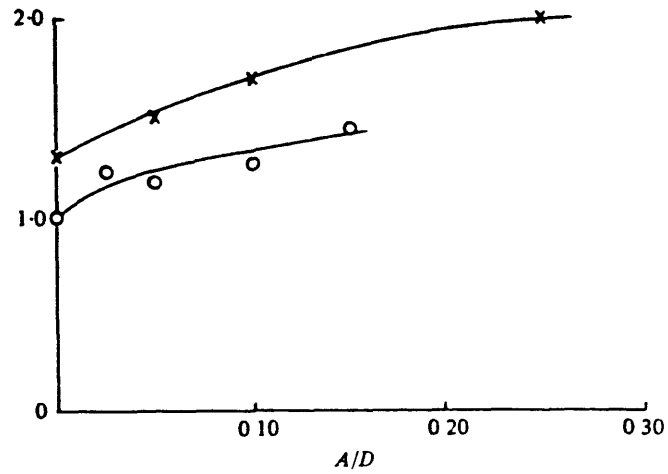


Fig. 1.14(a) Coefficient of fluctuating lift, measured in the vortex lock-in region, versus amplitude ratio. x, Bearman & Obasaju's results estimated from fluctuating pressure; O, results of Nakamura & Mizota (1975) estimated from total force measurements. From Bearman & Obasaju (1982).

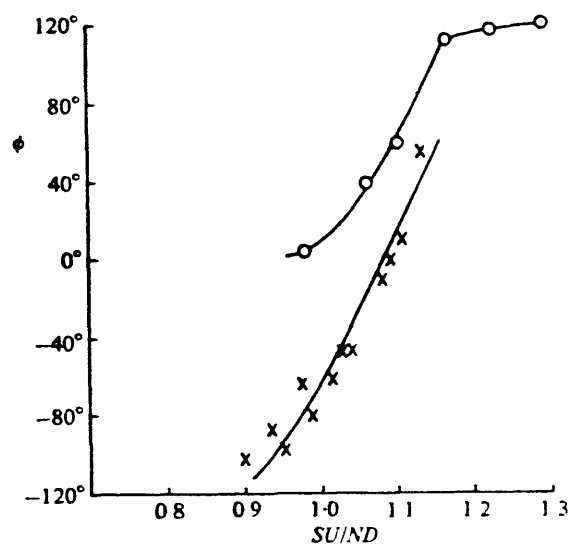


Fig. 1.14(b) Variation through lock-in range of the phase angle between surface suction and cylinder displacement. x,A/D = 0.11, square cylinder, pressure measuring point at the centre of a side face. o, results of Bearman & Currie (1979), A/D = 0.11, circular cylinder, pressure measuring point at 90 degrees from front stagnation point. From Bearman & Obasaju (1982).

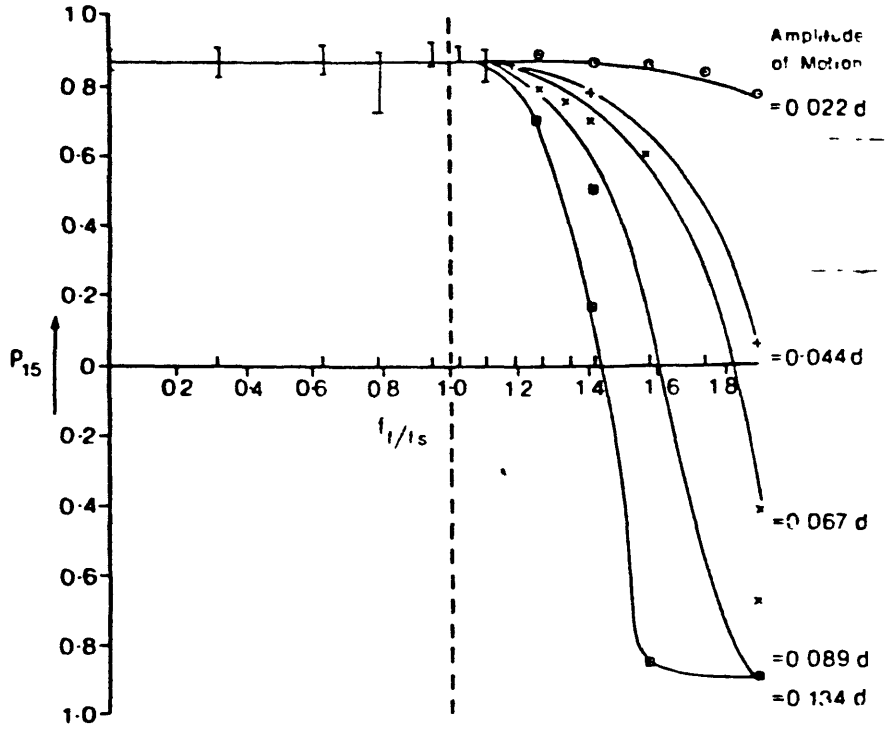


Fig. 1.15 Chordwise pressure correlation ρ_{15} on side face of oscillating cylinder. From Wilkinson (1981(a)).

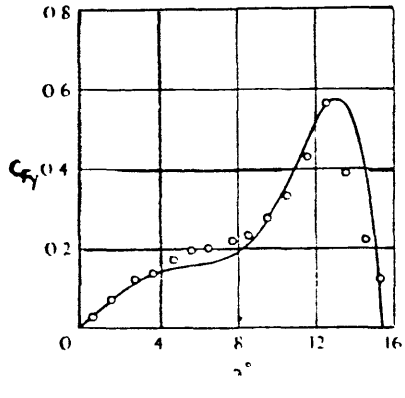


Fig. 1.16 Lateral force coefficient vs angle of incidence. o, experiment, Reynolds number 22300; ——— polynomial approximation, A = 2.69, B = 168, C = 270, D = 59900. From Parkinson & Smith (1964).

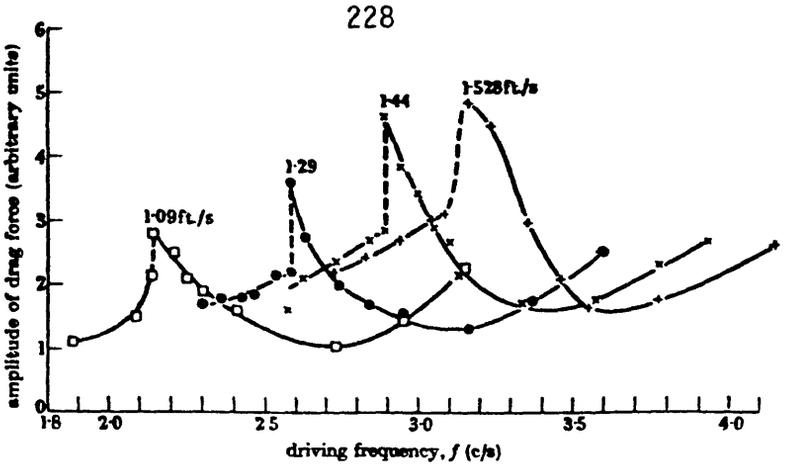


Fig. 1.17(a) Amplitude of drag force vs driving frequency. From Bishop & Hassan (1964(b)).

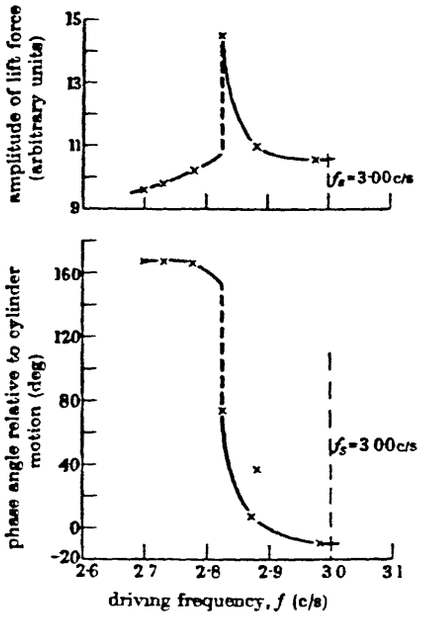


Fig. 1.17(b) Amplitude and phase of lift force vs driving frequency. From Bishop & Hassan (1964(b)).

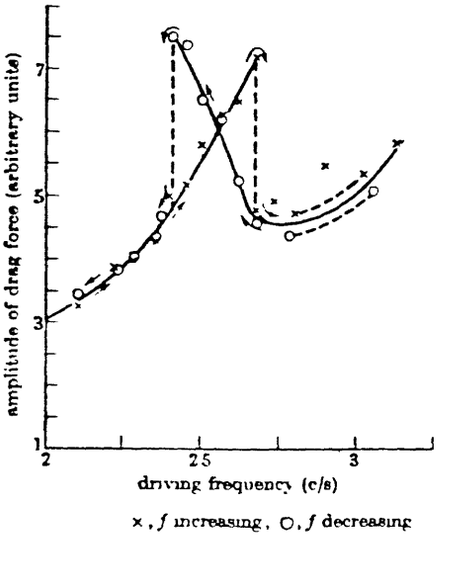


Fig. 1.17(c) Hyteresis effect. Amplitude of drag force vs driving frequency. From Bishop & Hassan (1964(b)).

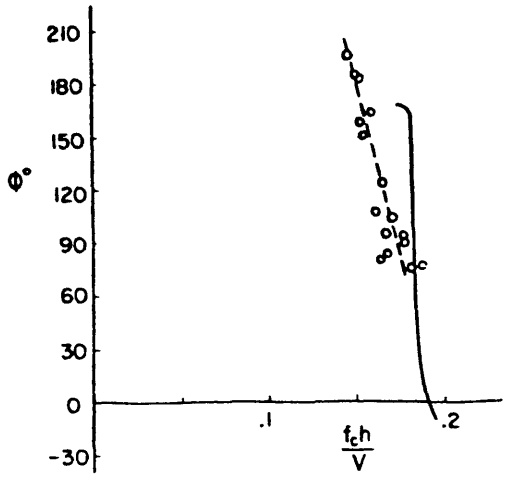


Fig. 1.18 Phase angle between lift force and displacement vs reduced cylinder frequency. o, Ferguson & Parkinson; ——— Bishop & Hassan (1964(b)). From Ferguson & Parkinson (1967).

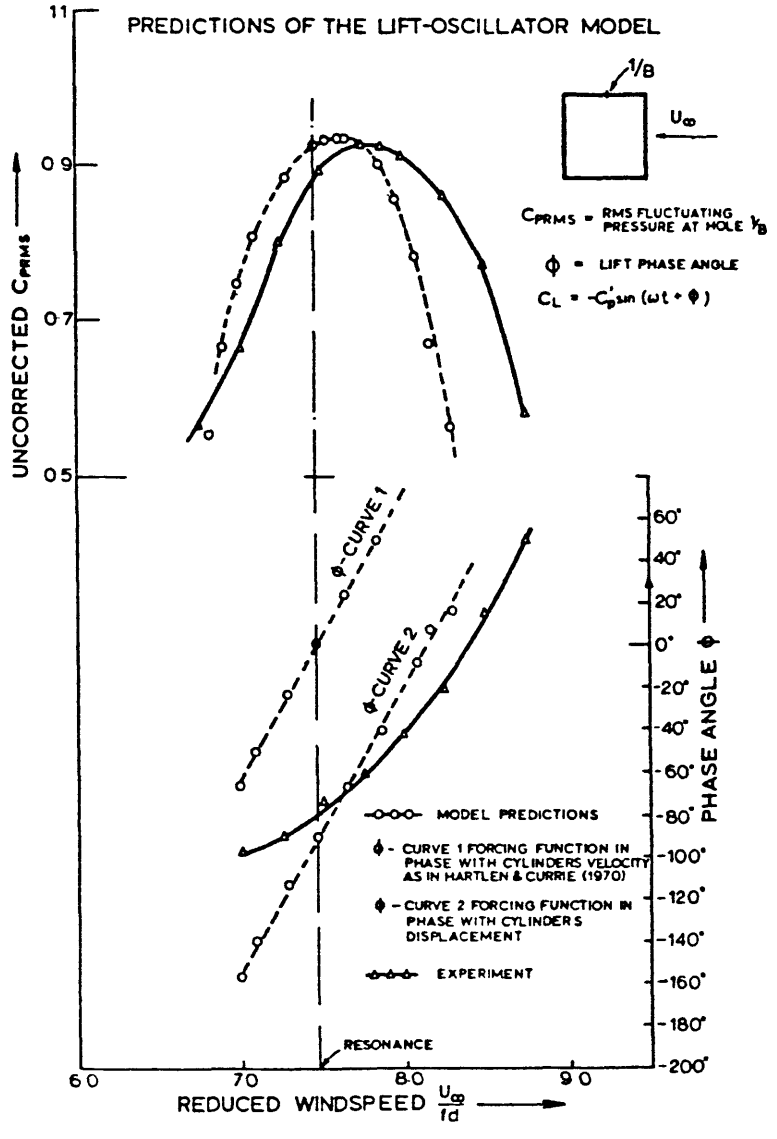


Fig. 1.23 Comparison of theoretical and experimental values of C_{pRMS} and ϕ for synchronised oscillation. From Obasaju (1977).

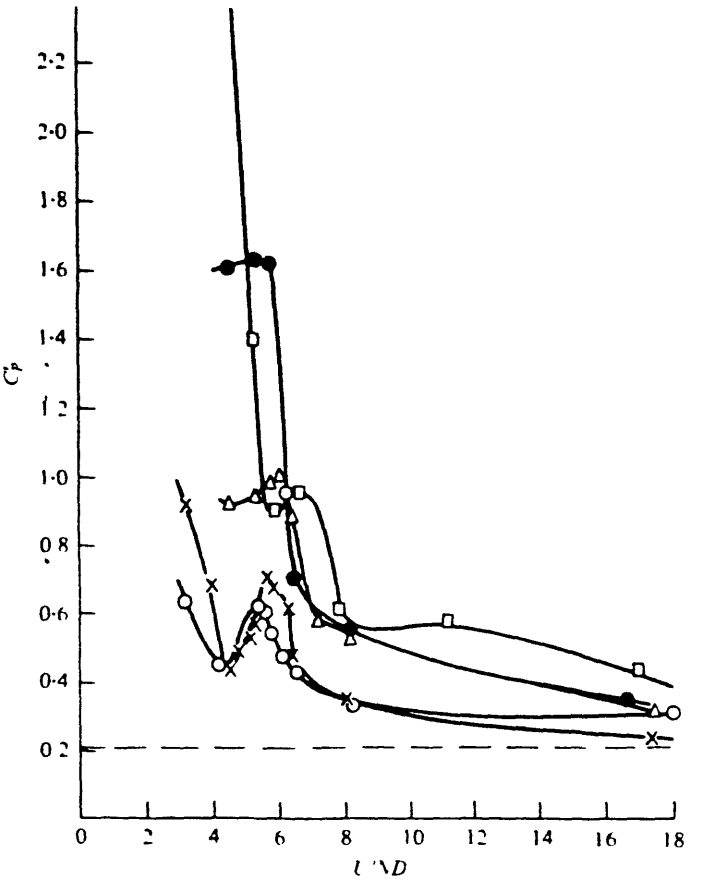


Fig. 1.19(a) Pressure fluctuation at θ = 90 degrees vs reduced velocity, — — , A/D = 0; o, A/D = 0.11; x, A/D = 0.22; Δ, A/D = 0.44; •, A/D = 0.89; □ , A/D = 1.33. From Bearman & Currie (1979).

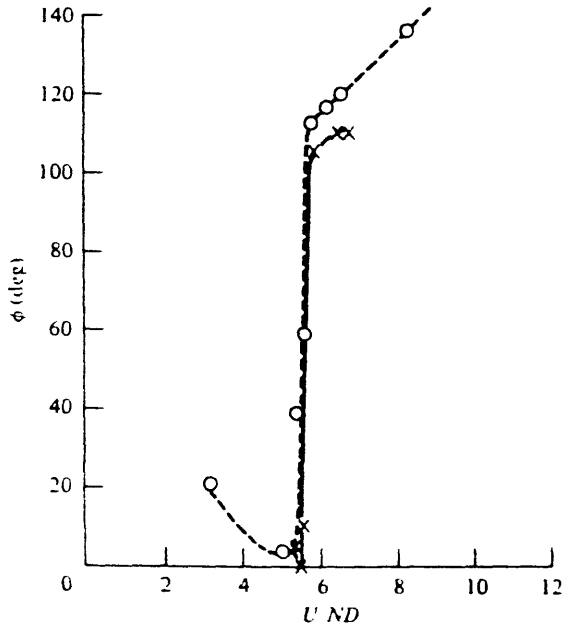


Fig. 1.19(b) Phase measurements on a forced and freely vibrating cylinder at A/D = 0.11. o, forced; x, free (Feng (1966)). From Bearman & Currie (1979).

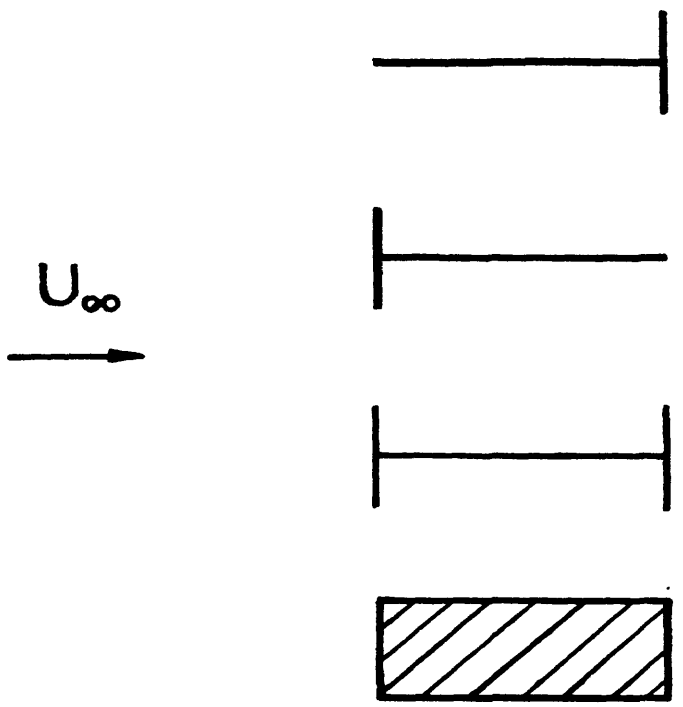


Fig. 1.20 From top to bottom T, L, H and R cylinder used by Komatsu & Kobayashi (1980).

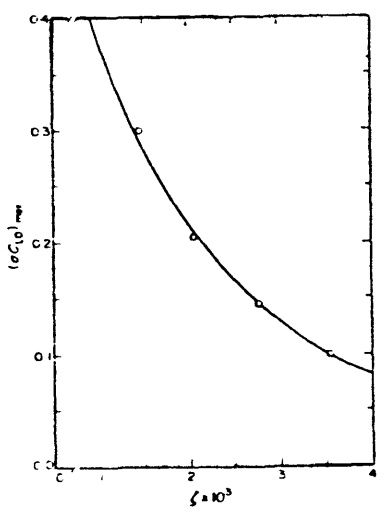


Fig. 1.21 Theoretical values for the peak cylinder response amplitude as a function of ζ with $\mu = 1.48 \times 10^{-3}$. Circles denote observations of Parkinson et al. (1968). From Skop & Griffin (1973).

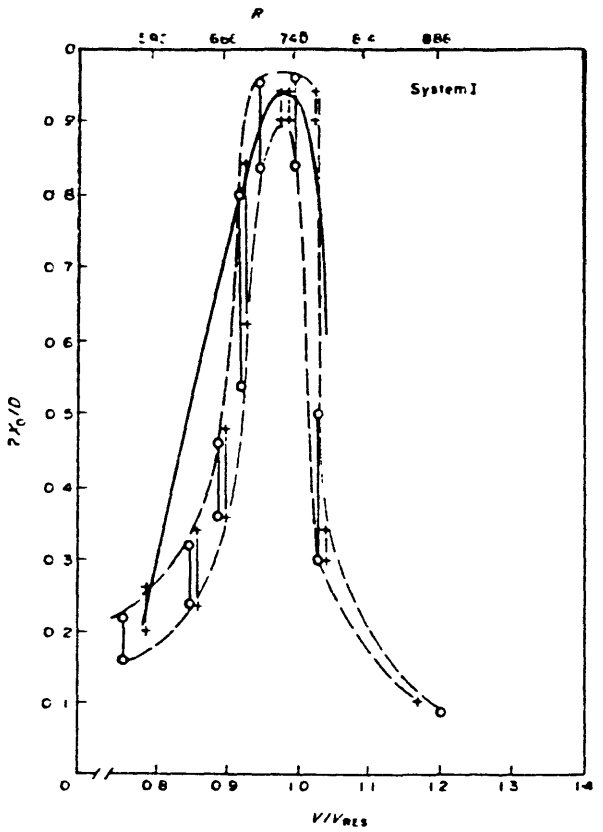


Fig. 1.22 (a) Measured amplitude of vortex excited oscillation for system I as a function of free stream flow speed V. Points taken with wind speed increasing (+), with wind speed decreasing (o). Wake oscillation model from section 4 of Griffin et al, —— V_{res} = 1.9 m/s. From Griffin et al. (1973).

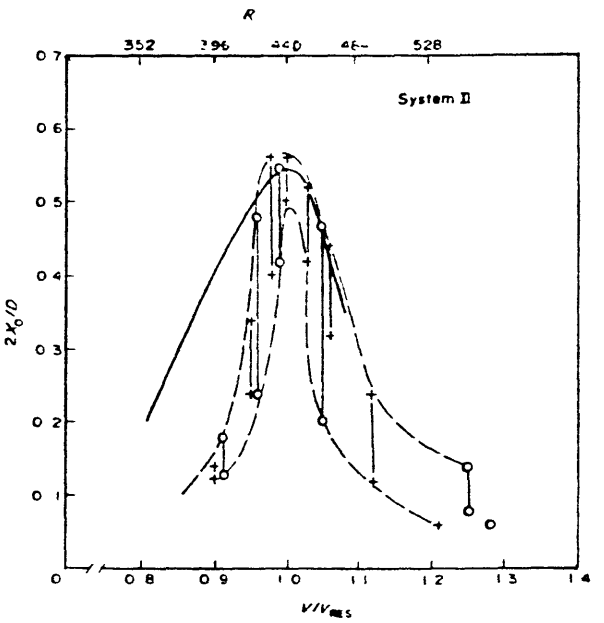
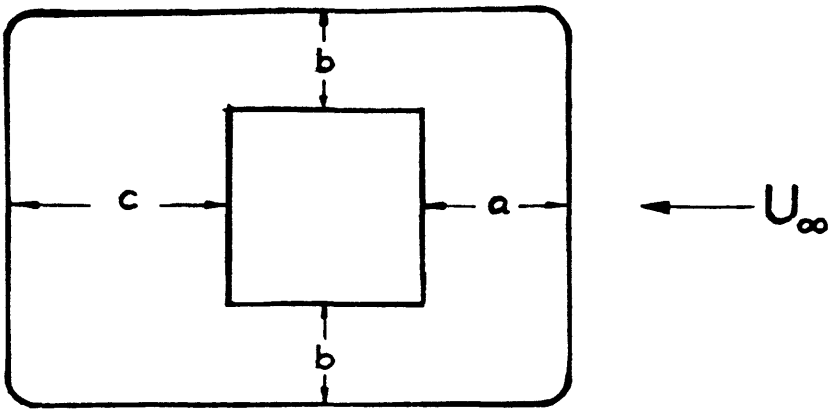


Fig. 1.22(b) Measured amplitude of vortex-excited oscillation for system II as a function of free stream flow speed V. Points taken with wind speed increasing (+), with wind speed decreasing (o). Wake oscillator model from section 4 of Griffin et al. —— V_{res} = 1.2 m/s. From Griffin et al. (1973).



End Plates	a	b	c
Steel (for Al cy.) type 1	1"	3.5"	6"
Steel (for Al cy.) type 2	4"	3.5"	6"
Steel (for Al cy.) type 3	4"	6"	8"
Perspex (for wood cy.)	4.5"	3.5"	5.5"

Fig. 2.1 End plates details.

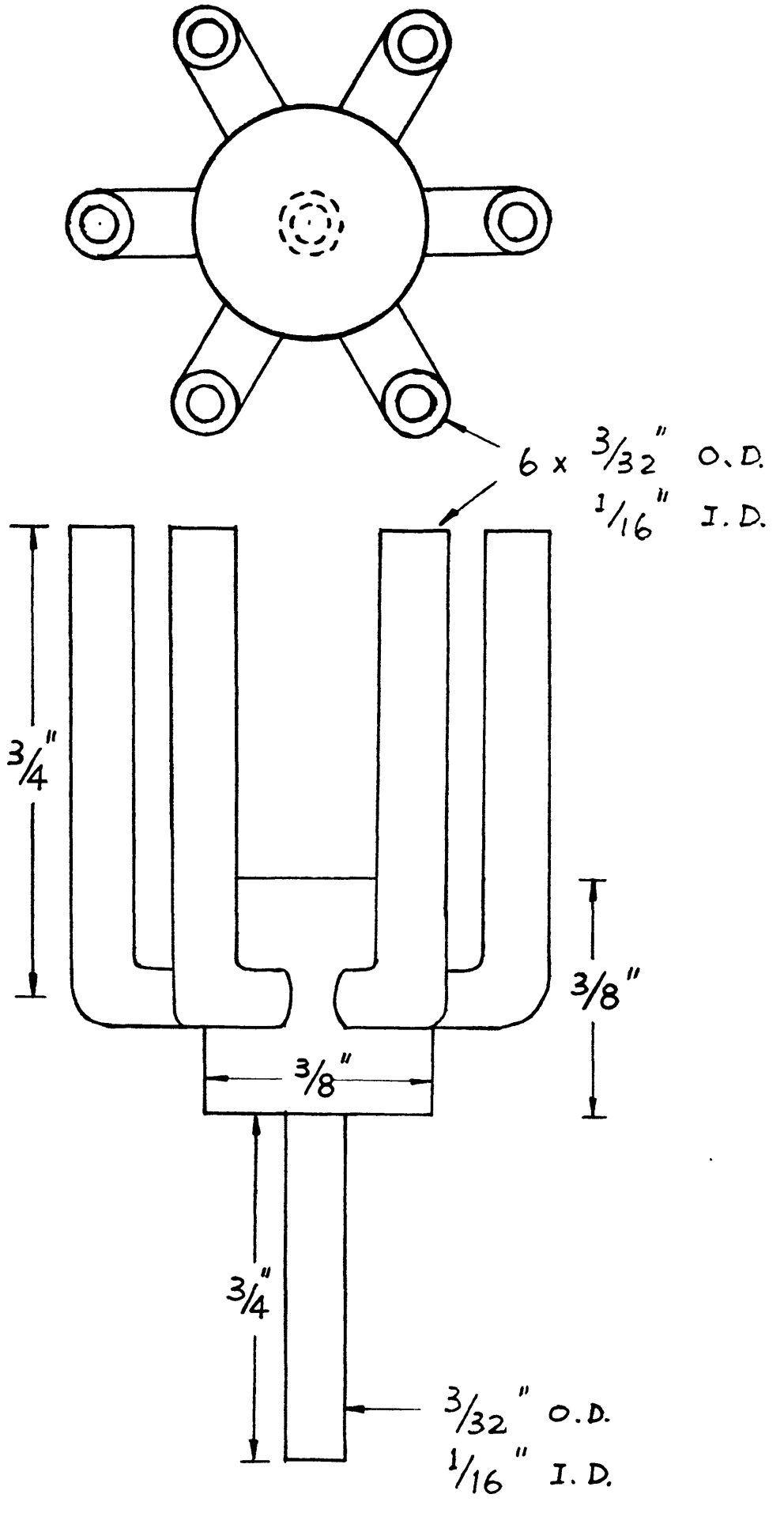


Fig. 2.2 Pressure averager details.

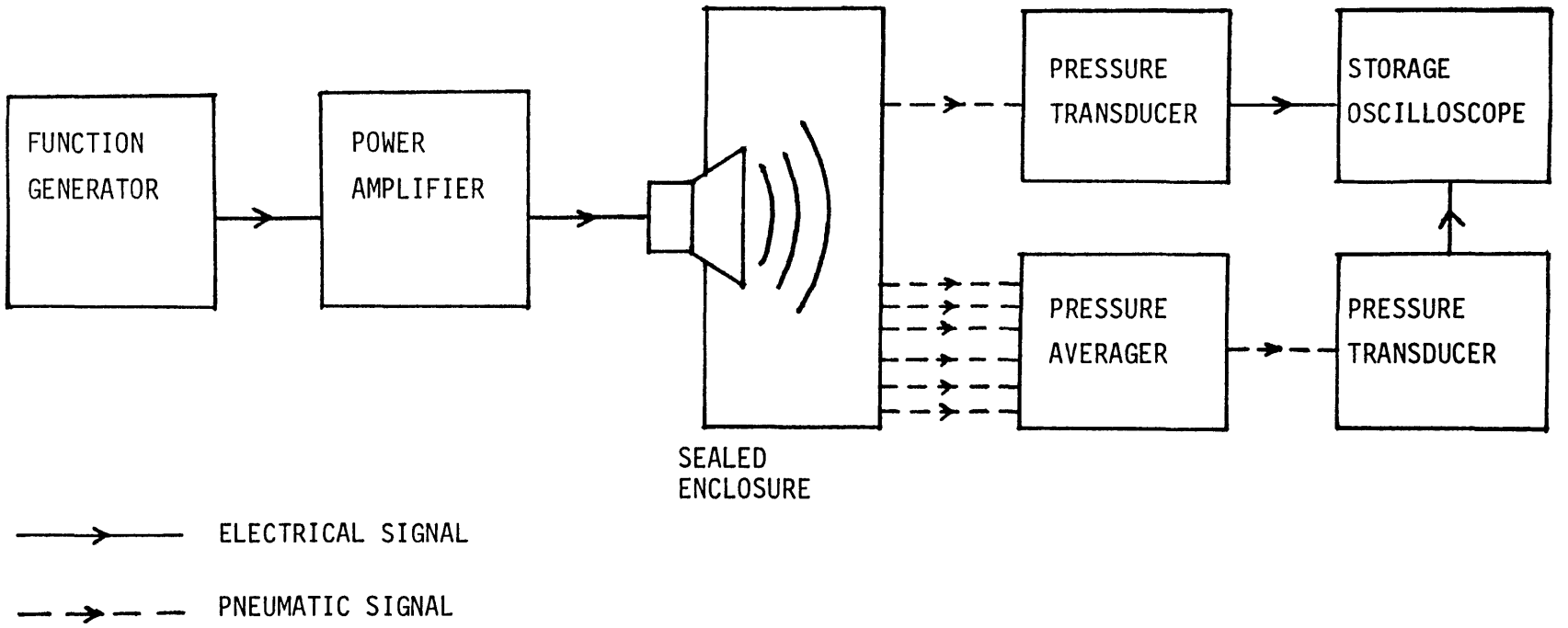


Fig. 2.3 Set-up for pressure averager calibration.

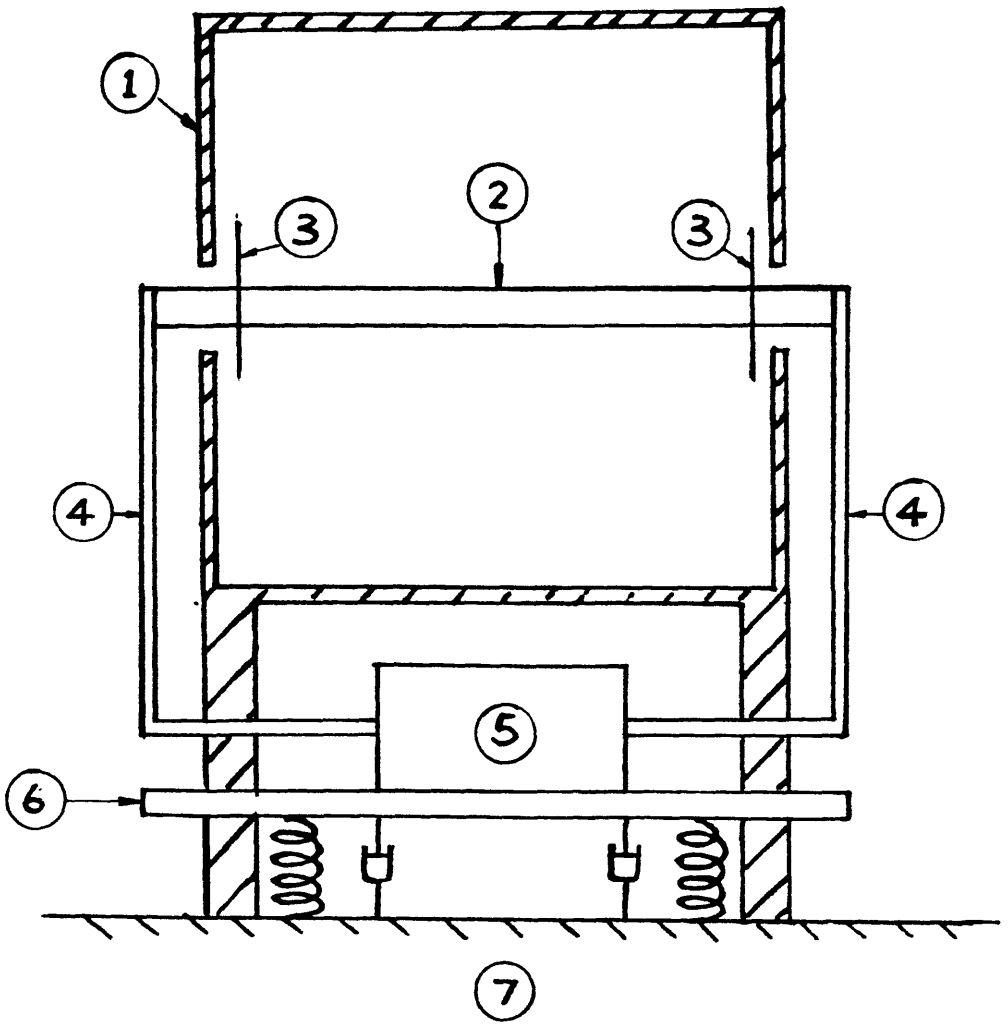


Fig. 2.4 Set-up of cylinder and oscillating mechanism.

1. Wind tunnel
2. Square-Section Cylinder
3. End plates
4. Vertical pushrod
5. Motor and reduction gearbox
6. Chassis of oscillating mechanism
7. Ground

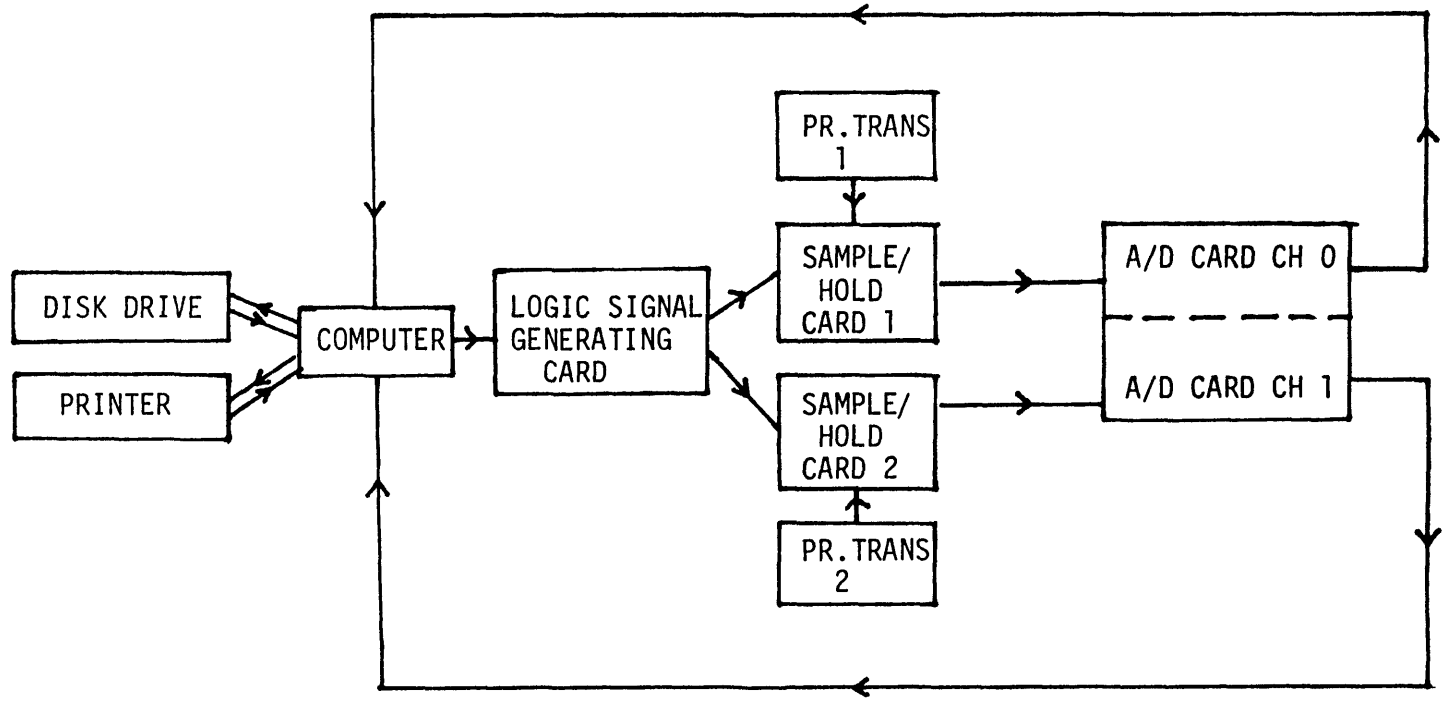


Fig. 3.1 Interfacing of computer and peripheral devices.

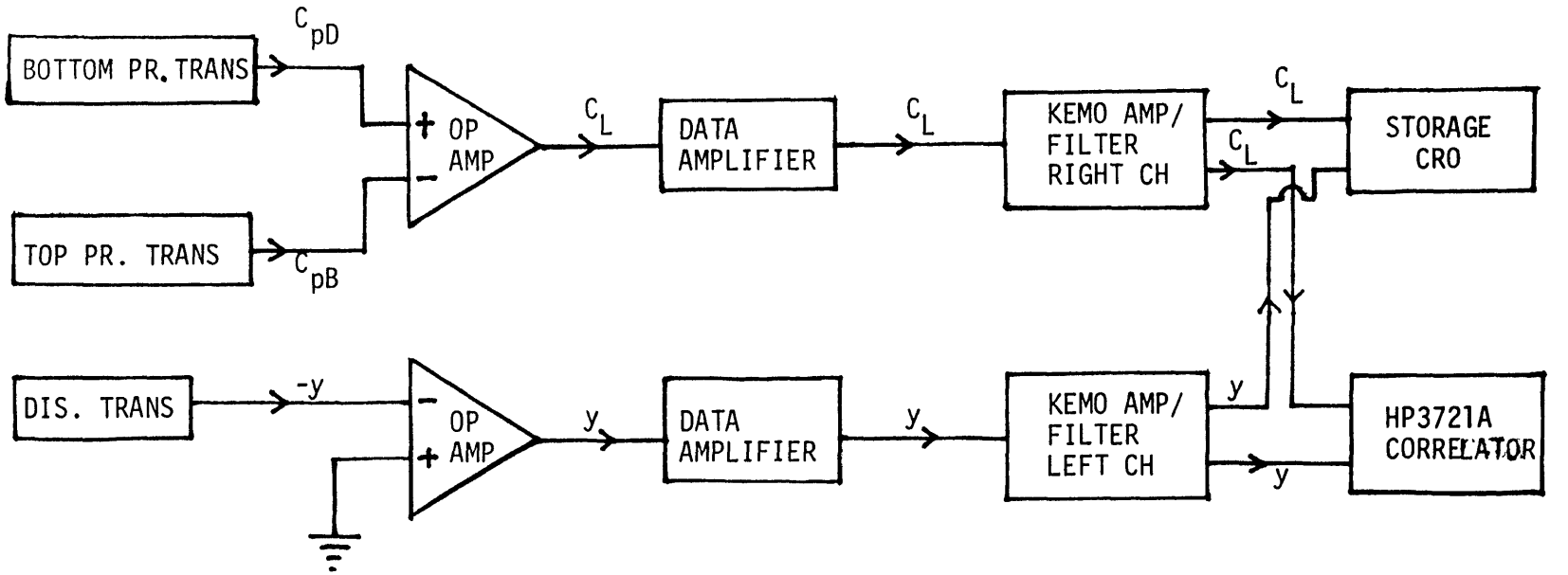
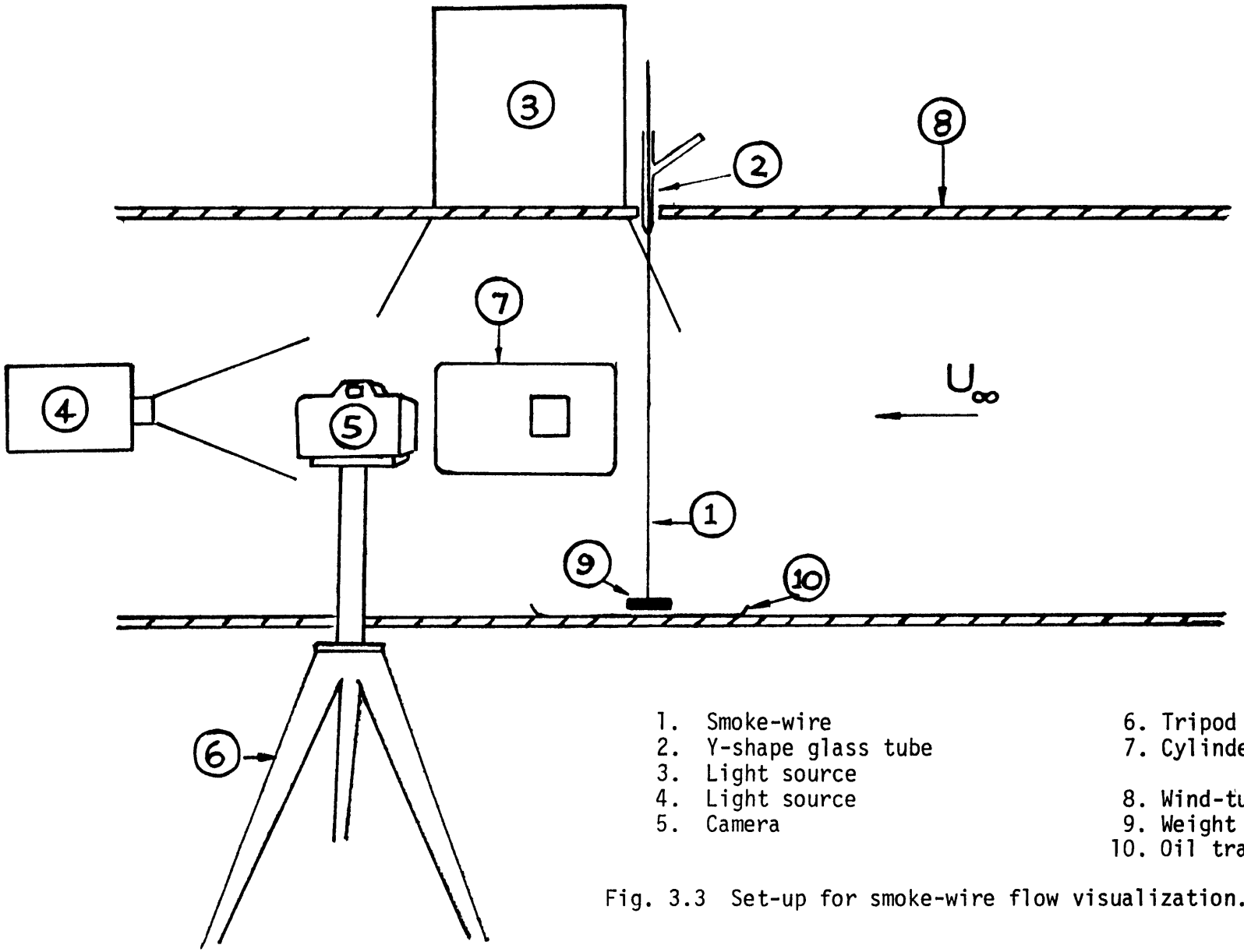


Fig. 3.2 Set-up for ϕ versus U_r measurements and Cophese recording (HP3721A replaced by SElab open real tape recorder)



1. Smoke-wire
2. Y-shape glass tube
3. Light source
4. Light source
5. Camera
6. Tripod
7. Cylinder/end plates assembly
8. Wind-tunnel
9. Weight to straighten wire
10. Oil tray.

Fig. 3.3 Set-up for smoke-wire flow visualization.

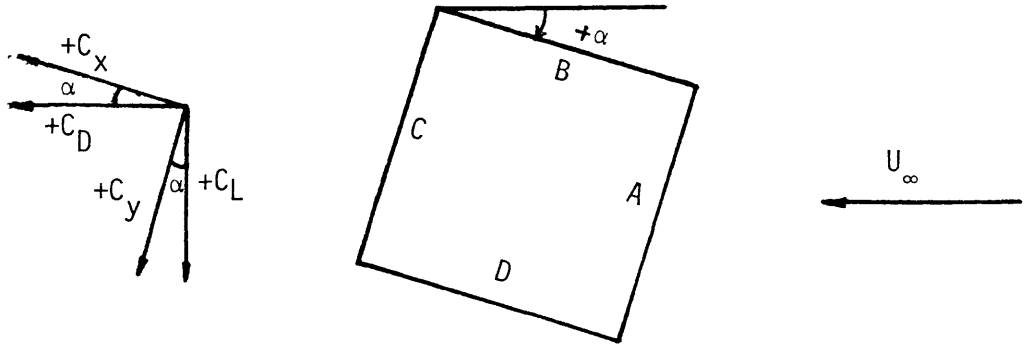
NOTES ON CHAPTER FOUR'S FIGURES

1. The definition of faces A, B, C and D are shown in fig. 1.1.

2. Unless otherwise stated, all the results shown in this chapter are corrected for wind tunnel blockage effect.

3. Unless otherwise stated, all the results shown in this chapter and in the next chapter are measured with number 2 end plates installed.

Sign convention for Chapter 4 to 8.



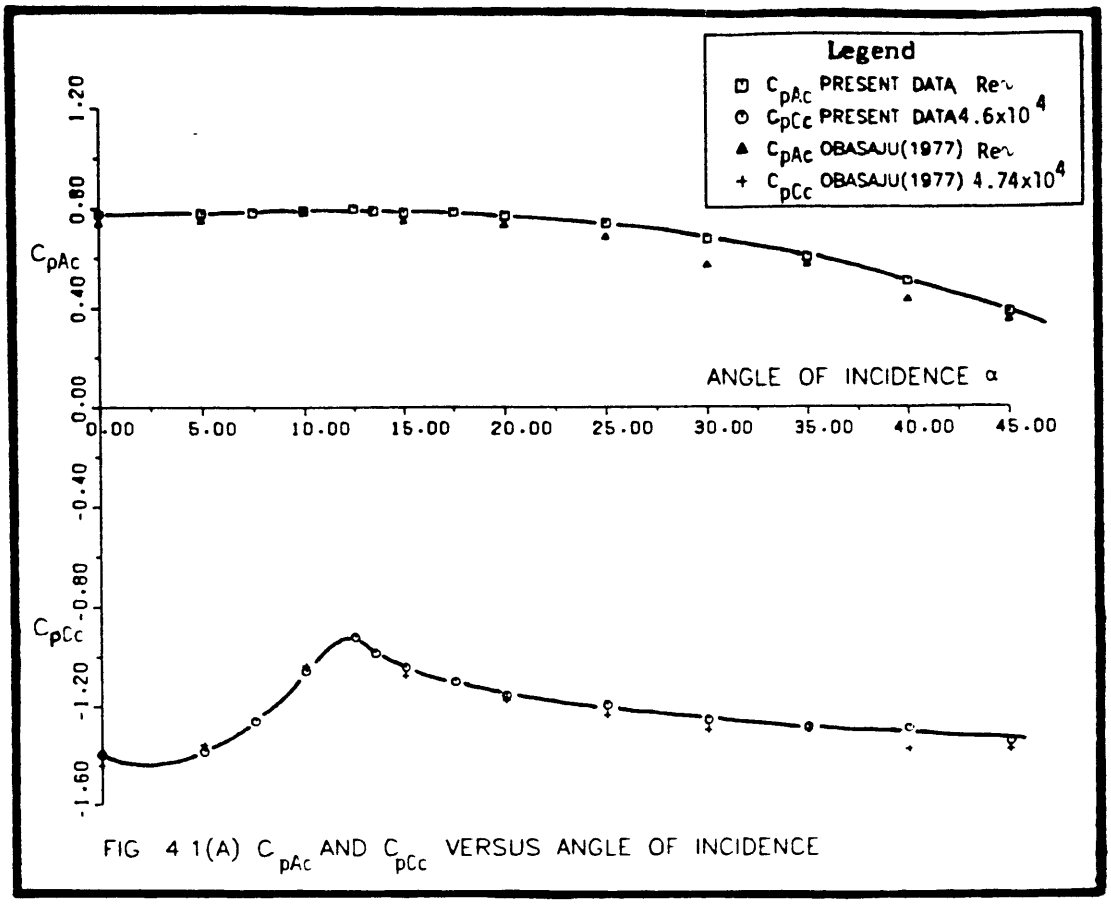


FIG 4 1(A) C_{pAc} AND C_{pCc} VERSUS ANGLE OF INCIDENCE

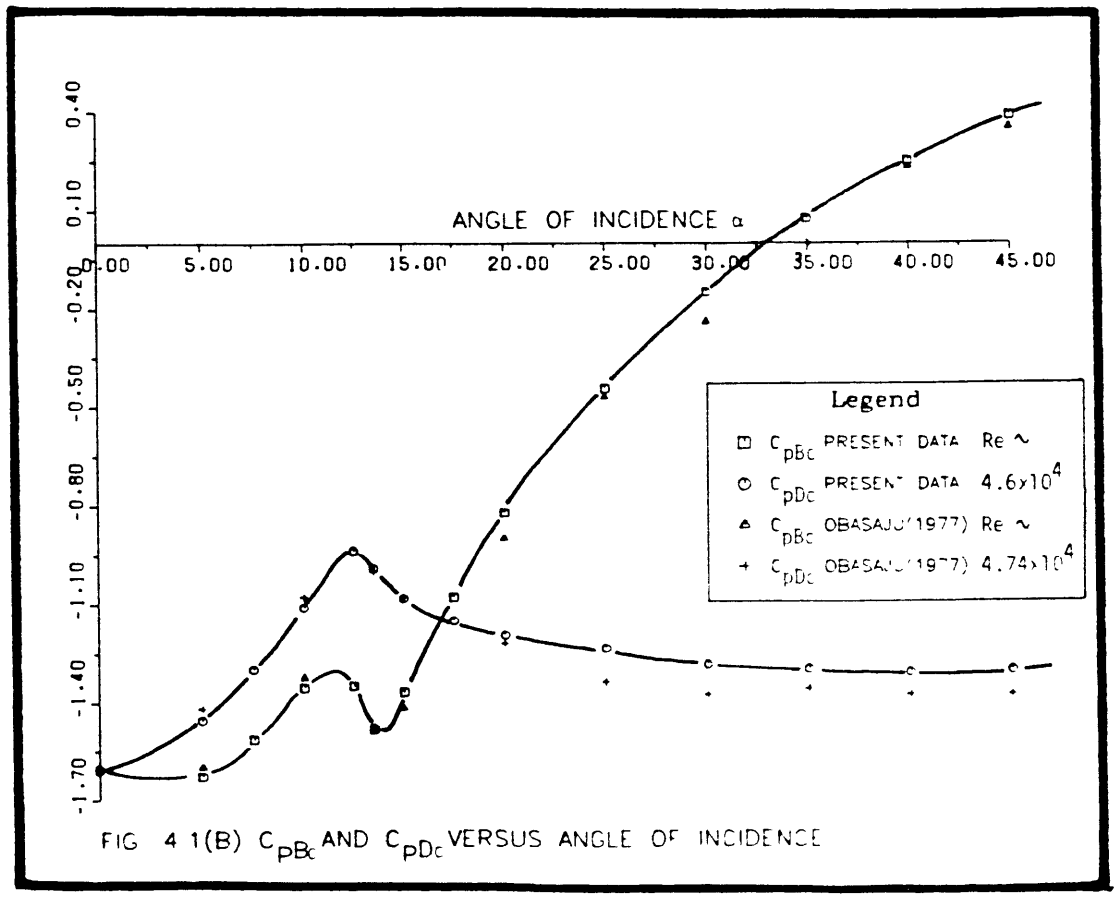


FIG 4 1(B) C_{pBc} AND C_{pDc} VERSUS ANGLE OF INCIDENCE

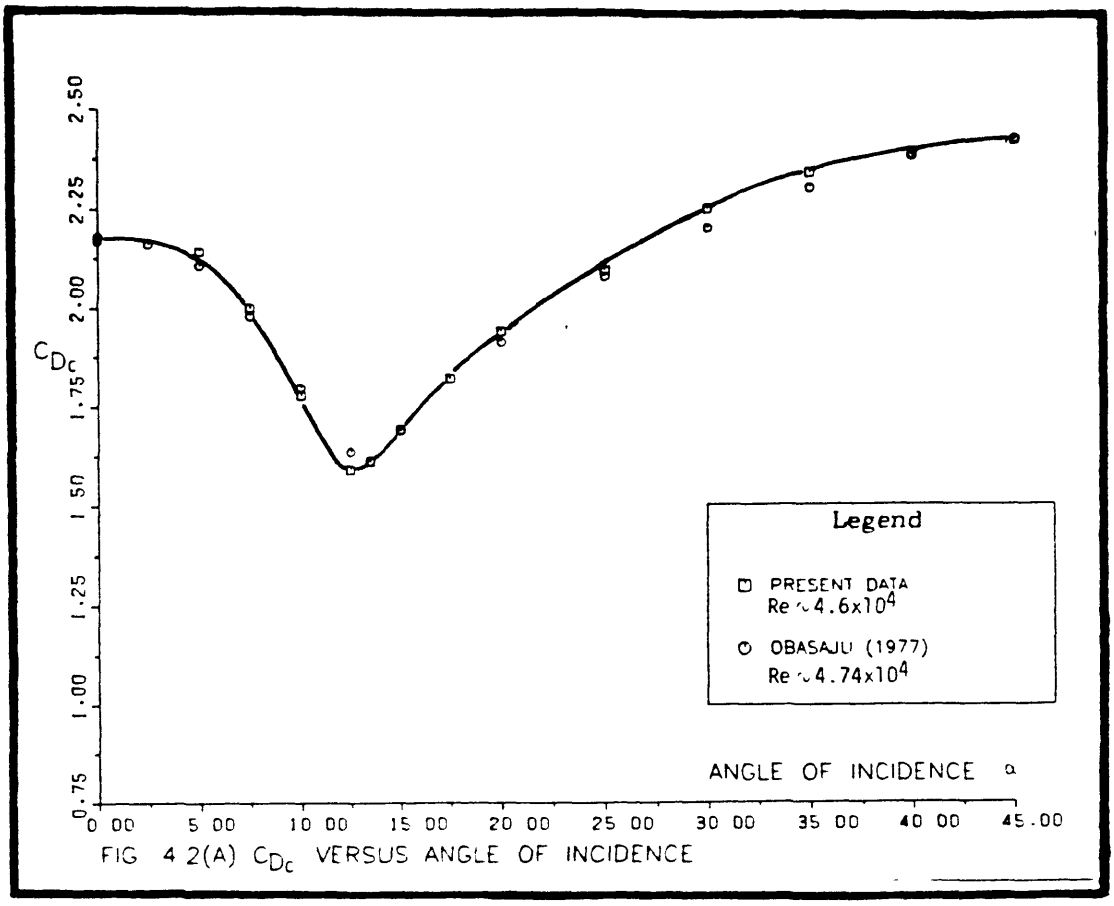


FIG 4.2(A) C_{Dc} VERSUS ANGLE OF INCIDENCE

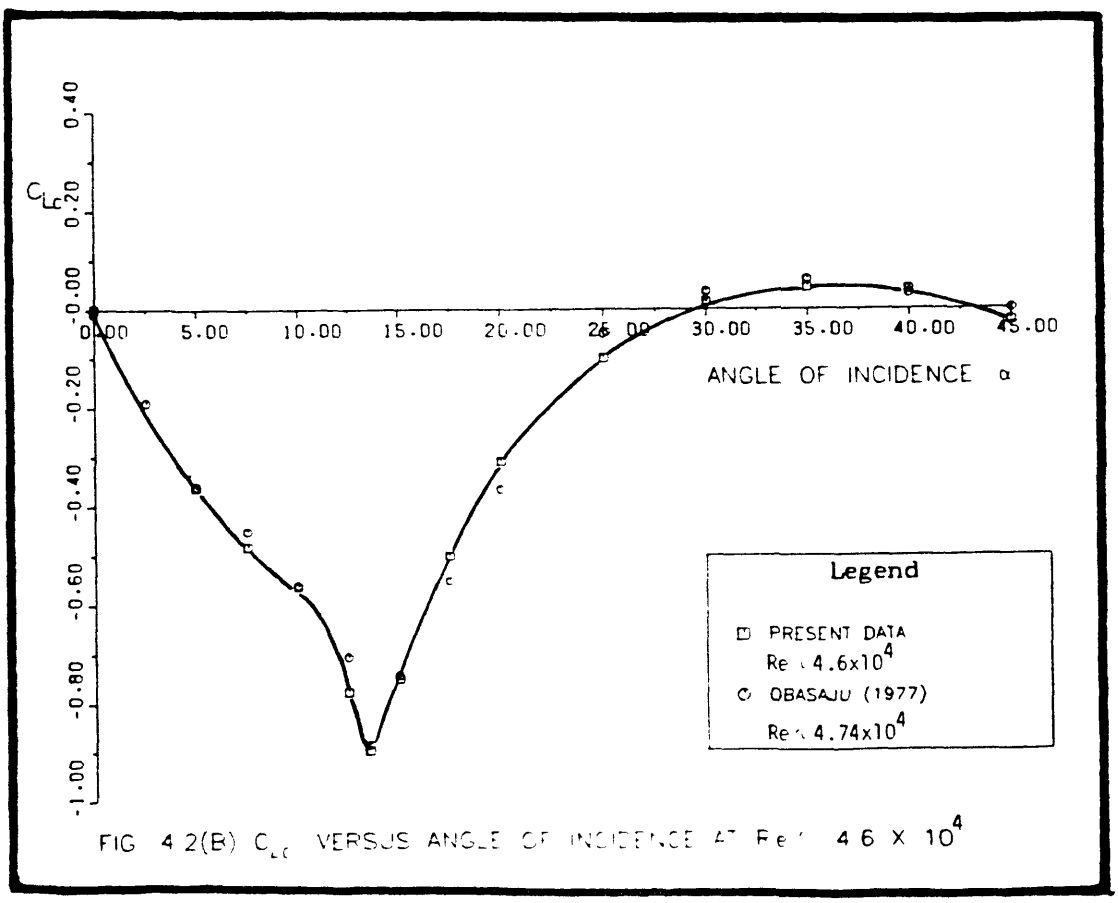


FIG 4.2(B) C_{Lc} VERSUS ANGLE OF INCIDENCE AT Re ≈ 4.6 X 10^4

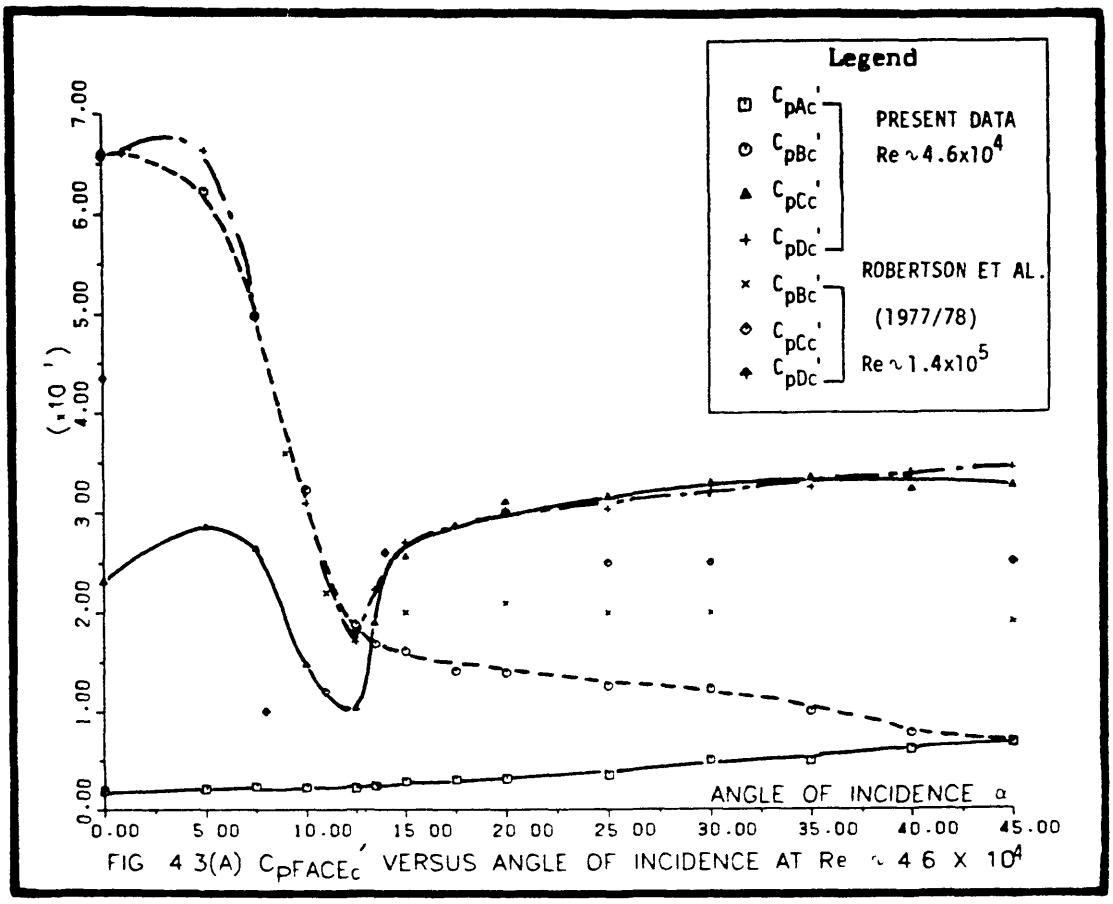


FIG 4.3(A) C_{pFACEc}' VERSUS ANGLE OF INCIDENCE AT Re ~ 4.6 X 10^4

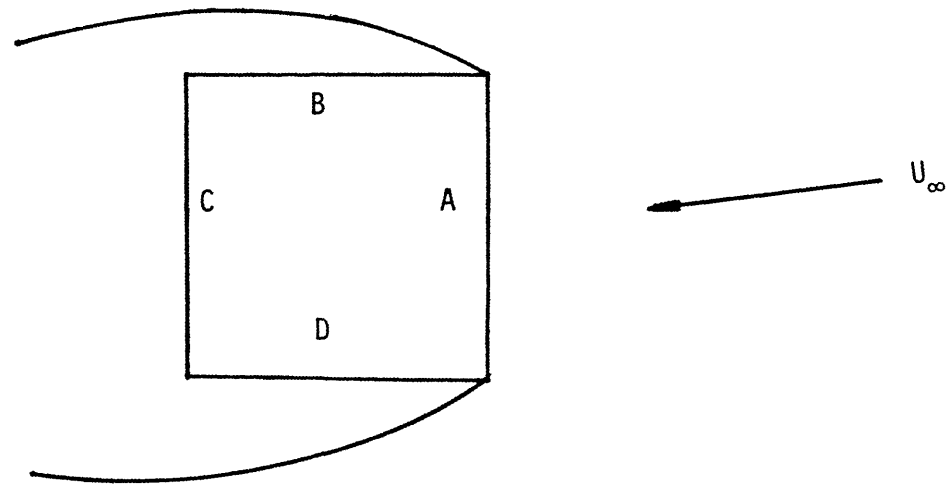


Fig. 4.3(b) $\alpha < \alpha_{crit}$, $C_{pB}' \sim C_{pD}'$

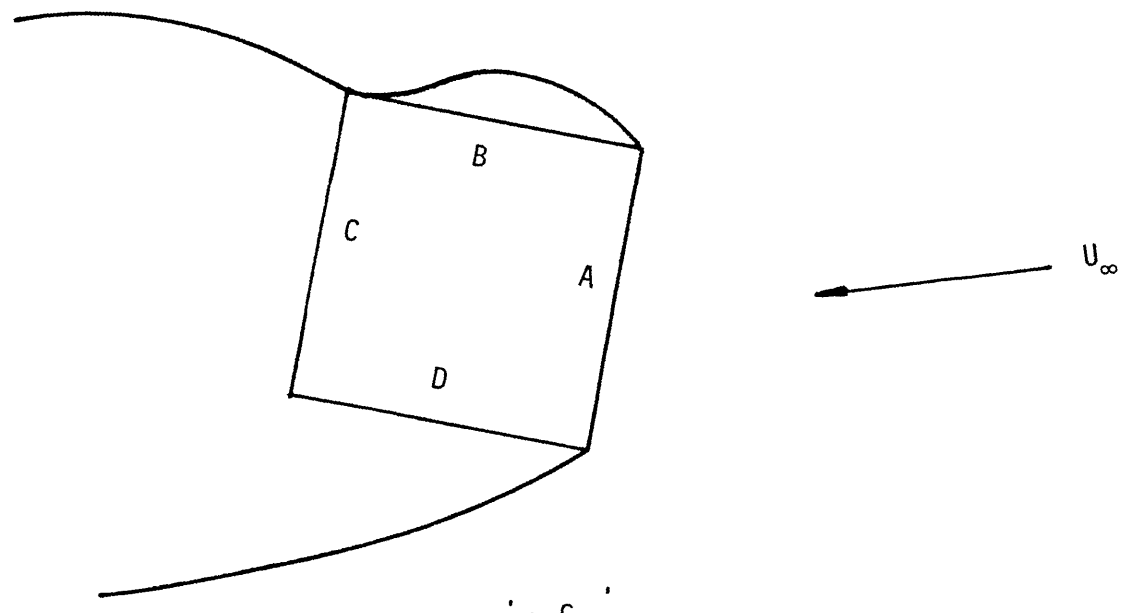


Fig. 4.3(c) $\alpha > \alpha_{crit}$, $C_{pC}' \sim C_{pD}'$

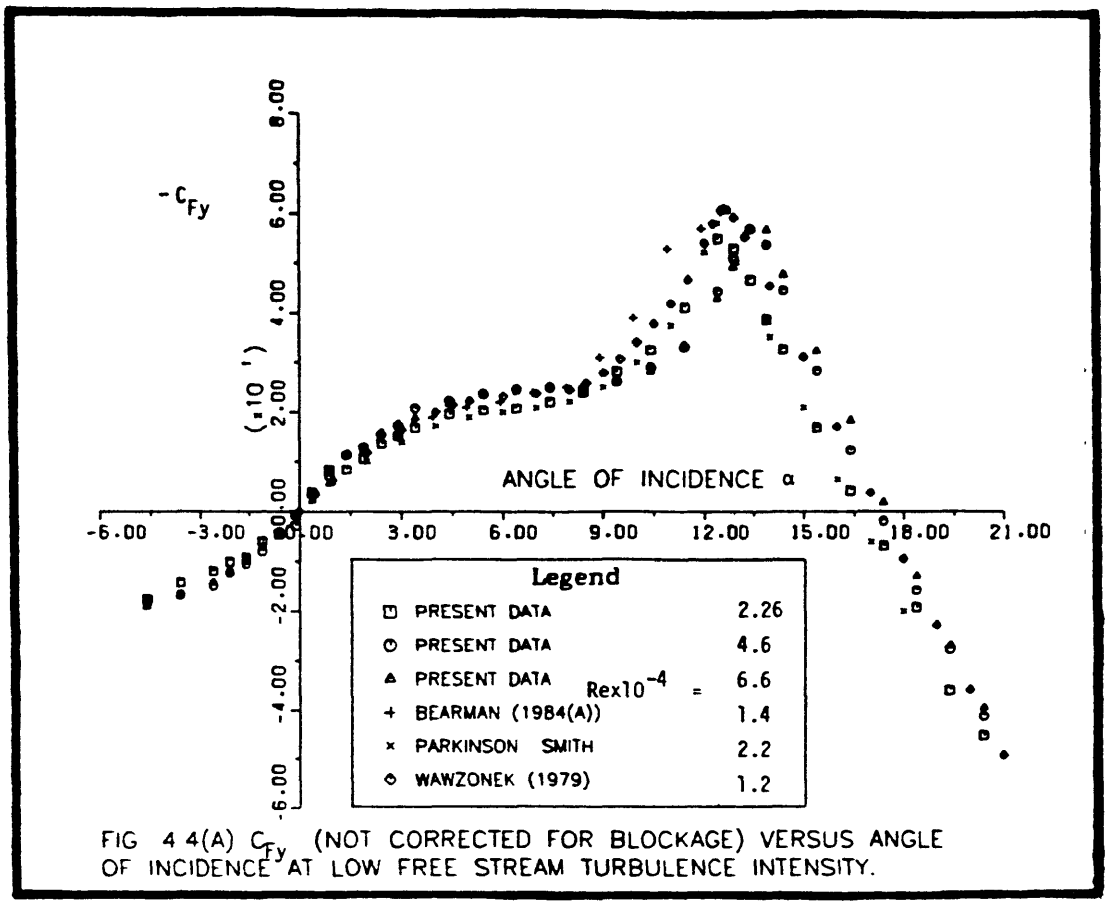


FIG 4 4(A) C_{Fy} (NOT CORRECTED FOR BLOCKAGE) VERSUS ANGLE OF INCIDENCE AT LOW FREE STREAM TURBULENCE INTENSITY.

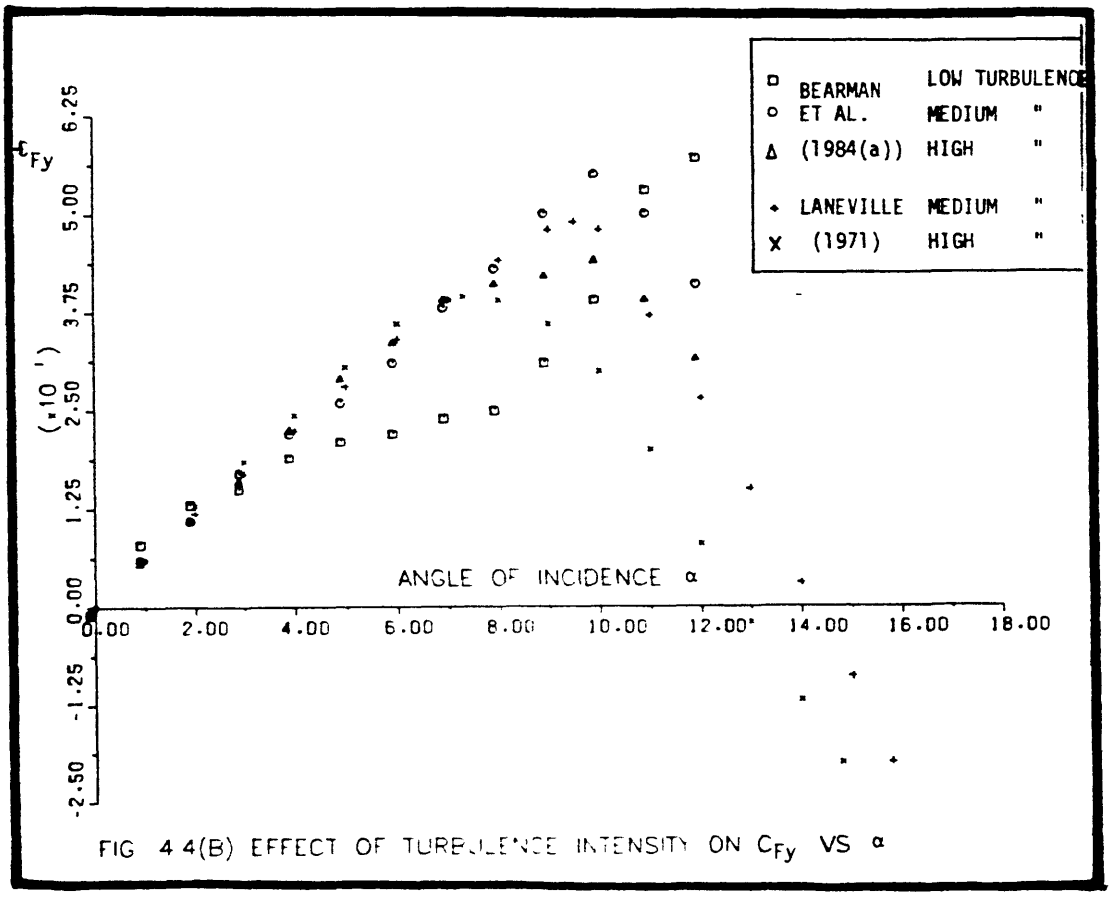


FIG 4 4(B) EFFECT OF TURBULENCE INTENSITY ON C_{Fy} VS α

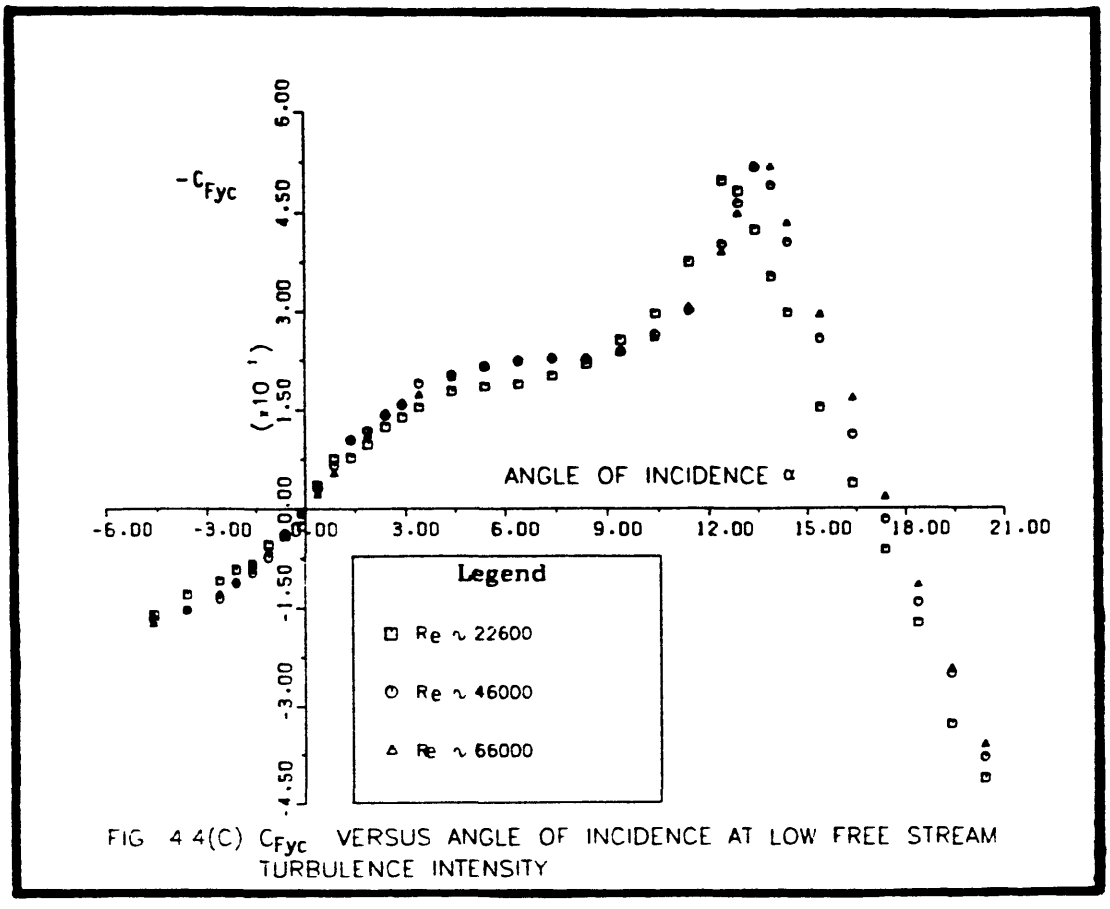


FIG 4.4(C) C_{Fyc} VERSUS ANGLE OF INCIDENCE AT LOW FREE STREAM TURBULENCE INTENSITY

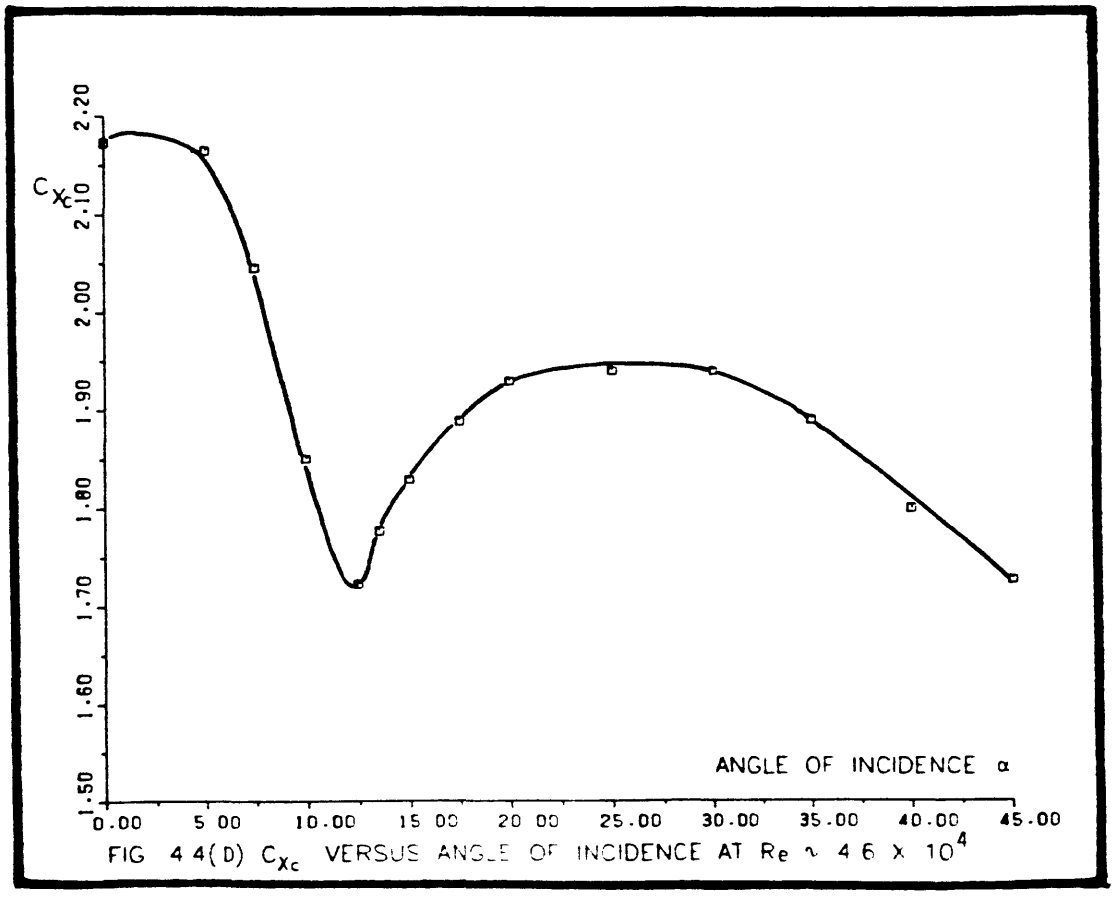


FIG 4.4(D) C_{Xc} VERSUS ANGLE OF INCIDENCE AT $Re \sim 4.6 \times 10^4$

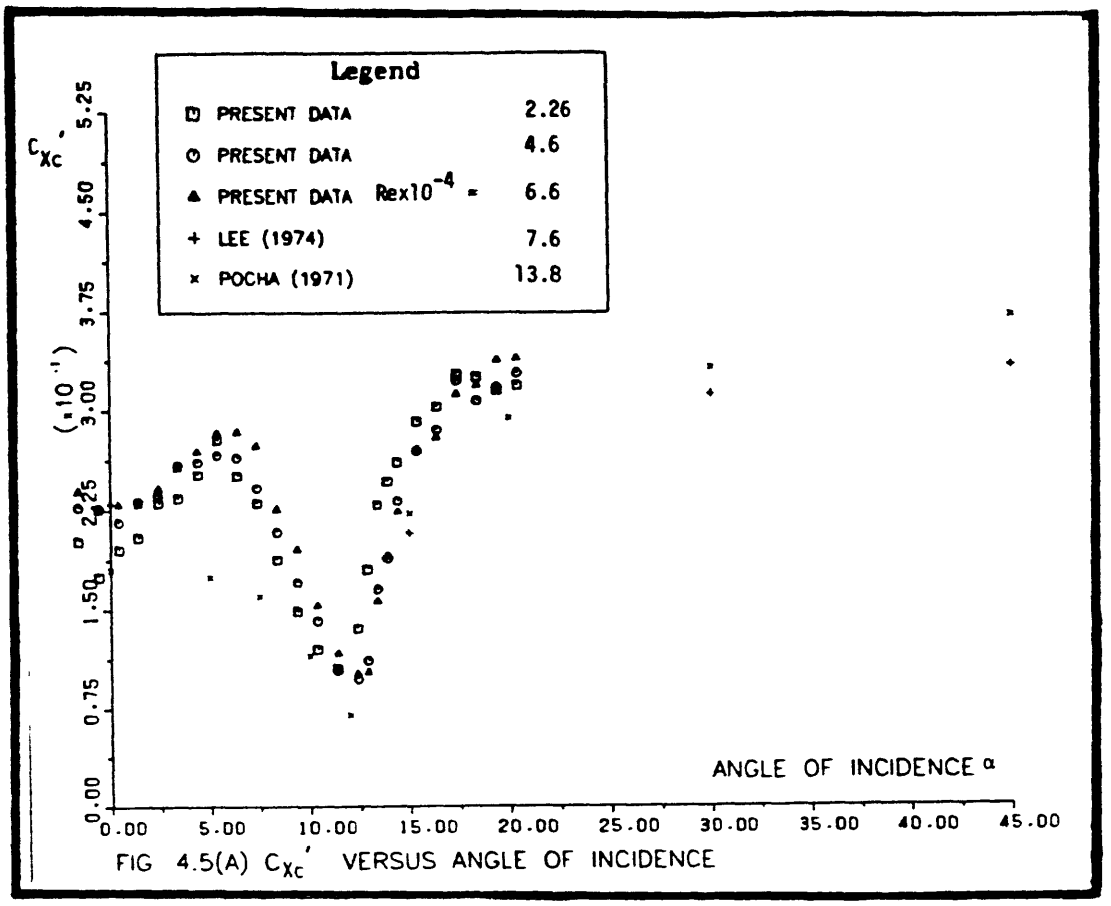


FIG 4.5(A) C_{Xc}' VERSUS ANGLE OF INCIDENCE

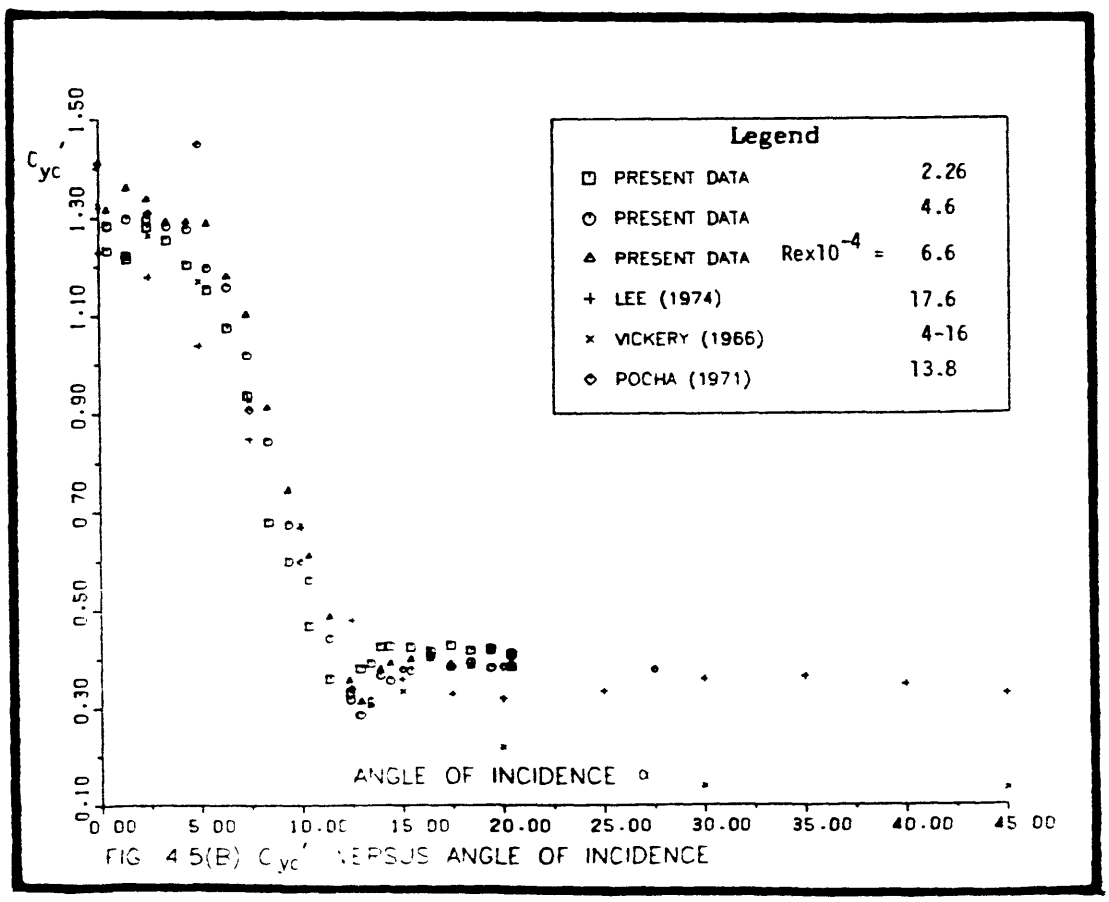


FIG 4.5(B) C_{yc}' VERSUS ANGLE OF INCIDENCE

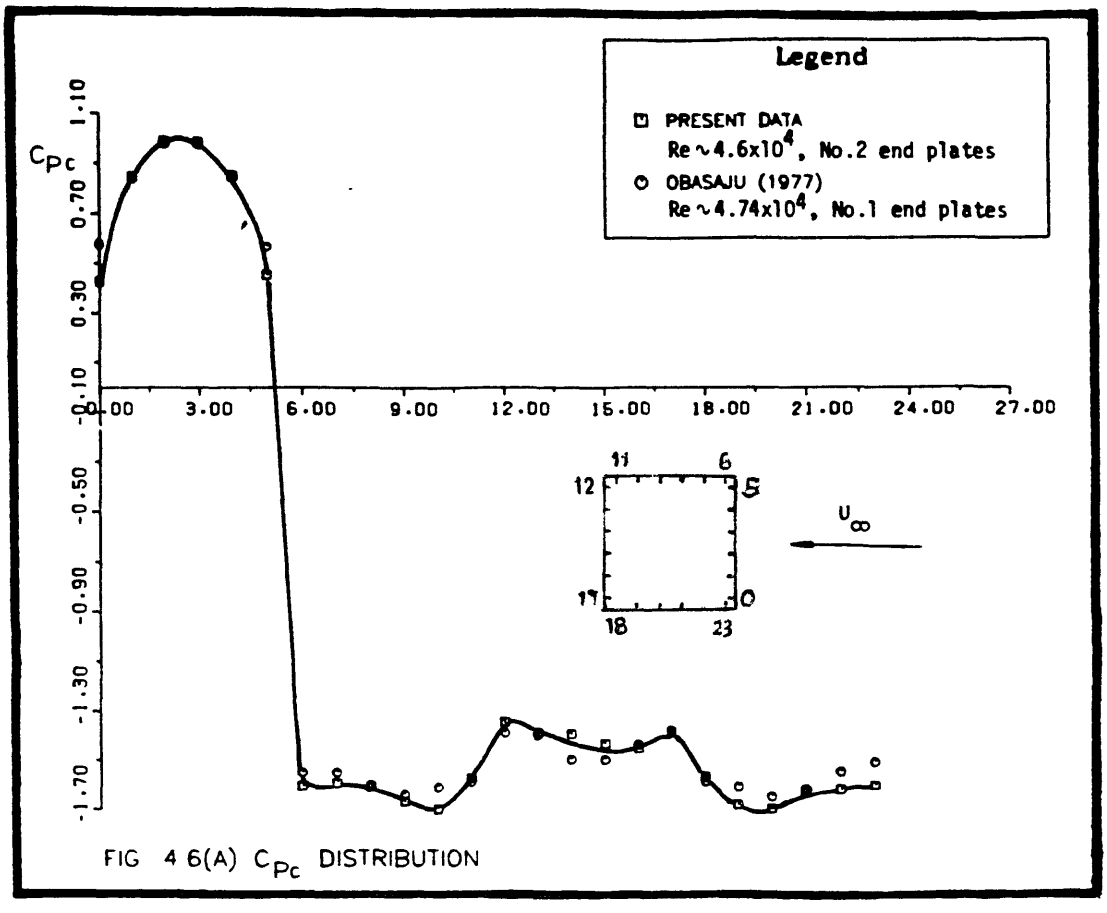


FIG 4 6(A) C_{Pc} DISTRIBUTION

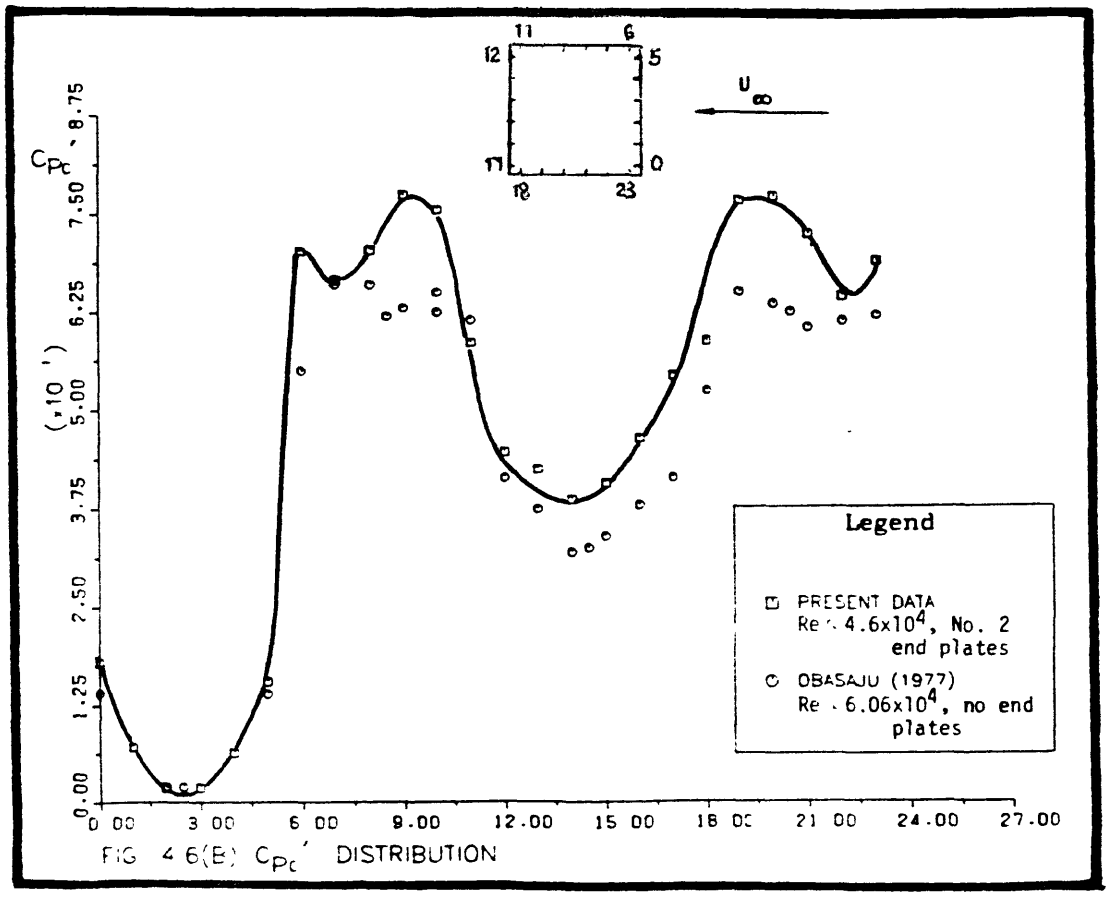


FIG 4 6(B) C_{Pc}' DISTRIBUTION

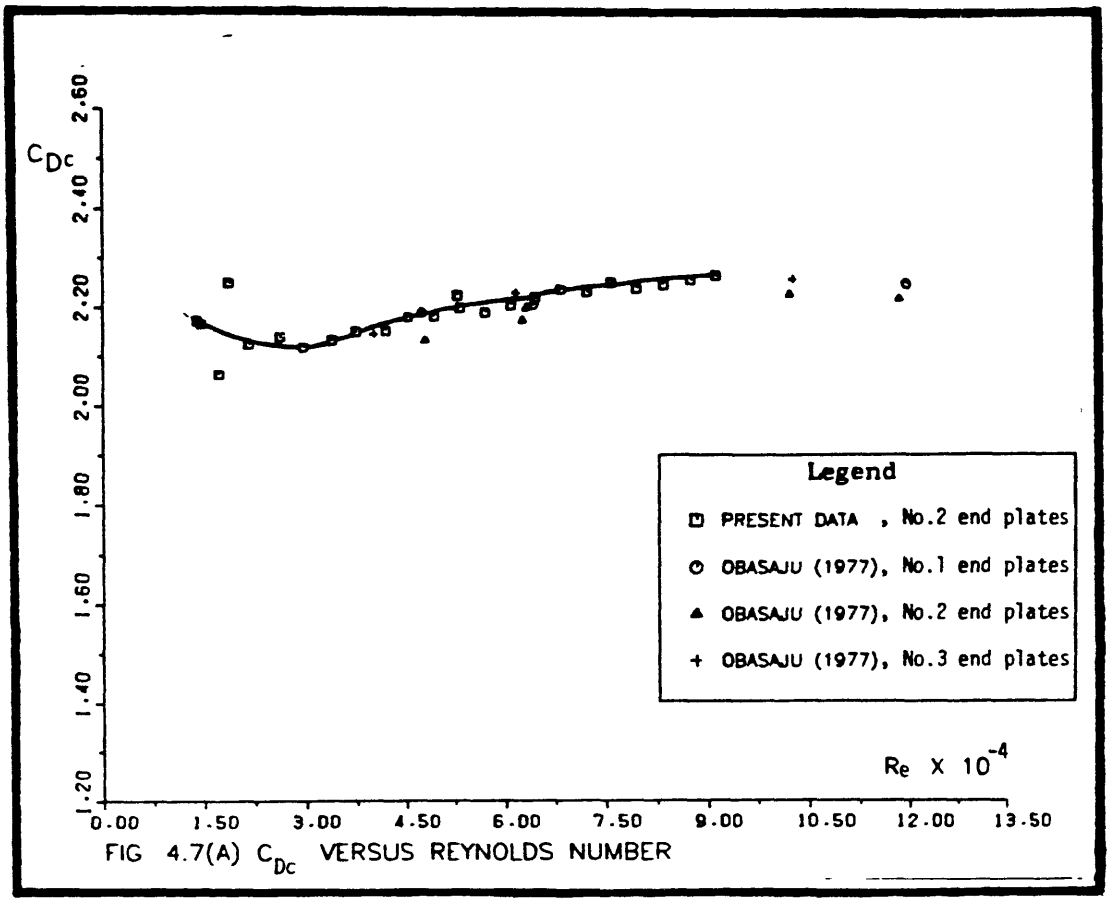


FIG 4.7(A) C_{Dc} VERSUS REYNOLDS NUMBER

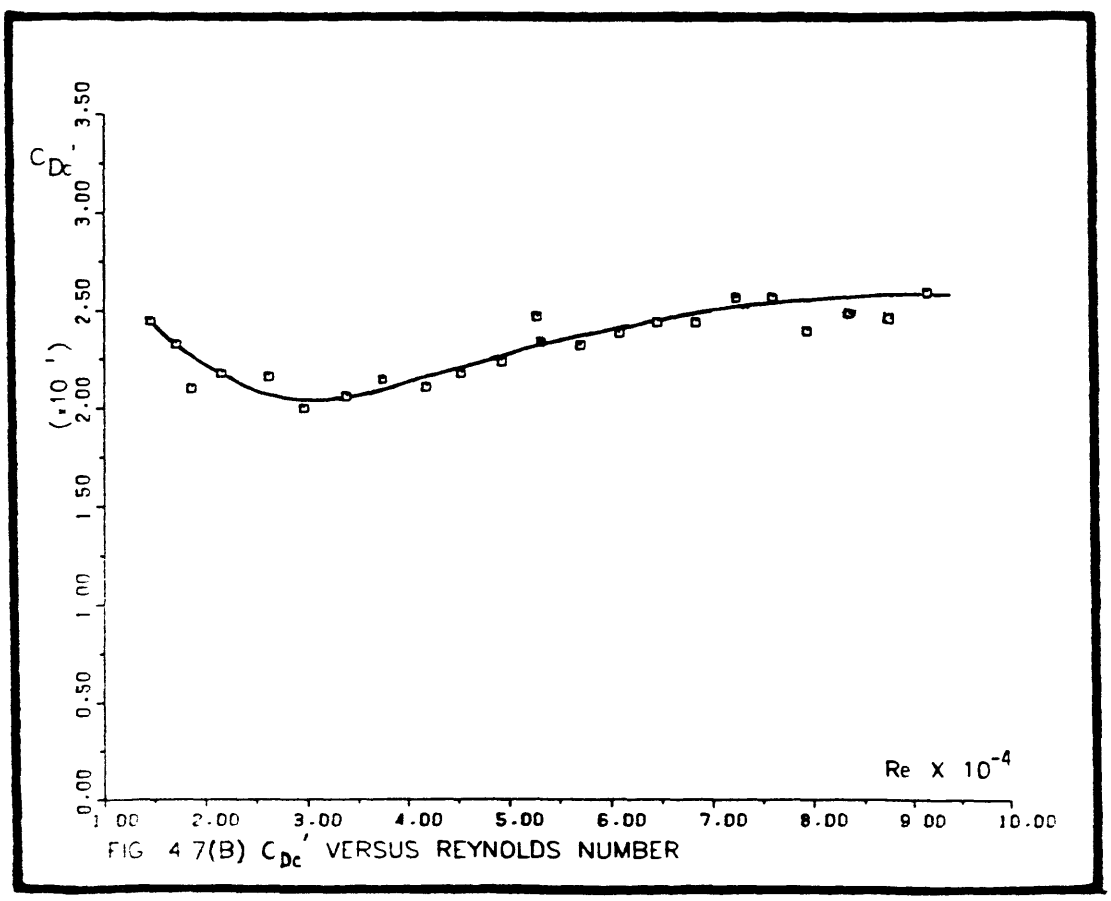


FIG 4.7(B) C_{Dc}' VERSUS REYNOLDS NUMBER

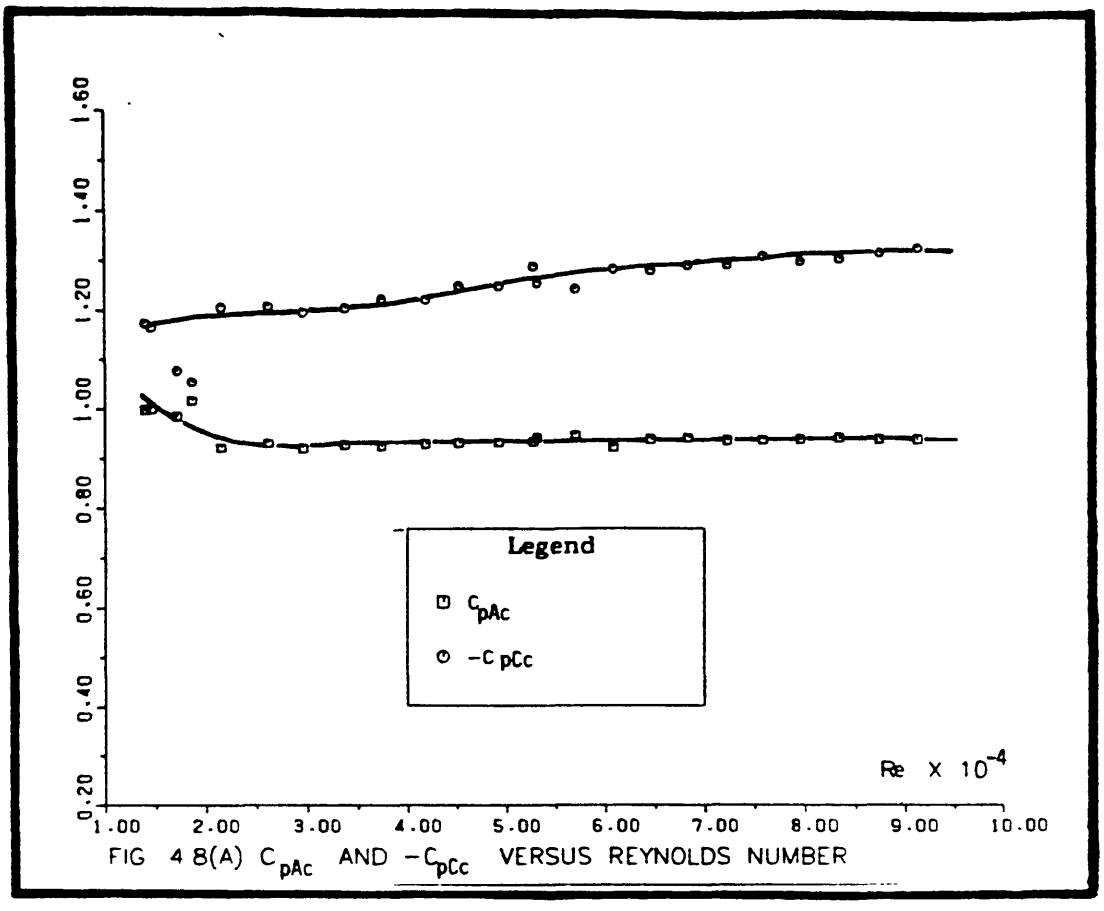


FIG 4.8(A) C_{pAc} AND $-C_{pCc}$ VERSUS REYNOLDS NUMBER

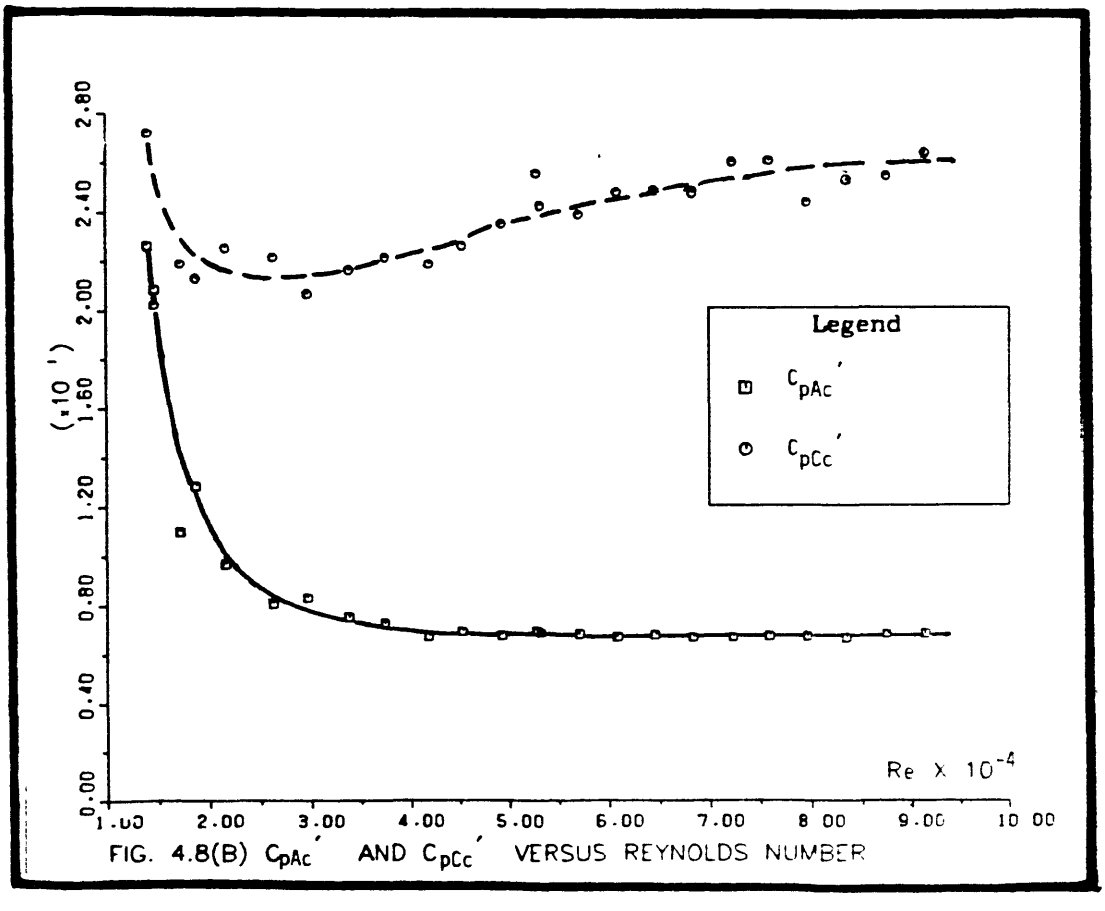


FIG. 4.8(B) C_{pAc}' AND C_{pCc}' VERSUS REYNOLDS NUMBER

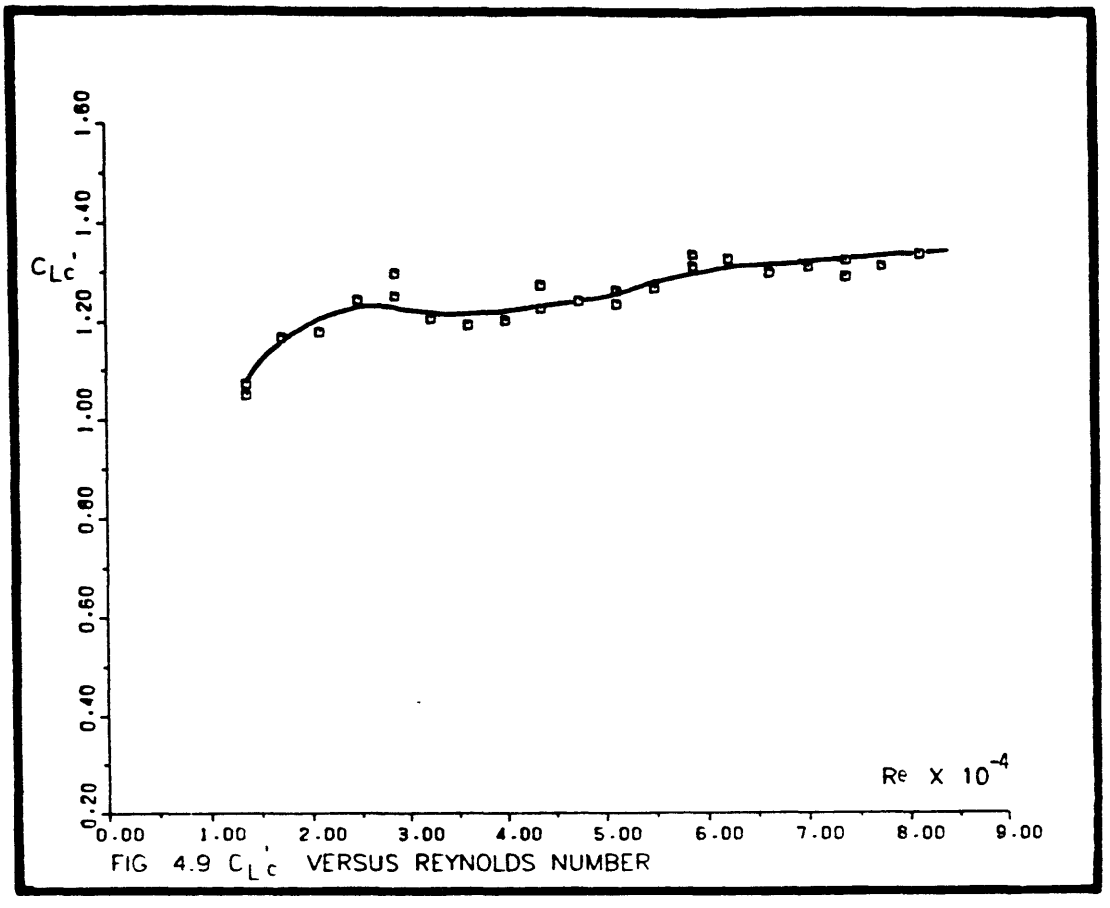


FIG 4.9 $C_{L'c}$ VERSUS REYNOLDS NUMBER

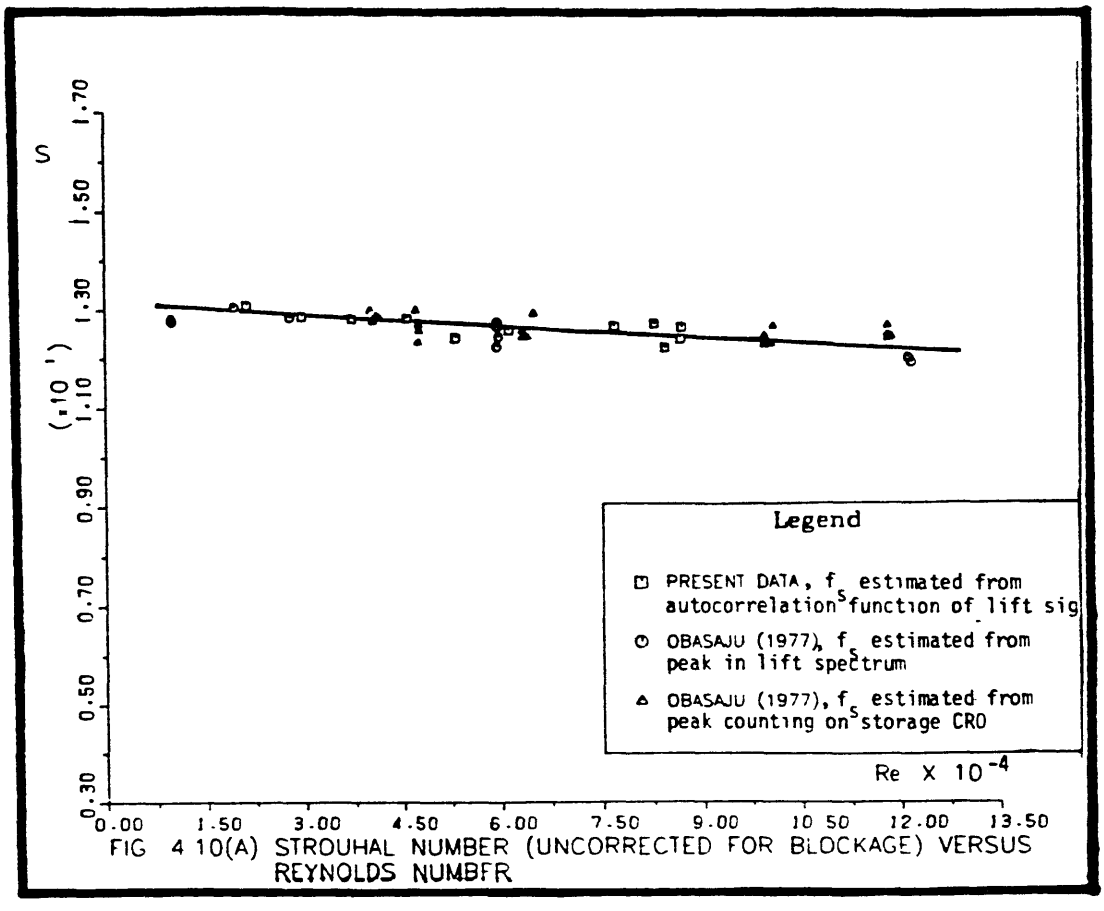


FIG 4 10(A) STROUHAL NUMBER (UNCORRECTED FOR BLOCKAGE) VERSUS REYNOLDS NUMBFR

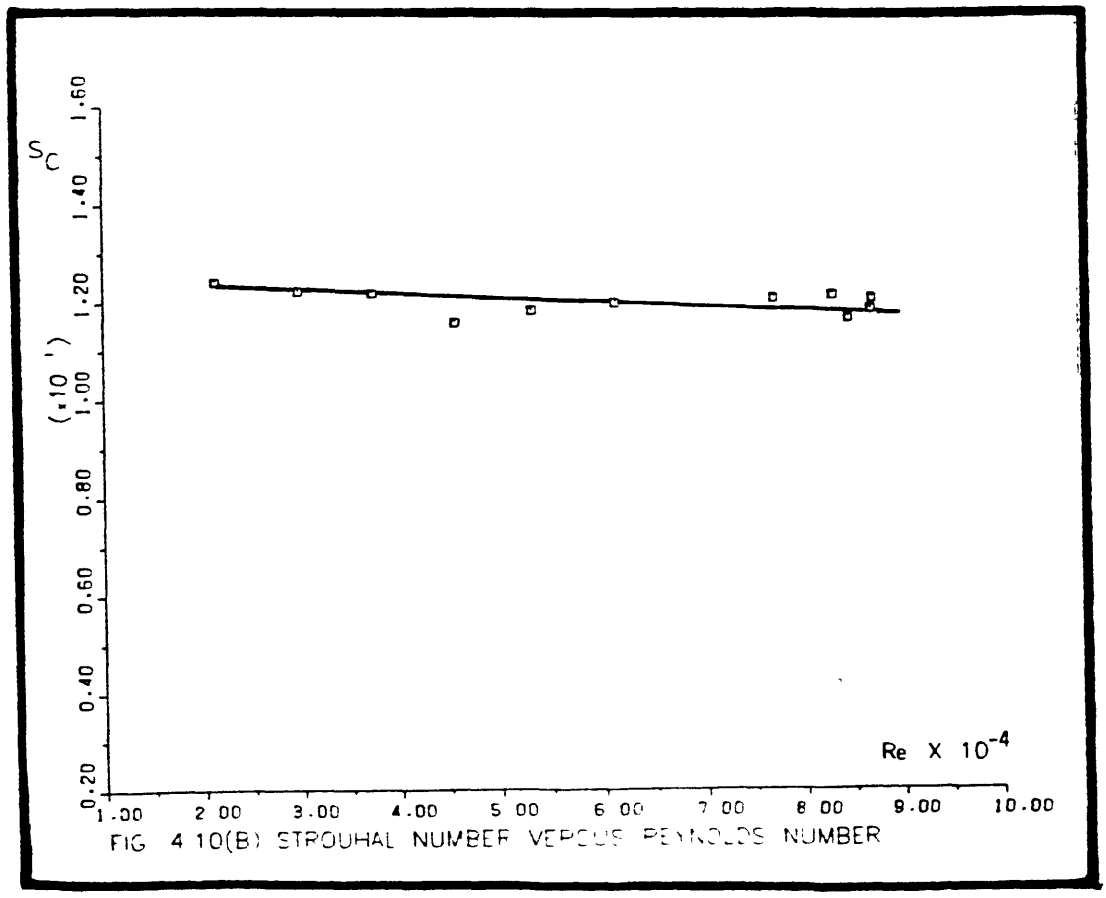


FIG 4 10(B) STROUHAL NUMBER VERSUS REYNOLDS NUMBER

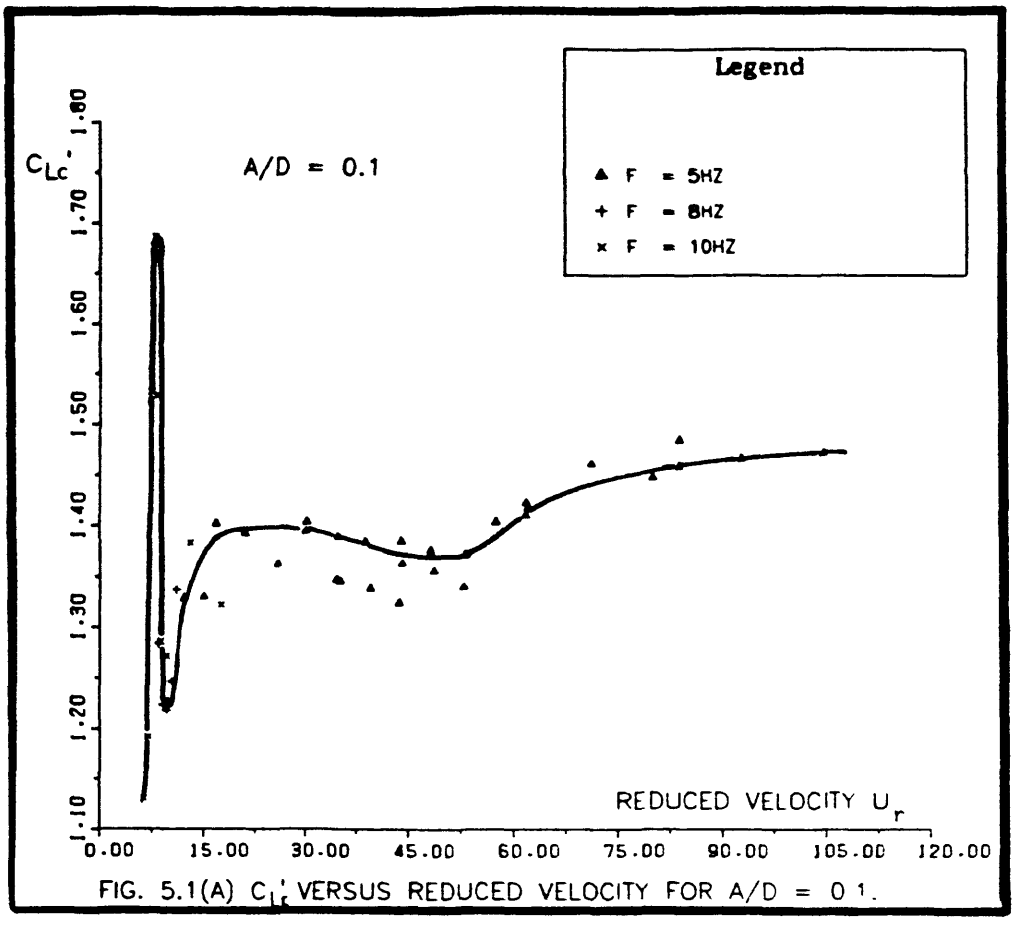


FIG. 5.1(A) C_{Lc}' VERSUS REDUCED VELOCITY FOR A/D = 0.1.

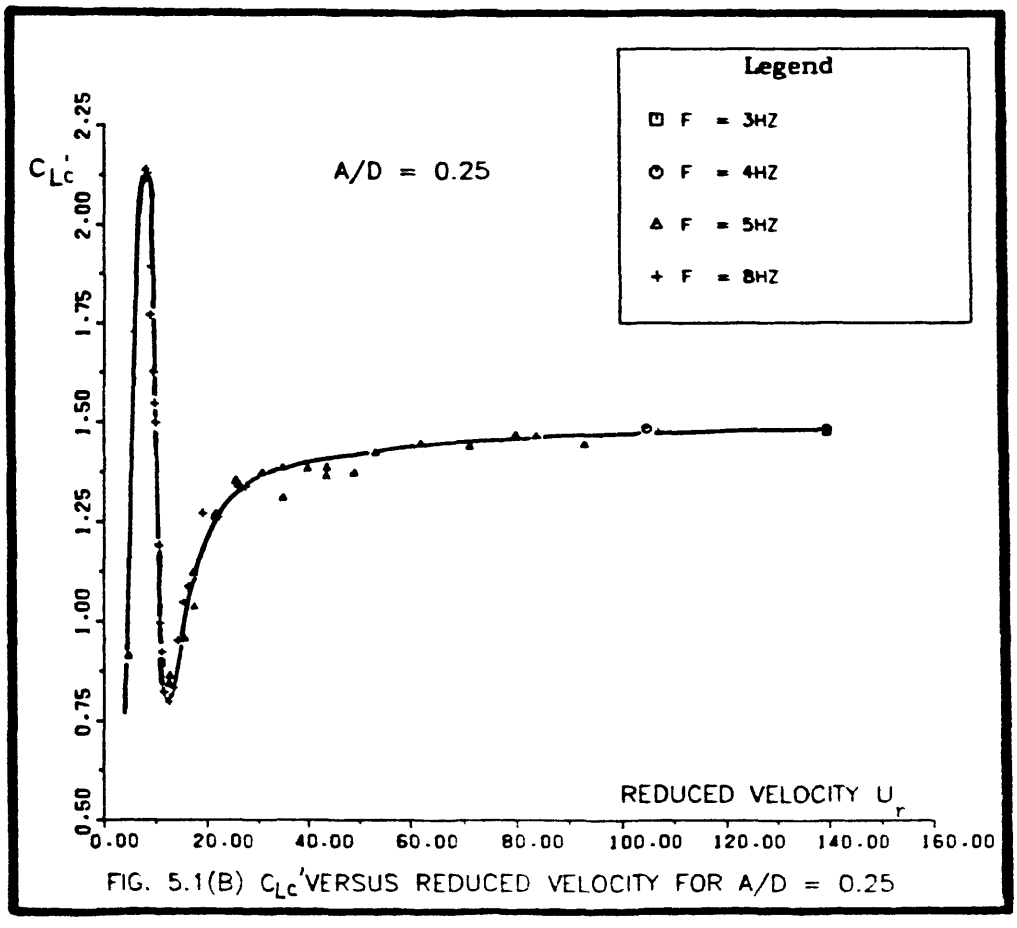


FIG. 5.1(B) C_{Lc}' VERSUS REDUCED VELOCITY FOR A/D = 0.25

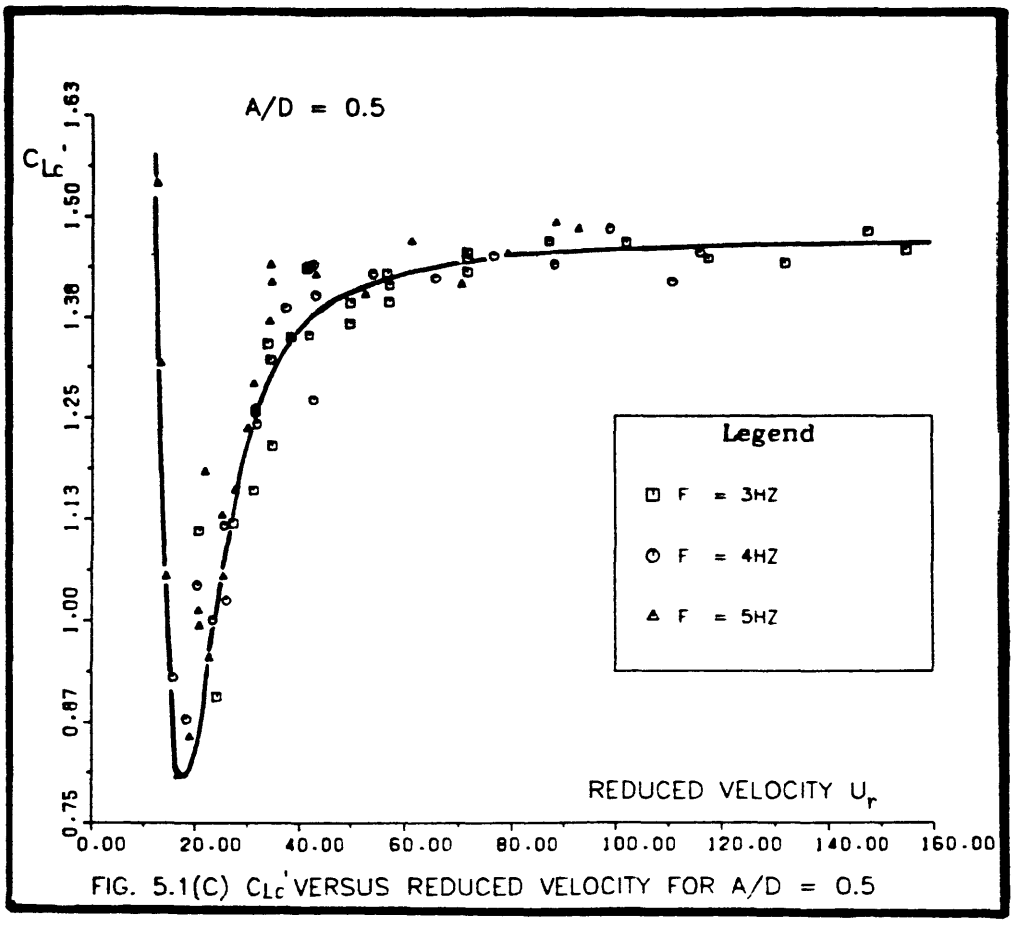


FIG. 5.1(C) C_{Lc}'VERSUS REDUCED VELOCITY FOR A/D = 0.5

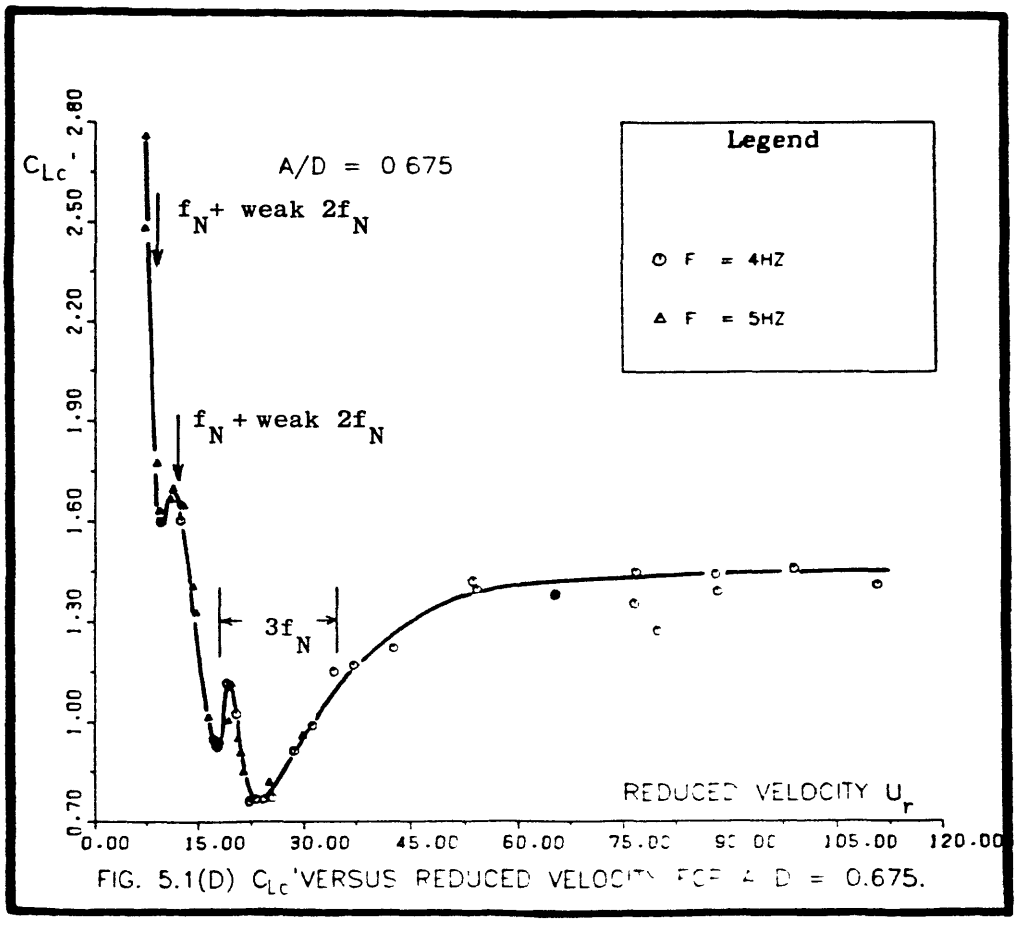


FIG. 5.1(D) C_{Lc}'VERSUS REDUCED VELOCITY FOR A/D = 0.675.

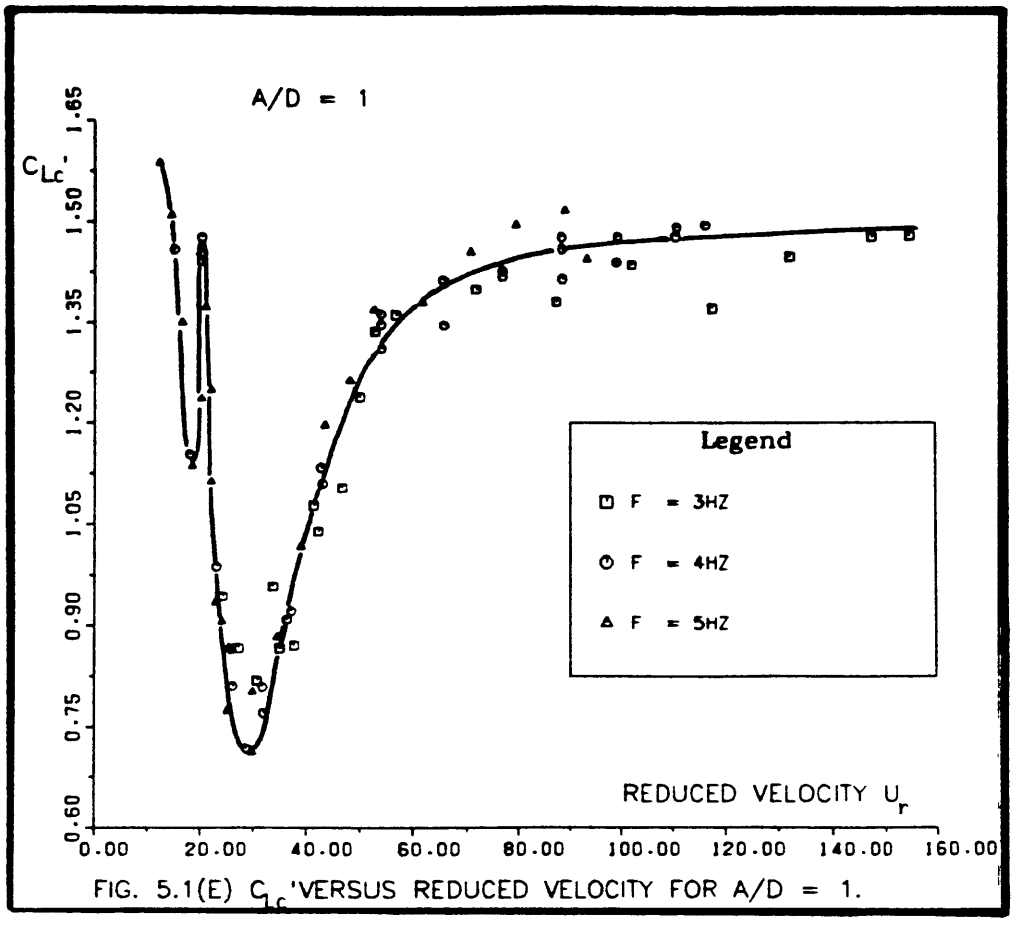


FIG. 5.1(E) C_{Lc} VERSUS REDUCED VELOCITY FOR A/D = 1.

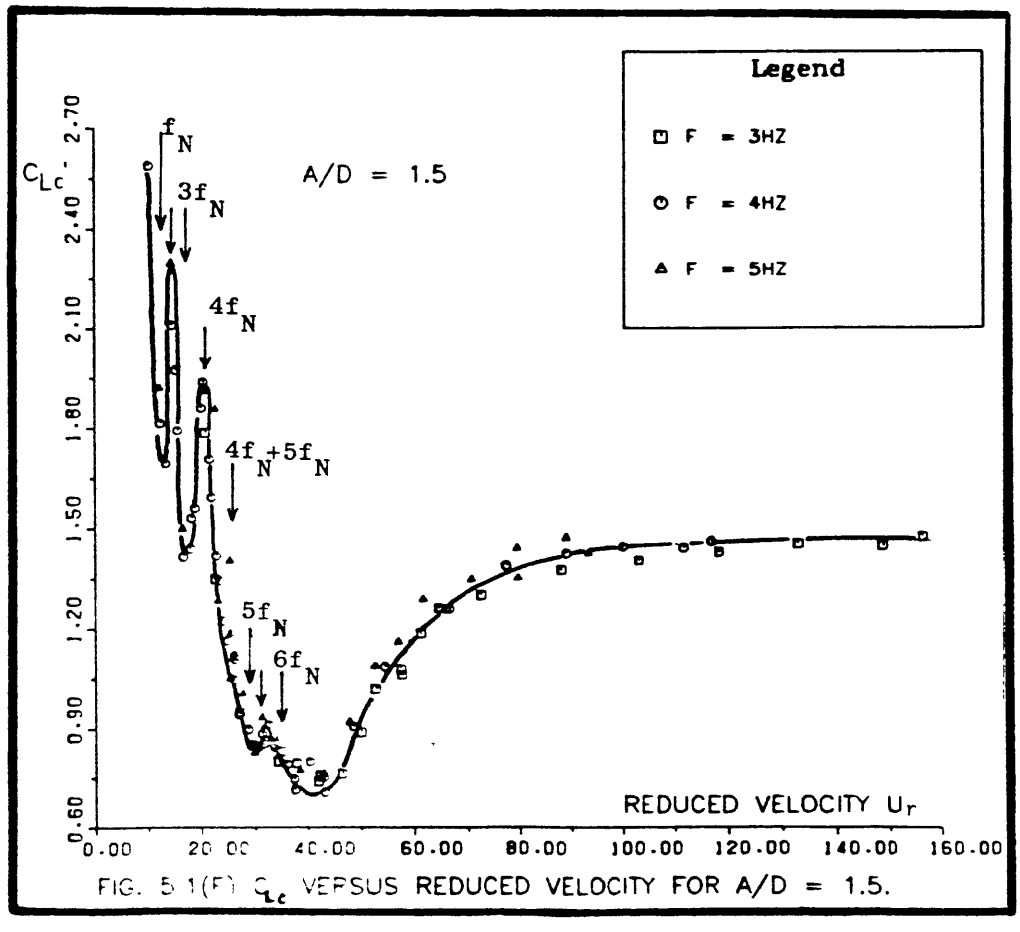


FIG. 5.1(F) C_{Lc} VERSUS REDUCED VELOCITY FOR A/D = 1.5.

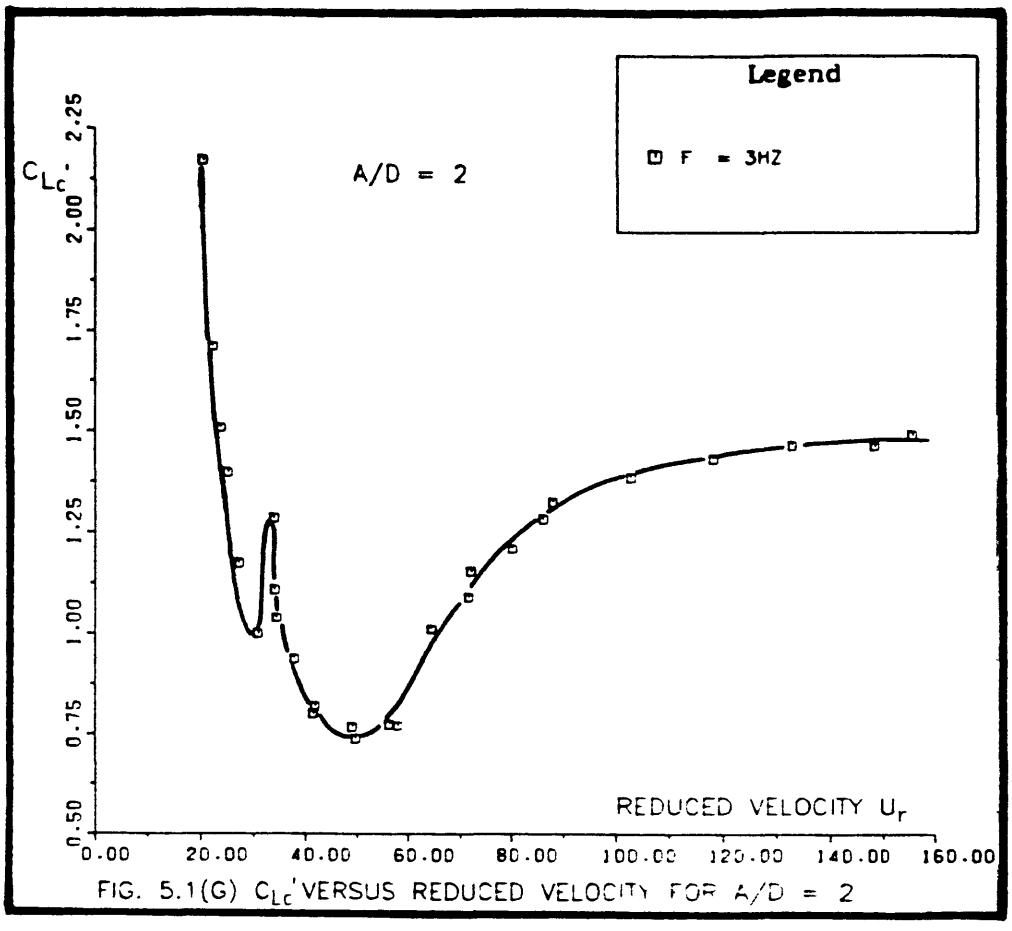


FIG. 5.1(G) C_{Lc} VERSUS REDUCED VELOCITY FOR A/D = 2

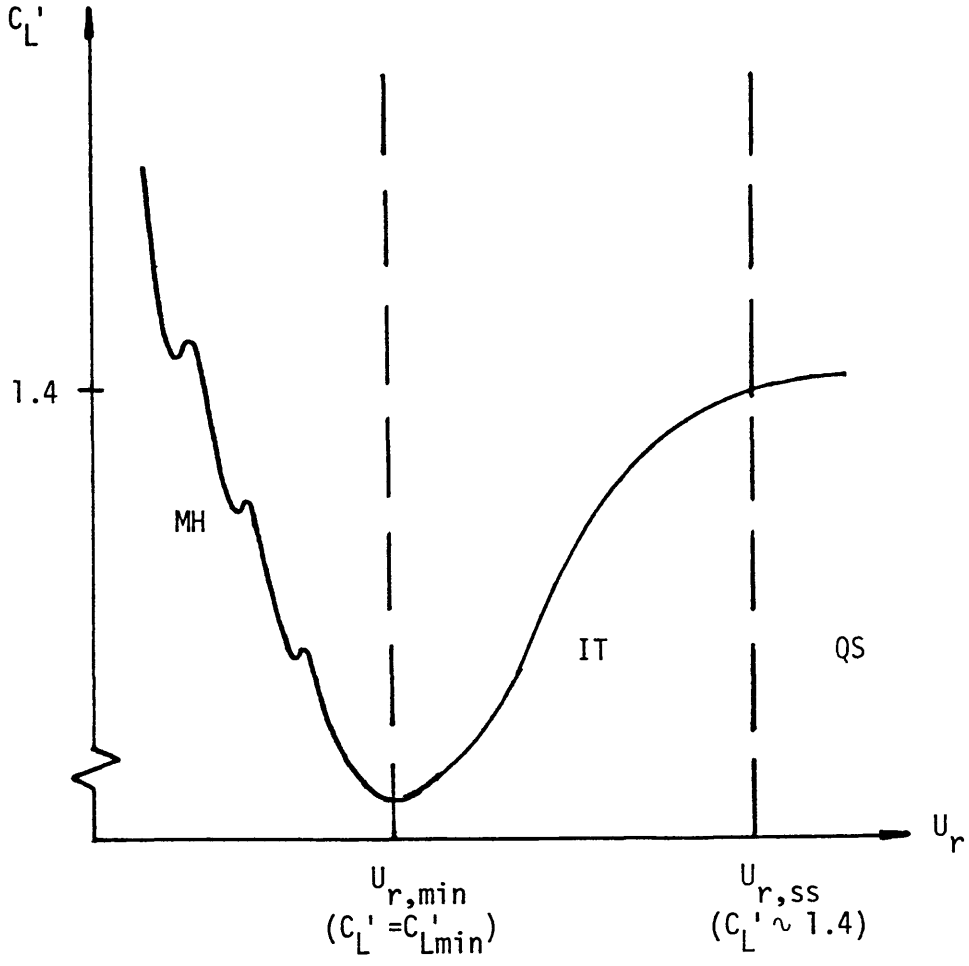


Fig. 5.2 Classification of flow region
MH = Multiple Harmonic
IT = Intermediate Transition
QS = Quasi-Steady

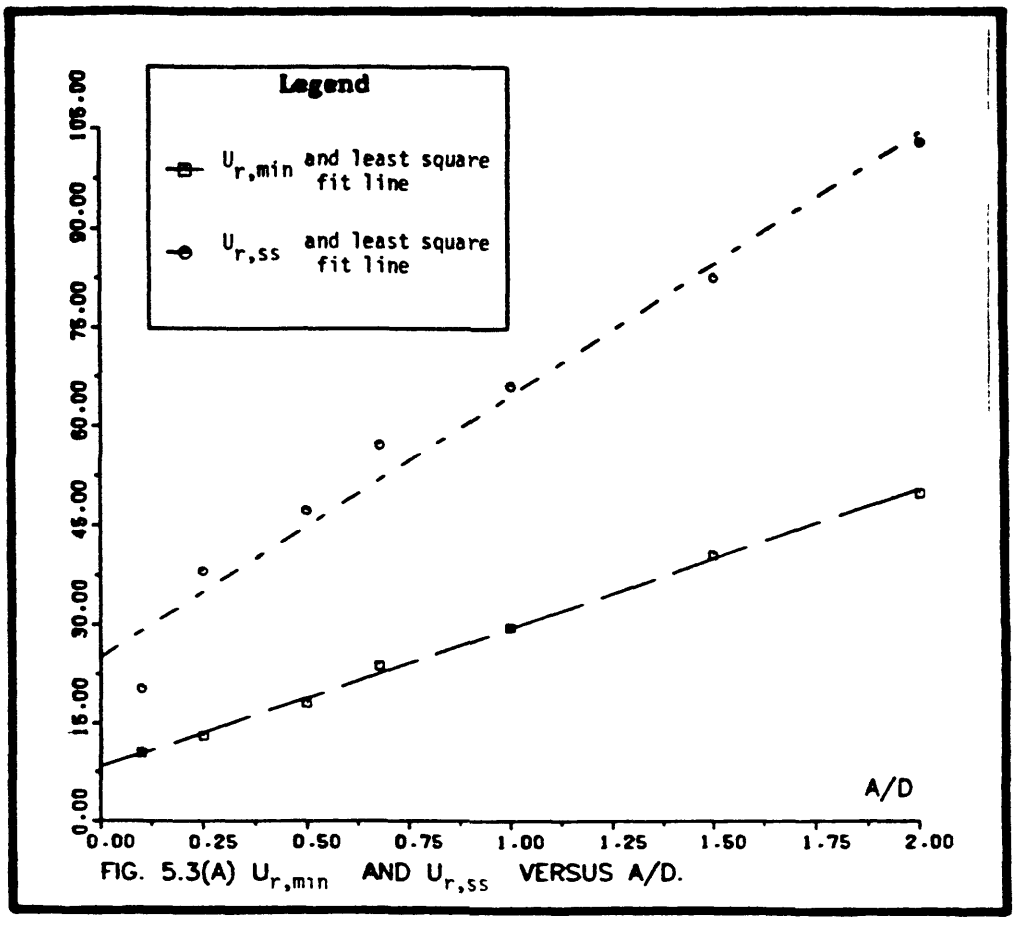


FIG. 5.3(A) $U_{r,min}$ AND $U_{r,ss}$ VERSUS A/D.

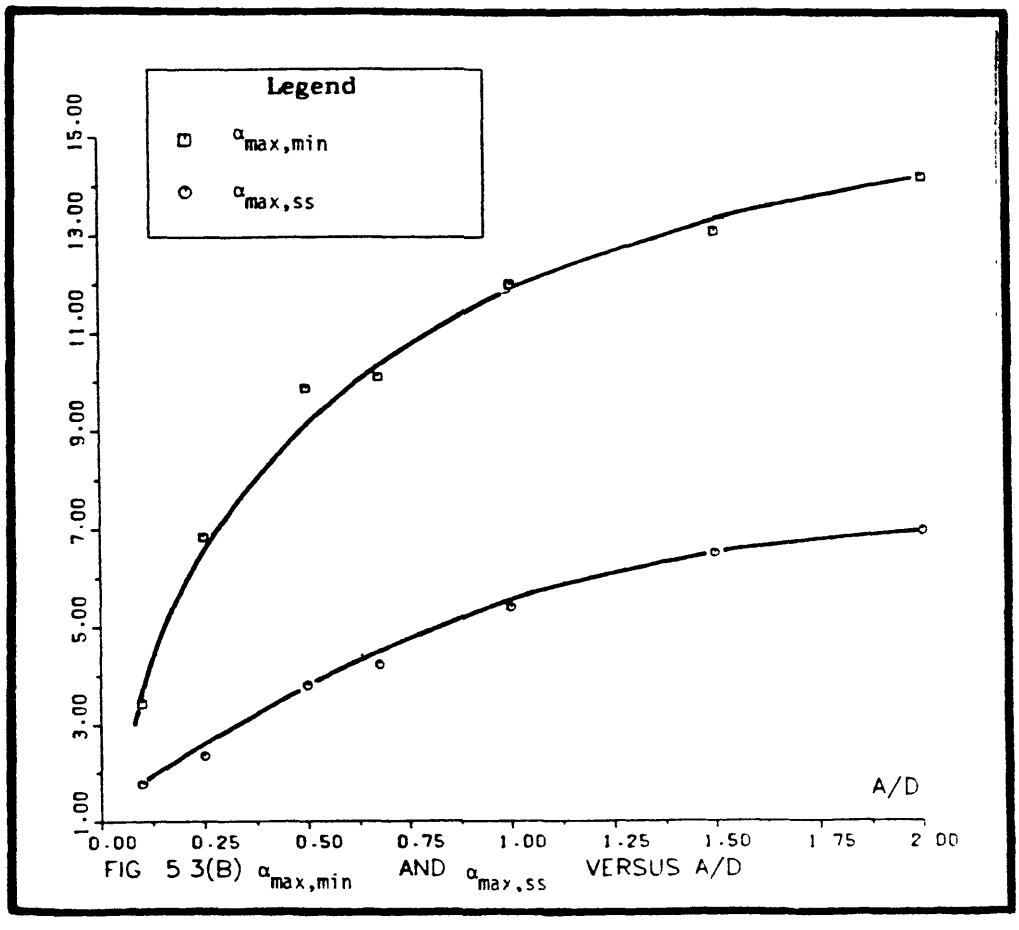


FIG 5.3(B) $\alpha_{max,min}$ AND $\alpha_{max,ss}$ VERSUS A/D

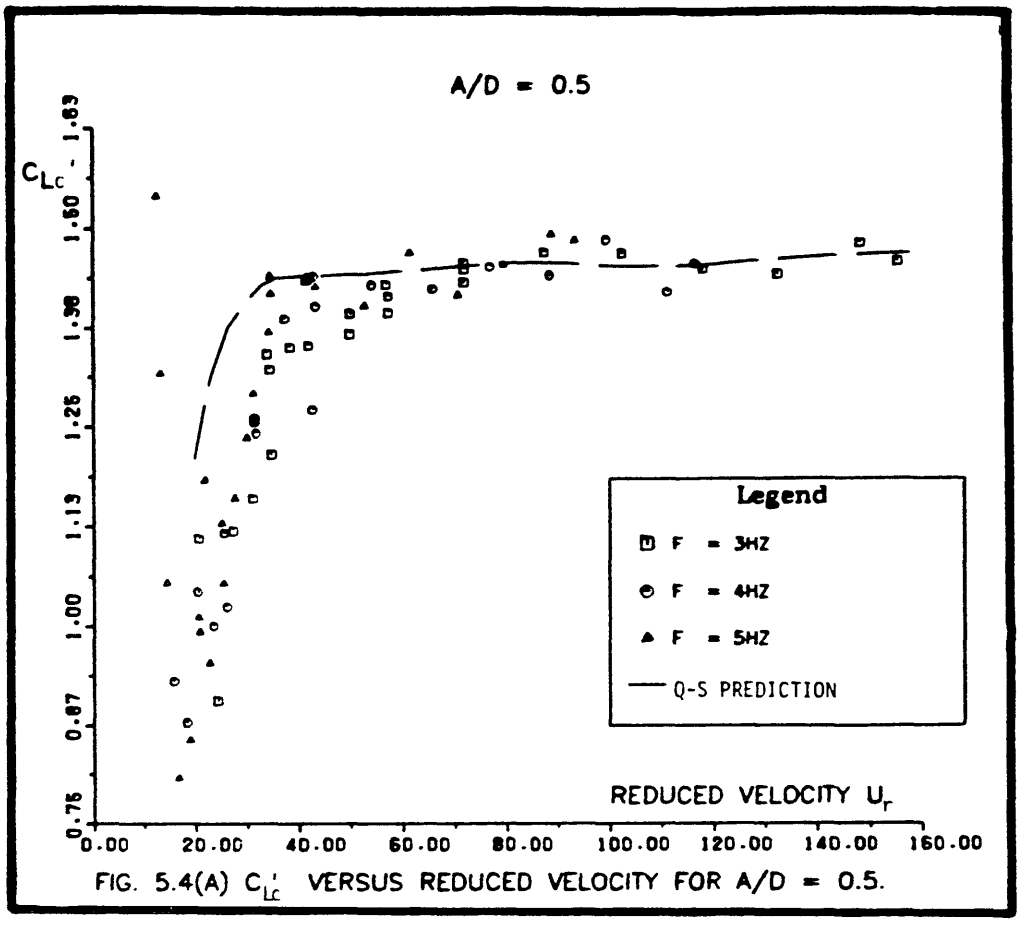


FIG. 5.4(A) C_{Lc}' VERSUS REDUCED VELOCITY FOR A/D = 0.5.

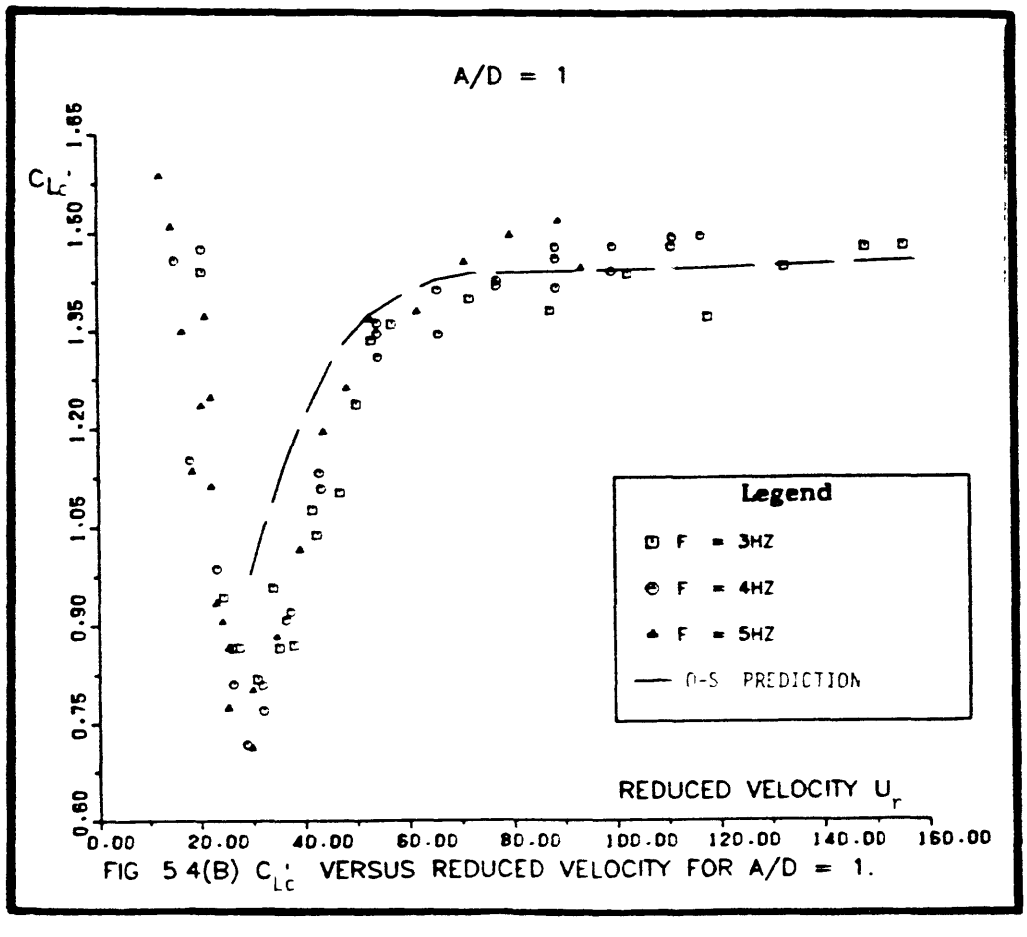


FIG 5.4(B) C_{Lc}' VERSUS REDUCED VELOCITY FOR A/D = 1.

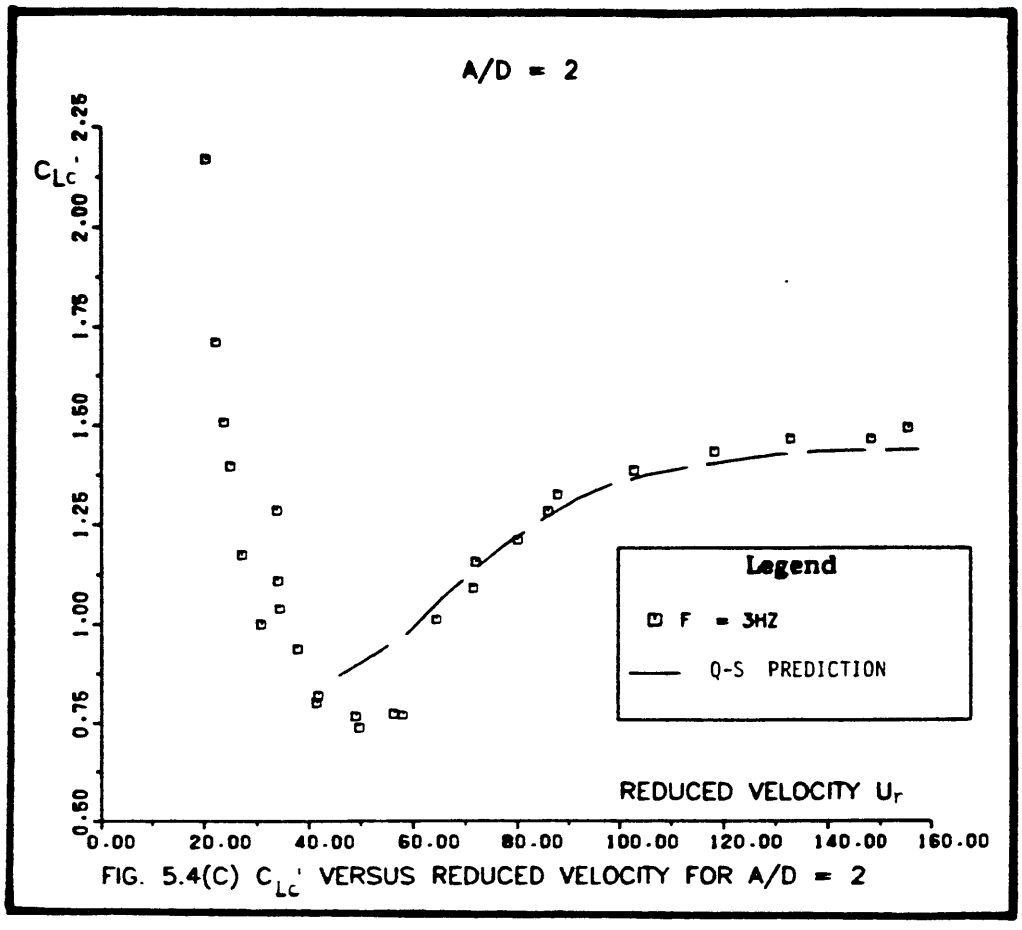


FIG. 5.4(C) C_{Lc}' VERSUS REDUCED VELOCITY FOR A/D = 2

FIG. 5.5 --- A NOTE ON ITS INTERRETATION

1. In each CRO photograph, the top trace represents the lift force and the bottom trace represents the cylinder displacement.

2. CRO phogographs in fig. 5.5 always appear in pairs of two. The first one applies to when the square cylinder is oscillating transversely to the free stream while the second one applies to when the cylinder is stationary in an otherwise identical free stream.

3. Between each pair of oscillating and stationary cylinder CRO photographs, the time scale (horizontal axis) and the scale for the lift force (vertical axis) are always identical.

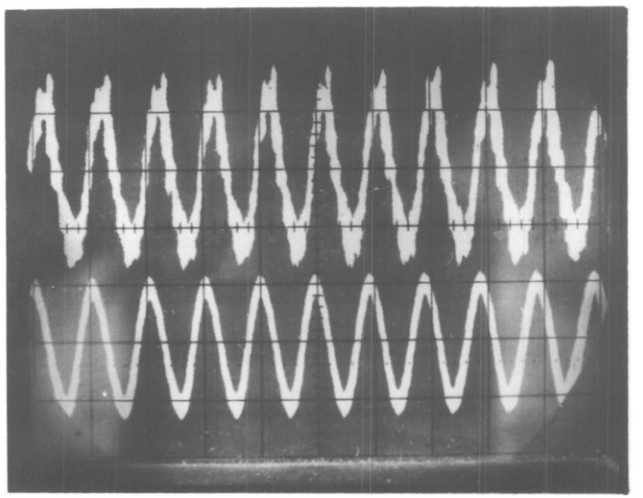


Fig. 5.5(a) $U_r \sim 7.75$, $Re \sim 0.65 \times 10^4$

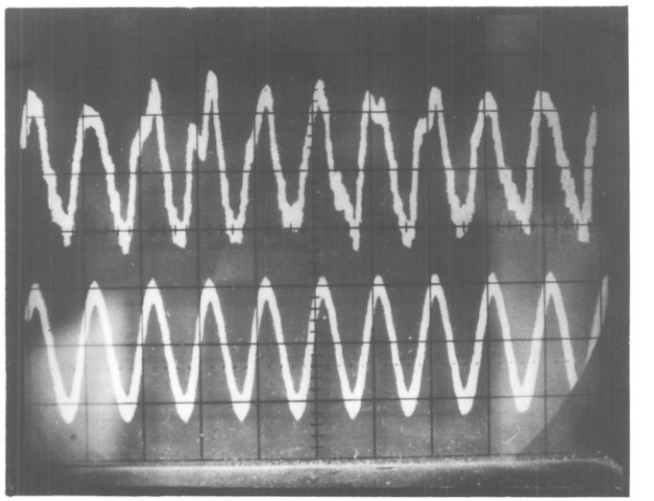


Fig. 5.5(c) $U_r \sim 14.37$, $Re \sim 1.21 \times 10^4$

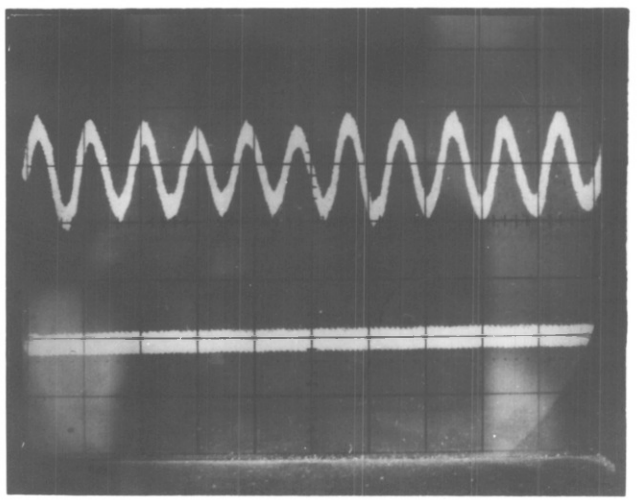


Fig. 5.5(b) $Re \sim 0.65 \times 10^4$

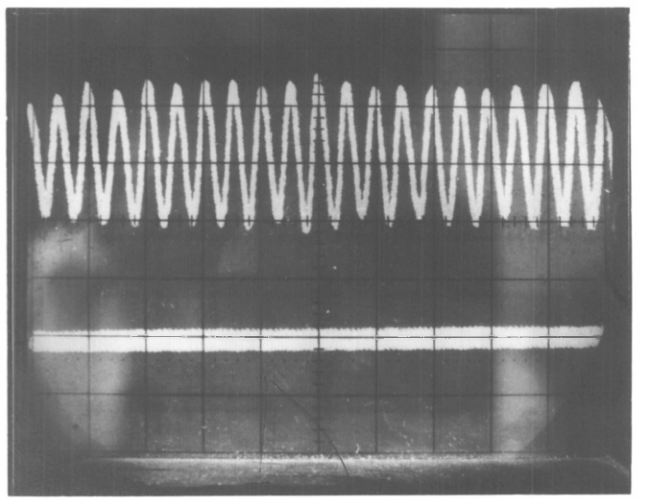


Fig. 5.5(d) $Re \sim 1.21 \times 10^4$

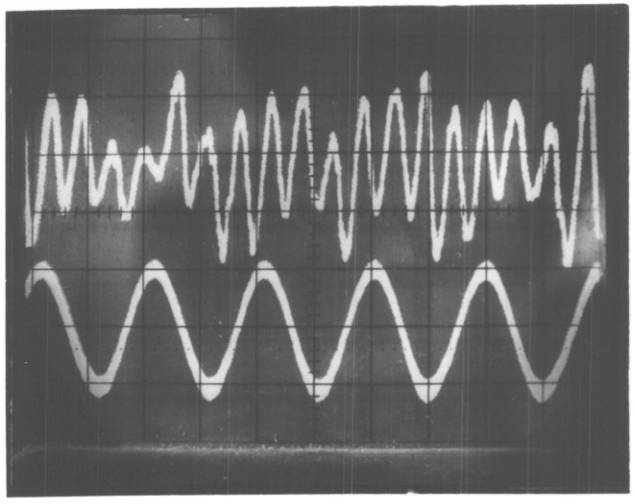


Fig. 5.5(e) $U_r \sim 21.60$, $Re \sim 1.81 \times 10^4$

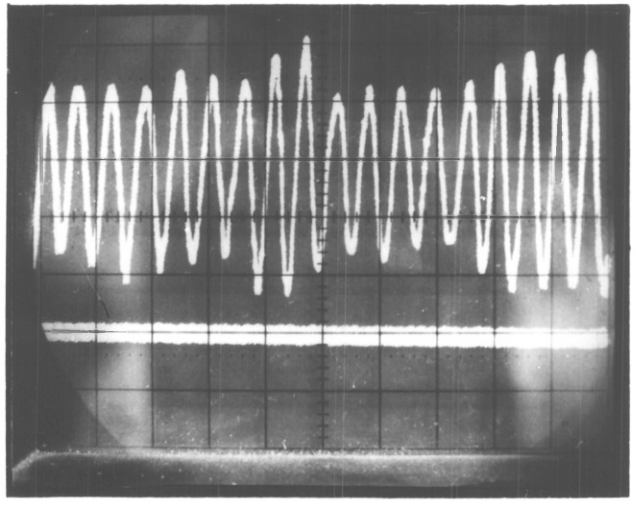


Fig. 5.5(f) $Re \sim 1.81 \times 10^4$

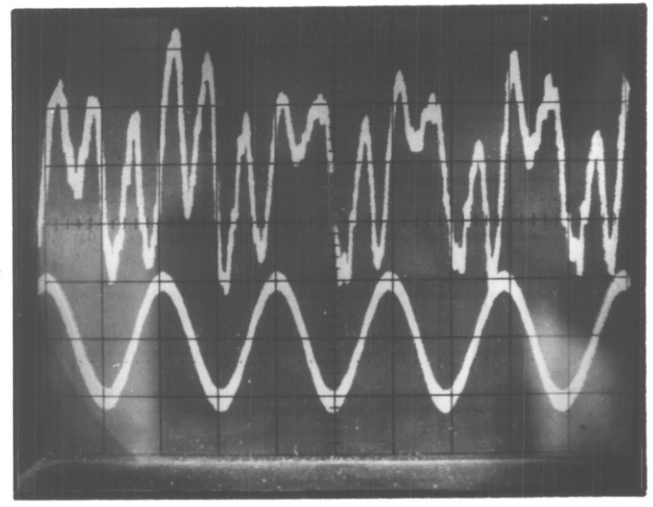


Fig. 5.5(g) $U_r \sim 27.04$, $Re \sim 2.27 \times 10^4$

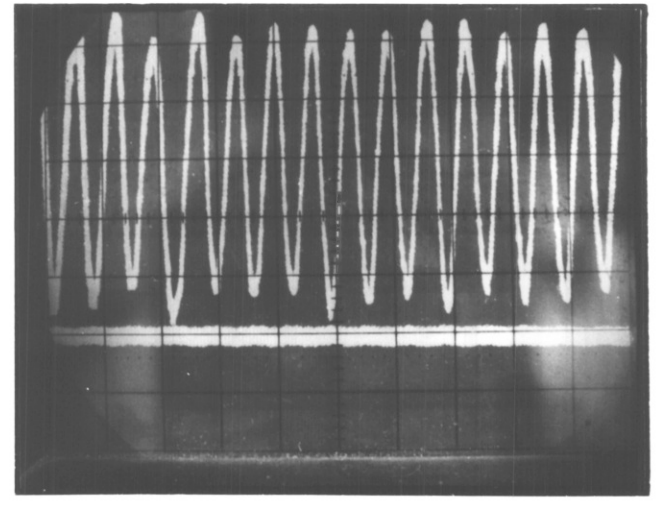


Fig. 5.5(h) $Re \sim 2.27 \times 10^4$

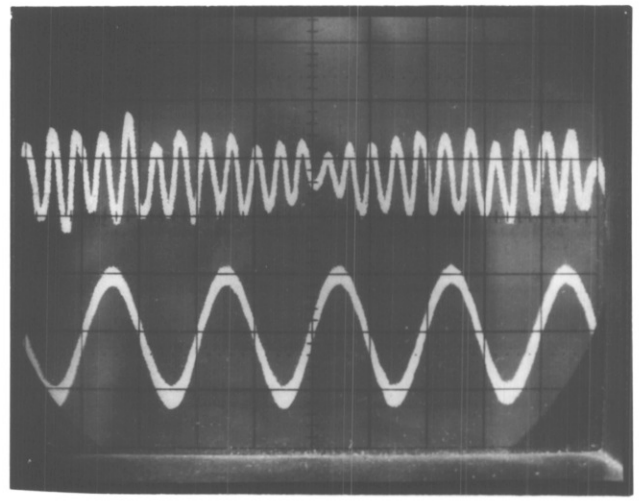


Fig. 5.5(i) $U_r \sim 35.79$, $Re \sim 3.01 \times 10^4$

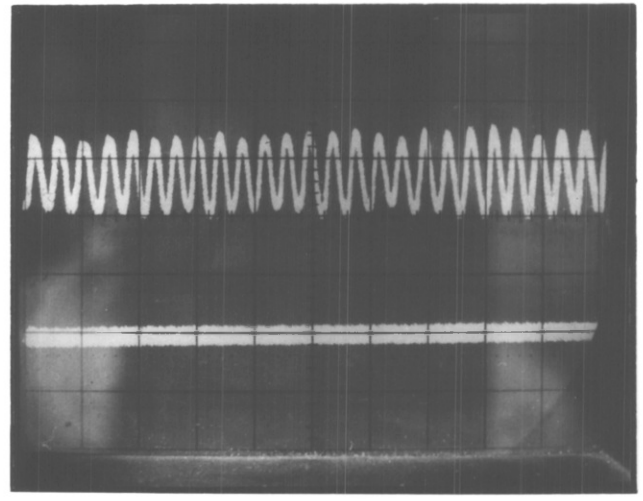


Fig. 5.5(j) $Re \sim 3.01 \times 10^4$

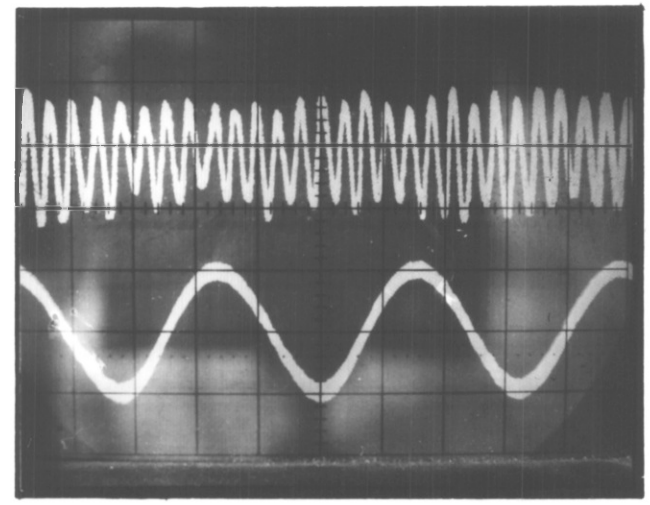


Fig. 5.5(k) $U_r \sim 72.76$, $Re \sim 3.69 \times 10^4$

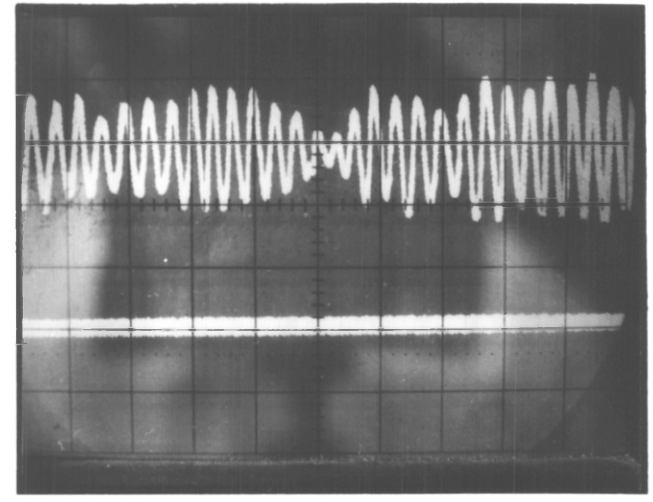


Fig. 5.5(l) $Re \sim 3.69 \times 10^4$

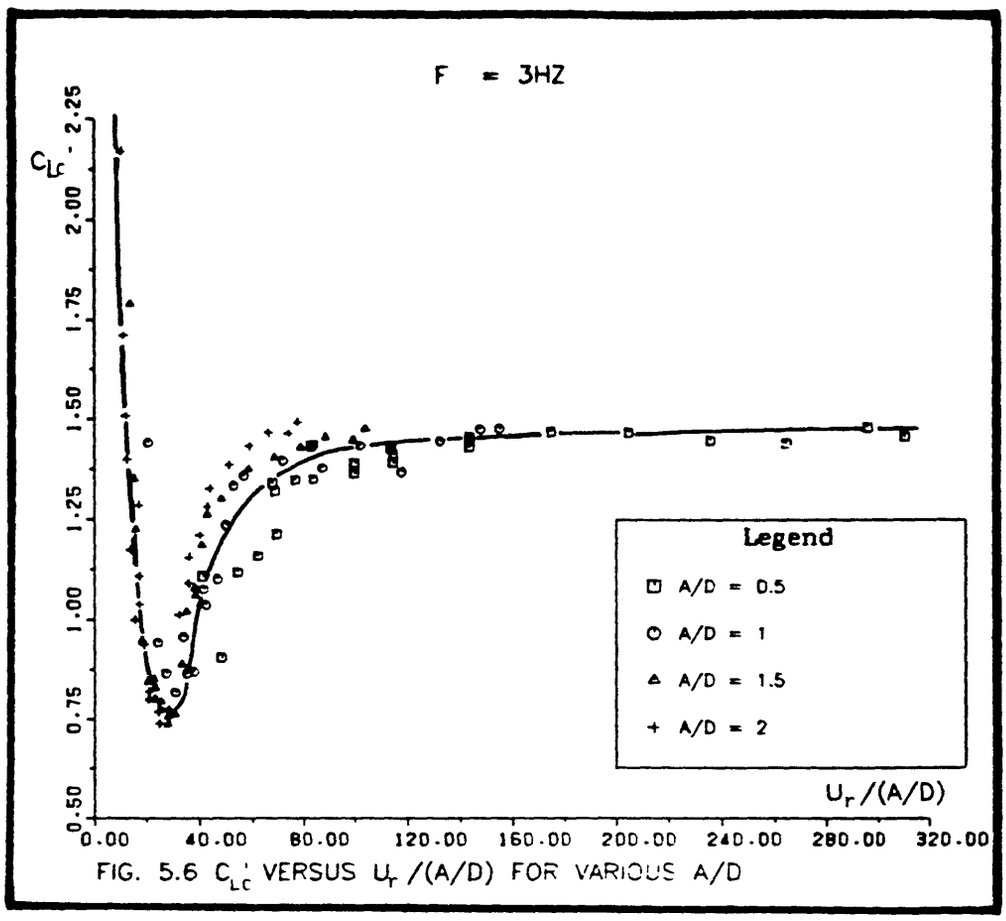


FIG. 5.6 C_{LC}' VERSUS $U_r/(A/D)$ FOR VARIOUS A/D

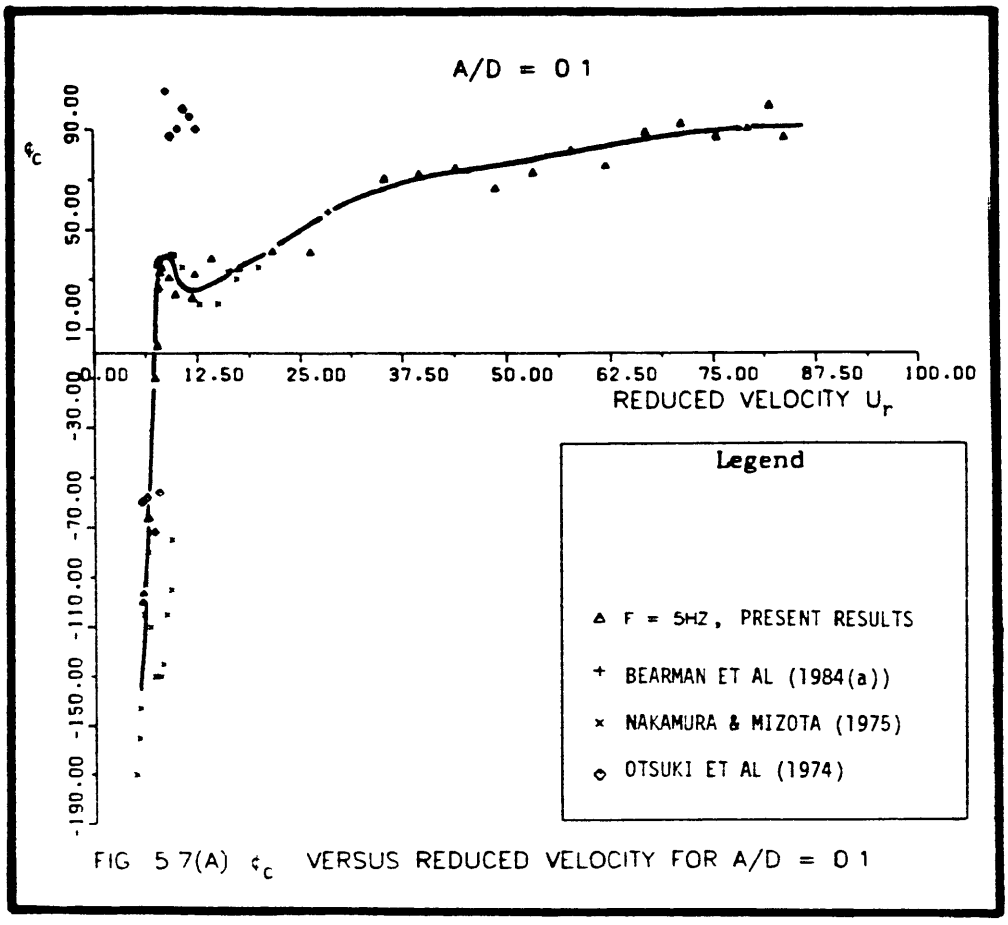


FIG 5 7(A) ϕ_c VERSUS REDUCED VELOCITY FOR A/D = 0 1

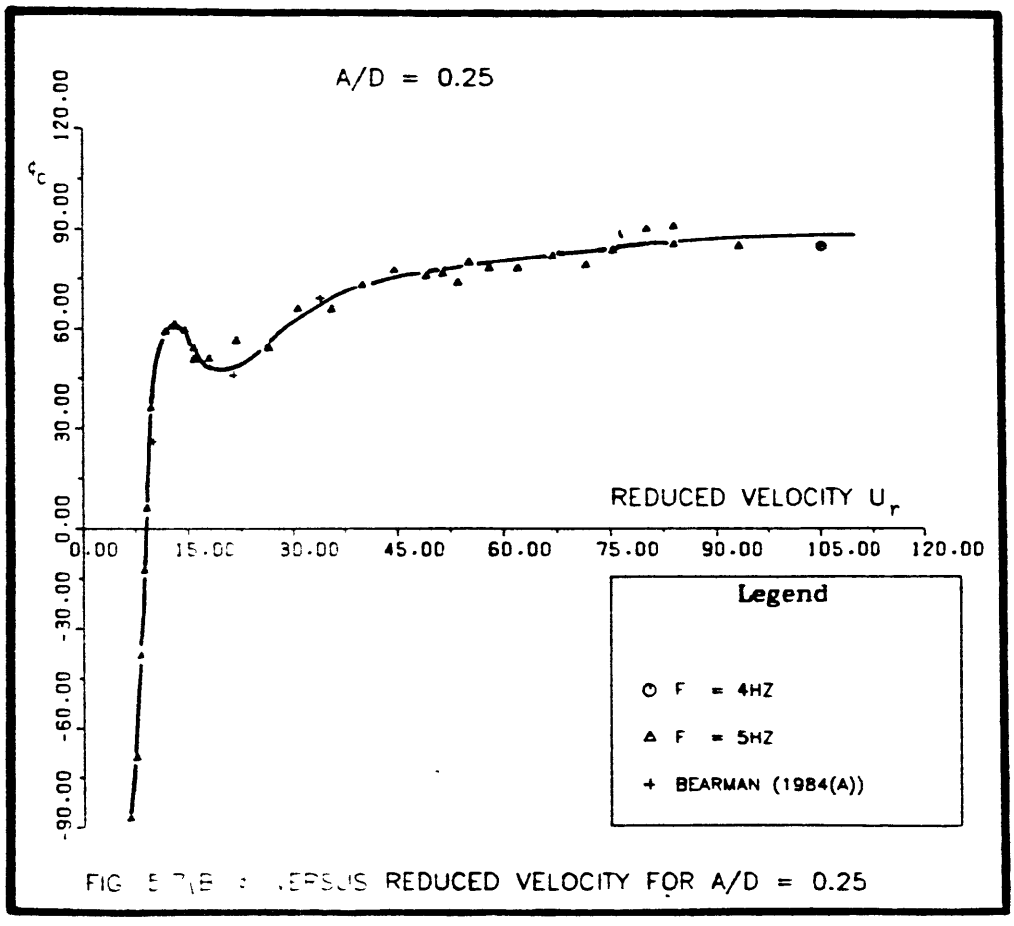


FIG 5 7(B) VERSUS REDUCED VELOCITY FOR A/D = 0.25

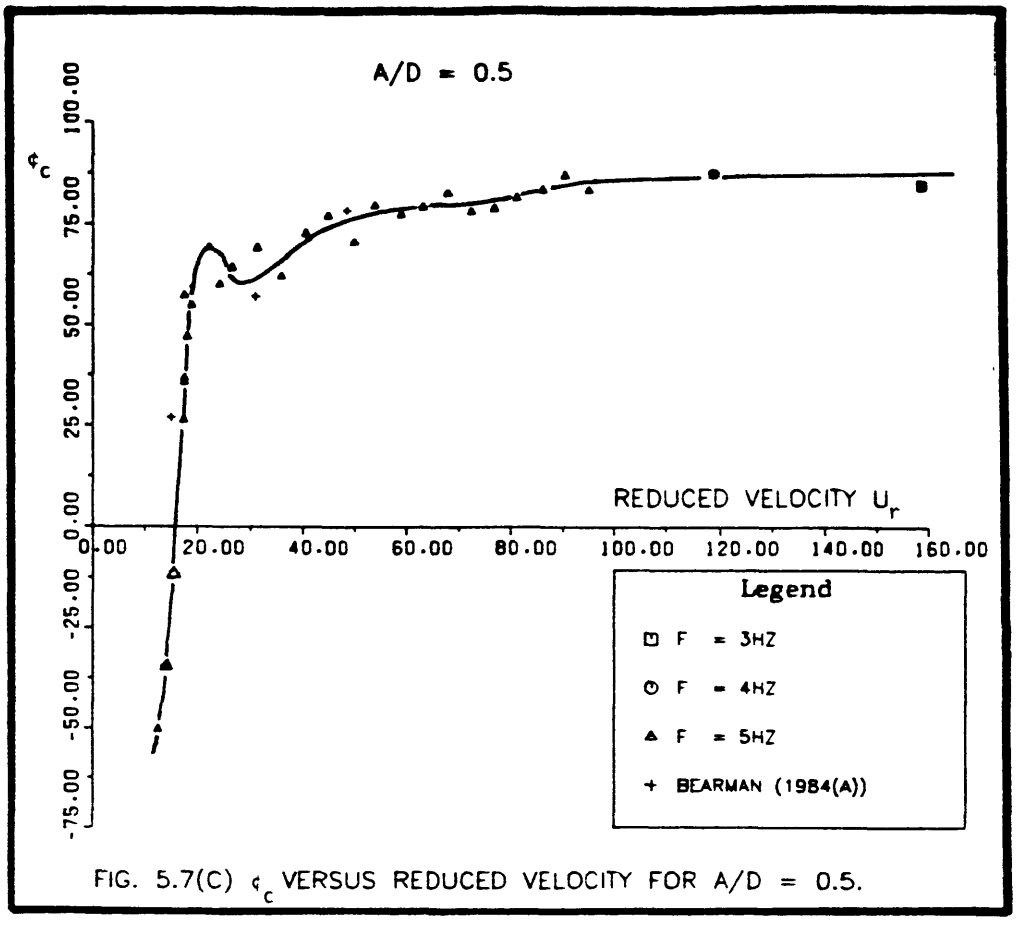


FIG. 5.7(C) ϕ_c VERSUS REDUCED VELOCITY FOR A/D = 0.5.

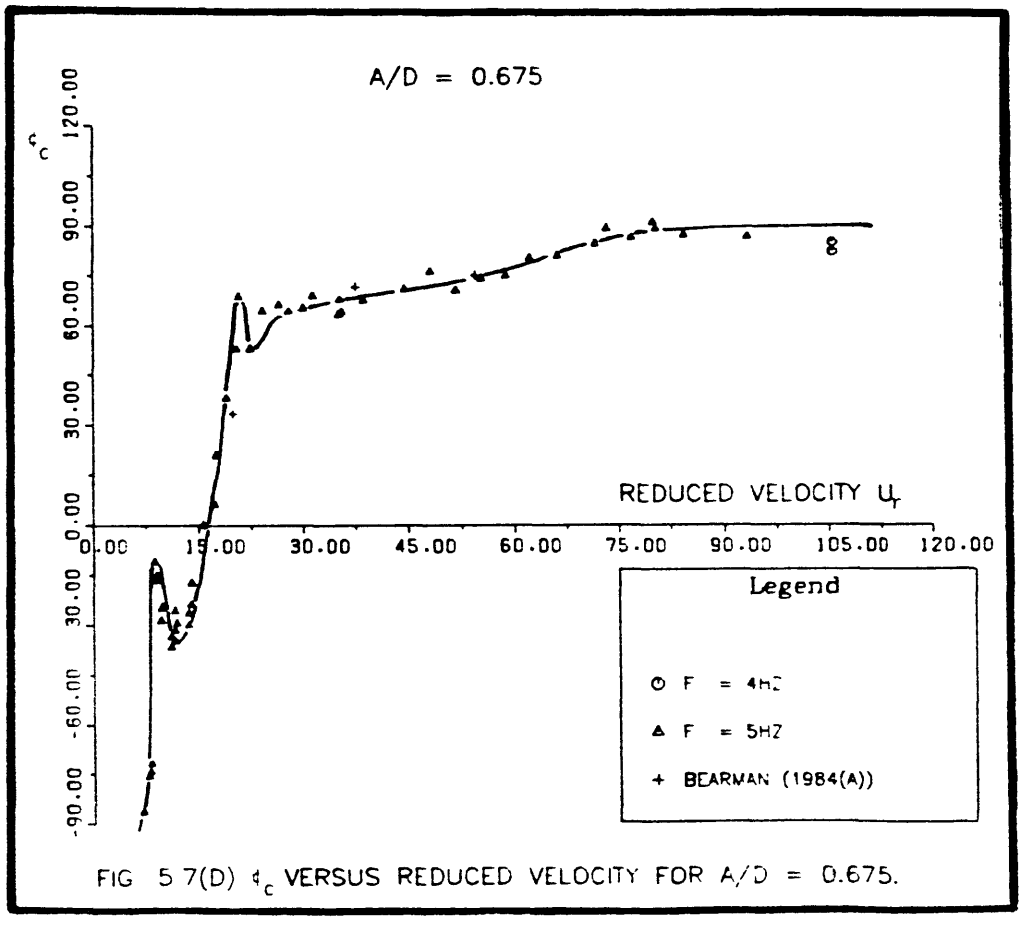


FIG 5.7(D) ϕ_c VERSUS REDUCED VELOCITY FOR A/D = 0.675.

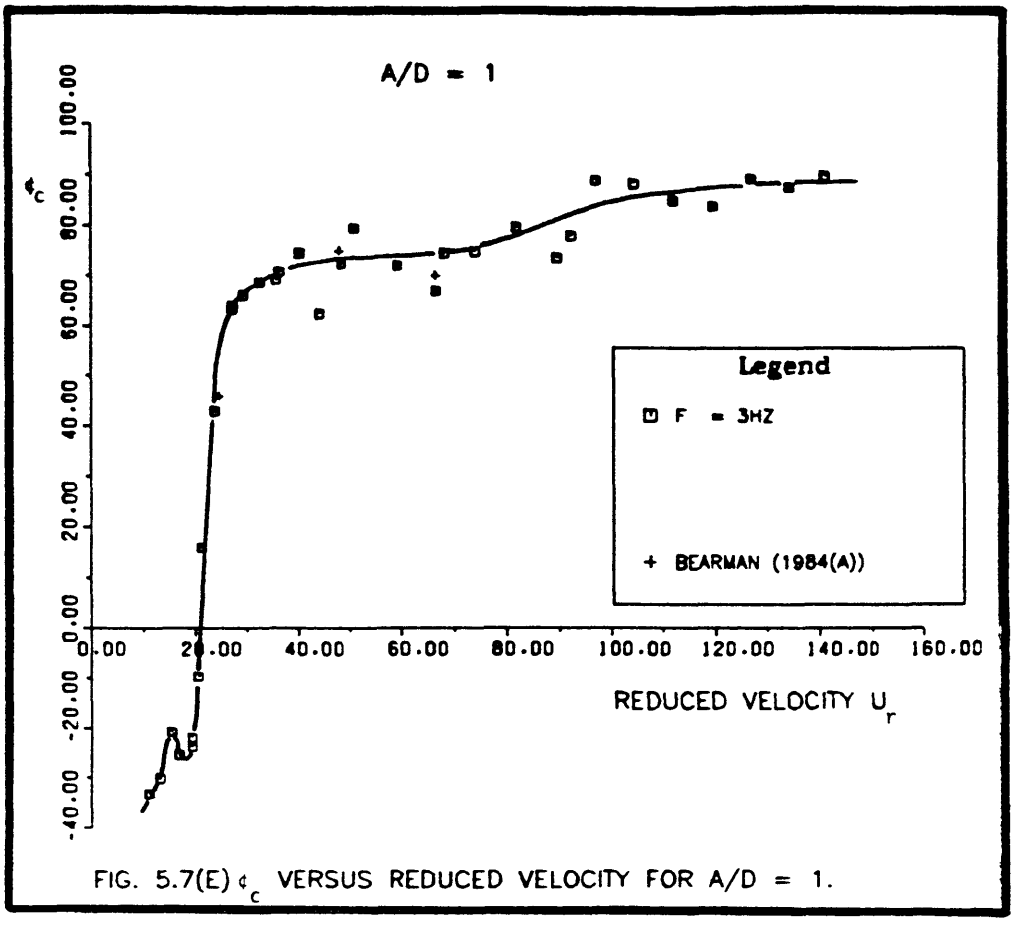


FIG. 5.7(E) C_c VERSUS REDUCED VELOCITY FOR A/D = 1.

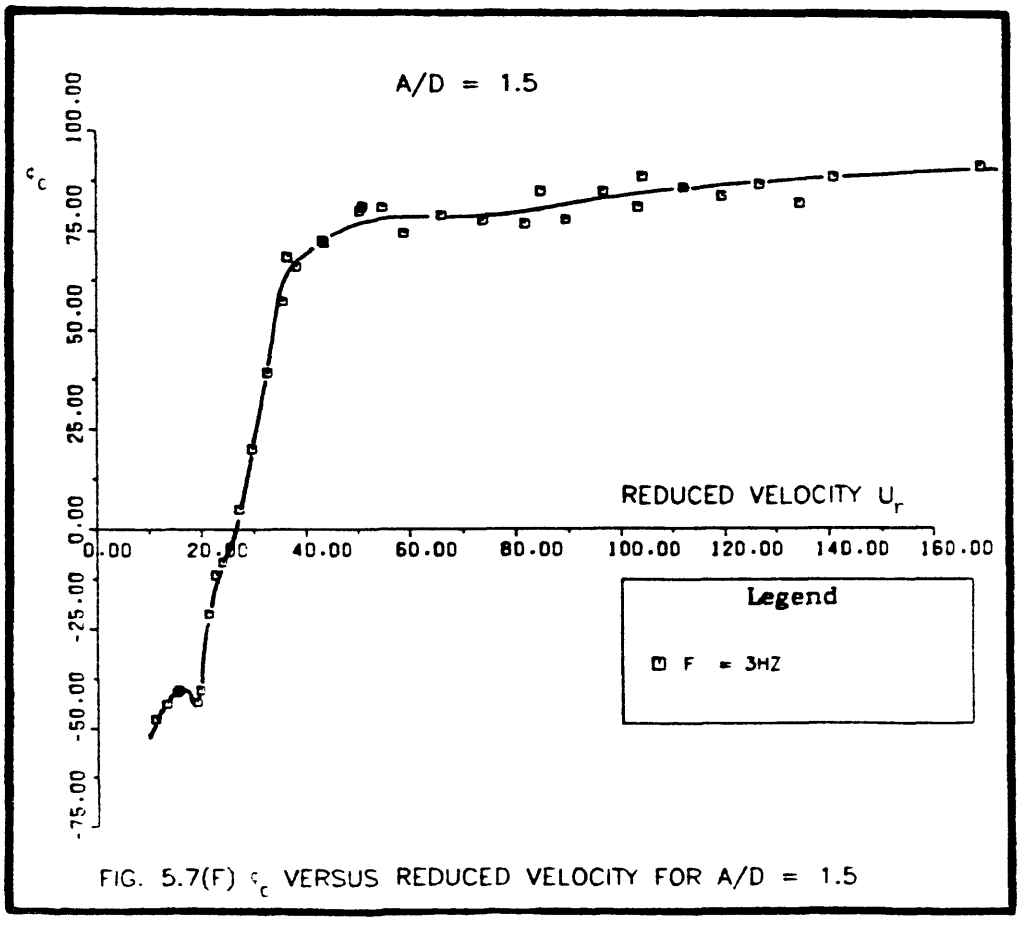


FIG. 5.7(F) C_c VERSUS REDUCED VELOCITY FOR A/D = 1.5

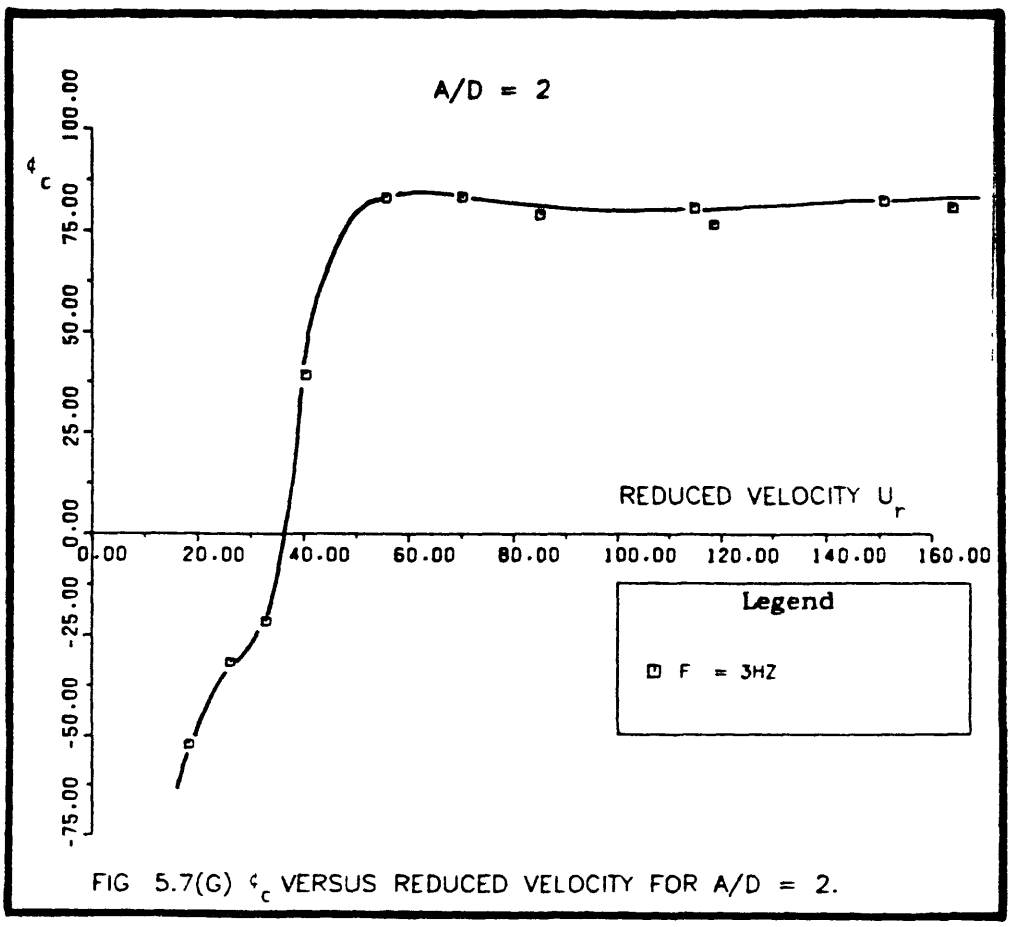


FIG 5.7(G) ϕ_c VERSUS REDUCED VELOCITY FOR A/D = 2.

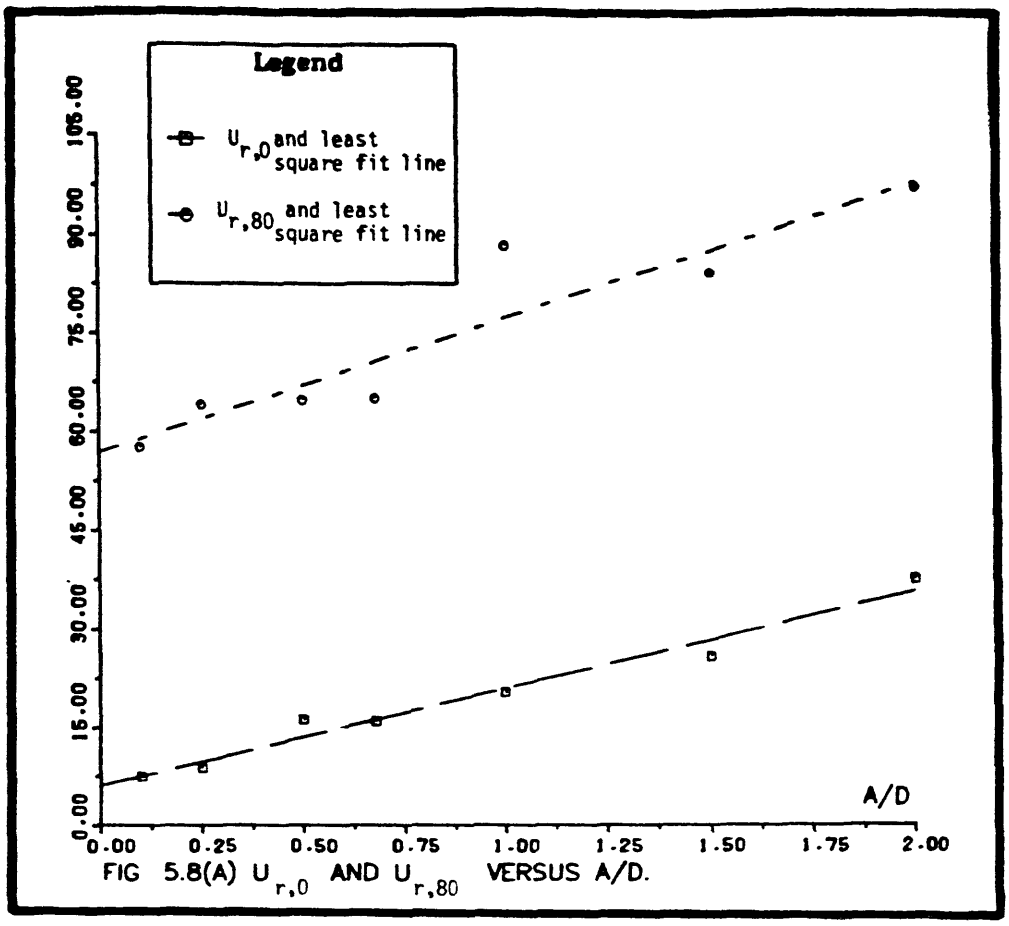


FIG 5.8(A) $U_{r,0}$ AND $U_{r,80}$ VERSUS A/D.

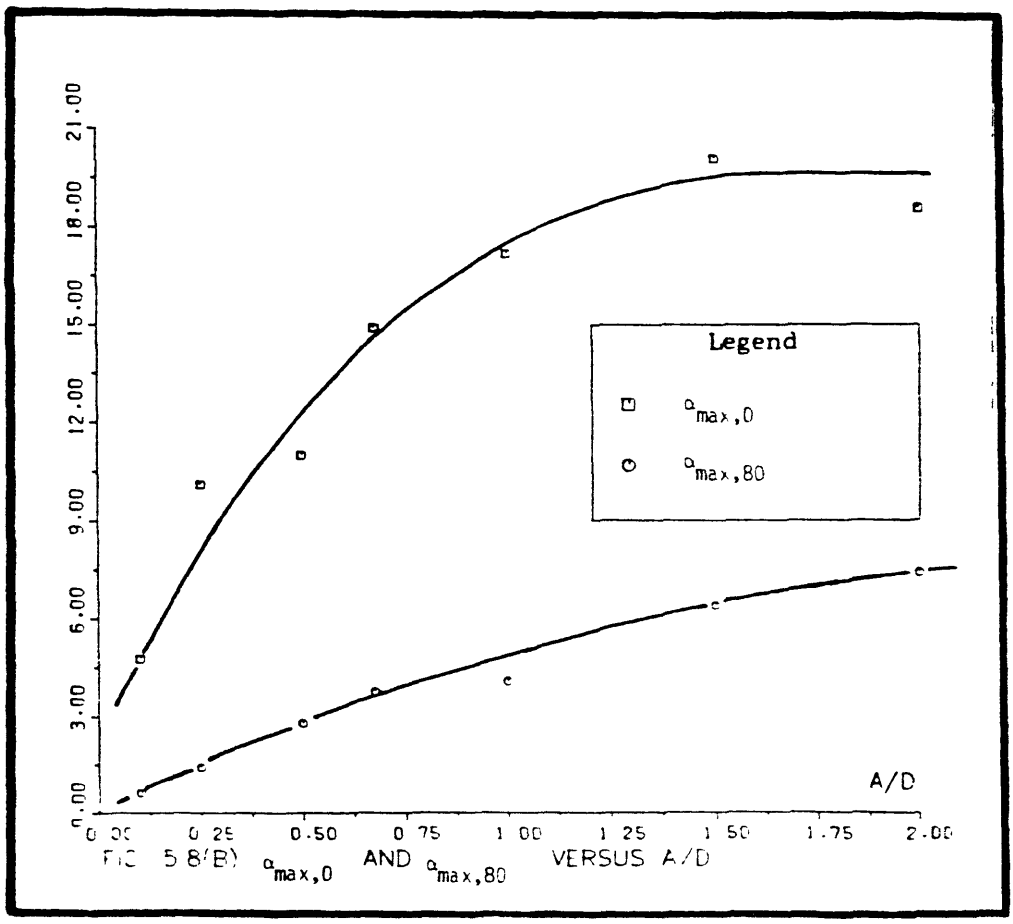


FIG 5.8(B) $\alpha_{max,0}$ AND $\alpha_{max,80}$ VERSUS A/D

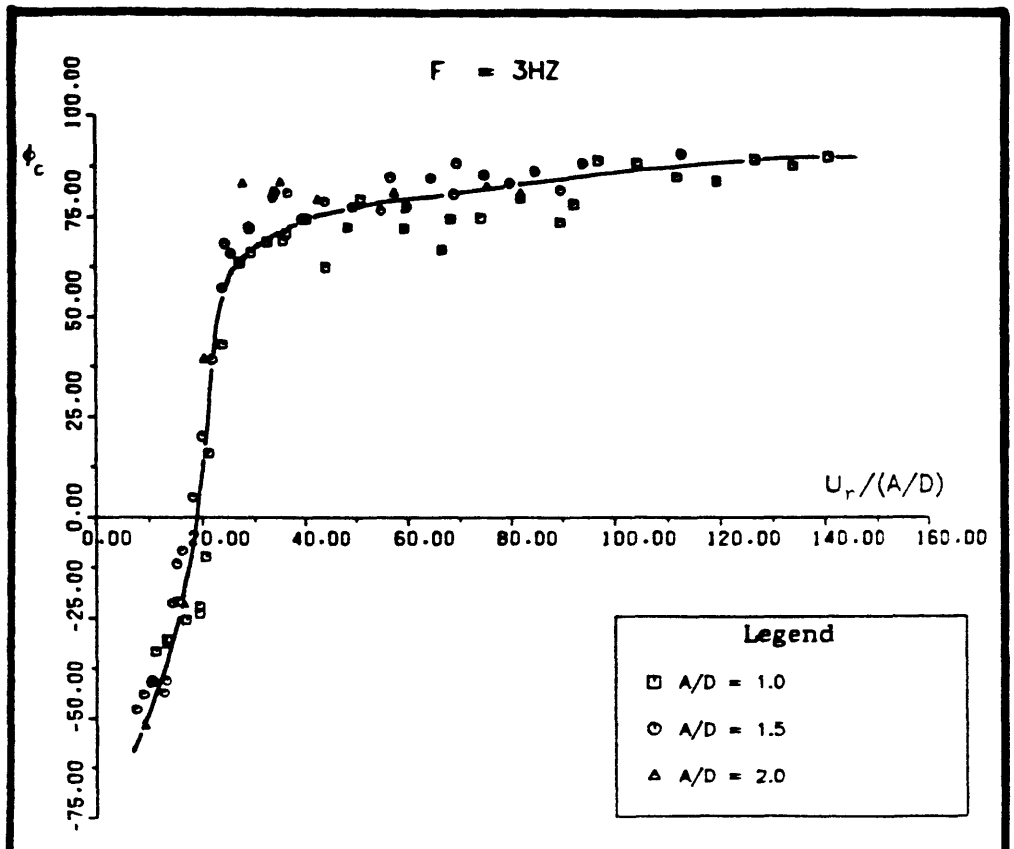


FIG. 5.9 ϕ_c VERSUS $U_r/(A/D)$ FOR VARIOUS A/D.

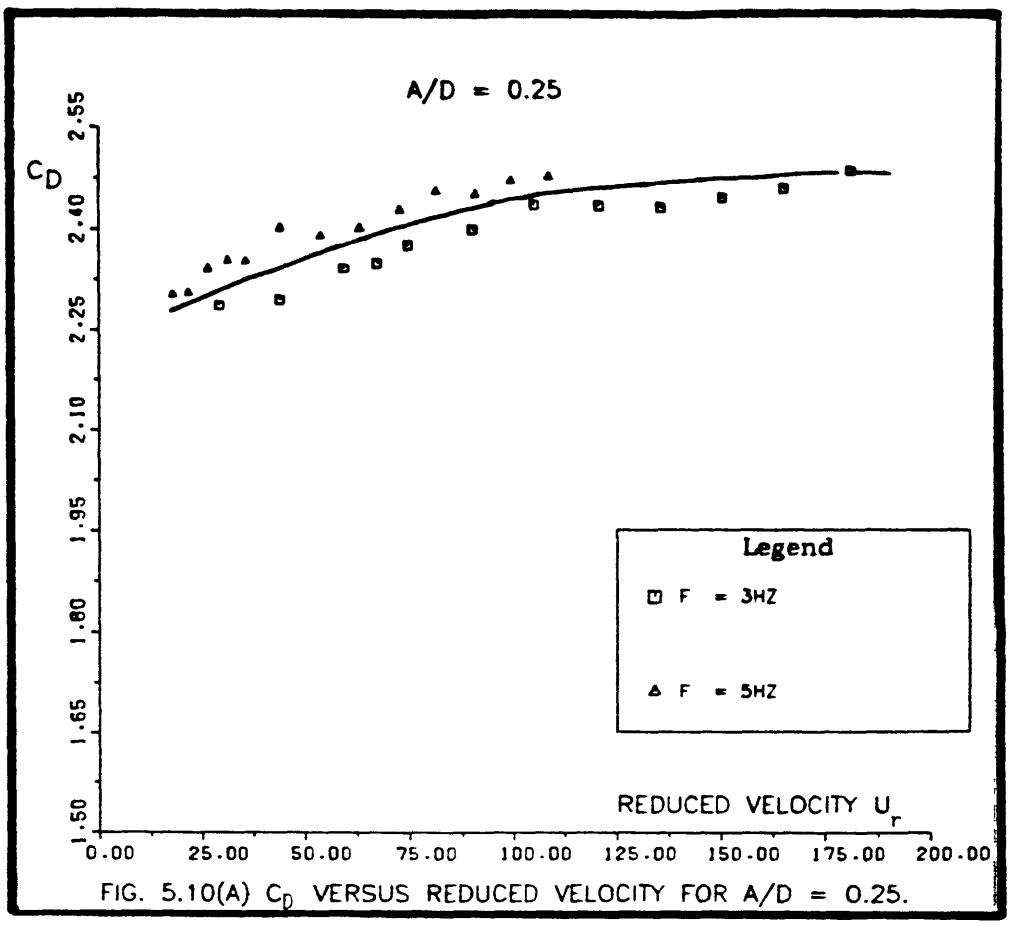


FIG. 5.10(A) C_D VERSUS REDUCED VELOCITY FOR A/D = 0.25.

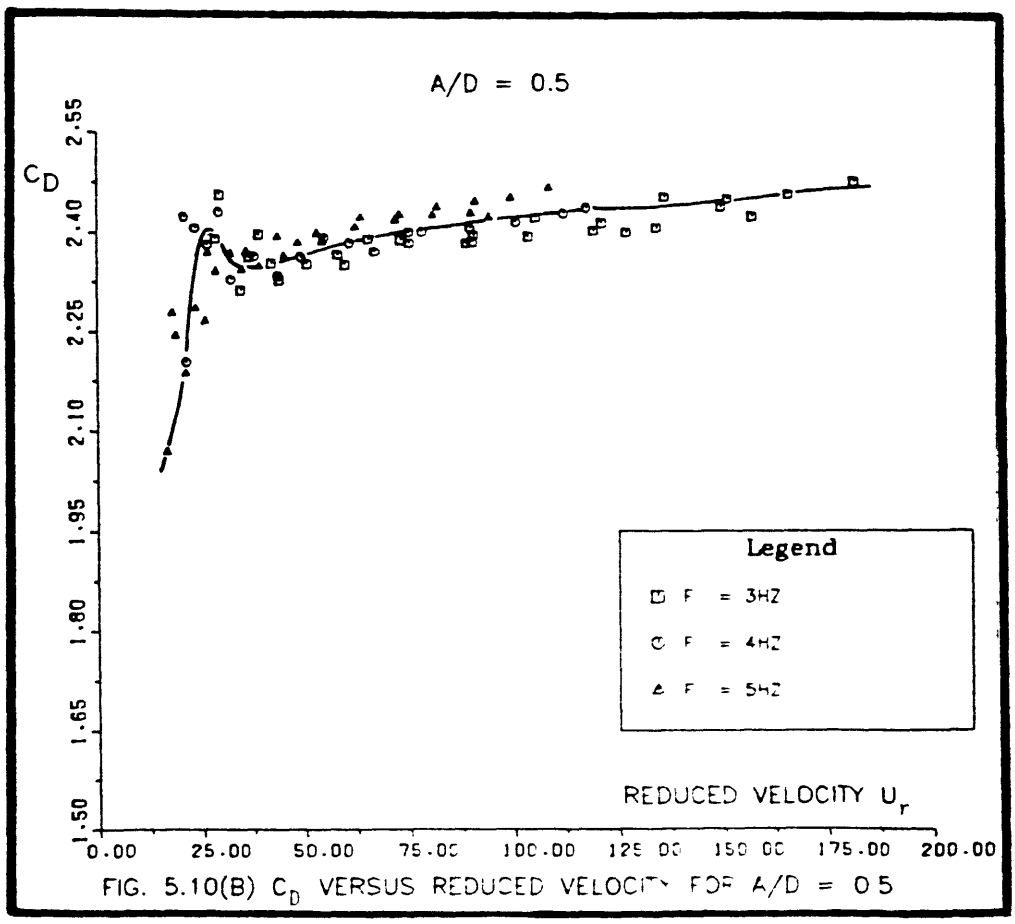


FIG. 5.10(B) C_D VERSUS REDUCED VELOCITY FOR A/D = 0.5

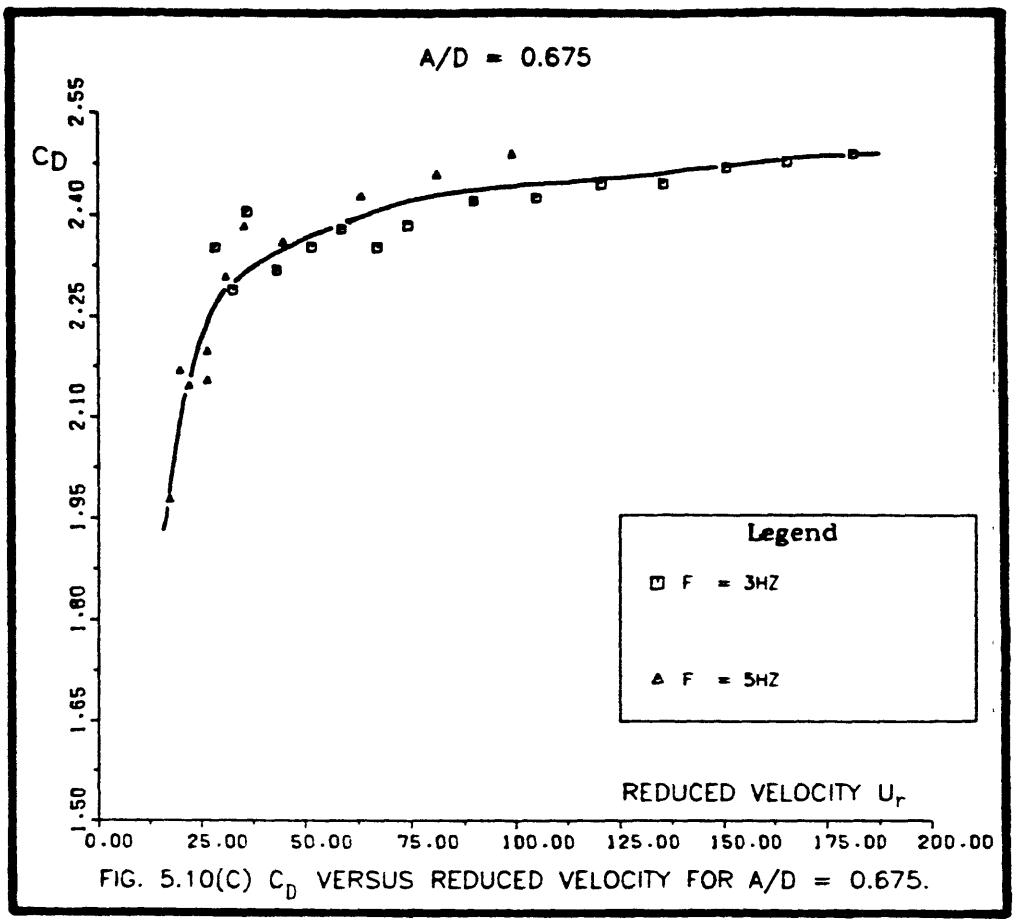


FIG. 5.10(C) C_D VERSUS REDUCED VELOCITY FOR A/D = 0.675.

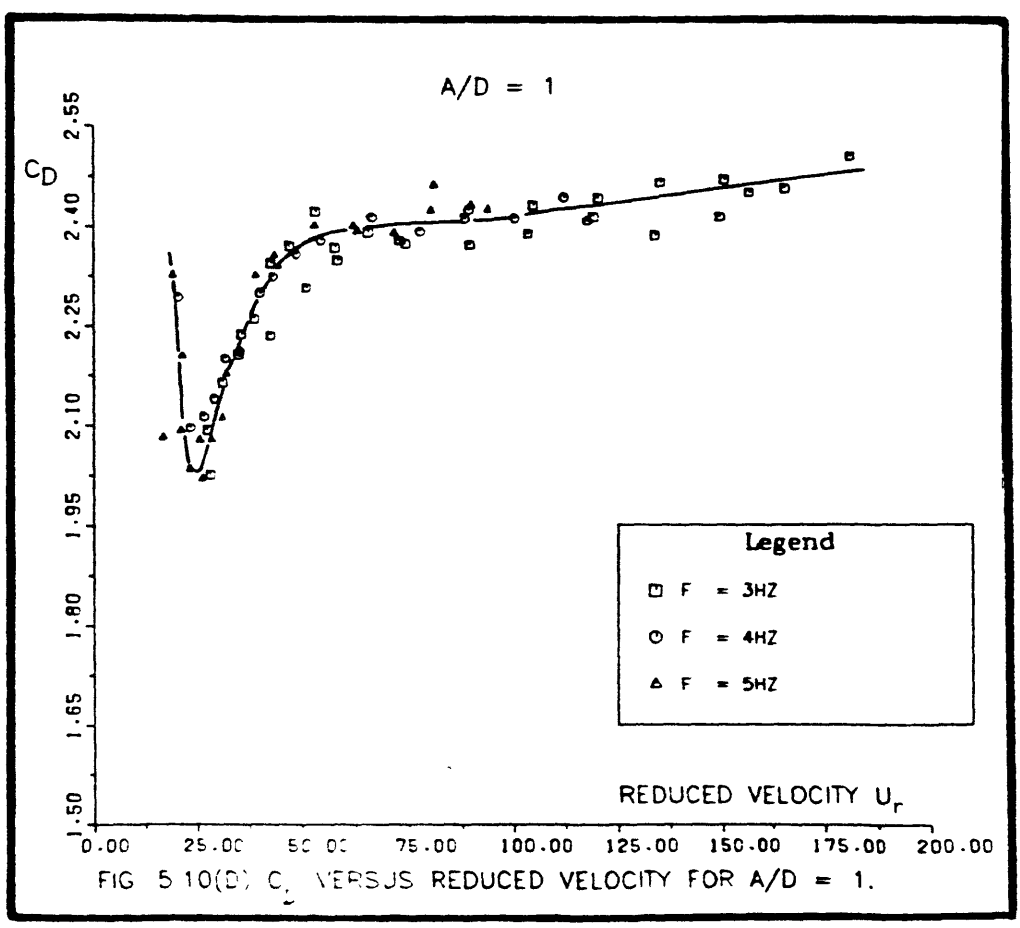


FIG 5.10(D) C_D VERSUS REDUCED VELOCITY FOR A/D = 1.

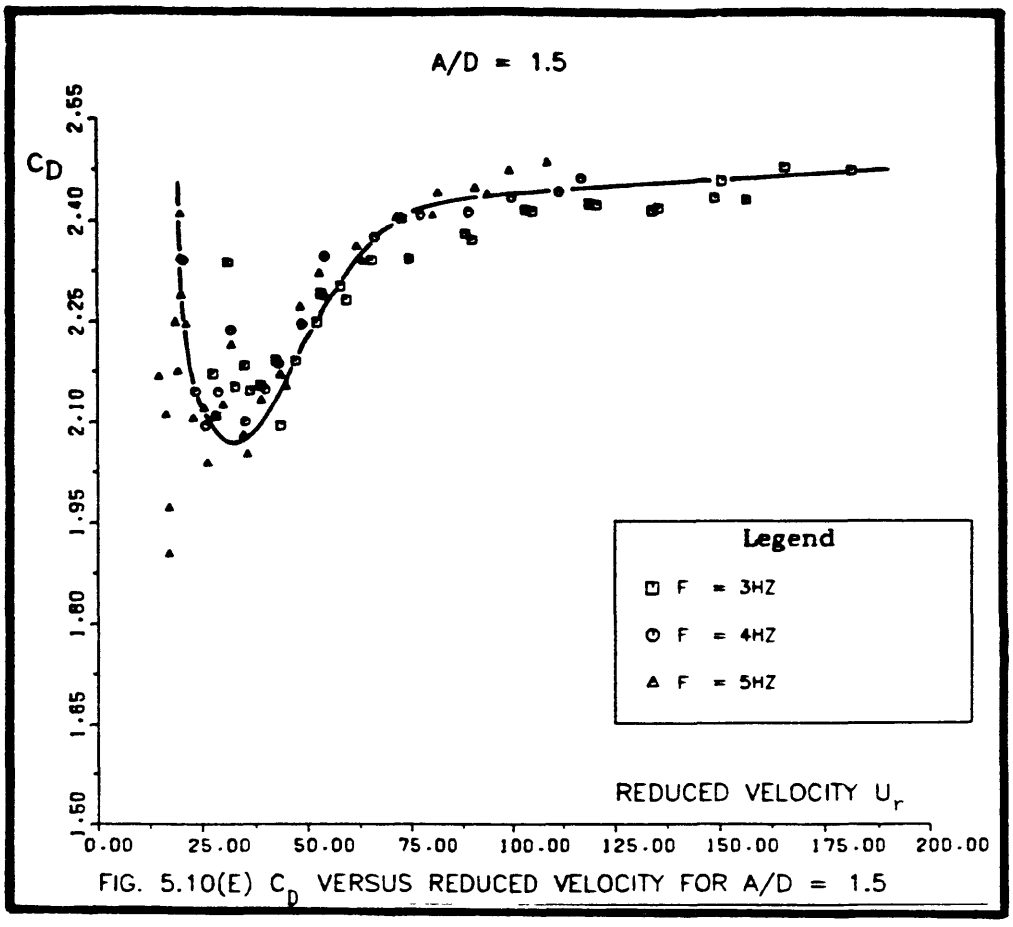


FIG. 5.10(E) C_D VERSUS REDUCED VELOCITY FOR A/D = 1.5

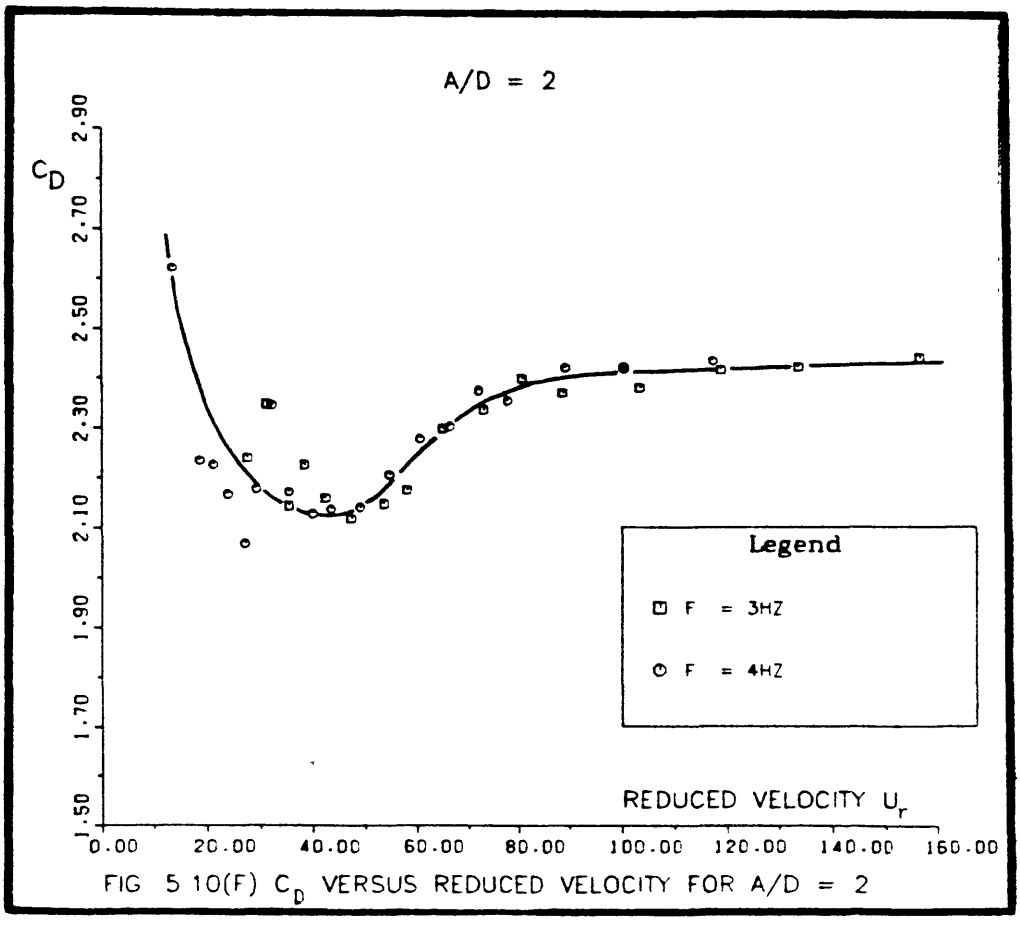


FIG 5.10(F) C_D VERSUS REDUCED VELOCITY FOR A/D = 2

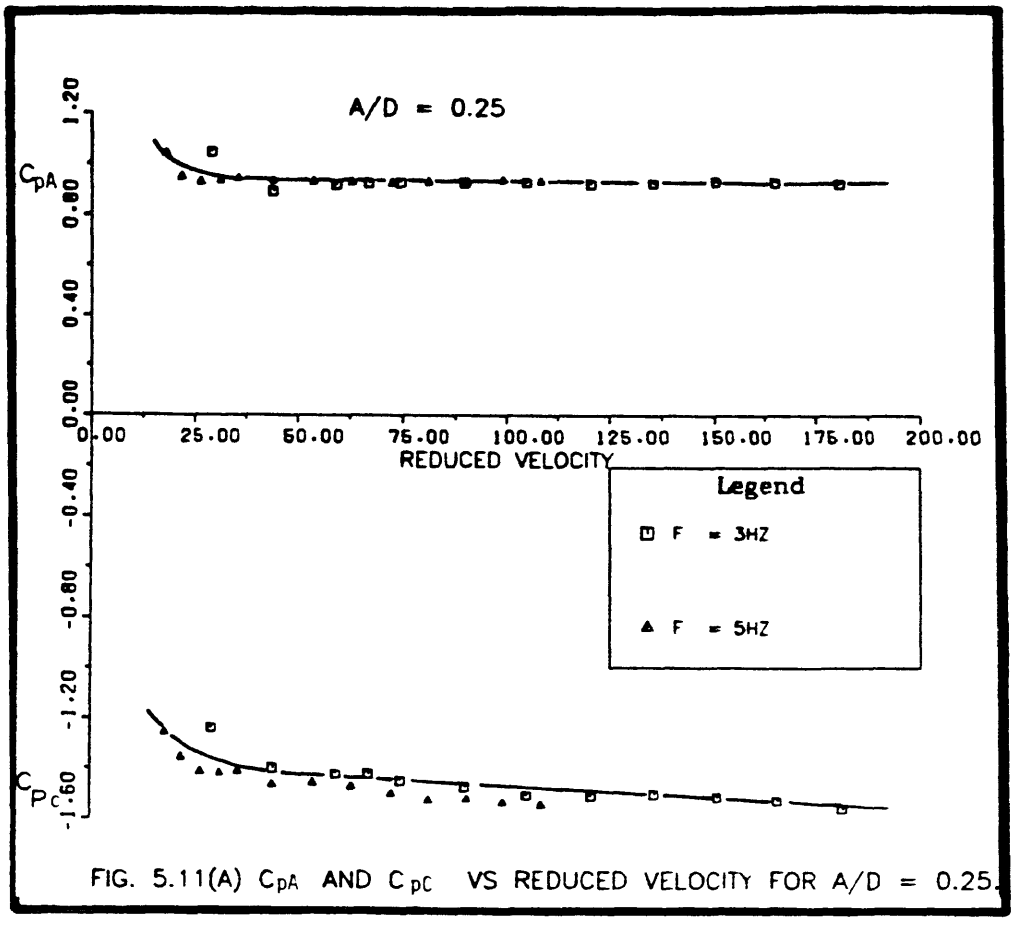


FIG. 5.11(A) C_{pA} AND C_{pC} VS REDUCED VELOCITY FOR A/D = 0.25.

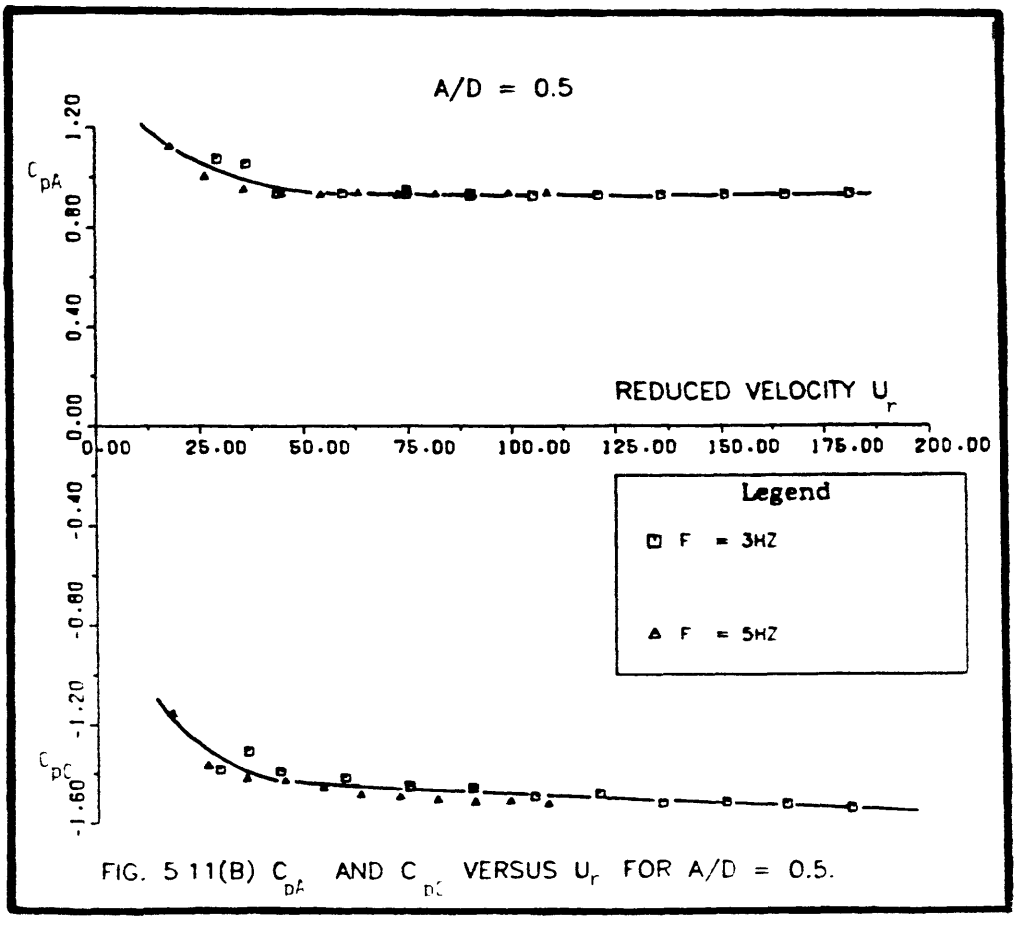


FIG. 5.11(B) C_{pA} AND C_{pC} VERSUS U_r FOR A/D = 0.5.

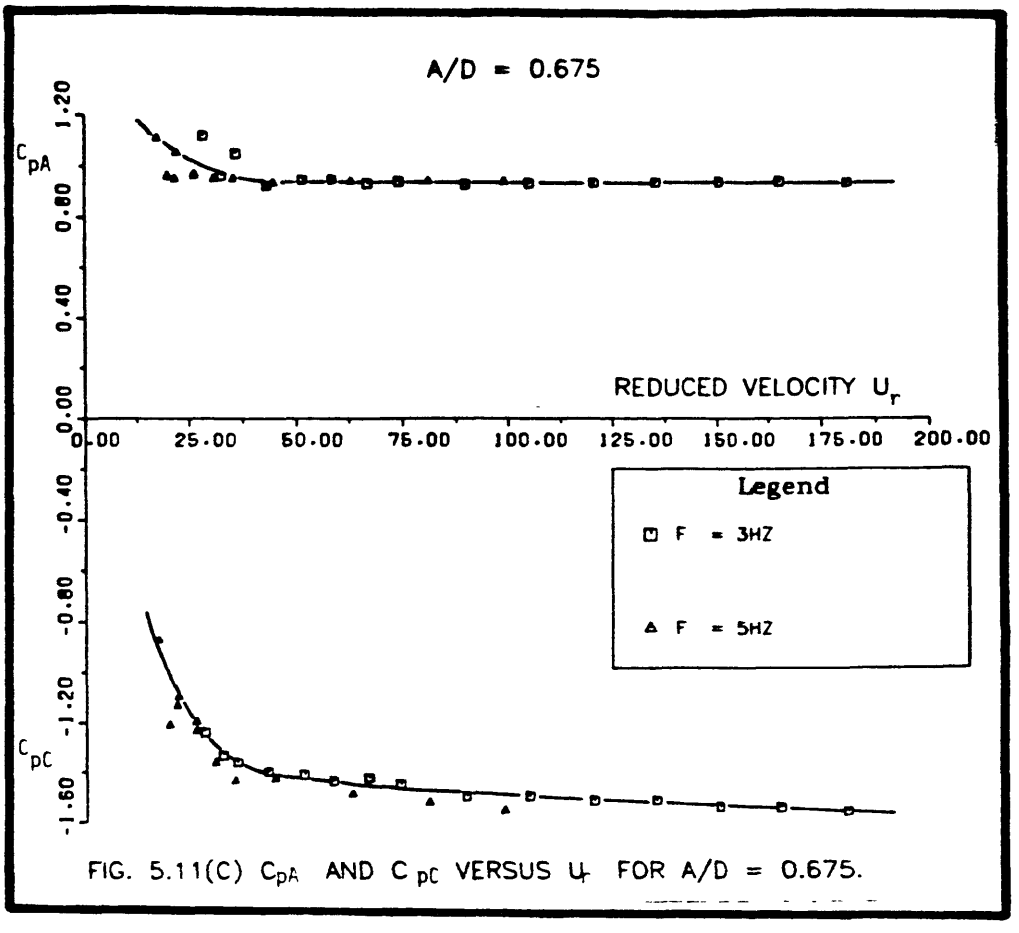


FIG. 5.11(C) C_{pA} AND C_{pC} VERSUS U_r FOR A/D = 0.675.

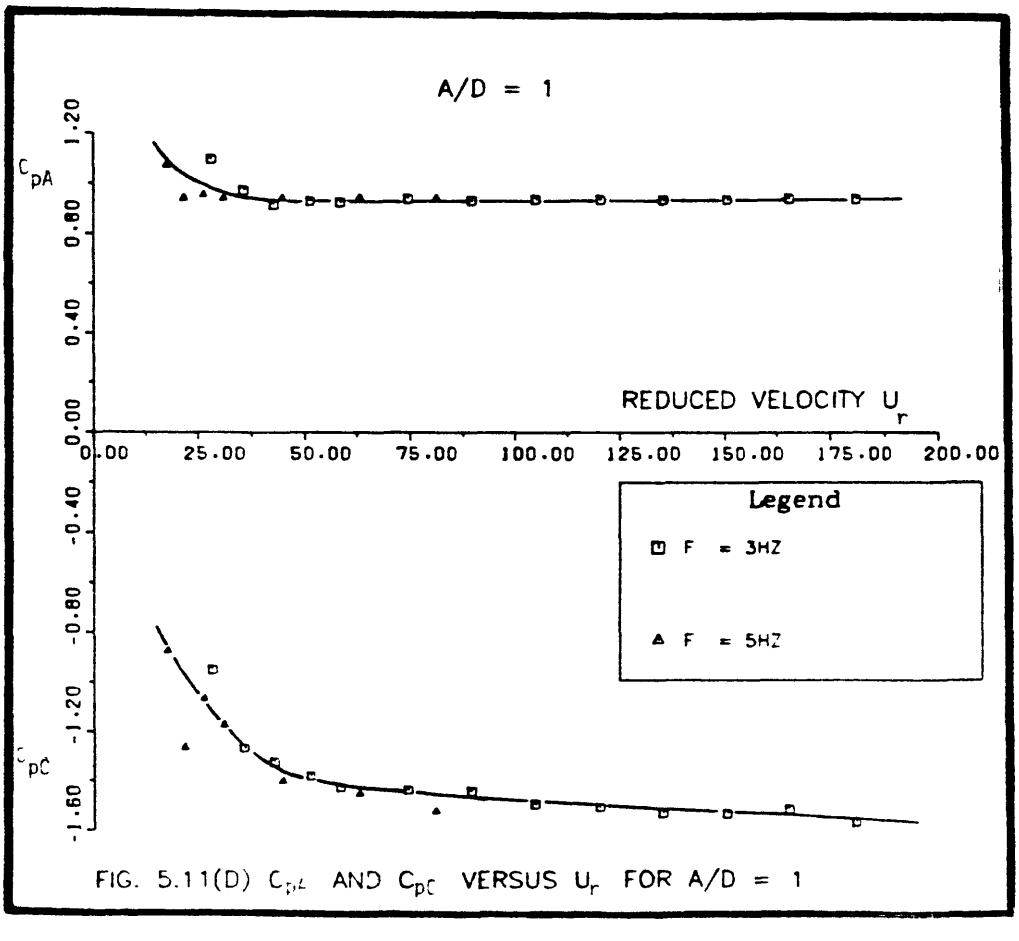


FIG. 5.11(D) C_{pA} AND C_{pC} VERSUS U_r FOR A/D = 1

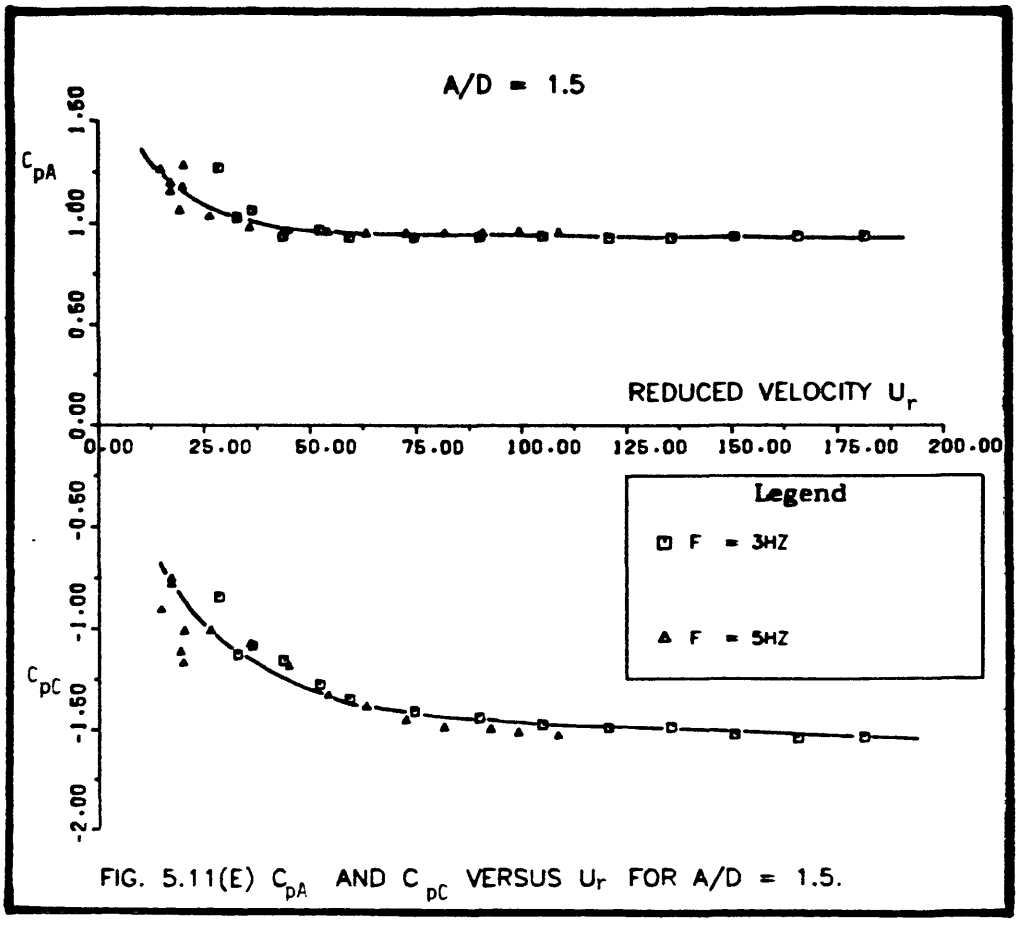


FIG. 5.11(E) C_{pA} AND C_{pC} VERSUS U_r FOR A/D = 1.5.

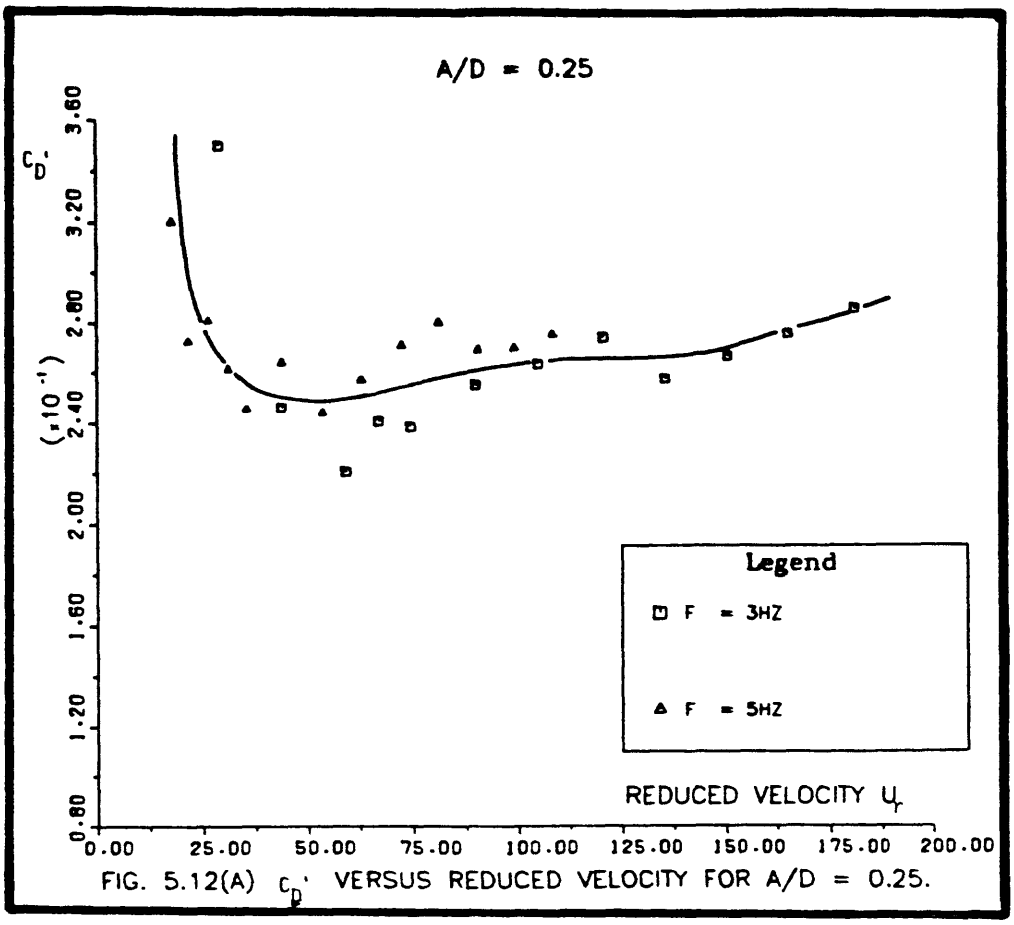


FIG. 5.12(A) C_D' VERSUS REDUCED VELOCITY FOR A/D = 0.25.

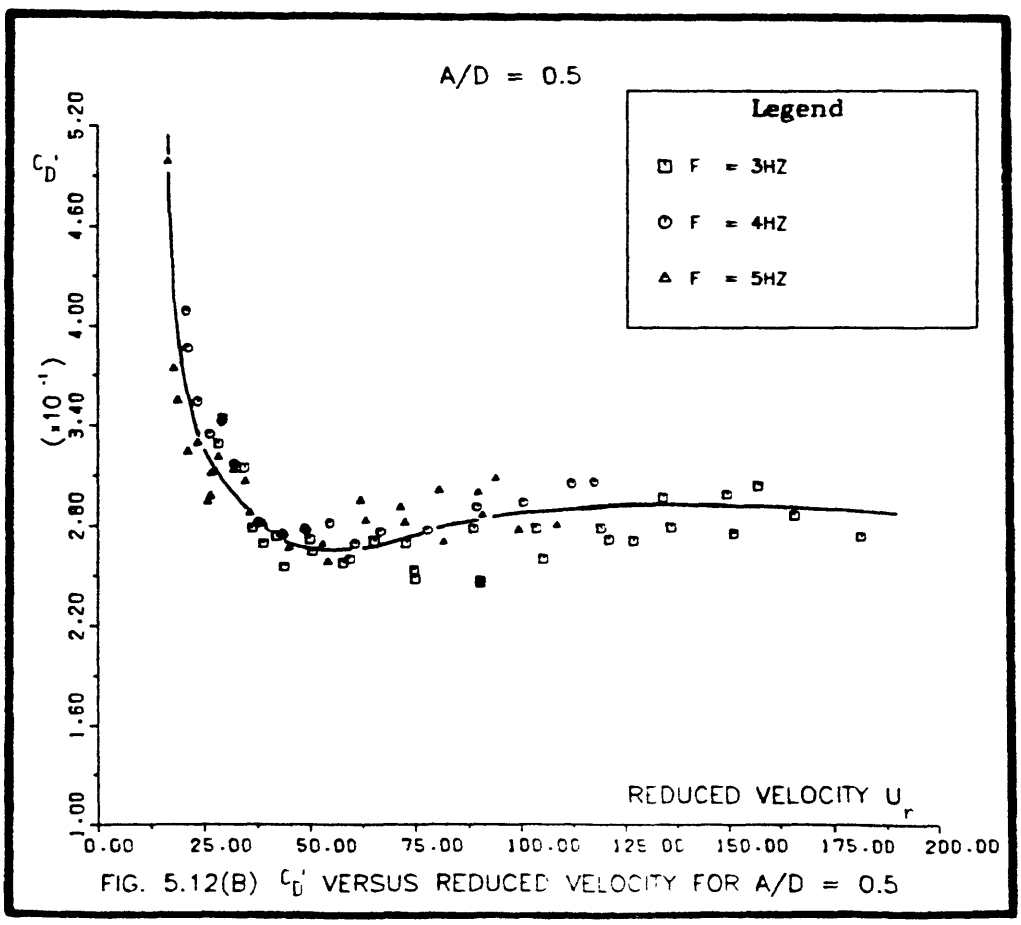


FIG. 5.12(B) C_D' VERSUS REDUCED VELOCITY FOR A/D = 0.5

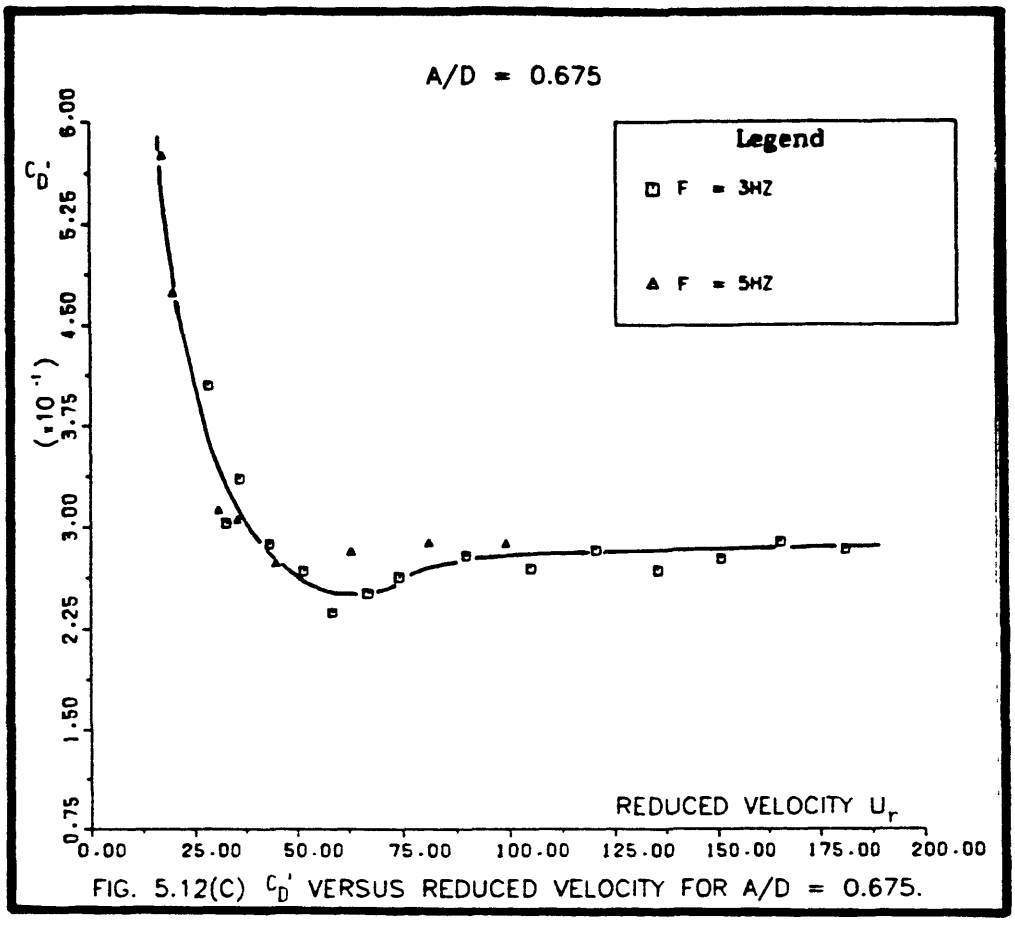


FIG. 5.12(C) C_D' VERSUS REDUCED VELOCITY FOR A/D = 0.675.

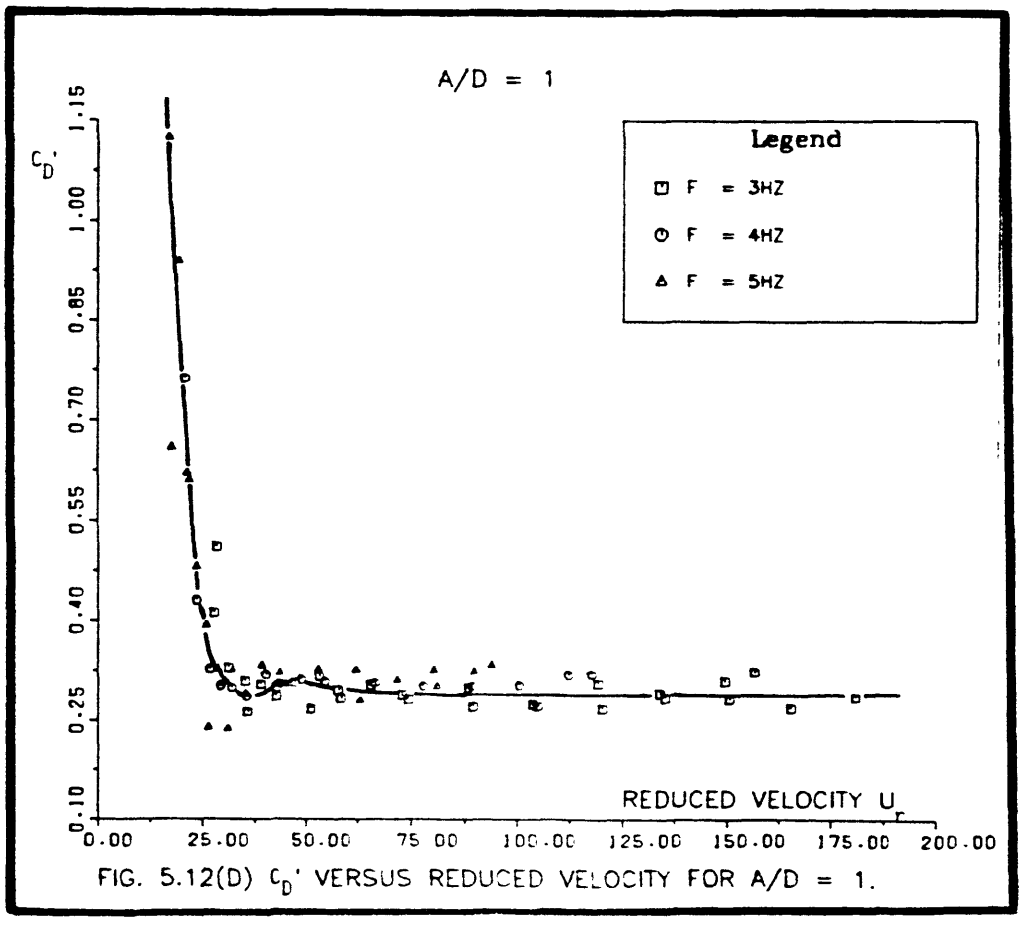


FIG. 5.12(D) C_D' VERSUS REDUCED VELOCITY FOR A/D = 1.

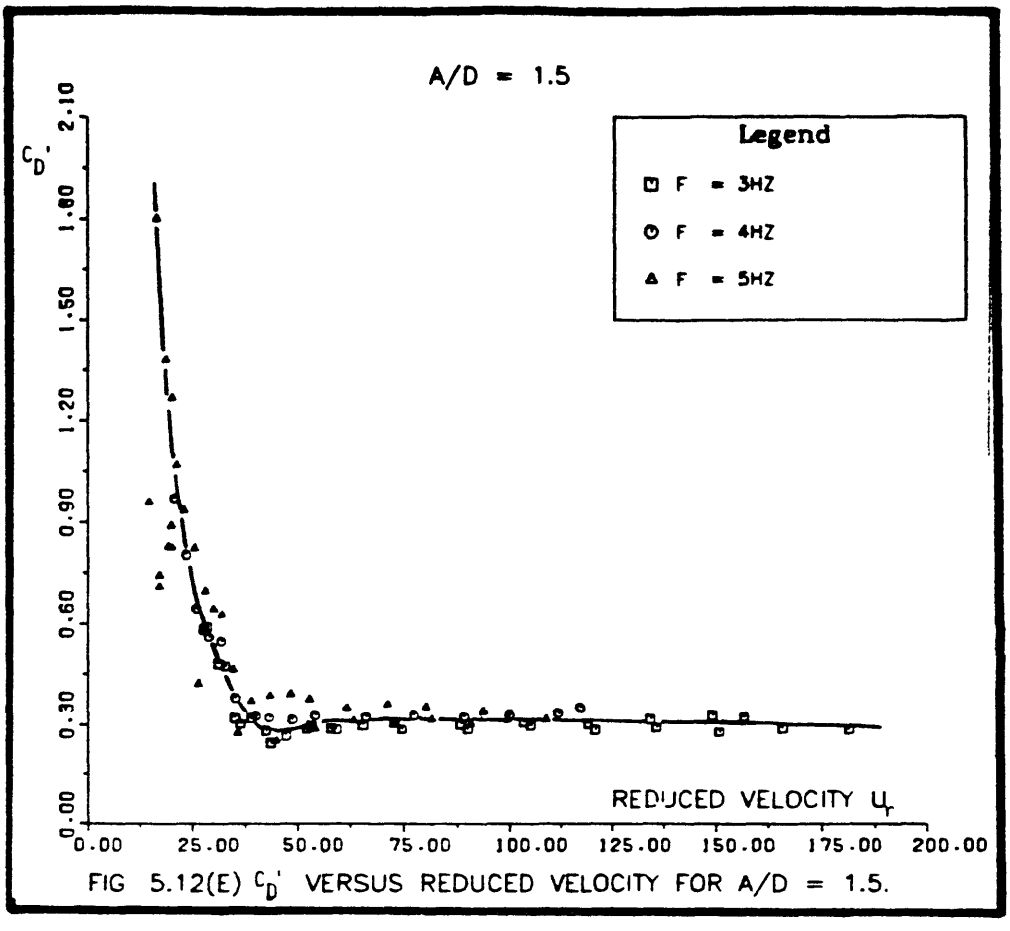


FIG 5.12(E) C_D' VERSUS REDUCED VELOCITY FOR A/D = 1.5.

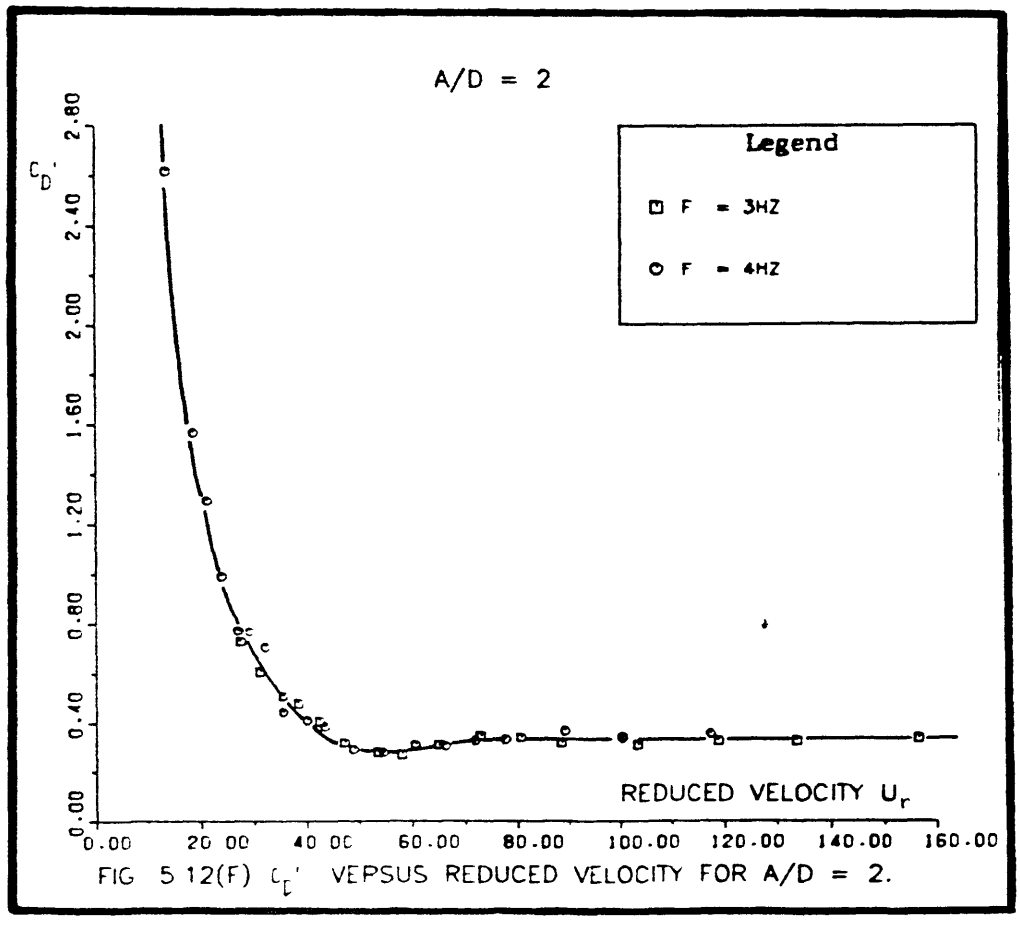


FIG 5.12(F) C_D' VERSUS REDUCED VELOCITY FOR A/D = 2.

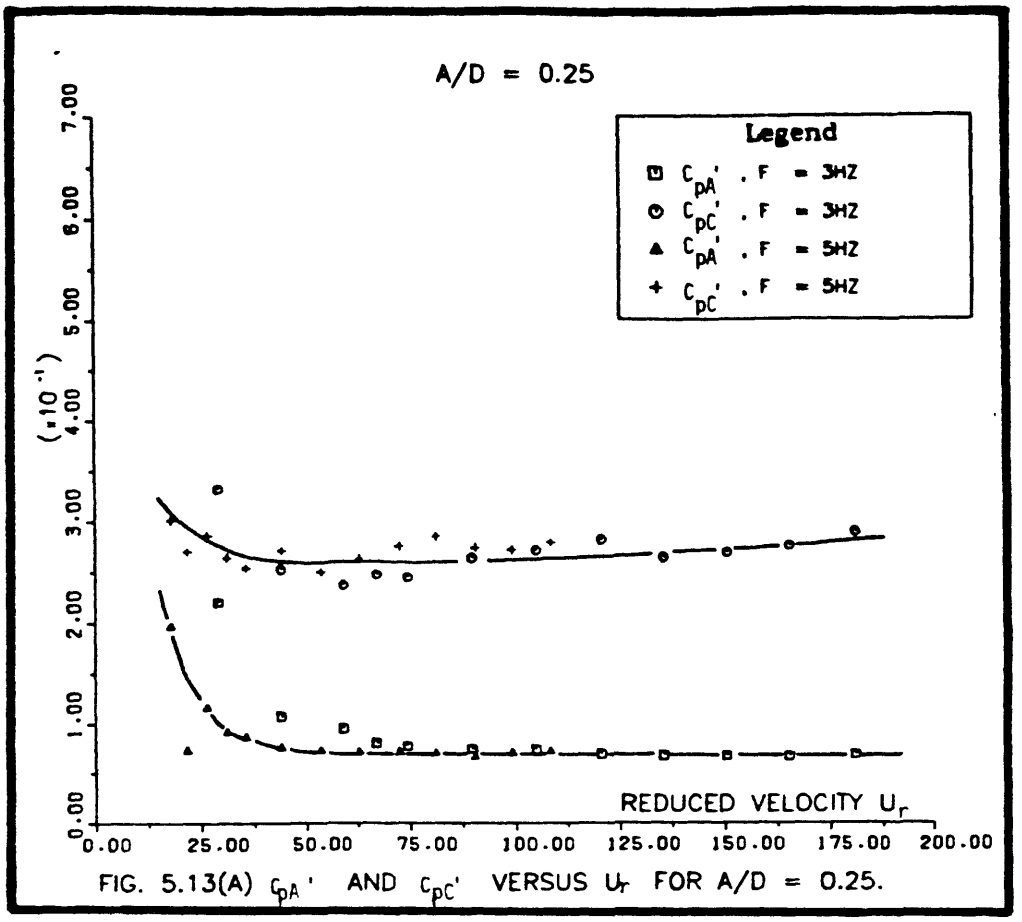


FIG. 5.13(A) C_{pA}' AND C_{pC}' VERSUS U_r FOR A/D = 0.25.

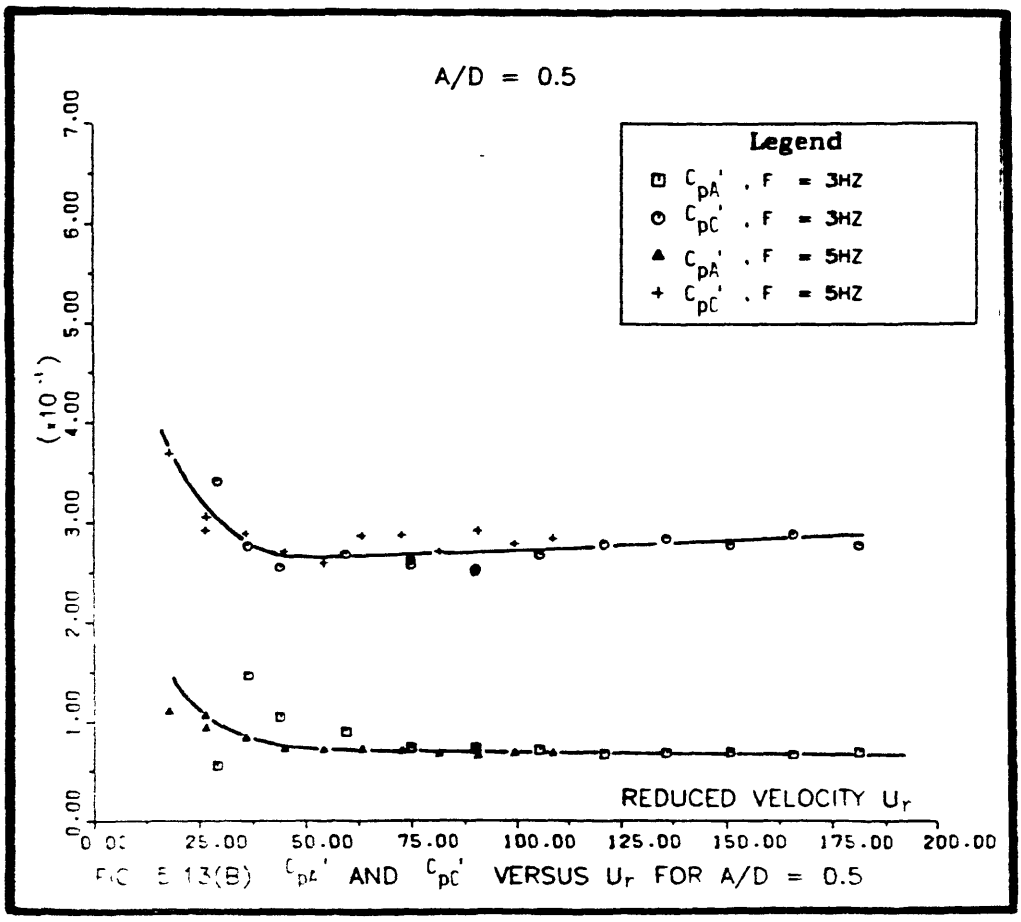


FIG. 5.13(B) C_{pA}' AND C_{pC}' VERSUS U_r FOR A/D = 0.5

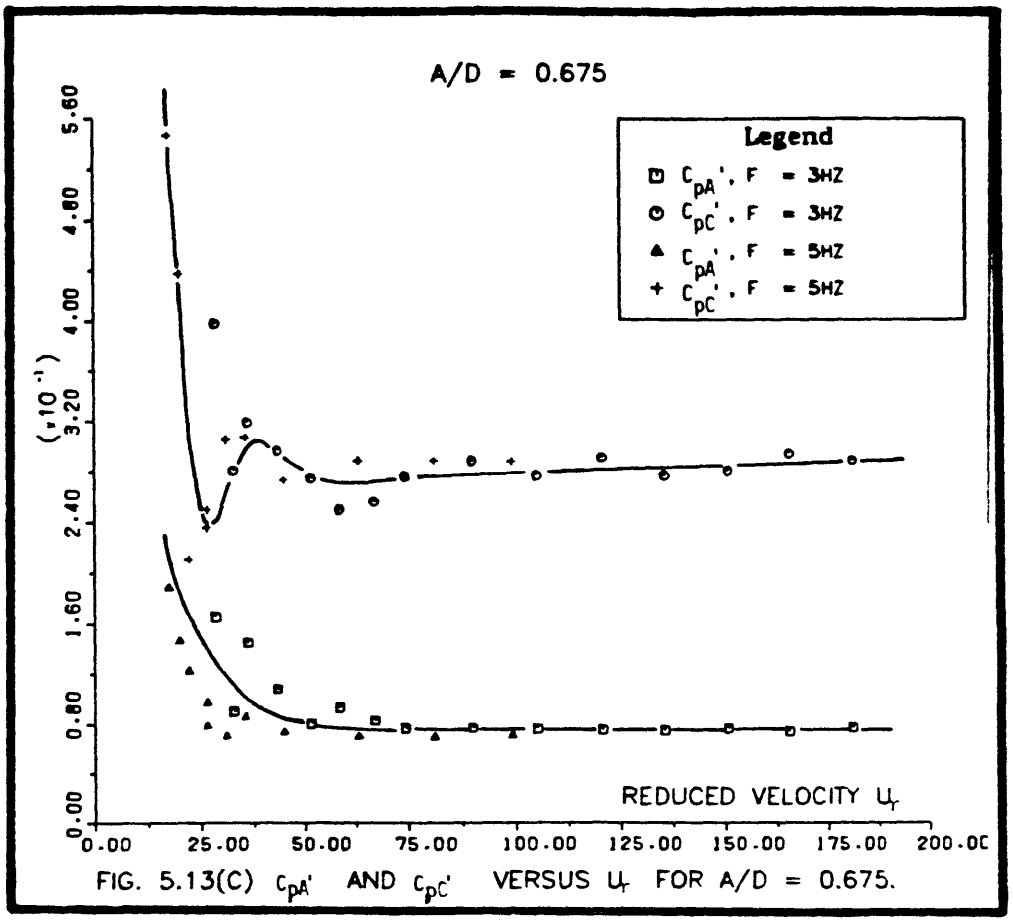


FIG. 5.13(C) $C_{pA'}$ AND $C_{pC'}$ VERSUS U_r FOR A/D = 0.675.

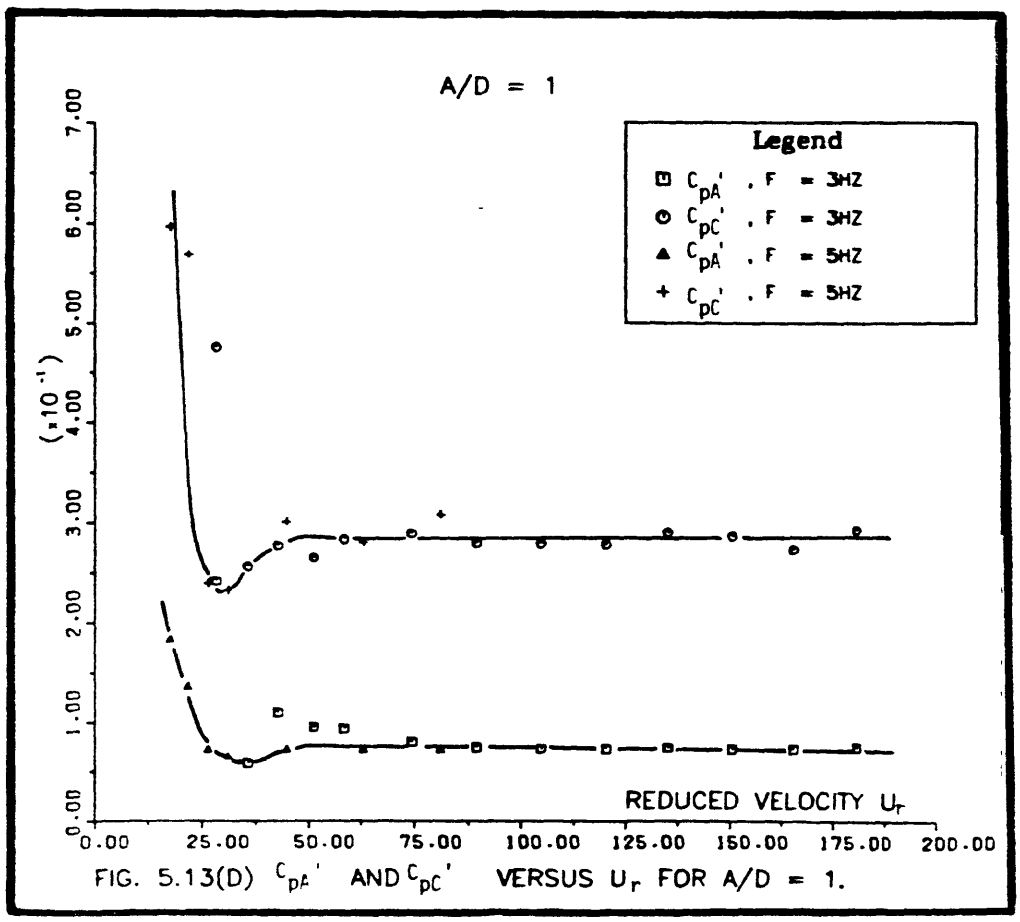


FIG. 5.13(D) $C_{pA'}$ AND $C_{pC'}$ VERSUS U_r FOR A/D = 1.

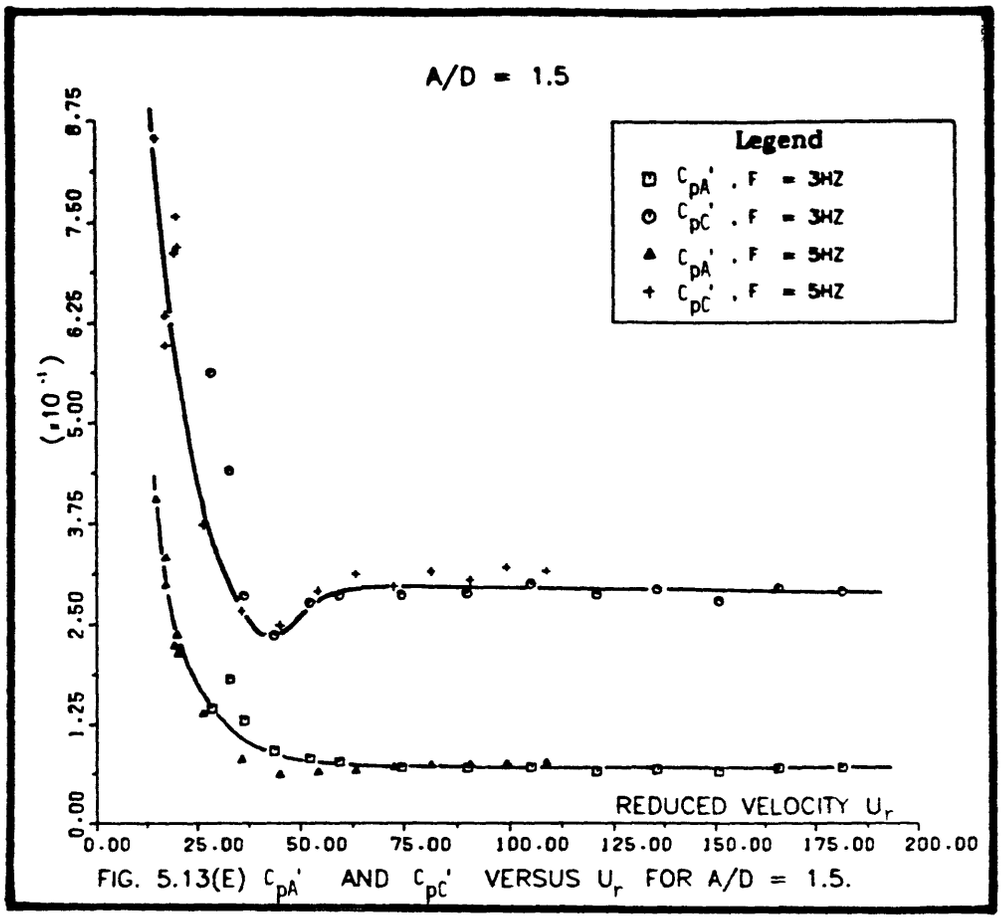
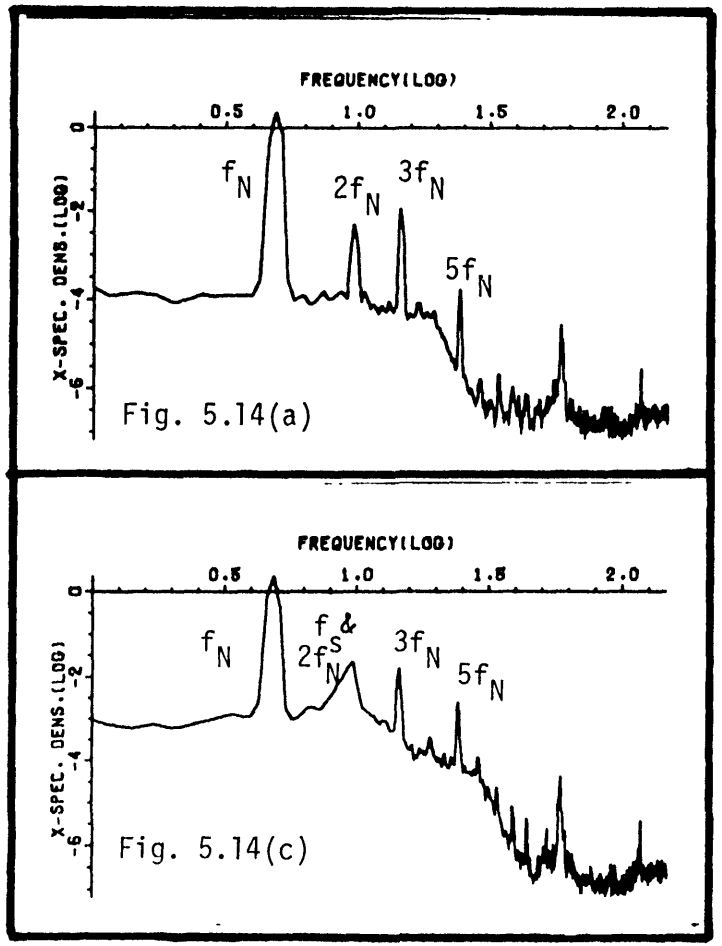


FIG. 5.13(E) C_{pA}' AND C_{pC}' VERSUS U_r FOR A/D = 1.5.



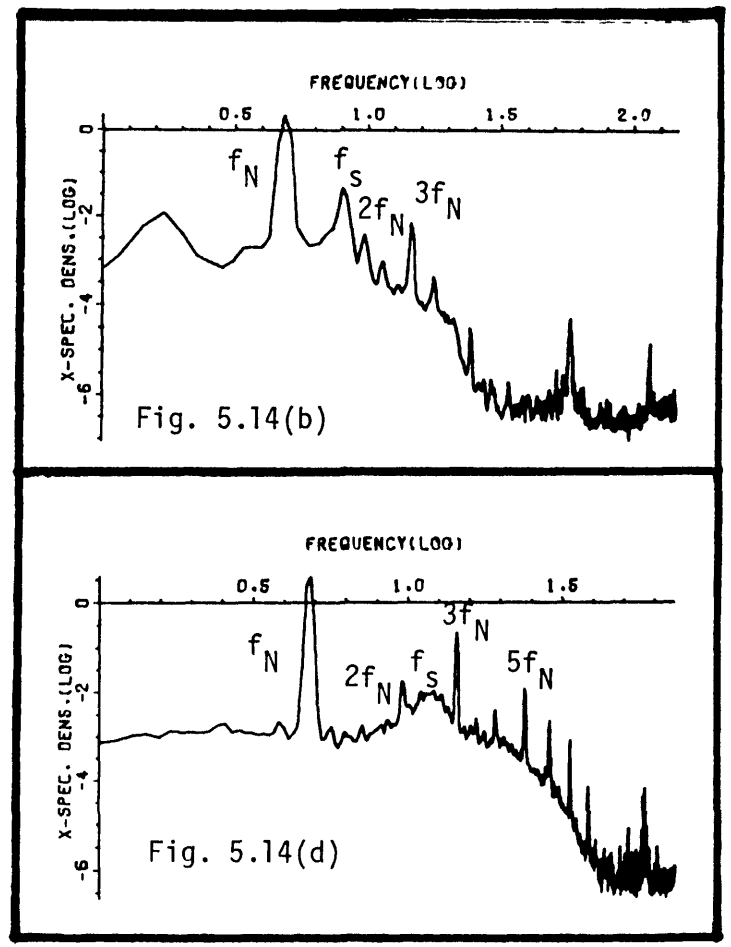
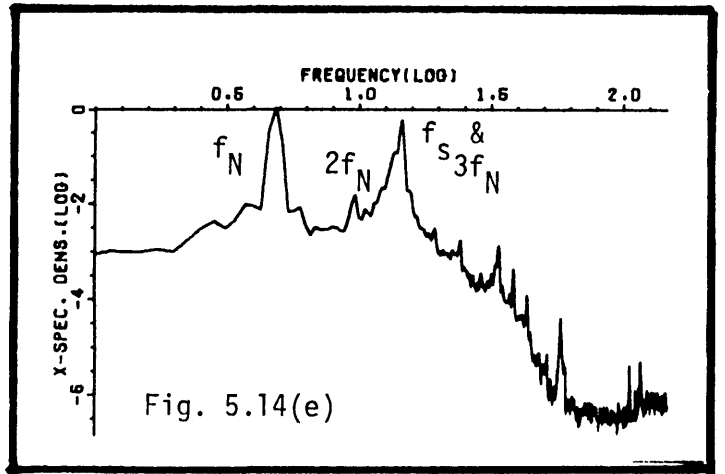


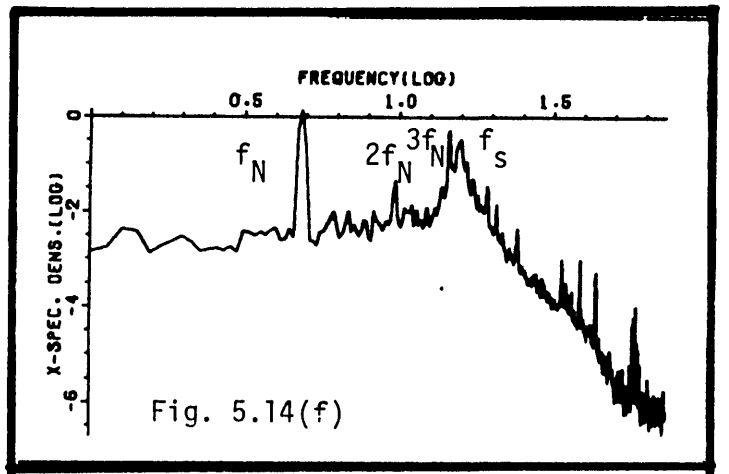
Fig. 5.14(a) Lift spectrum, A/D = 0.675, f_N = 5Hz, $U_r \sim 8.05$

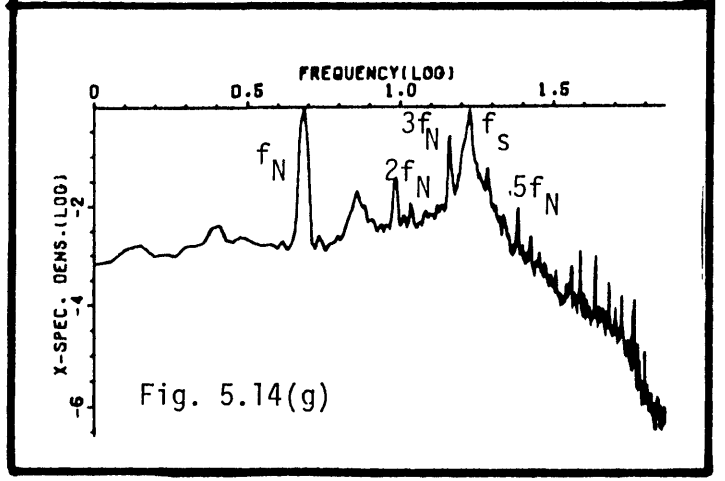
Fig. 5.14(b) Lift spectrum, A/D = 0.675, f_N = 5Hz, $U_r \sim 11.25$

Fig. 5.14(c) Lift spectrum, A/D = 0.675, f_N = 5Hz, $U_r \sim 12.98$

Fig. 5.14(d) Lift spectrum, A/D = 1 , f_N = 5Hz, $U_r \sim 16.89$







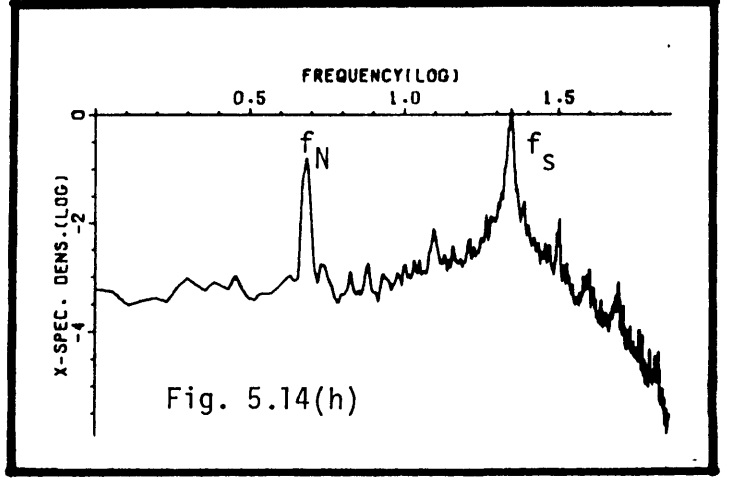


Fig. 5.14(e) Lift spectrum, A/D = 0.675, f_N = 5Hz, $U_r \sim 19.54$

Fig. 5.14(f) Lift spectrum, A/D = 0.675, f_N = 5Hz, $U_r \sim 23.57$

Fig. 5.14(g) Lift spectrum, A/D = 0.675, f_N = 5Hz, $U_r \sim 25.45$

Fig. 5.14(h) Lift spectrum, A/D = 0.675, f_N = 5Hz, $U_r \sim 35.42$

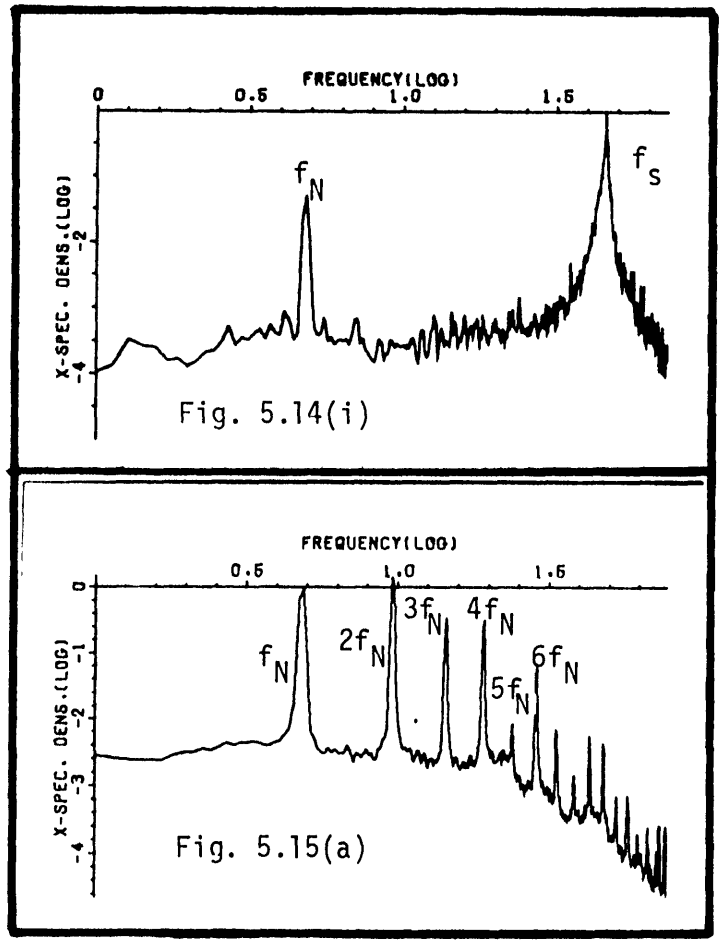


Fig. 5.14(i)

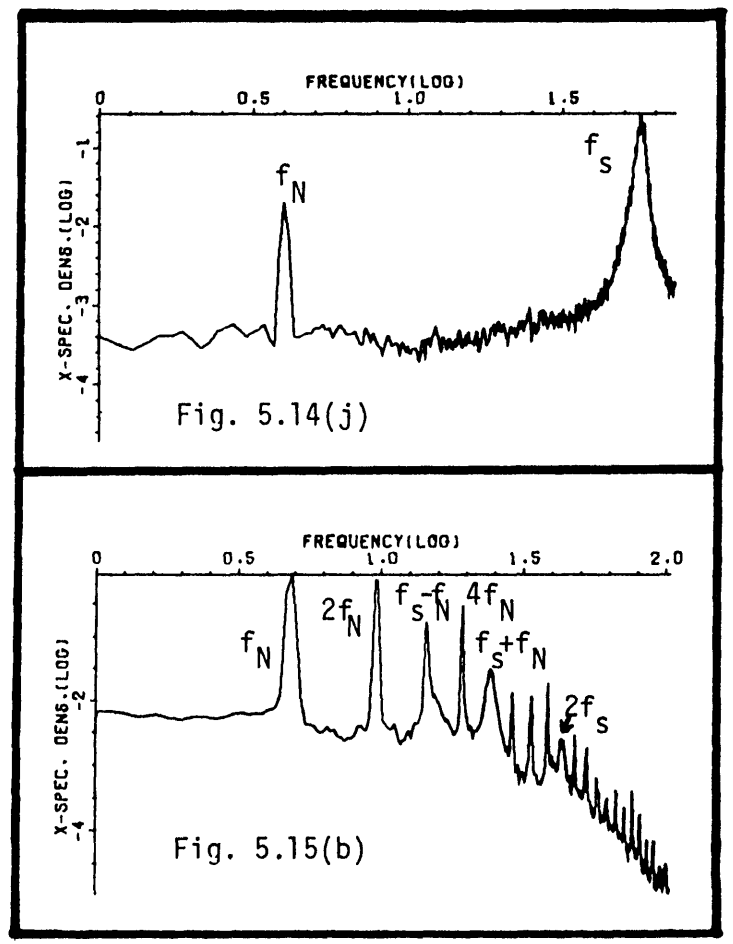


Fig. 5.14(j)

Fig. 5.15(a)

Fig. 5.15(b)

Fig. 5.14(i) Lift spectrum, A/D = 0.675, f_N = 5Hz, $U_r \sim 72.68$

Fig. 5.14(j) Lift spectrum, A/D = 0.675, f_N = 5Hz, $U_r \sim 110.68$

Fig. 5.15(a) Drag spectrum, A/D = 1.5 , f_N = 4.88Hz, $U_r \sim 20.56$

Fig. 5.15(b) Drag spectrum, A/D = 1.5 , f_N = 4.88Hz, $U_r \sim 26.11$

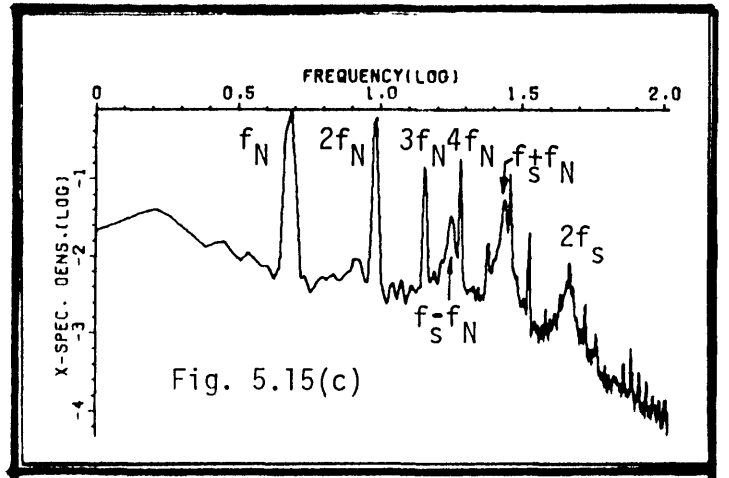


Fig. 5.15(c)

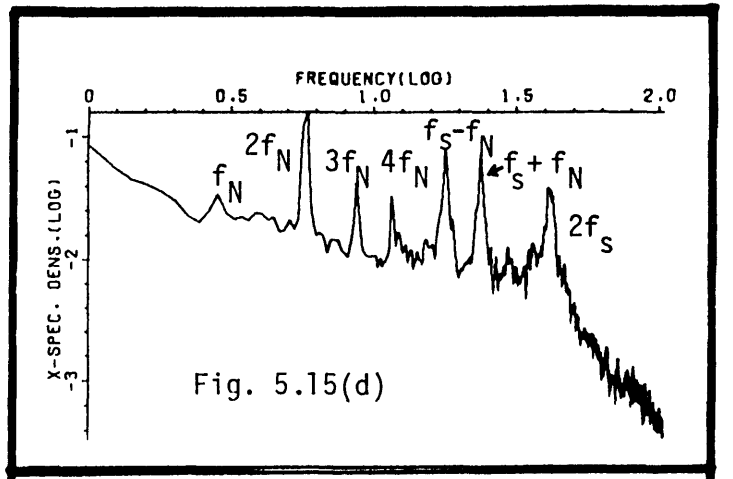


Fig. 5.15(d)

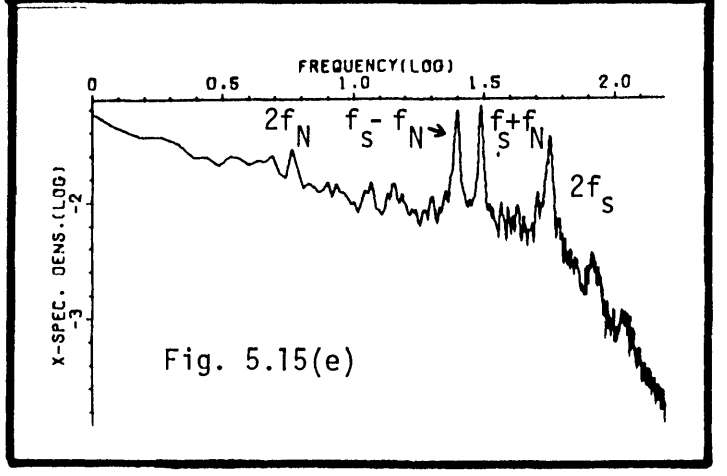


Fig. 5.15(e)

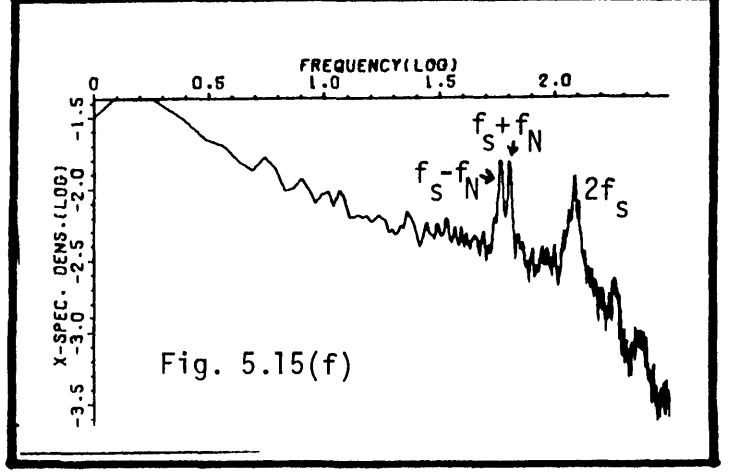


Fig. 5.15(f)

Fig. 5.15(c) Drag spectrum, A/D = 1.5, f_N = 4.88Hz, $U_r \sim 30.9$

Fig. 5.15(d) Drag spectrum, A/D = 1.5, f_N = 2.84Hz, $U_r \sim 55.54$

Fig. 5.15(e) Drag spectrum, A/D = 1.5, f_N = 3Hz, $U_r \sim 72.26$

Fig. 5.15(f) Drag spectrum, A/D = 1.5, f_N = 3Hz, $U_r \sim 159.07$

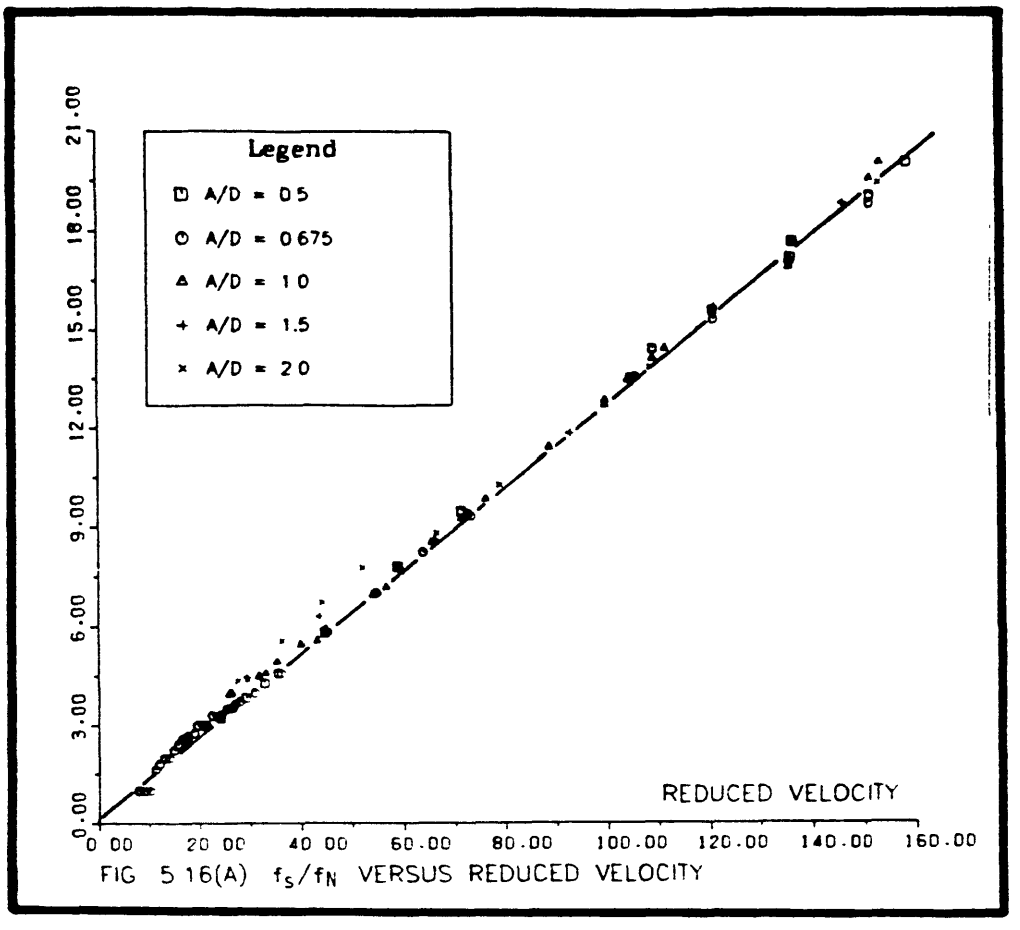


FIG 5.16(A) f_s/f_N VERSUS REDUCED VELOCITY

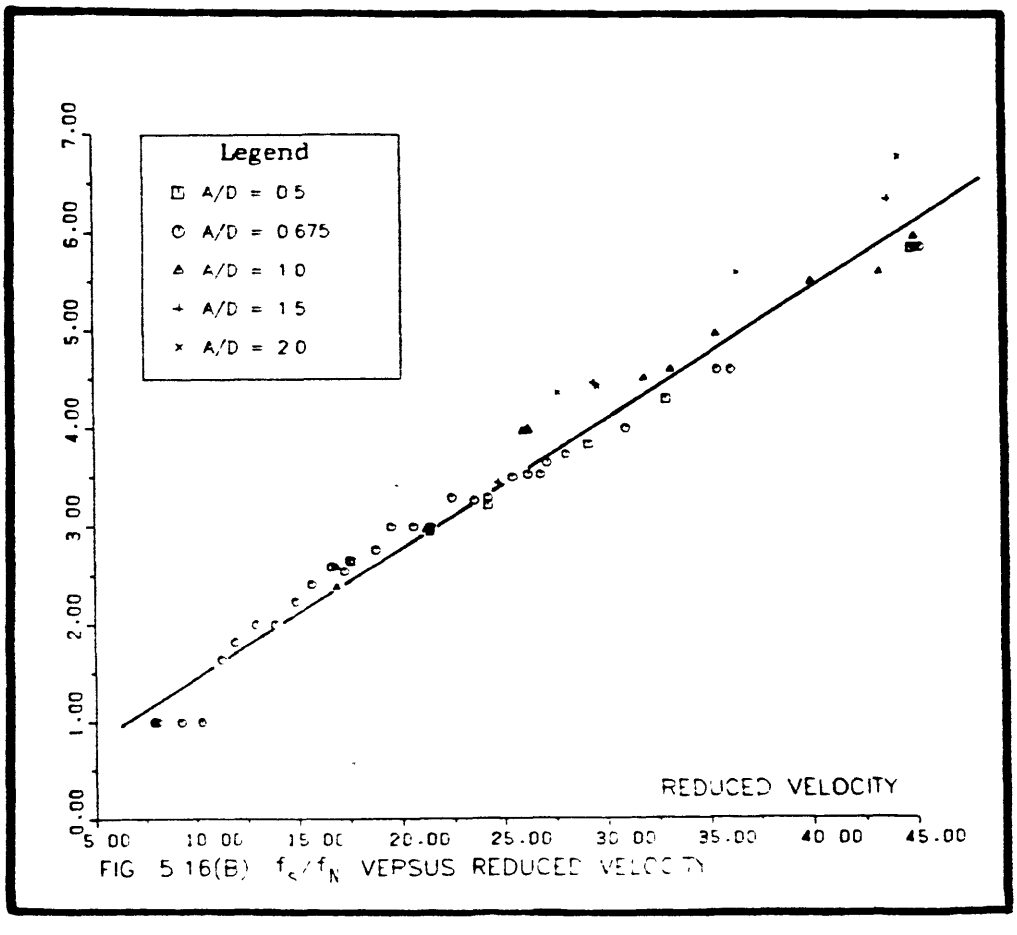


FIG 5.16(B) f_s/f_N VERSUS REDUCED VELOCITY

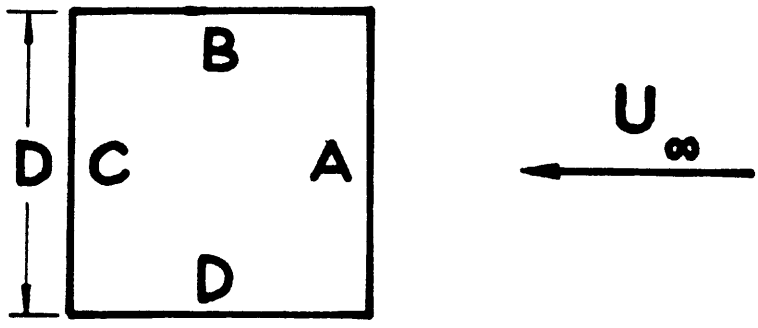


Fig. 6.1(a) Nomenclature of faces.

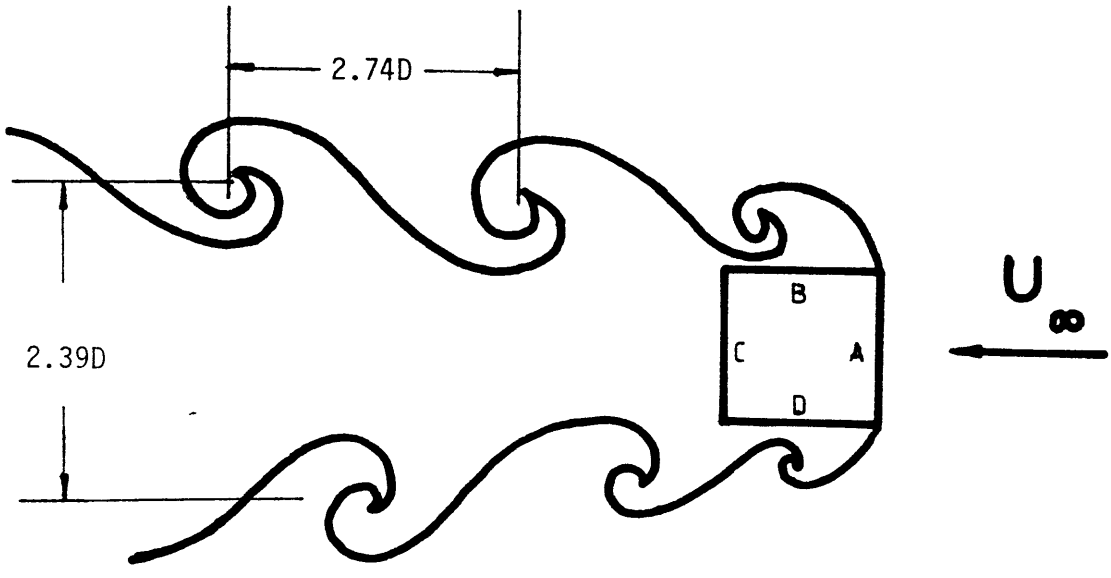


Fig. 6.1(c) Typical wake for lock-on type A.

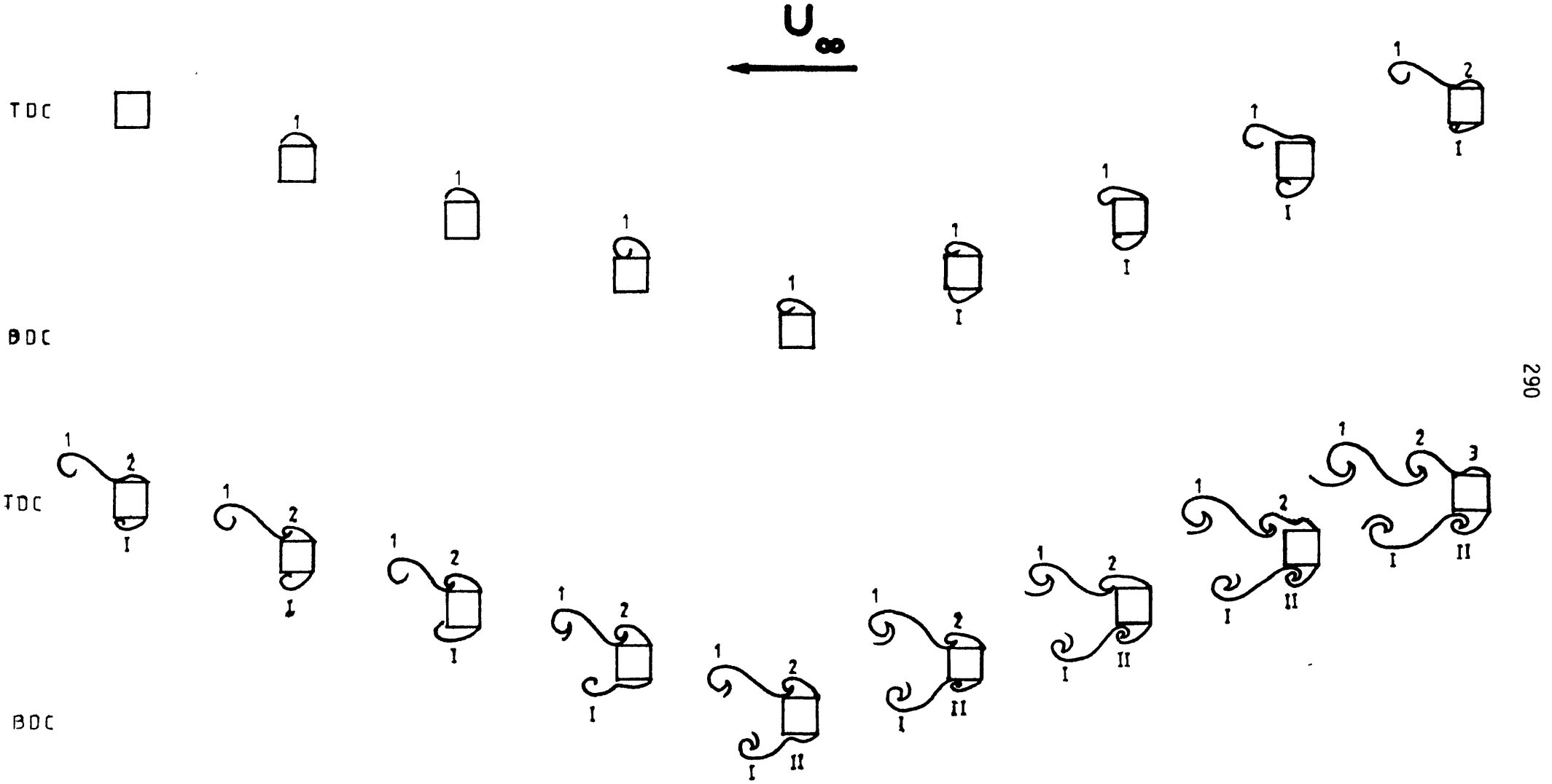


Fig. 6.1(b) Vortex shedding sequence for lock-on type A.

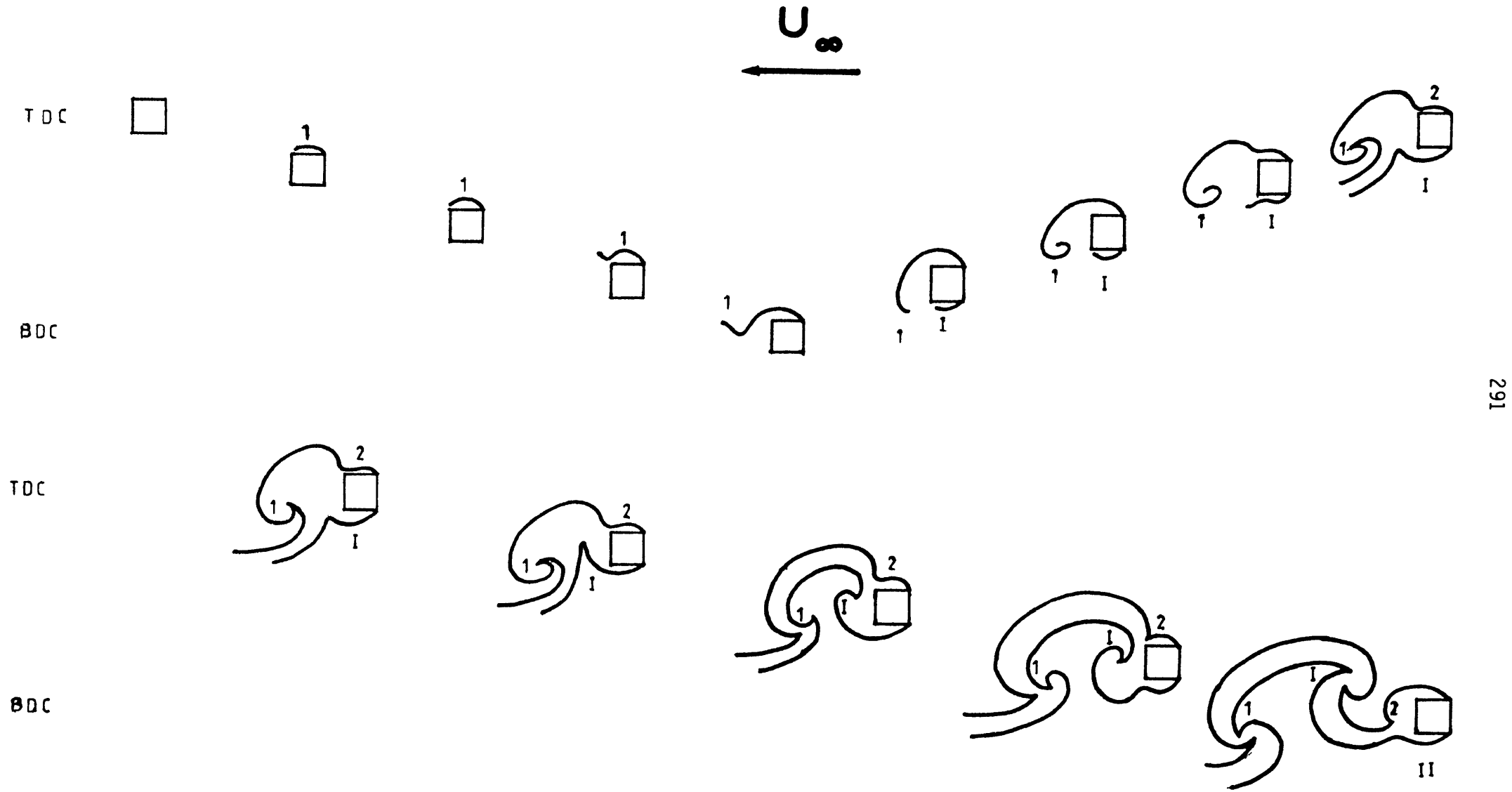


Fig. 6.2(a) Vortex shedding sequence for lock-on type B.

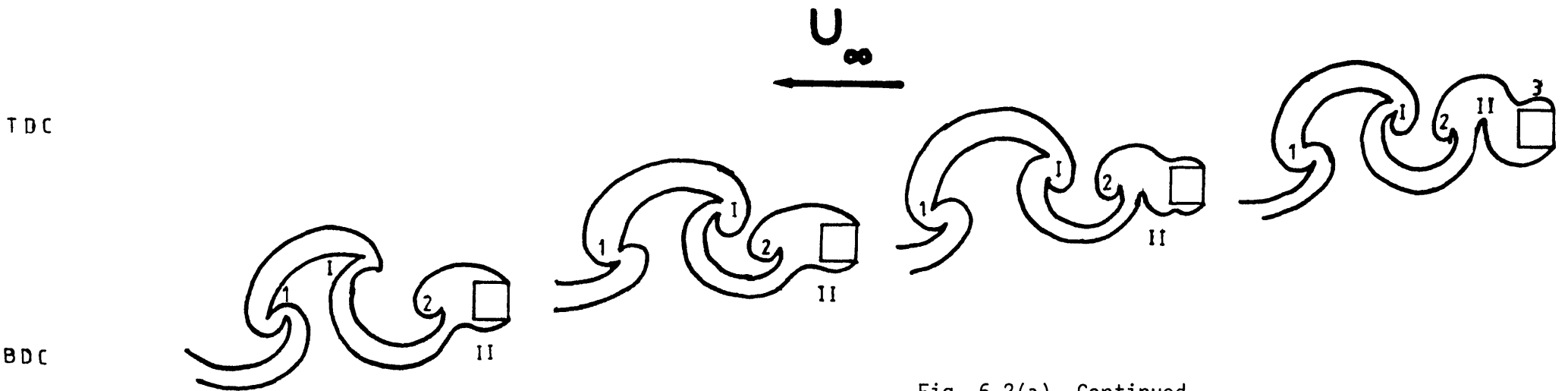


Fig. 6.2(a) Continued.

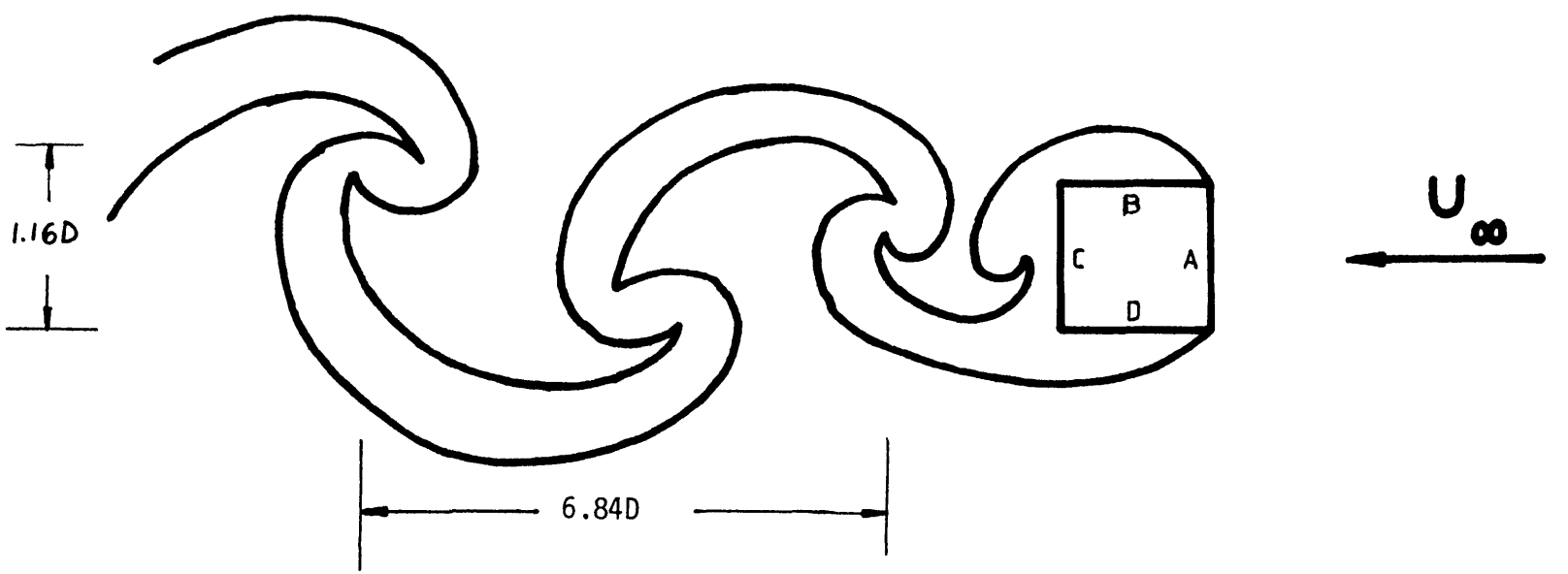


Fig. 6.2(b) Typical wake for lock-on type B.

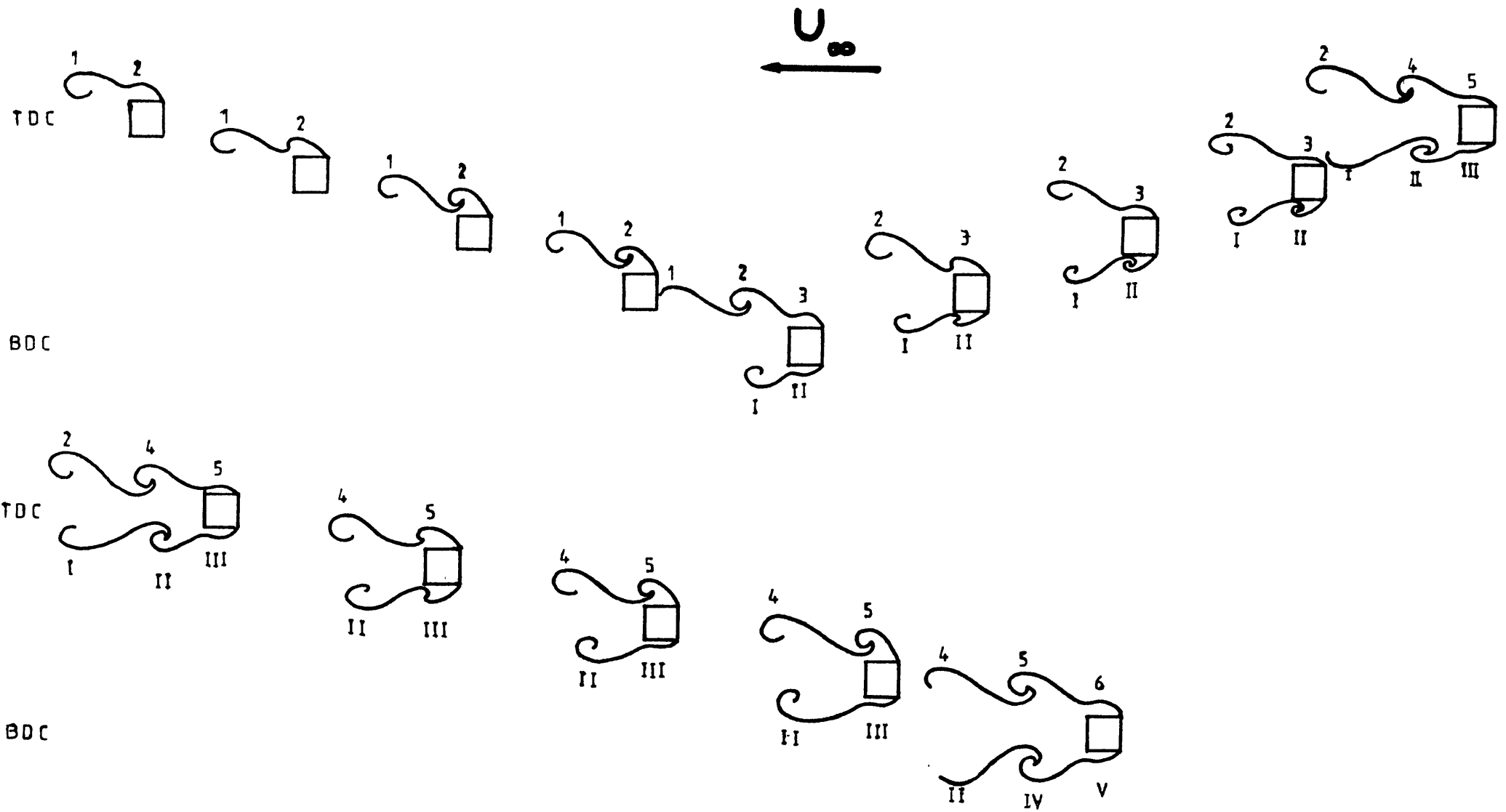


Fig. 6.3(a) Vortex shedding sequence for triple lock-on .

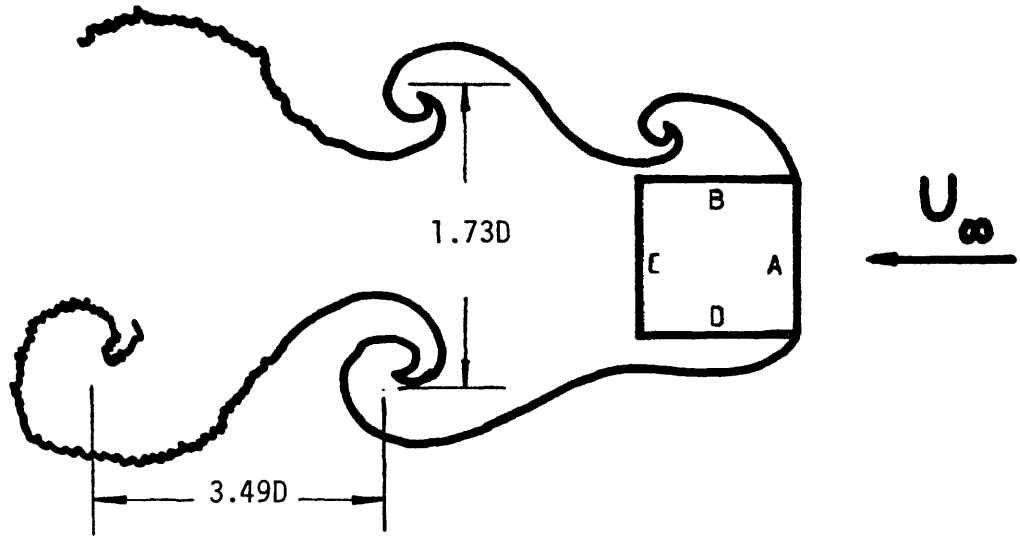


Fig. 6.3(b) Typical wake for triple lock-on.

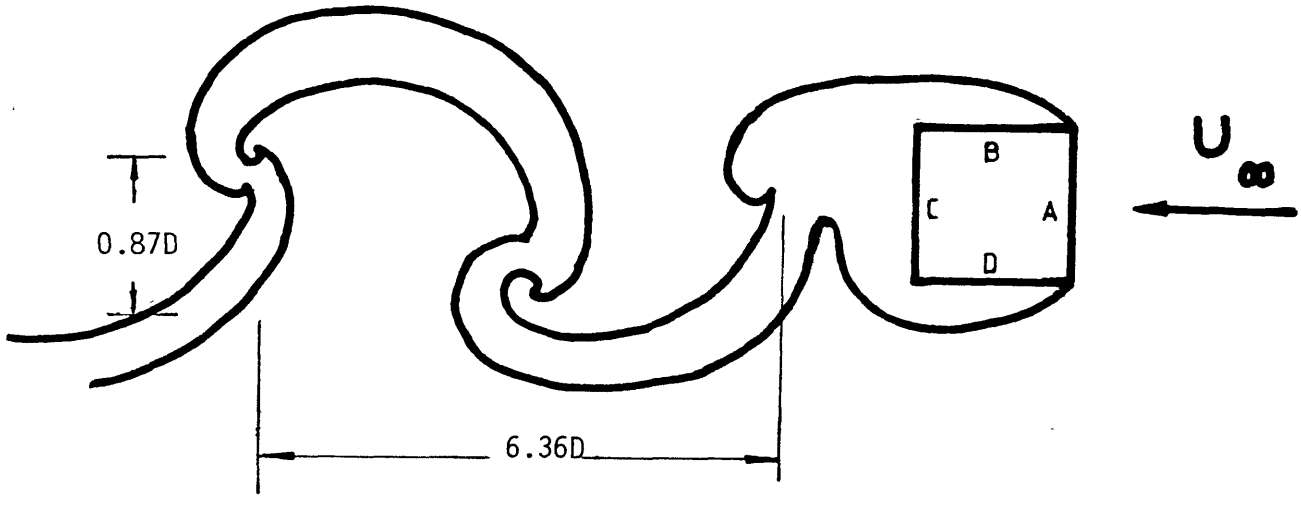


Fig. 6.4 Typical wake for quasi-steady.

Fig. 6.5 Lock-on Type A.
$U_\infty = 2.72 ms^{-1}$, $f_N = 7Hz$, $U_r = 7.65$.

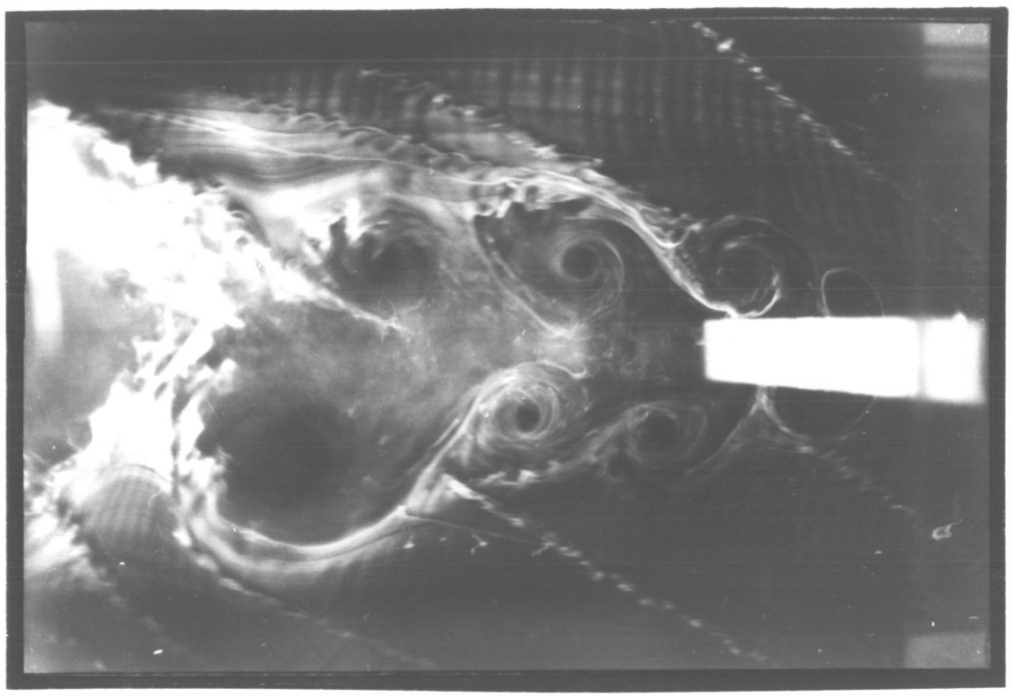


Fig. 6.5(a) Cylinder moving from TDC to BDC, vortex is growing near the top face.

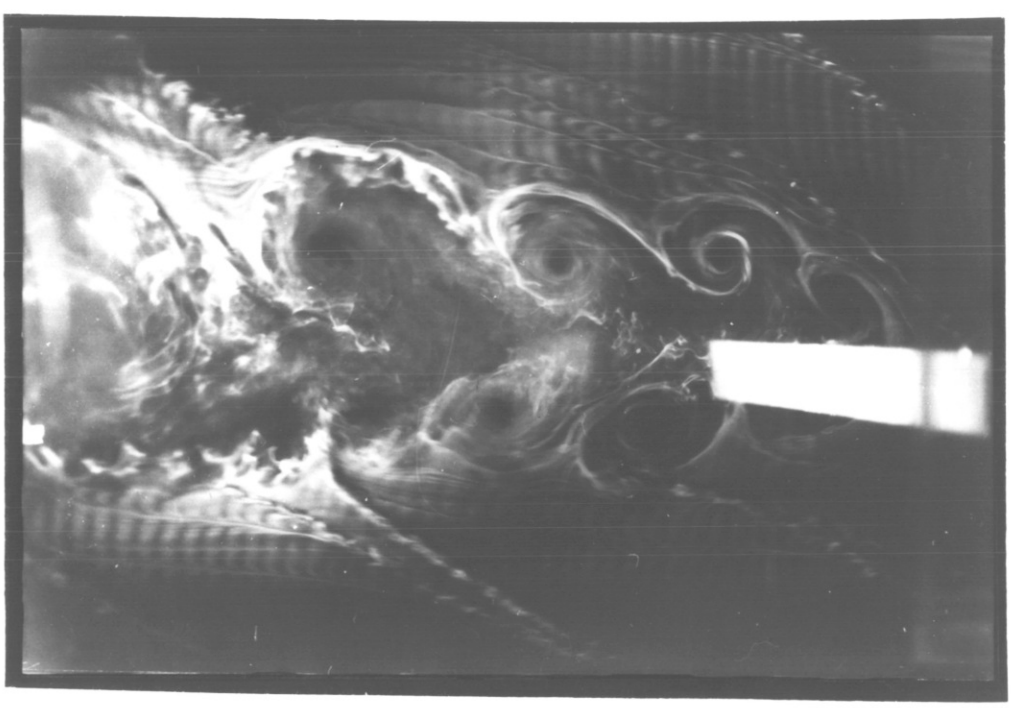


Fig. 6.5(b) Cylinder has almost reached BDC, top vortex is almost fully grown.

Fig. 6.5 Lock-on Type A.
$U_\infty = 2.72 ms^{-1}$, $f_N = 7Hz$, $U_r = 7.65$

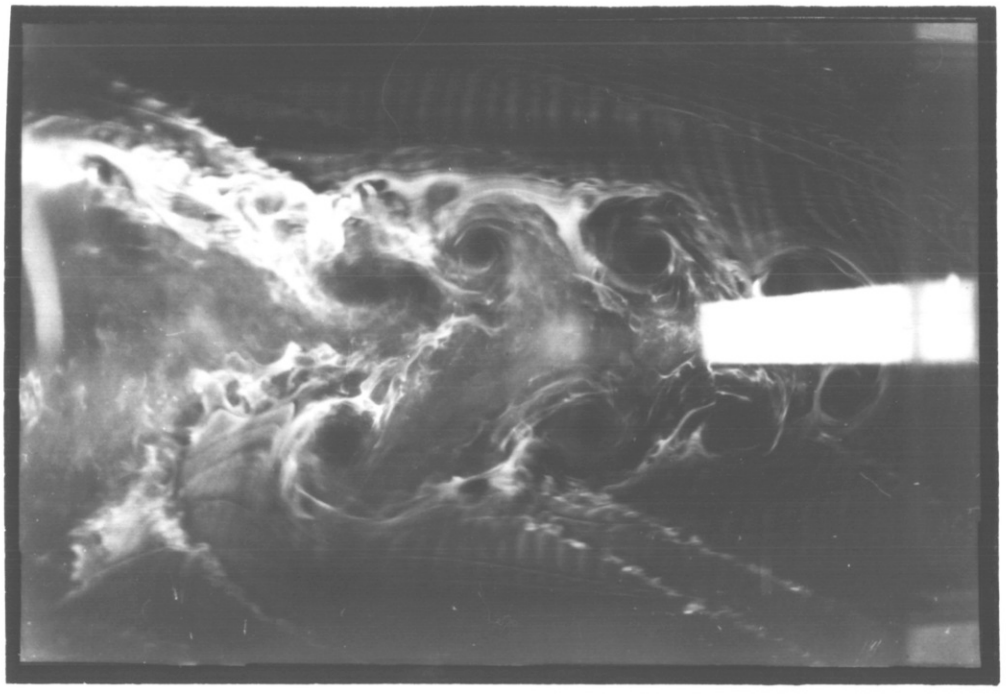


Fig. 6.5(c) The reverse (now upwards) motion of the cylinder forces the top vortex to go downstream.

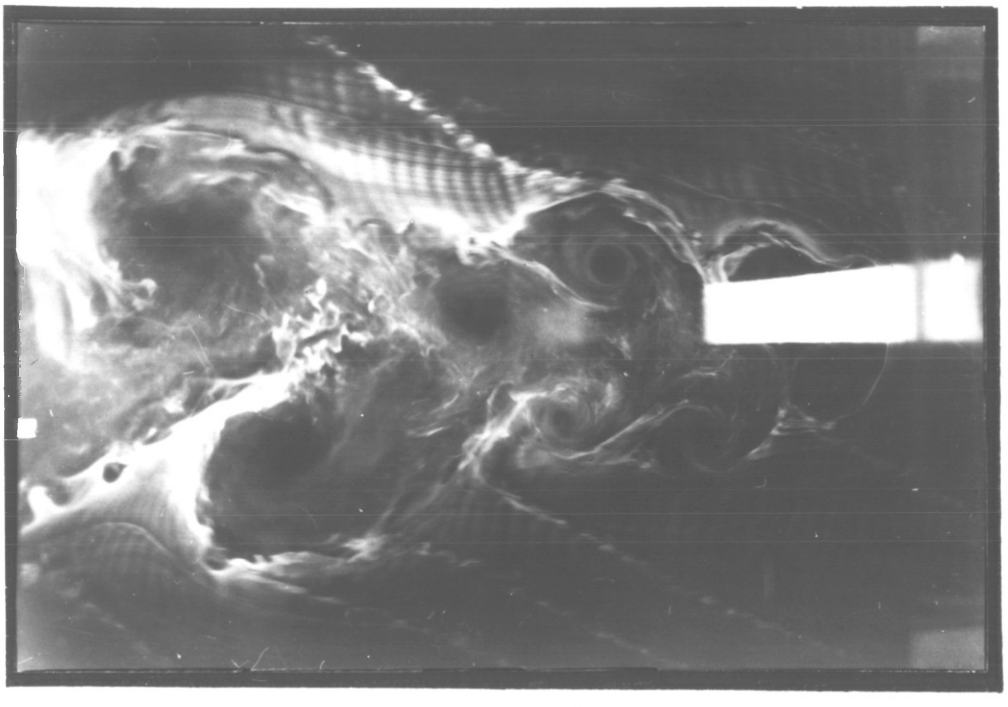


Fig. 6.5(d) Temporary flow reattachment on top face cuts top vortex off from feeding shear layer.

Fig. 6.6 Lock-on Type B.
$U_\infty = 2.72 ms^{-1}$, $f_N = 4Hz$, $U_r = 13.39$

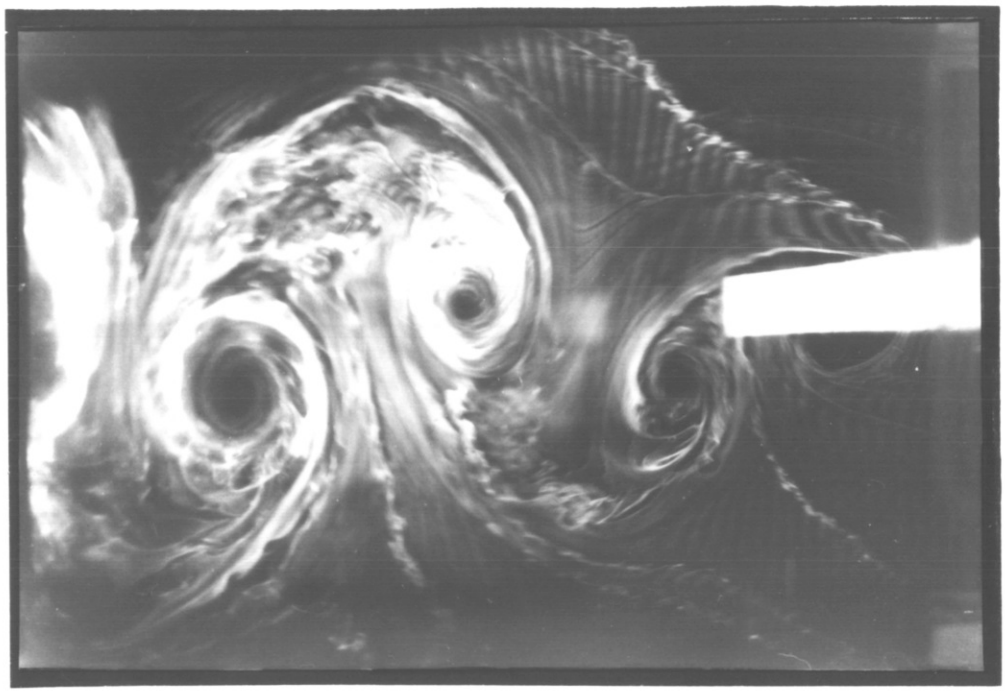


Fig. 6.6(a) Cylinder near TDC, bottom vortex is almost fully grown and is sited near bottom trailing corner CD.

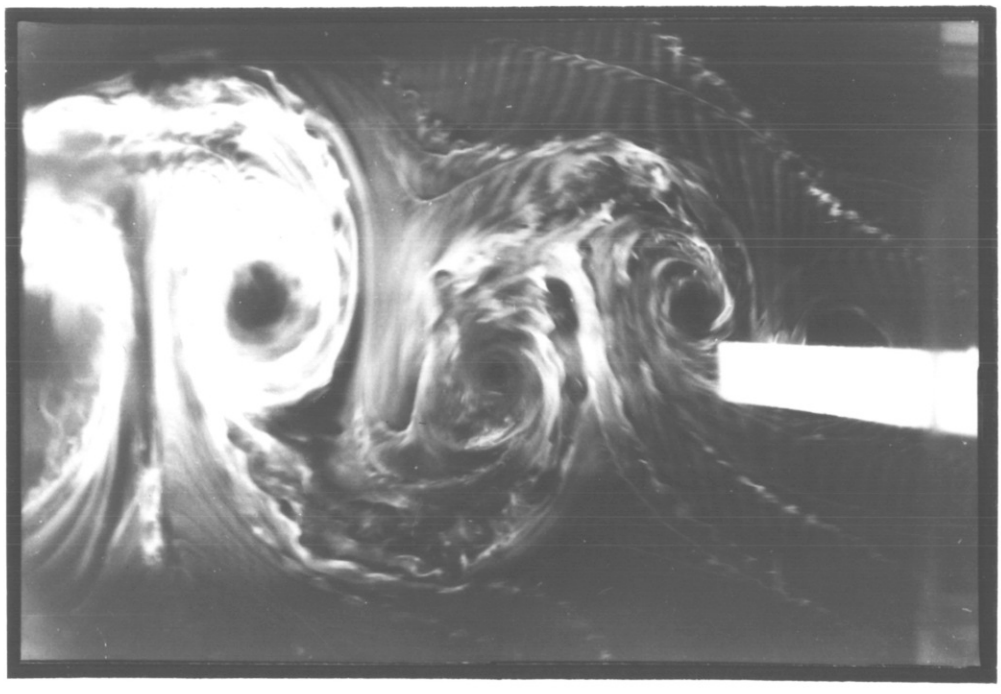


Fig. 6.6(b) Cylinder almost reaches BDC, top vortex is near trailing corner BC.

Fig. 6.6 Lock-on Type B
$U_\infty = 2.72 ms^{-1}$, $f_N = 4Hz$, $U_r = 13.39$

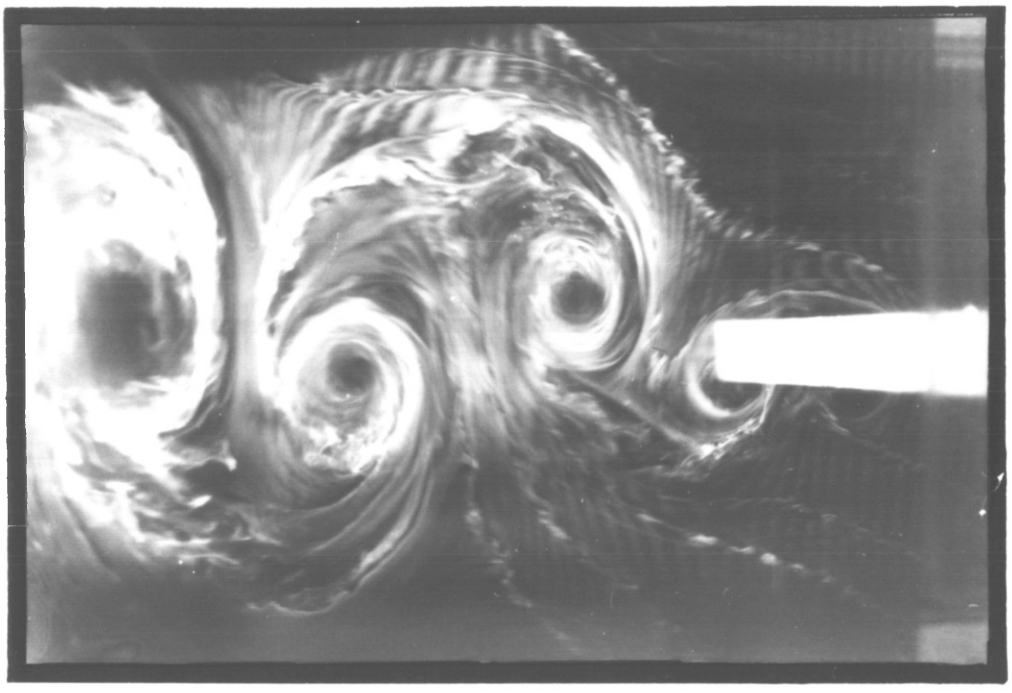


Fig. 6.6(c) Cylinder begins to reverse its direction and moves upwards. Top vortex is being drawn across the wake to join the bottom row of vortices.

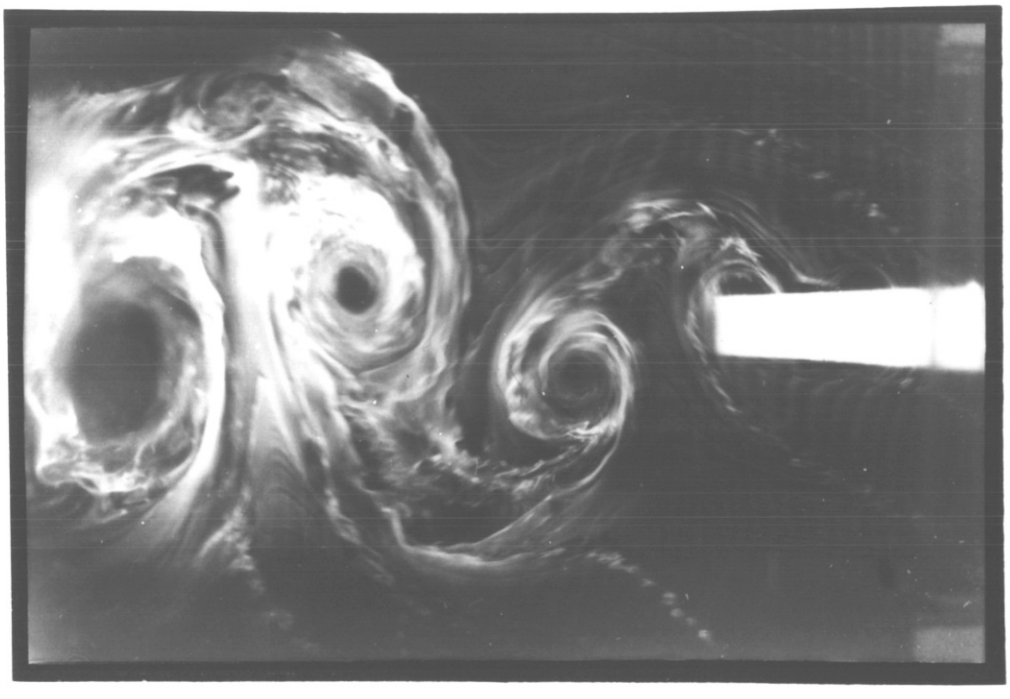


Fig. 6.6(d) Reattachment occurs on top face near trailing corner BC.

Fig. 6.7 Triple Lock-on.
$U_\infty = 2.72 ms^{-1}$, $f_N = 2.5Hz$, $U_r = 21.42$

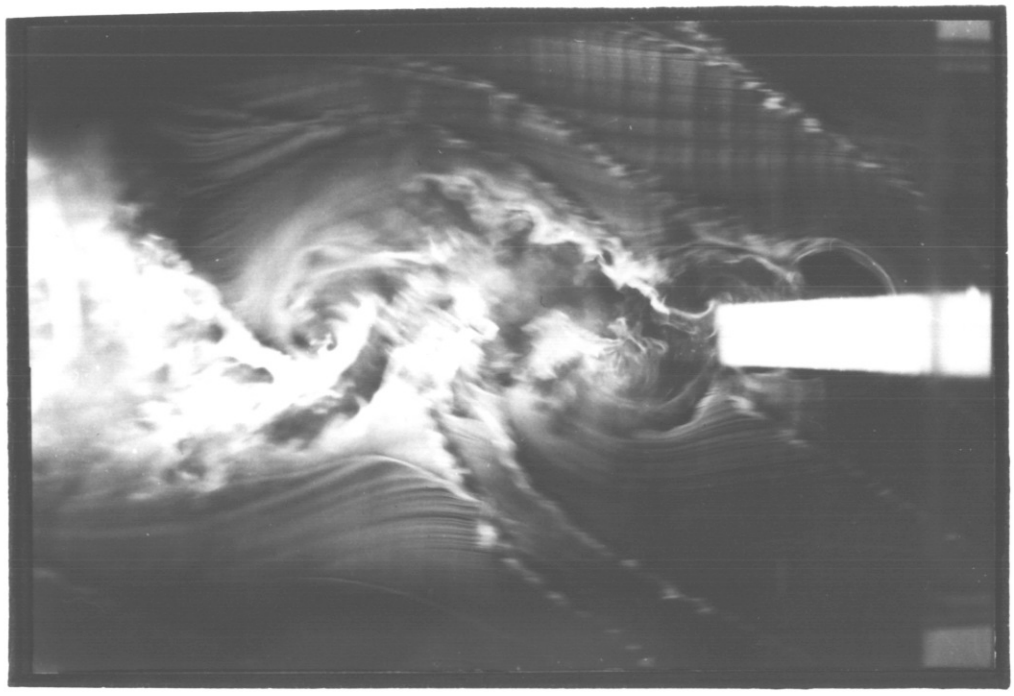


Fig. 6.7(a) Cylinder moves from TDC to BDC, two consecutive vortices fed by the top shear layer begin to grow near the top face of the cylinder.

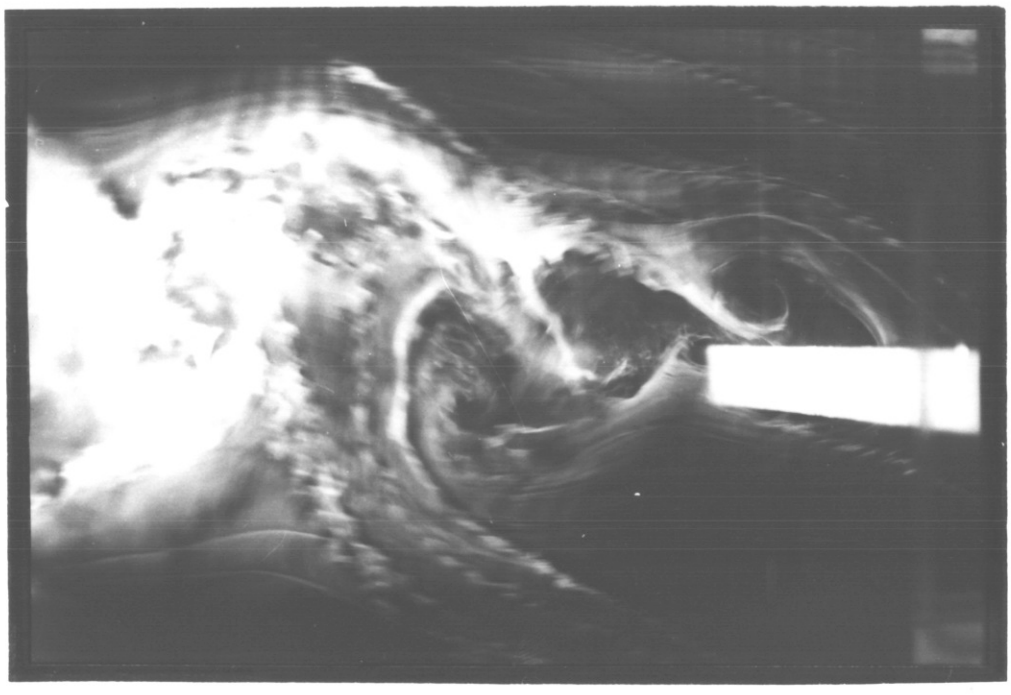


Fig. 6.7(b) Cylinder continues to move downstream and almost reaches the BDC, the two consecutive vortices fed by the top shear layer are almost fully grown.

Fig. 6.7 Triple Lock-on.
$U_\infty = 2.72 ms^{-1}$, $f_N = 2.5 Hz$, $U_r = 21.42$.

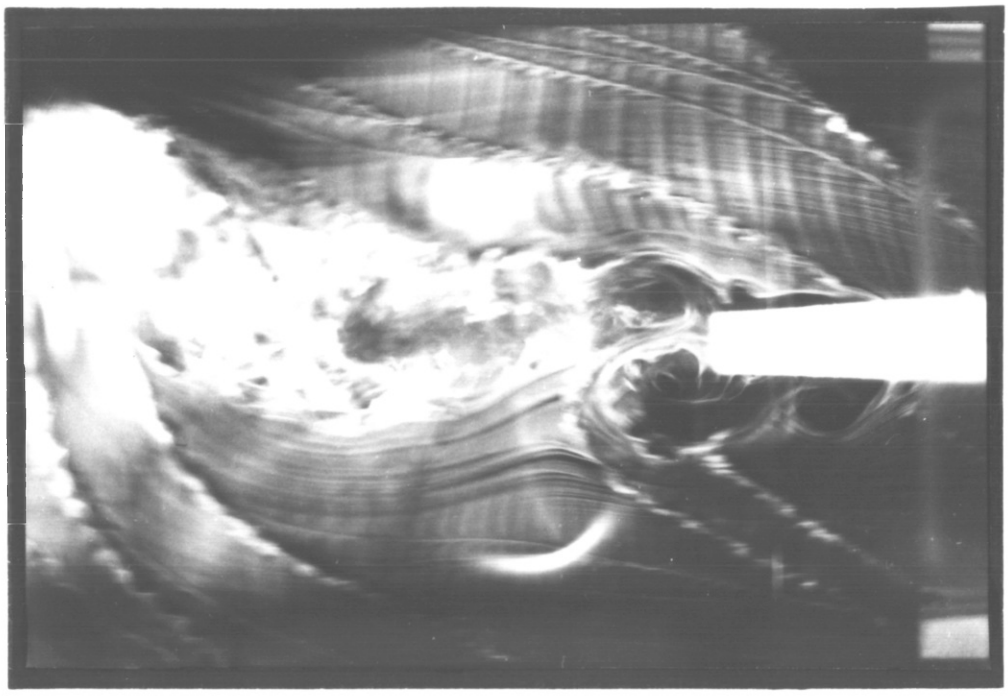


Fig. 6.7(c) Cylinder moving upwards from BDC to TDC. A third and very weak vortex shed by the top shear layer can barely be seen (near corner BC). Two vortices are shed by the bottom shear layer.



Fig. 6.7(d) The cylinder continues to move upwards and almost reaches the TDC.

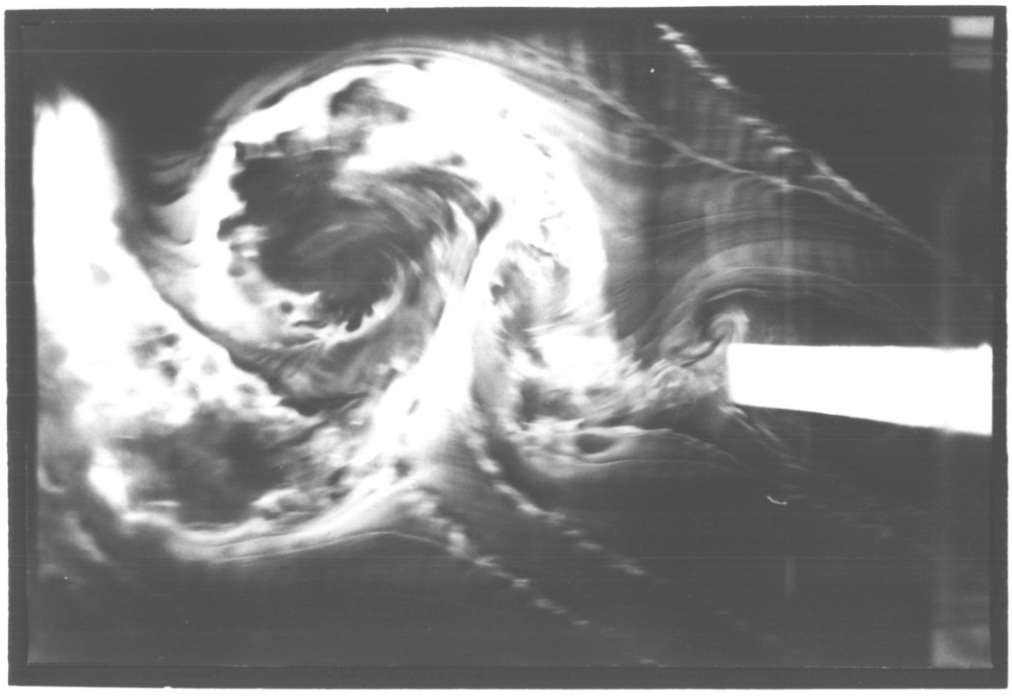


Fig. 6.8 Quasi-steady. $U_\infty = 2.72ms^{-1}$, $f_N = 0.63Hz$, $U_r = 85.02$.

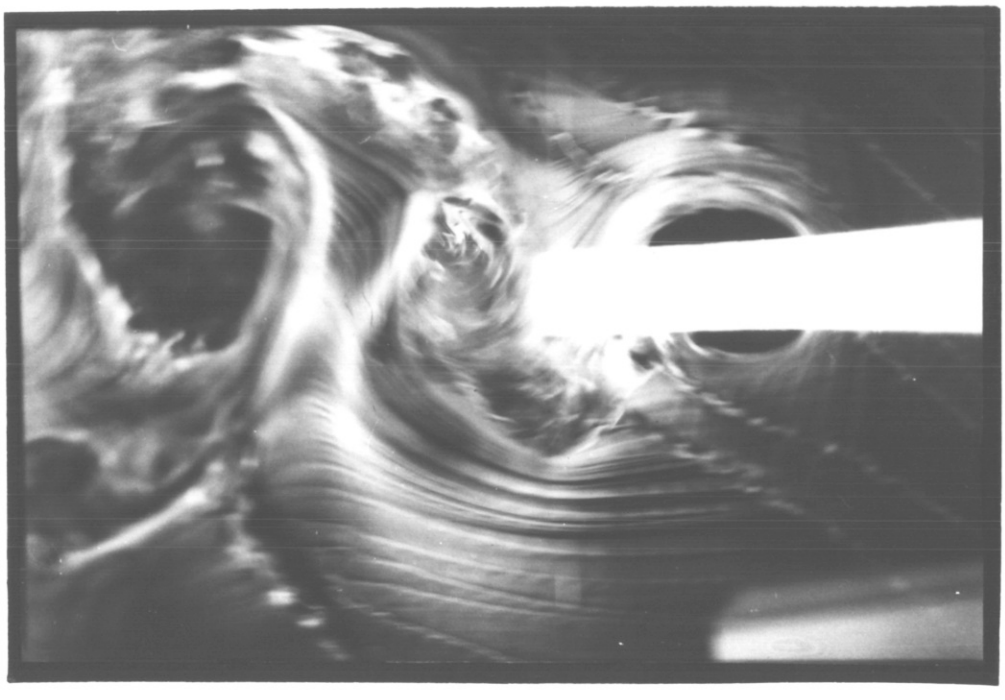


Fig. 6.10 Stationery cylinder. $U_\infty = 2.72ms^{-1}$.

Fig. 6.9 Intermediate Stages

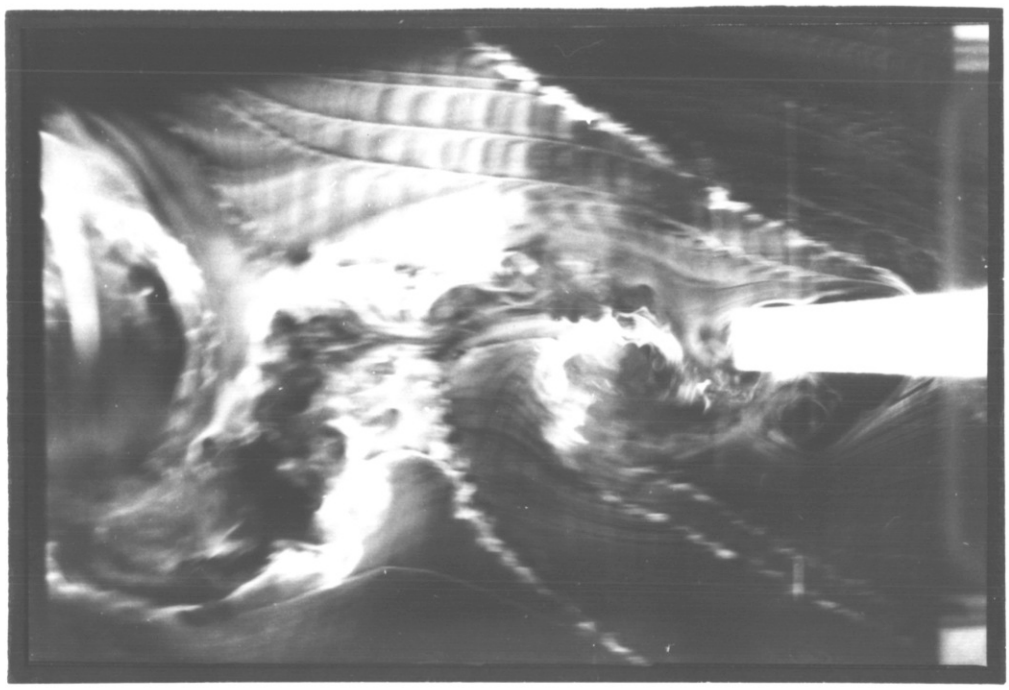


Fig. 6.9(a) U_∞ = 2.72ms^{-1}, f_N= 2Hz, U_r=26.78

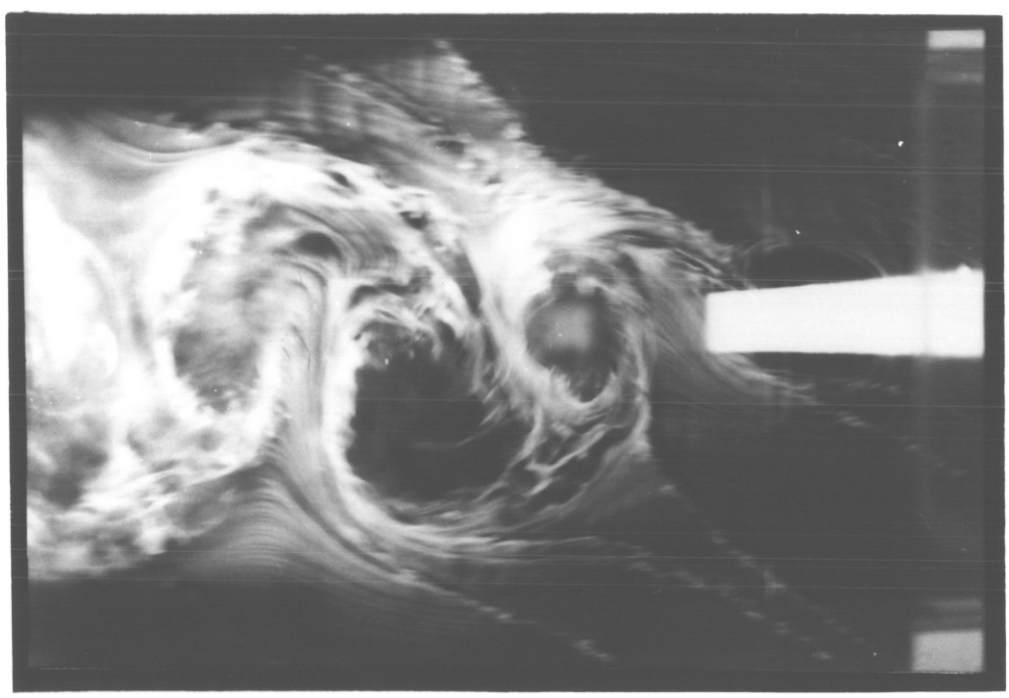


Fig. 6.9(b) U_∞ = 2.72ms^{-1}, f_N= 1.5Hz, U_r= 35.71

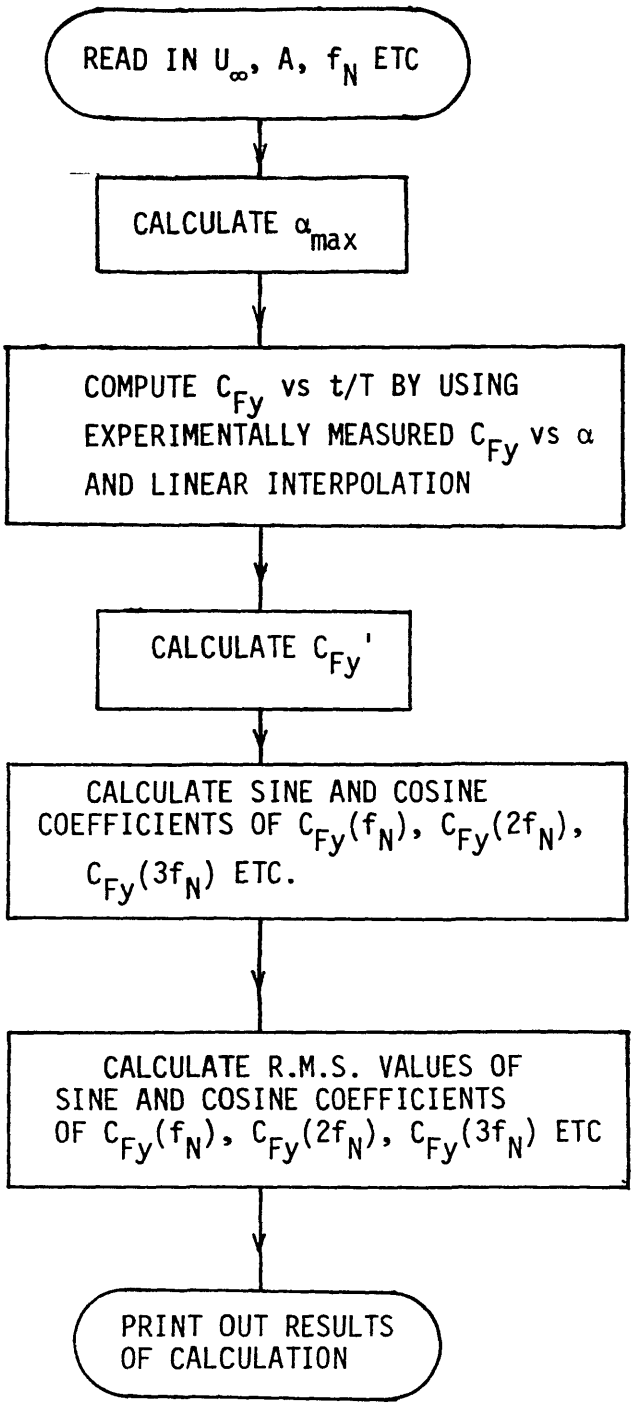


FIG. 7.1 FLOW CHART OF "QUASI PREDICT"

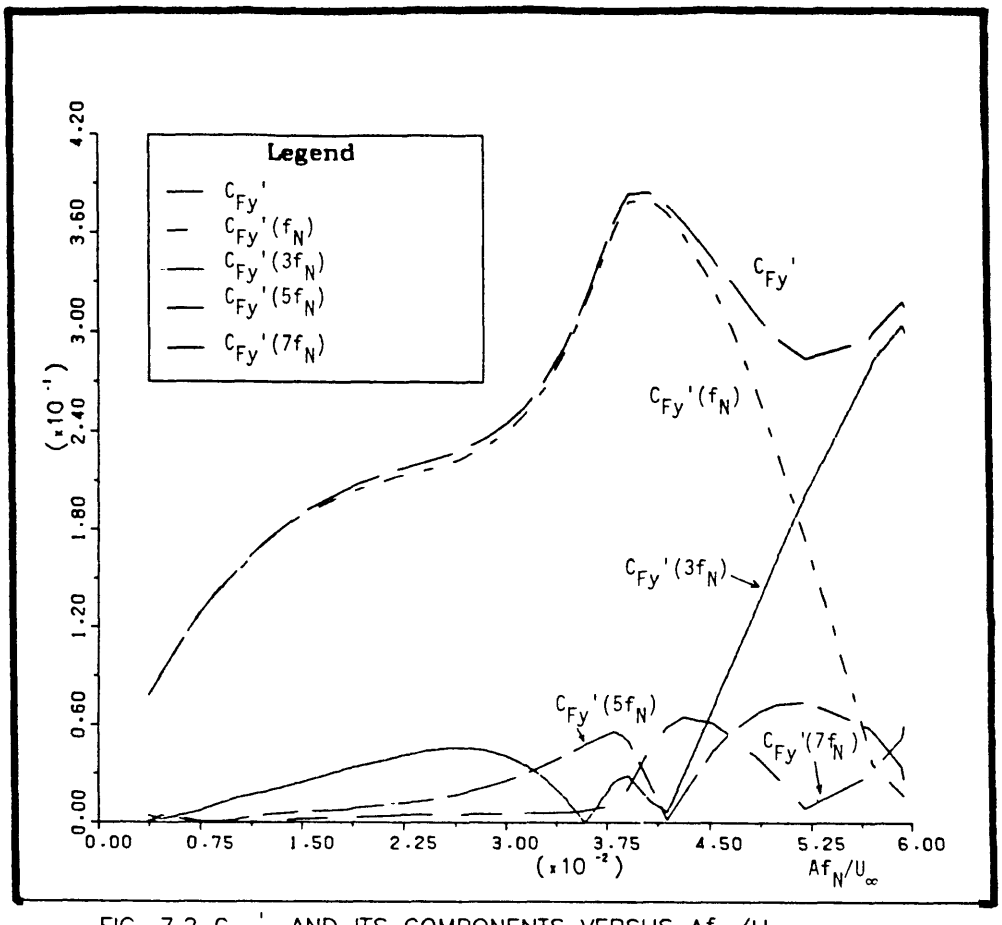


FIG 7 2 C_{Fy}' AND ITS COMPONENTS VERSUS Af_N/U_∞

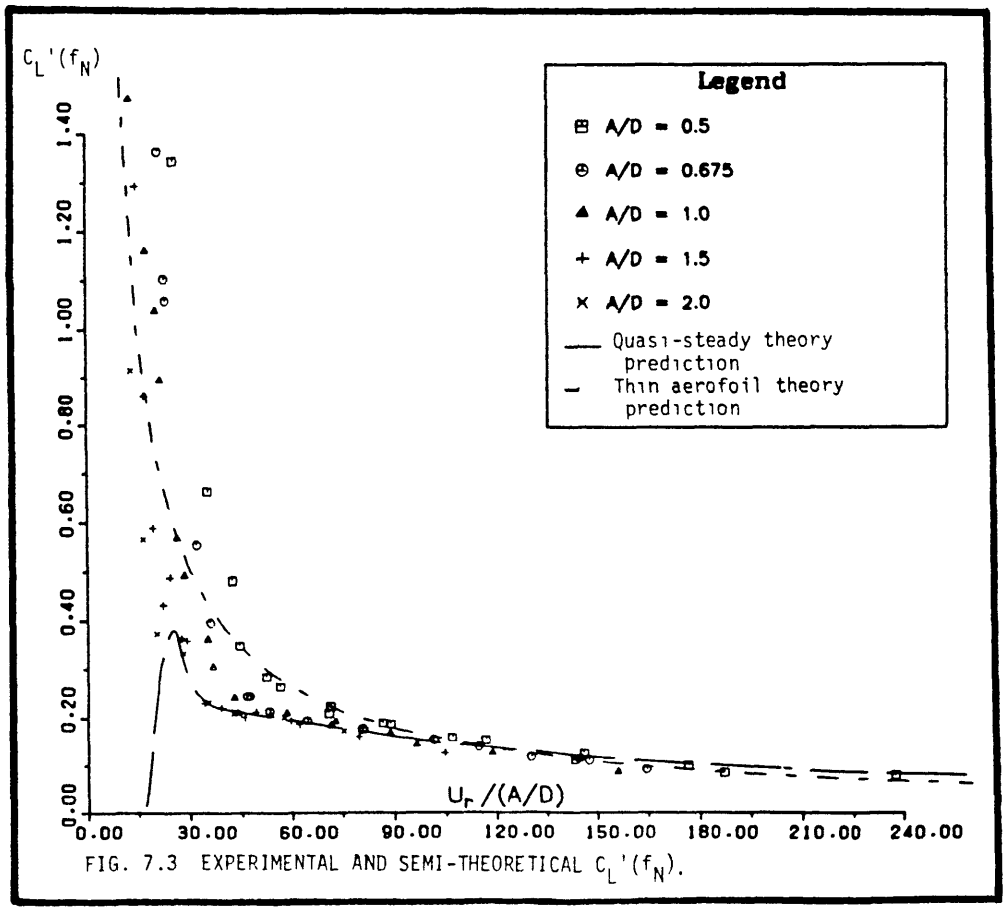


FIG. 7.3 EXPERIMENTAL AND SEMI-THEORETICAL $C_L'(f_N)$.

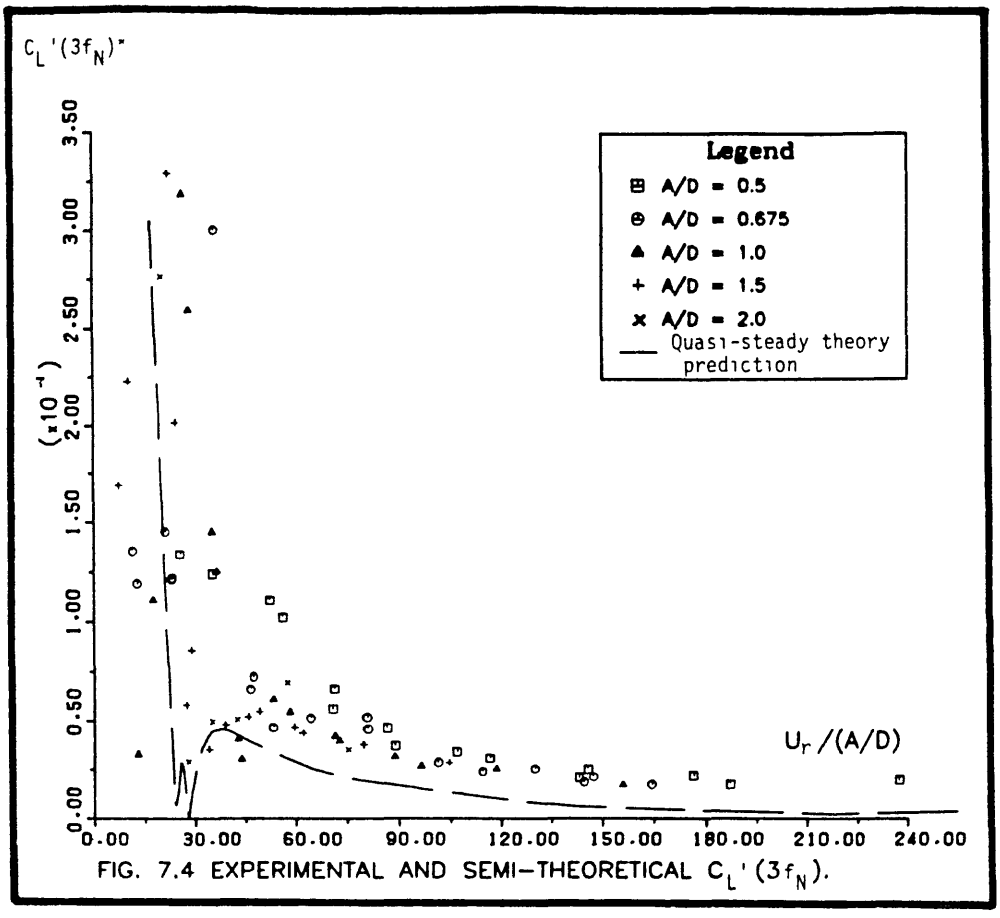


FIG. 7.4 EXPERIMENTAL AND SEMI-THEORETICAL $C_L'(3f_N)$.

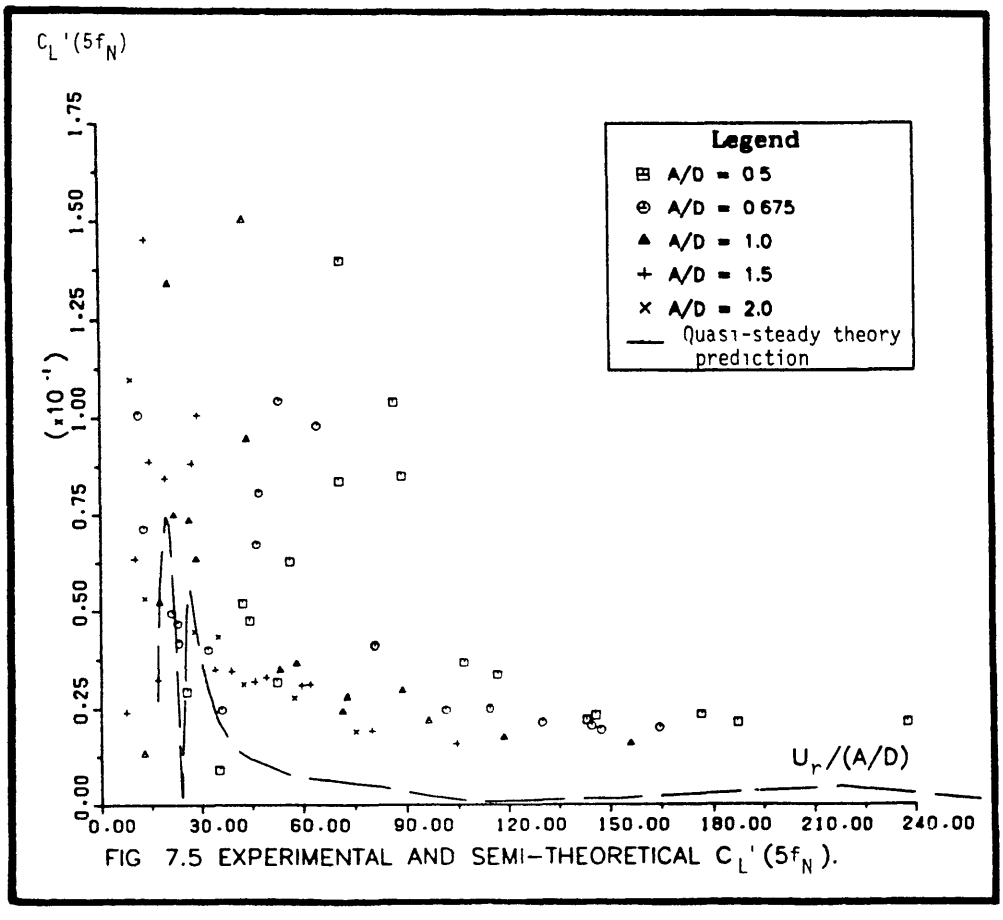


FIG 7.5 EXPERIMENTAL AND SEMI-THEORETICAL $C_L'(5f_N)$.

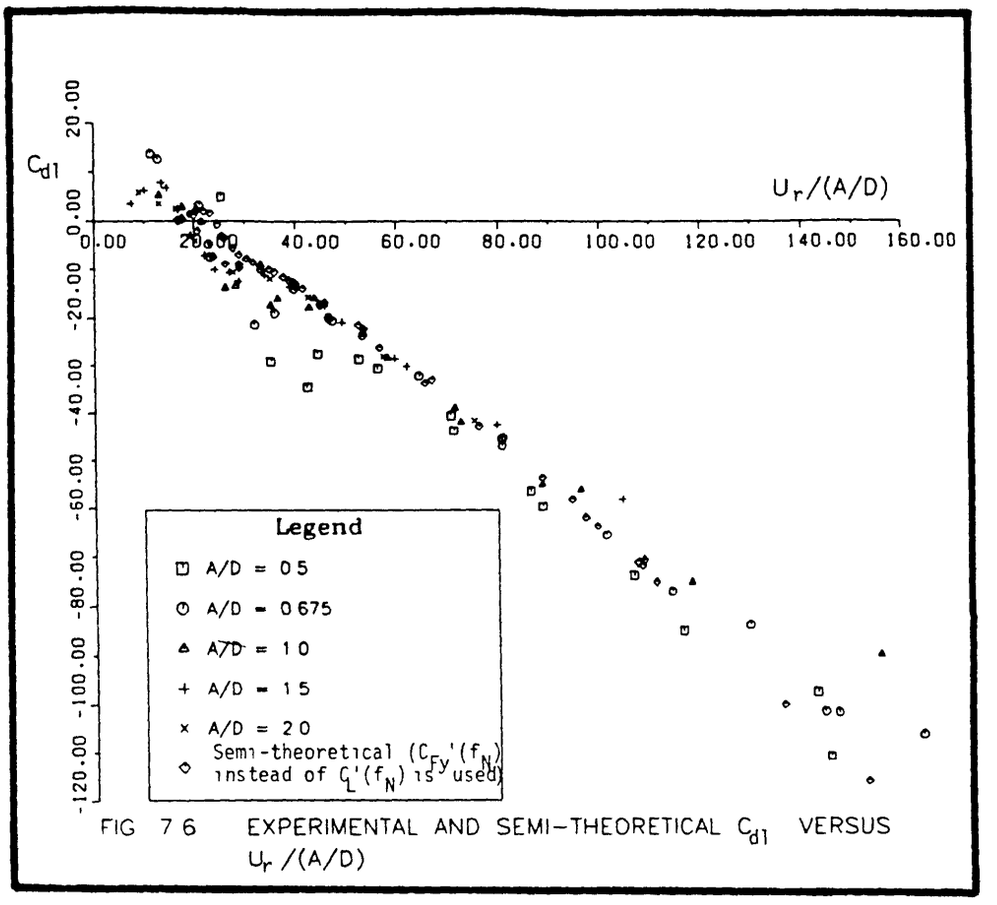


FIG 7.6 EXPERIMENTAL AND SEMI-THEORETICAL C_{dl} VERSUS $U_r/(A/D)$

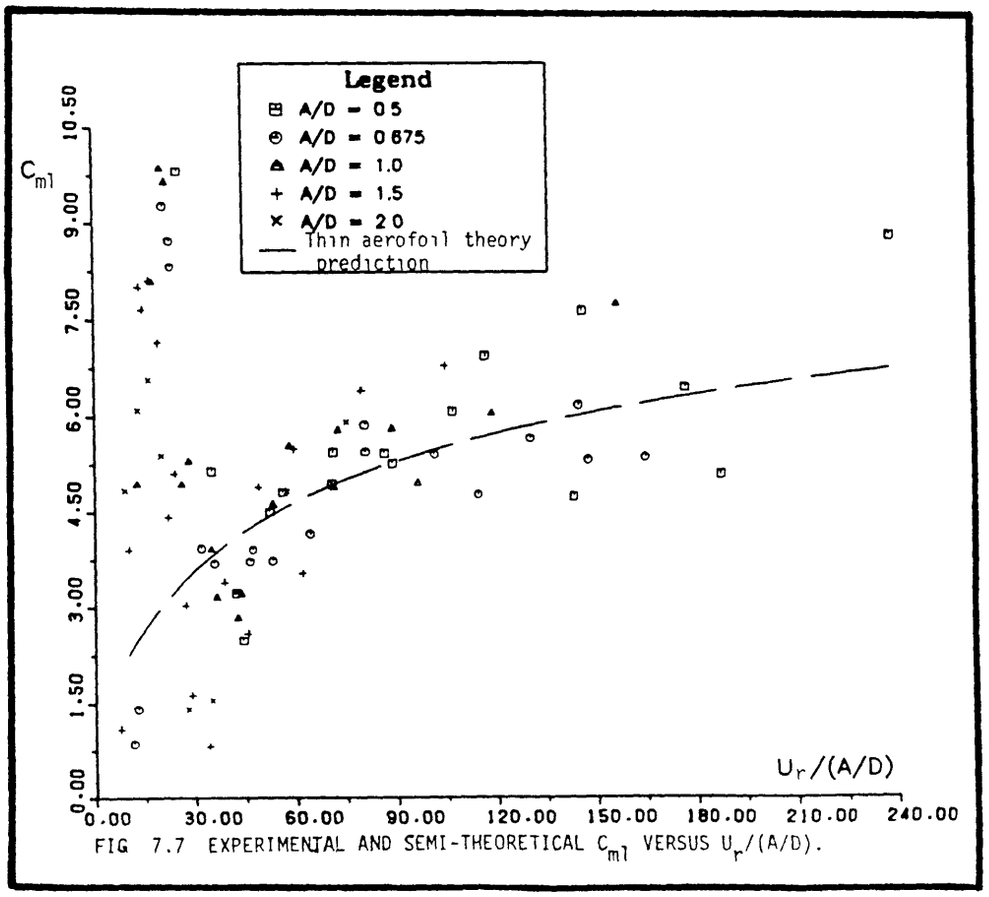


FIG 7.7 EXPERIMENTAL AND SEMI-THEORETICAL C_{ml} VERSUS $U_r/(A/D)$.

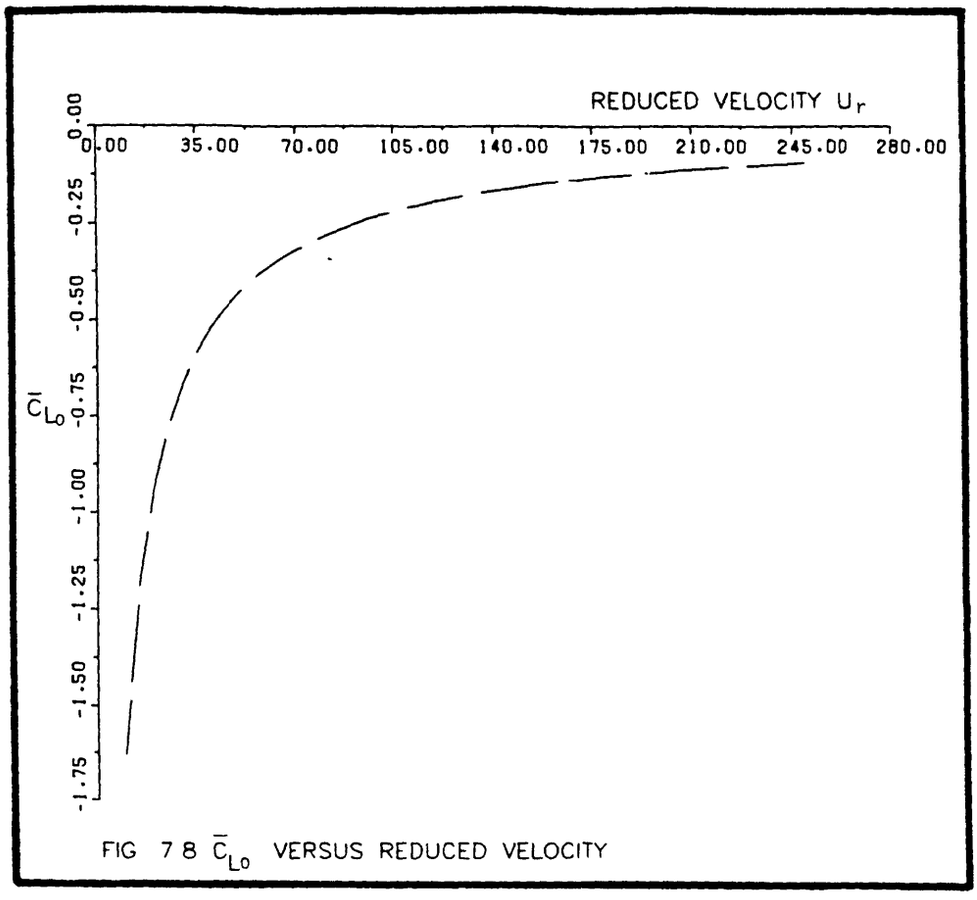


FIG 7 8 $\bar{C}_{Lo}$ VERSUS REDUCED VELOCITY

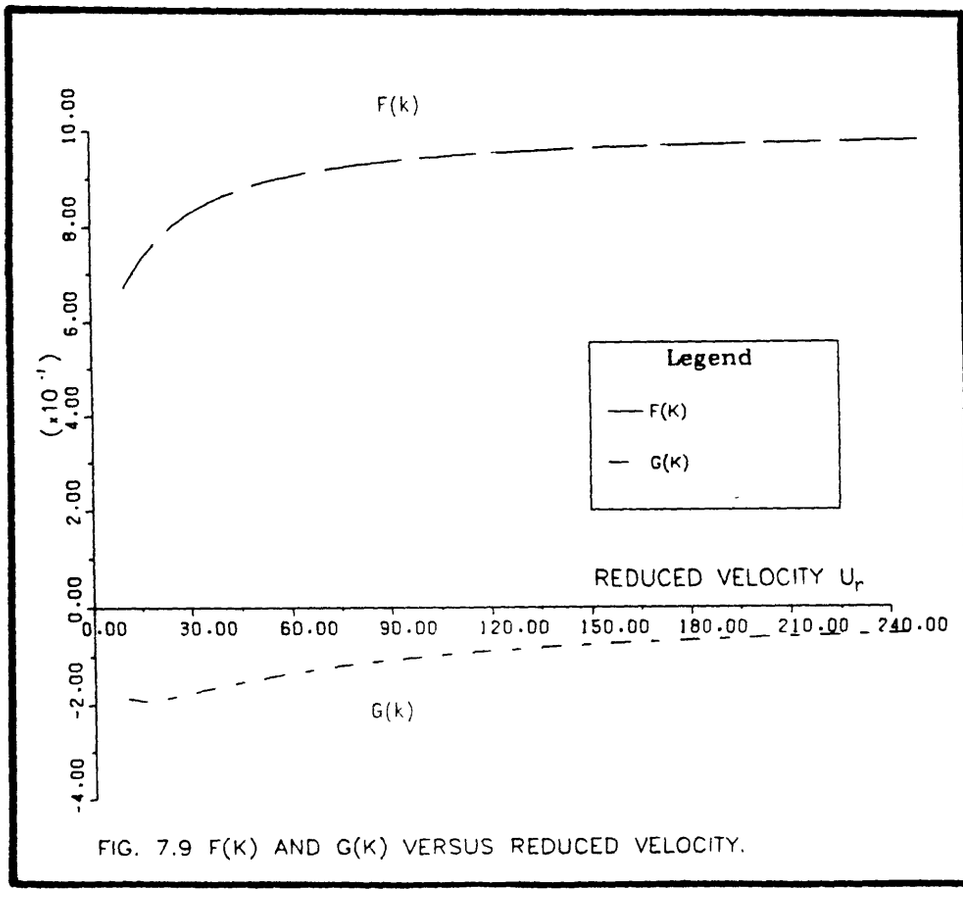


FIG. 7.9 F(K) AND G(K) VERSUS REDUCED VELOCITY.

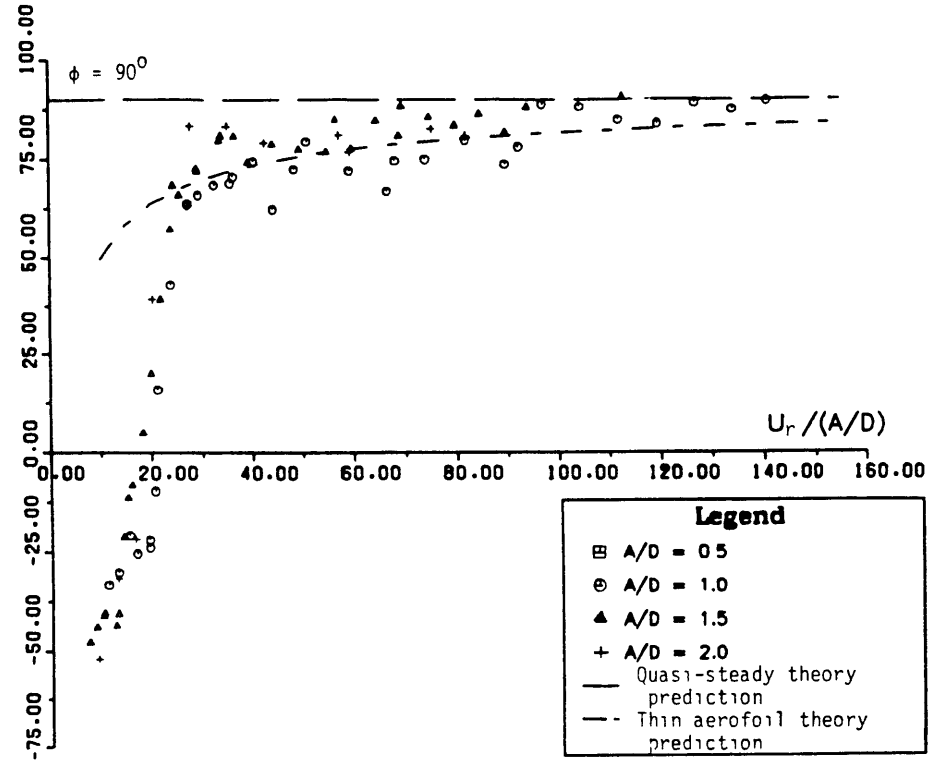


FIG. 7.10 EXPERIMENTAL AND SEMI-THEORETICAL ϕ VERSUS $U_r/(A/D)$.